SYNTHESIS AND GAS ADSORPTION STUDY OF POROUS METAL-ORGANIC FRAMEWORK MATERIALS

A Dissertation
Presented to
The Academic Faculty

by

Bin Mu

In Partial Fulfillment
of the Requirements for the Degree
Doctor of Philosophy in the
School of Chemical & Biomolecular Engineering

Georgia Institute of Technology
August 2011

SYNTHESIS AND GAS ADSORPTION STUDY OF POROUS METAL-ORGANIC FRAMEWORK MATERIALS

Approved by:

Dr. Krista S. Walton, Advisor
School of Chemical & Biomolecular Engineering
Georgia Institute of Technology

Dr. William J. Koros
School of Chemical & Biomolecular Engineering
Georgia Institute of Technology

Dr. Christopher W. Jones
School of Chemical & Biomolecular Engineering
Georgia Institute of Technology

Dr. Carsten Sievers
School of Chemical & Biomolecular Engineering
Georgia Institute of Technology

Dr. Seth Marder
School of Chemistry and Biochemistry
Georgia Institute of Technology

Date Approved: May 3, 2011

To my wife, Wei Gao and my daughter, Claire Gao Mu

ACKNOWLEDGEMENTS

By acknowledgements, I would like to express my sincere gratitude to several people who have played a significant role throughout my graduate education and wonderful life in the USA, who deserve much more than one sentence of appreciation.

First, I wish to thank Dr. Krista S. Walton. Looking back at the past five years, I have been very fortunate to have Dr. Walton as my advisor. She is a very nice and generous person in front of students. For me, she has always been a patient listener, a trustable friend, and a very supportive mentor. Without her encouragement and help, I would not be as great as I am. Dr. Walton is also a perfect role model to me to pursue my dream being a faculty. Her charming personality and excellent leadership have been attracting and inspiring me to make efforts towards my dream. As her first graduate student, I can tell that I feel happy and lucky!

It is my great honor to have Dr. William J. Koros, Dr. Christopher W Jones, Dr. Carsten Sievers, and Dr. Seth Marder on my thesis committee. I am thankful to them for their invaluable advice and help to improve my studies. Especially, I am grateful to Dr. Koros and Dr. Jones for their blessing and support in helping me obtain a great post-doctoral position at MIT.

I would like to thank Dr. Feng Li and Dr. Yougui Huang for their help in chemistry and crystallography. Their rich experience and generous attitude have made my life much easier. Appreciation is also given to the entire Walton group.

Friendship is important and unforgettable. I have enjoyed good times with Dr. Aibin Shi, Kebin Yu, Xin Sun (Selma), Xiaochun Sun and their families at Manhattan,

Kansas, and Dr. Dong Ding and Yan Qian, Dr. Mingfei Liu and Lily, Sheng Dai and Tingting Wang, Jason and Jasmine, Zhixuan Xia and Dong Yang in Atlanta, Georgia.

Last but not least, I would like to thank my parents-in-law. I would not be here without their encouragement and support. I owe special thanks to my dear wife, Wei Gao. I am great only in her love!

Bin Mu

03.18.2011, Atlanta

TABLE OF CONTENTS

LIST OF TABLES

LIST OF FIGURES

SUMMARY

Metal-organic frameworks (MOFs) or porous coordination polymers (PCPs) have become the focus of intense study over the past decade due to their potential for advancing a variety of applications including air purification, gas storage, adsorption separations, catalysis, gas sensing, drug delivery, and so on. These materials have some distinct advantages over traditional porous materials such as the well-defined structures, uniform pore sizes, chemically functionalized sorption sites, and potential for post-synthetic modification, etc. Thus, synthesis and adsorption studies of porous MOFs have increased substantially in recent years. Among various prospective applications, air purification is one of the most immediate concerns, which has urgent requirements to improve current nuclear, biological, and chemical (NBC) filters involving commercial and military purposes. Thus, the major goal of this funded project is to search, synthesize, and test these novel hybrid porous materials for adsorptive removal of toxic industrial chemicals (TICs) and chemical warfare agents (CWAs), and to install the benchmark for new-generation NBC filters. The objective of this study is three-fold: (i) Advance our understanding of coordination chemistry by synthesizing novel MOFs and characterizing these porous coordination polymers; (ii) Evaluate porous MOF materials for gas-adsorption applications including CO_2 capture, CH_4 storage, other light gas adsorption and separations, and examine the chemical and physical properties of these solid adsorbents including thermal stability and heat capacity of MOFs; (iii) Evaluate porous MOF materials for next-generation NBC filter media by adsorption breakthrough

measurements of TICs on MOFs, and advance our understanding about structure-property relationships of these novel adsorbents.

CHAPTER 1

INTRODUCTION

Ordered porous materials are crucial for a variety of industrial applications including catalysis, ion exchange, separation, and purification. According to the size of pores, porous solids are classified into three groups: micropores ($d \leq 2$ nm), mesopores (2 nm $< d \leq 50$ nm), and macropores ($d > 50$ nm). Depending on the components of the framework, ordered porous materials include organically templated inorganic porous solids and organic-inorganic hybrid porous solids. The classical example of inorganic porous solids is zeolites including aluminosilicates, aluminophosphates, and other inorganic derivatives of zeolites. Hyrid porous solids involve pillared layered materials, metal-organic polyhedra, and metal-organic frameworks (MOFs).

Our research direction is the design or identification of novel porous materials for improved air purification systems involving commercial and military purposes. Particularly, it is the major goal of this funded project to search, synthesize, and test MOFs for adsorptive removal of toxic industrial chemicals (TICs) and chemical warfare agents (CWAs), and install the benchmark for new-generation nuclear, biological, and chemical (NBC) filters.

To achieve the goal in adsorption applications, it is needed to develop an in-depth understanding of structure-property relations and host-guest interactions. With this critical information of the adsorption mechanisms, i.e., how, where, and why a molecule adsorbs in a certain material, we can then exploit this knowledge to design structures that interact more effectively with the molecule of interest. From the results of well-studied

traditional porous materials, we do know that making materials with simple porosity is definitely not enough to achieve the goal. Thus, impregnation approaches of "active sorption sites" were proposed to improve the adsorption capacity of the target molecules. For example, a specific impregnated activated carbon (I-AC) was applied in the traditional NBC filter systems. However, disordered or nonuniform distribution of the impregnated heteroatoms and the difficulty of chemical modification of adsorbents largely restrict the effects of impregnation. Two possible solutions exist: new technology to introduce "active sorption sites" on a porous material or novel porous materials possessing "active sorption sites".

The discovery of MOFs has provided a promising platform for achieving advanced adsorbents. First, the building-block approach to MOF design provides tremendous flexibility in tailoring these porous materials to have specific physical properties and chemical functionalities, in which we can say they possess "active sorption sites". Second, the post-synthesis approach to chemical modification of MOFs provides numerous opportunities to play with the functional groups of the adsorbent, in which we can introduce "active sorption sites". Thus, MOFs are regarded as a highly promising candidate to replace current air purification media. Our work will mainly focus on the synthesis, characterization, and gas adsorption study of novel MOF materials. At the same time, to compare adsorption properties of MOFs and gain a better understanding of the adsorption mechanism, gas adsorption measurements of other types of porous materials including activated carbon and zeolites will fall into my work area as well. In short, the objective of this research is three-fold:

(1) Advance our understanding of coordination chemistry by synthesizing novel MOFs and characterizing these porous coordination polymers as contributions towards fundamental research.

(2) Evaluate porous MOF materials for gas-adsorption applications including CO_2 capture, CH_4 storage, other light gas adsorption and separations, and examine the chemical and physical properties of these solid adsorbents including thermal stability and heat capacity of MOFs.

(3) Evaluate porous MOF materials for next-generation NBC filter media by adsorption breakthrough measurements of TICs on MOFs, and advance our understanding about structure-property relationships of these novel adsorbents.

1.1 ORIGIN, STRUCTURE, AND CLASSIFICATION OF MOFS

There was a long-held belief that it was impossible to synthesize materials with three-periodic frameworks composed of atoms linked by directional covalent bonds.[1] However, in the past two decades, cutting-edge work from the Yaghi group in the US, Kitagawa group in Japan, and Ferey group in France has solved this "crystallization problem", and led to a huge research explosion towards hybrid inorganic-organic framework materials. These hybrid porous materials are called metal-organic frameworks (MOFs), or porous coordination polymers (PCPs), indicating they are originally from the field of coordination chemistry. Indeed, the coordinate covalent bonds play a major role to form MOFs.

The term, "coordination polymers" appeared in the early 1960s, and the related research was first reviewed in 1964.[2] Since then, scientists and engineers have developed versatile studies focused on the synthesis, characterization, and application of

coordination polymers. In particular, remarkable progress has been made in the past fifteen years, which can be demonstrated from the number of published articles in the related area (Figure 1.1).

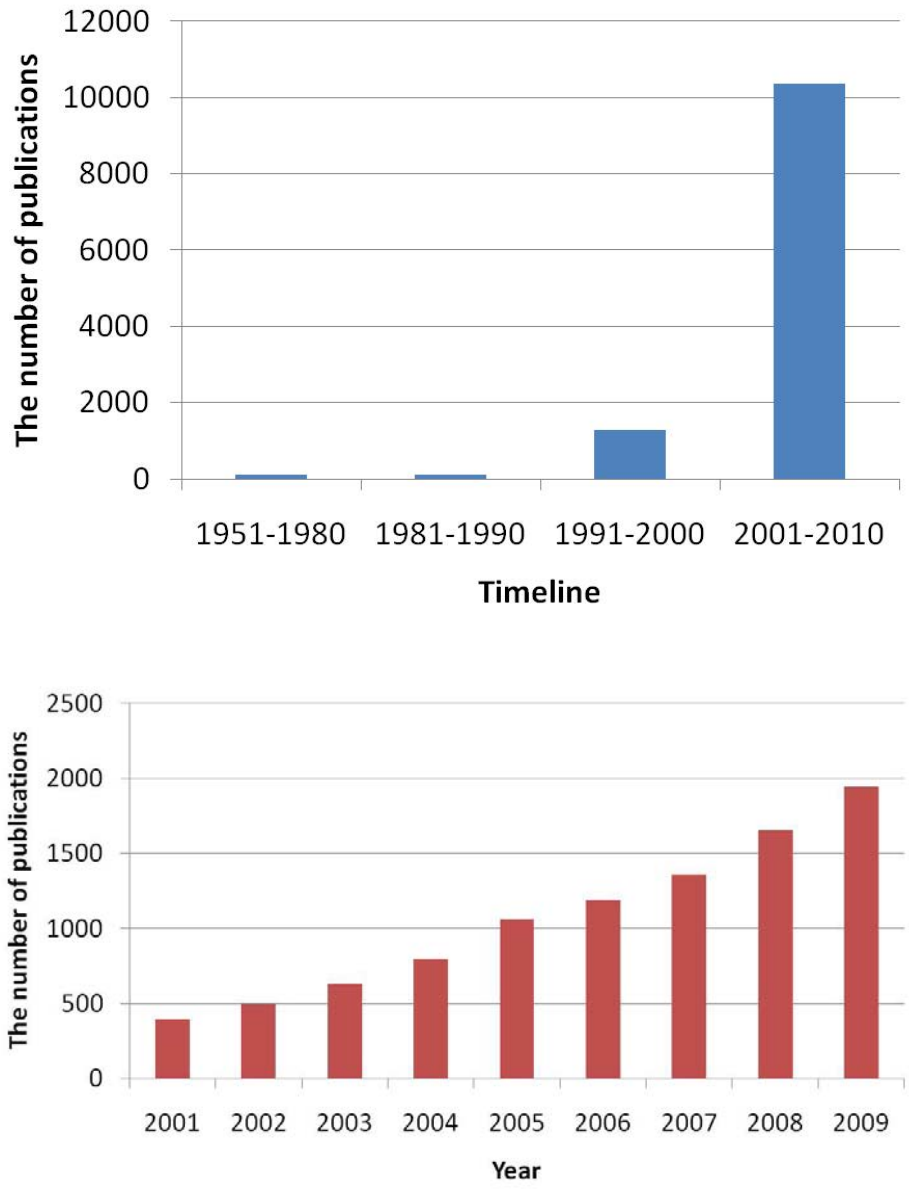

Figure 1.1 The number of published articles containing the topic "coordination polymers" surveyed using Web of Science database.

MOFs are composed of metal ions as connectors and organic ligands as linkers. Depending on the metal ion and its oxidation state, coordination numbers could commonly be 2 to 6 for transition metals, or 6 to 12 for lanthanides. Different coordination numbers result in various geometries, which can be linear, T or Y shaped, tetrahedral, square-planar, square-pyramidal, trigonal-bipyramidal, octahedral, trigonal-prismatic, pentagonal-bipyramidal, or polyhedral coordination geometry, and the corresponding distorted forms.[2] Assemblies of these polyhedra normally composed of metal carboxylate clusters are called secondary building units (SBU). The three-dimensional skeleton can be described by the association of secondary building units (SBU).

According to the spatial dimensions, there are four types of porous coordination polymers: 0D dots, 1D channels, 2D layers, 3D intersecting channels.[2] 0D dots are completely surrounded by wall molecules, which are divided into two situations: solid without windows and solids with windows which are too small to allow the guest molecules to pass. In those cavities, the guest molecules are isolated from their neighbors and from the outside world. Pillared layer structures with 1D channels are often found in ancient buildings, such as the Parthenon in Athens. Such motif is also very useful to assemble porous frameworks on the microscopic scale. Modification of the pillar ligands enables us to realize systematic control not only of the pore size, but also of the surface functionality. In 2D layer-type framework, hydrogen bonding and π-π interaction play an important role to link the layers. Various guest molecules could be intercalated between the layers by above-mentioned forces. Thus, compared with other types of porous coordination polymers, such sheet structure could be more flexible and amenable to

intercalation of guest molecules. Compared with the development of inorganic porous solids, 3D intersecting channels occurs much later in coordination polymers due to the framework instability associated with high porosity. One classic example is IRMOF series, which are made of Zn-O-C clusters and dicarboxylate ligands with different length.

According to the classification of framework robustness, there are three categories, 1st, 2nd, and 3rd generation.[2] The first generation MOFs shows the irreversible framework collapse once the guest molecules were removed. The second generation MOFs has stable and rigid frameworks, which possess permanent porosity even after the guest molecules were removed. The third generation MOFs has flexible and dynamic frameworks, which can change their channels or pores reversibly, responding to external stimuli such as electric field, pressure, light, etc.

1.2 SYNTHESIS OF METAL-ORGANIC FRAMEWORKS

Generally, MOFs are synthesized at low temperature (< 250 ^{o}C) using a solvothermal reaction technique. Besides metal ion and ligand, other factors including counter ion, solvent, acidity and concentration of solution, temperature and time of reaction all play a role in forming the final crystal structure. If water were used as solvent, it is called hydrothermal reaction. Often-used organic solvents include N,N-dimethylformamide (DMF), N,N-diethylformamide (DEF), N,N-dimethylacetamide (DMA), ethanol, methanol, dimethyl sulfoxide (DMSO), etc. To select proper solvents, one should consider association constants, solubility, evaporability, thermal stability, and sometimes polarity. Besides typical solvothermal or hydrothermal reaction technique, other approaches to produce MOFs involve interface-diffusion method[3], ionothermal

synthesis using ionic liquids[4-5], microwave synthesis[6-7], electrochemical route[8], ultrasonic synthesis[9], and high throughput synthesis[10].

Compared with the synthesis of classic zeolite-related inorganic solids, the solvothermal synthesis of MOFs is a much simpler and possesses the following advantages: (1) The solvent itself in the reaction acts as the main template, which results in a great advantage, the skeleton of most MOFs being neutral.[11] In MOFs, the solvents have weaker interactions with the neutral framework and thus easily evolve the structure at low temperature, often keeping the framework intact after removing associated guest molecules and yielding better porosity; (2) The existence of inorganic and organic parts in the structure allows hydrophilic and hydrophobic features to coexist within the pores and may have important impact on the physical properties of the bulk material, especially in adsorption applications; (3) While zeolites are often based on a small variety of cations, MOFs can apply almost all the cations as the connectors; (4) Considering a large choice of functionalized organic linkers adopted by MOFs, there are almost uncountable combination of connectors and linkers to create new MOFs, at least in theory, which can be supported by the reported number of MOF structures.

1.3 PROSPECTIVE APPLICATIONS OF MOFS

Porous crystallized solids have always attracted the attention of chemists, physicists, material scientists, and chemical engineers because of not only scientific interests on fundamental research, but also practical industrial applications. Traditionally, applications of porous materials involve ion exchange, adsorption separation, and catalysis. Zeolites, as the forerunner of MOFs among porous solids, have been strategic materials since the 1960s.[11] Their applications are majorly concerned with

petrochemistry, catalysis, and selective separation. Their principal limitation has been due to the relatively small size of the pores and difficulty for chemical modification. In addition, only 38 natural and 194 synthetic zeolites structures have been identified so far, which obviously limits their options in application. Thus, the generation of MOFs made a significant breakthrough. These organic-inorganic hybrid-materials bring us several advantages over pure inorganic porous materials in the following respects:

(1) Available large pore volume. Many MOFs possess pore volume more than 1 cc/g, and some of them are larger than 2 cc/g, such as UMCM-1,[12] DUT-6,[13] etc.

(2) Achievable high surface area. Many MOFs possess surface area larger than 2000 m^2/g, and some of them are remarkably higher than 5000 m^2/g, such as UMCM-2,[14] IRMOF-16,[15] etc.

(3) Adjustable pore size. The size of pore is well defined ranging from microporous channel (Cu-BTC,[16] IRMOF-1[17] etc.) to mesoporous cage (UMCM-1,[12] MIL-101,[18] DUT-6,[13] etc.). A classic example is the IRMOF series,[19] which is made of Zn-O-C clusters and dicarboxylate ligands of varying lengths to control the pore size.

(4) Variety of structures. There are thousands of new MOF structures reported every year, and the rate of publication keeps increasing.[20] The accumulated amount of MOFs will be much larger than that of any other types of porous materials, which provides almost uncountable candidates for various applications.

(5) Large diversity in the architecture of MOFs. This enriches our knowledge about topology, crystallography, and solid geometry. I believe that the beauty of symmetry ubiquitous in MOFs will attract not only scientists, but also artists.

(6) Plentiful supply of organic parts in MOFs makes post-synthesis modification possible.

Such a powerful technique endows MOFs with versatile characteristics so that desired optical, electronic, magnetic, catalytic, or even biological properties could be obtained. Thus, it is not surprising to see that the next-generation multifunctional materials may come from the family of MOFs.

In spite of these important advantages, there are several crucial weaknesses in some MOFs. Many MOFs tend to decompose once exposed to humid air.[21-24] In addition, reported porous MOFs so far are unlikely to compete with zeolites and other oxide-based porous materials in high-temperature applications due to their limited long-term stability under such conditions and high cost. Based on the above recognition of MOFs, many detailed studies have been performed to explore the potential of these hybrid materials, which have broadened their emerging application range beyond the traditional use as catalysts and adsorbents. In fact, they now seem set to contribute to developments in areas ranging from microelectronics to medical diagnosis.

1.3.1 Air Purification

When a solid is exposed to a gas, the gas molecules will attach to the surface of the solid due to physical or chemical interactions between the solid and the gas molecules. This phenomenon is termed adsorption. Various technologies are related to adsorption phenomenon. Besides widely civil applications for gas separation in the chemical and petrochemical industries, military application is also explored. In particular, because toxic industrial chemicals (TICs) and chemical warfare agents (CWAs) are a growing concern to modern military operations, it is required to develop an effective

chemical filter in individual and collective protection systems. Currently used nuclear, biological, and chemical (NBC) filters containing an impregnated activated carbon (I-AC) were developed around 60 years ago. The I-AC filters toxic vapors or gases by two mechanisms, physical adsorption in the pores of the activated carbon and chemical reaction with the impregnants.[25]

In 1998, to address the broader issue of industrial-based chemicals, a short-list of 98 chemicals out of tens of thousands of chemicals was generated from cooperation of a trinational group. The 98 TICs were classified into three hazard-index rankings as provided by the international group: 21 high-, 41 medium-, and 36 low-hazard vapors and gases. These chemicals present a broad range of physical and chemical properties, among which concerned physical properties are vapor pressure and molecular weight. In general, an increase in the TICs' vapor pressure will decrease the adsorption potential and thus reduce the adsorption capacity. Thus, when tested for single-pass filters operated at normal ambient temperatures, physisorption on activated carbon adsorbents are not effective enough to filter chemicals with a vapor pressure above about 100 mm Hg at 25 ^{o}C. The examined TICs must undergo chemical reactions with either the impregnants or the adsorbent's surface.

Ammonia (NH_3) and sulfur dioxide (SO_2) are regarded as the high-hazard gases according to the above-mentioned classification, and both of them are high vapor pressure chemicals (7600 and 2994 mm Hg at 25 ^{o}C, respectively). Current NBC filters provide poor protection from the two gases. Particularly, ammonia is chemically stable on the I-AC adsorbent, and chemisorption is expected to be negligible. Thus, there has been a strong requirement to find proper adsorbents to improve current NBC filter

performance. Recently, a report about the adsorption removal of sulfur dioxide, ammonia, chlorine, dichloromethane, ethylene oxide, and carbon monoxide on MOFs indicates the great potential of these hybrid porous materials as novel air filters.[26] However, very few adsorption studies have been performed for TIC/MOF systems. Thus, there are significant knowledge gaps in this area.

1.3.2 Energy Gas Adsorption Storage

Hydrogen is one of the leading candidates as an energy carrier of the future in terms of its high energy content and clean burning, potentially renewable nature.[27-29] On the other hand, methane as the major component of natural gas is an abundant fuel that is cleaner burning than gasoline. And fuel cells based on methane present an appealing alternative to the internal combustion engine. However, many challenges limit the effectiveness for use of these energy gases in transportation. A central problem is the ability to store gases in a safe, cheap, and convenient manner. Gas adsorption in a porous material as a widely-studied technology is regarded as one of the competent candidates for the final solution. Thus, methane and hydrogen have been the most extensively studied gases for adsorption in MOFs, and gas storage for alternative fuel vehicles continues to be an important driver for this research area.

In 2000, the US Department of Energy (DOE) set a target for material-based adsorbed methane storage which is 180 cm^3(STP) cm^{-3} at 298 K and 35 bar so that the energy density is comparable to that of compressed natural gas (CNG).[30] In 2005, DOE set a target for hydrogen storage capacity for mobile applications that is 6.0 wt% and 45 g/L by 2010 and 9.0 wt% and 81 g/L by 2015 at near-ambient temperature and applicable pressures.[31] If we realized that the density of liquid hydrogen is 70.8 g/L, the DOE's

target is intimidating if not impossible. Thus, DOE revised the targets in February 2009. By 2010, the targets for system gravimetric capacity and system volumetric capacity were lowered to 45 g/g and 28 g/L, respectively. By 2015, the targets have been set as 55 g/g and 40 g/L, and the ultimate targets are 75 g/g and 70 g/L. In addition, the lifetime of the storage system is targeted at 1000 cycles by 2010, and 1500 cycles by 2015 as the ultimate target; the operating temperature should range from -40 to 85 ^{o}C, and the operating pressure should be less than 100 bar.[32]

Since the first report of methane adsorption on coordination polymers in 1997[33] and hydrogen adsorption on a porous MOFs in 2003[34], hundreds of porous MOFs have been evaluated as adsorbents for energy gas storage applications, and many excellent review articles on current progress are available.[27-32,34-42] Yaghi et al.[19] demonstrated a series of MOF materials with remarkable methane storage capacity, among which IRMOF-6 is impressive with an uptake of 240 cm^3/g at 298 K and 36 atm. Frost et al.[43] studied the influences of surface area, free volume, and heat of adsorption on hydrogen adsorption in a series of MOFs. Their GCMC simulation results indicated that the predominant factors affecting hydrogen uptake depend on heat of adsorption at low pressure, surface area at intermediate pressure, and free volume at high pressure. It has also been shown that structural properties such as unsaturated metal centers can be incorporated into materials to increase the magnitude of hydrogen interaction with the framework.[27] However, to further illustrate structure-performance correlations, systematic investigation of the effects of other factors such as pore size, ligand functionalization etc. on energy gas storage in porous MOFs is still needed, and this demands more studies to screen existing MOFs as well as to develop new structures.

1.3.3 Greenhouse gas capture

The detrimental influence of greenhouse gases on the pollution of the planet is now well documented and an intense international research is currently in progress to find various solutions to this problem. The capture of carbon dioxide, a gas which is a major player in climate change, becomes the first target to attack. Lots of studies have explored approaches of physisorption using porous materials for the abatement of carbon dioxide. In 1998, Yaghi's group reported the first study of carbon dioxide adsorption on MOFs, which was MOF-2, with a "paddlewheel" structure based on Zn and benzenedicarboxylate.[44] Since then, Yaghi and coworkers have subsequently reported that many MOFs present remarkable carbon dioxide adsorption capacities, which exceed those of zeolites and activated carbons.[45] Zhong's group[46] and Jiang's group[47] studied carbon dioxide storage capacity on different MOF materials using grand canonical Monte Carlo (GCMC) simulations and found that IRMOF-16 has the highest capacity of 64 mmol/g at 50 bar.

1.3.4 Adsorptive separation and purification

Separation and purification of multicomponent gas mixtures by adsorption is an established process technology. The mechanisms of gas adsorptive separation using porous materials may involve one or more of the following respects: (1) molecular sieving effect because of size or shape exclusion of adsorbates; (2) thermodynamic equilibrium effect because of different interactions between adsorbent and adsorbates; (3) kinetic effect because of different diffusing rates of adsorbates; (4) quantum sieving effect because of preferential adsorption of heavier isotopes caused by different quantum

energy levels of atoms or molecules confined in a very narrow space that is comparable to the de Broglie wave length.[48]

Recently, with the synthesis of more and more new sorbent materials with tailor-made porosity and surface properties and the urgent demand for economical separation procedures, adsorptive separation and purification is becoming increasingly more important. Conceptually, separation processes using adsorption can be divided into two classifications: bulk separation and purification. The former is defined as having the concentration of the adsorbed component above 10 wt % in the feed, while the latter implies that the concentration of the adsorbed component is generally less than 2 wt % in the feed.[49] Important separation and purification applications include air separation, carbon dioxide/methane separation, hydrogen and methane purification, carbon monoxide removal for fuel cell technology, desulfurization of transportation fuels, and separation of normal paraffins.[50]

As potential adsorbents in gas separation and purification, MOFs offer unique advantages for specific applications based on their structural characteristics.[51] However, the investigation of MOFs as adsorbents in separation and purification is still in its early stage; most of the research is focused on the basic single-component adsorption-desorption isotherm measurements. An excellent review article summarized the recent progress about the gas separation and purification in MOFs.[48]

1.3.5 Other emerging applications

Besides the above mentioned studies focused on gas adsorption application, an increasing number of MOFs are now being explored for their interesting properties. These emerging application-oriented studies include heterogeneous catalysis,[52] chiral

separation,[53-54] drug delivery,[55-59] luminescence,[60] magnetism,[61-62] nonlinear optics,[63-65] semiconductivity,[66-67] and as nanoreactors.[11] Due to lower relativity with my research objective, I am not going to expand the review of these applications but list some references here.

1.4 REFERENCES

(1) O'Keeffe, M. *Chem Soc Rev* **2009**, *38*, 1215.

(2) Kitagawa, S.; Kitaura, R.; Noro, S. *Angew Chem Int Edit* **2004**, *43*, 2334.

(3) Forster, P. M.; Thomas, P. M.; Cheetham, A. K. *Chem Mater* **2002**, *14*, 17.

(4) Cooper, E. R.; Andrews, C. D.; Wheatley, P. S.; Webb, P. B.; Wormald, P.; Morris, R. E. *Nature* **2004**, *430*, 1012.

(5) Lin, Z. J.; Wragg, D. S.; Morris, R. E. *Chem Commun* **2006**, 2021.

(6) Lu, C. M.; Liu, J.; Xiao, K. F.; Harris, A. T. *Chem Eng J* **2010**, *156*, 465.

(7) Haque, E.; Khan, N. A.; Park, J. H.; Jhung, S. H. *Chem-Eur J* **2010**, *16*, 1046.

(8) Mueller, U.; Schubert, M.; Teich, F.; Puetter, H.; Schierle-Arndt, K.; Pastre, J. *J Mater Chem* **2006**, *16*, 626.

(9) Khan, N. A.; Jhung, S. H. *B Korean Chem Soc* **2009**, *30*, 2921.

(10) Forster, P. M.; Stock, N.; Cheetham, A. K. *Angew Chem Int Edit* **2005**, *44*, 7608.

(11) Ferey, G. *Chem Soc Rev* **2008**, *37*, 191.

(12) Mu, B.; Schoenecker, P. M.; Walton, K. S. *J Phys Chem C* **2010**, *114*, 6464.

(13) Klein, N.; Senkovska, I.; Gedrich, K.; Stoeck, U.; Henschel, A.; Mueller, U.; Kaskel, S. *Angew Chem Int Edit* **2009**, *48*, 9954.

(14) Koh, K.; Wong-Foy, A. G.; Matzger, A. J. *J Am Chem Soc* **2009**, *131*, 4184.

(15) Bae, Y. S.; Dubbeldam, D.; Nelson, A.; Walton, K. S.; Hupp, J. T.; Snurr, R. Q. *Chem Mater* **2009**, *21*, 4768.

(16) Chui, S. S. Y.; Lo, S. M. F.; Charmant, J. P. H.; Orpen, A. G.; Williams, I. D. *Science* **1999**, *283*, 1148.

(17) Li, H.; Eddaoudi, M.; O'Keeffe, M.; Yaghi, O. M. *Nature* **1999**, *402*, 276.

(18) Ferey, G.; Mellot-Draznieks, C.; Serre, C.; Millange, F.; Dutour, J.; Surble, S.; Margiolaki, I. *Science* **2005**, *309*, 2040.

(19) Eddaoudi, M.; Kim, J.; Rosi, N.; Vodak, D.; Wachter, J.; O'Keeffe, M.; Yaghi, O. M. *Science* **2002**, *295*, 469.

(20) Long, J. R.; Yaghi, O. M. *Chem Soc Rev* **2009**, *38*, 1213.

(21) Kaye, S. S.; Dailly, A.; Yaghi, O. M.; Long, J. R. *J Am Chem Soc* **2007**, *129*, 14176.

(22) Huang, L. M.; Wang, H. T.; Chen, J. X.; Wang, Z. B.; Sun, J. Y.; Zhao, D. Y.; Yan, Y. S. *Micropor Mesopor Mat* **2003**, *58*, 105.

(23) Greathouse, J. A.; Allendorf, M. D. *J Am Chem Soc* **2006**, *128*, 10678.

(24) Kusgens, P.; Rose, M.; Senkovska, I.; Frode, H.; Henschel, A.; Siegle, S.; Kaskel, S. *Micropor Mesopor Mat* **2009**, *120*, 325.

(25) Karwacki, C. J., Paulette Jones *Toxic Industrial Chemicals Assessment of NBC Filter Performance*, Edgewood Chemical Biological Center, 2000.

(26) Britt, D.; Tranchemontagne, D.; Yaghi, O. M. *P Natl Acad Sci USA* **2008**, *105*, 11623.

(27) Dinca, M.; Long, J. R. *Angew Chem Int Edit* **2008**, *47*, 6766.

(28) Jia, C.; Yuan, X. X.; Ma, Z. F. *Prog Chem* **2009**, *21*, 1954.

(29) Hirscher, M.; Panella, B.; Schmitz, B. *Micropor Mesopor Mat* **2010**, *129*, 335.

(30) Zhou, W. *Chem Rec* **2010**, *10*, 200.

(31) Hu, Y. H.; Zhang, L. *Adv Mater* **2010**, *22*, E117.

(32) Ma, S. Q.; Zhou, H. C. *Chem Commun* **2010**, *46*, 44.

(33) Kondo, M.; Yoshitomi, T.; Seki, K.; Matsuzaka, H.; Kitagawa, S. *Angew. Chem.-Int. Edit. Engl.* **1997**, *36*, 1725.

(34) Rosi, N. L.; Eckert, J.; Eddaoudi, M.; Vodak, D. T.; Kim, J.; O'Keeffe, M.; Yaghi, O. M. *Science* **2003**, *300*, 1127.

(35) Duren, T.; Sarkisov, L.; Yaghi, O. M.; Snurr, R. Q. *Langmuir* **2004**, *20*, 2683.

(36) Sun, Y.; Liu, C. M.; Su, W.; Zhou, Y. P.; Zhou, L. *Adsorption* **2009**, *15*, 133.

(37) Zhao, D.; Yuan, D. Q.; Zhou, H. C. *Energ Environ Sci* **2008**, *1*, 222.

(38) Lin, X.; Jia, J. H.; Hubberstey, P.; Schroder, M.; Champness, N. R. *Crystengcomm* **2007**, *9*, 438.

(39) Murray, L. J.; Dinca, M.; Long, J. R. *Chem Soc Rev* **2009**, *38*, 1294.

(40) Xiao, B.; Yuan, Q. C. *Particuology* **2009**, *7*, 129.

(41) Han, S. S.; Mendoza-Cortes, J. L.; Goddard, W. A. *Chem Soc Rev* **2009**, *38*, 1460.

(42) Morris, R. E.; Wheatley, P. S. *Angew Chem Int Edit* **2008**, *47*, 4966.

(43) Frost, H.; Duren, T.; Snurr, R. Q. *J Phys Chem B* **2006**, *110*, 9565.

(44) Li, H.; Eddaoudi, M.; Groy, T. L.; Yaghi, O. M. *J Am Chem Soc* **1998**, *120*, 8571.

(45) Millward, A. R.; Yaghi, O. M. *J Am Chem Soc* **2005**, *127*, 17998.

(46) Yang, Q. Y.; Zhong, C. L.; Chen, J. F. *J Phys Chem C* **2008**, *112*, 1562.

(47) Babarao, R.; Jiang, J. W. *Langmuir* **2008**, *24*, 6270.

(48) Li, J. R.; Kuppler, R. J.; Zhou, H. C. *Chem Soc Rev* **2009**, *38*, 1477.

(49) Yang, R. T. *Adsorbents : fundamentals and applications*; Wiley-Interscience: Hoboken, N.J., 2003.

(50) Yang, R. T. *Gas separation by adsorption processes*; Butterworths: Boston, 1987.

(51) Snurr, R. Q.; Hupp, J. T.; Nguyen, S. T. *Aiche J* **2004**, *50*, 1090.

(52) Lee, J.; Farha, O. K.; Roberts, J.; Scheidt, K. A.; Nguyen, S. T.; Hupp, J. T. *Chem Soc Rev* **2009**, *38*, 1450.

(53) Morris, R. E.; Bu, X. H. *Nat Chem* **2010**, *2*, 353.

(54) Crassous, J. *Chem Soc Rev* **2009**, *38*, 830.

(55) An, J. Y.; Geib, S. J.; Rosi, N. L. *J Am Chem Soc* **2009**, *131*, 8376.

(56) Horcajada, P.; Serre, C.; Maurin, G.; Ramsahye, N. A.; Balas, F.; Vallet-Regi, M.; Sebban, M.; Taulelle, F.; Ferey, G. *J Am Chem Soc* **2008**, *130*, 6774.

(57) Horcajada, P.; Chalati, T.; Serre, C.; Gillet, B.; Sebrie, C.; Baati, T.; Eubank, J. F.; Heurtaux, D.; Clayette, P.; Kreuz, C.; Chang, J. S.; Hwang, Y. K.; Marsaud, V.; Bories, P. N.; Cynober, L.; Gil, S.; Ferey, G.; Couvreur, P.; Gref, R. *Nat Mater* **2010**, *9*, 172.

(58) Taylor-Pashow, K. M. L.; Della Rocca, J.; Xie, Z. G.; Tran, S.; Lin, W. B. *J Am Chem Soc* **2009**, *131*, 14261.

(59) Huxford, R. C.; Della Rocca, J.; Lin, W. B. *Curr Opin Chem Biol* **2010**, *14*, 262.

(60) Allendorf, M. D.; Bauer, C. A.; Bhakta, R. K.; Houk, R. J. T. *Chem Soc Rev* **2009**, *38*, 1330.

(61) Huang, Y. G.; Jiang, F. L.; Hong, M. C. *Coordin Chem Rev* **2009**, *253*, 2814.

(62) Kurmoo, M. *Chem Soc Rev* **2009**, *38*, 1353.

(63) Janiak, C. *Dalton T* **2003**, 2781.

(64) Yu, Z. P.; Xie, Y.; Wang, S. J.; Yong, G. P.; Wang, Z. Y. *Inorg Chem Commun* **2008**, *11*, 372.

(65) Zhang, L. J.; Yu, J. H.; Xu, J. Q.; Lu, J.; Bie, H. Y.; Zhang, X. *Inorg Chem Commun* **2005**, *8*, 638.

(66) Alvaro, M.; Carbonell, E.; Ferrer, B.; Xamena, F.; Garcia, H. *Chem-Eur J* **2007**, *13*, 5106.

(67) Silva, C. G.; Corma, A.; Garcia, H. *J Mater Chem* **2010**, *20*, 3141.

CHAPTER 2

RATIONALE FOR SYNTHESIS OF NOVEL MOFS

An incredible number of new MOFs have been synthesized since the late 1990s, among which CuBTC or HKUST-1,[1] and MOF-5 or IRMOF-1[2] are two famous MOFs of current focus. The corresponding articles were published in the same year 1999 on two famous journals, *Science* and *Nature*, respectively. Thus, as the preliminary practice in my early stage of PhD program, these two MOFs were chosen to synthesize and characterize.

During the initial trials, the most difficulties were poor repeatability of surface area of MOFs due to unknown instability of MOF materials, and the effect of post-operation procedures and activation conditions on the porosity. In particular, MOF-5 with high surface area is very difficult to repeat because of rapid structural transformation and decomposition once MOF-5 exposed to air. Thus, we failed many times to obtain MOF-5 with a surface area higher than 1000 m^2/g until a detailed report was published which discusses the impact of preparation and handling on the surface area and hydrogen storage properties of MOF-5.[3] According to our experimental experience and the reported results, the following tips are important: (1) Raising the temperature or extending the duration of the reaction will yield a product with reduced surface area. (2) Although N,N-dimethylformamide (DMF) could be applied to displace expensive N,N-diethylformamide (DEF) to produce MOF-5, the surface area of the resulting material was generally lower. (3) Employing anhydrous and fresh DEF for synthesis could produce the resulting material with higher surface area than using DEF which has been

exposed to air for a while. (4) In the case of absent inert gas protection, exposure time to moisture should be as short as possible to minimize the degree of decomposition. (5) Anhydrous dichloromethane (CH_2Cl_2) is better than chloroform ($CHCl_3$) for exchanging guest molecules associated in MOF-5. (6) During activation operation, temperature and duration of the heating is the key to obtain the final porous material. Lower temperature cannot completely remove the guest molecules, while improper high temperature will cause collapse of the framework partially. Both cases will yield poor surface area and porosity. After many trials, porous MOF-5 and CuBTC were repeated successfully in our lab. And then, some other porous MOFs were explored in our lab as well, including Zn(bdc)(ted),[4] UMCM-1,[5] etc. Here, the detailed synthesis and preparation approaches for three important MOFs are given.

MOF-5 could be prepared from the following chemicals as received without further purification: zinc nitrate hexahydrate, $Zn(NO_3)_2 \cdot 6H_2O$; terephthalic acid, H_2BDC; diethylformamide, DEF; dimethylformamide (DMF), dichloromethane, CH_2Cl_2. A mixture of $Zn(NO_3)_2 \cdot 6H_2O$ (3.57 g, 12.00 mmol), H_2BDC (0.67 g, 4.03 mmol), and DEF (30 mL) was placed into a Teflon-lined 45 mL reactor. The mixture was heated for 16 hours at 80 ^oC. After cooling to room temperature, cubic-shaped colorless crystals were obtained, and then washed with DMF three times. The crystals were then immersed in 30 mL CH_2Cl_2. During the following one week, CH_2Cl_2 was replaced once per day. The crystals were then filtered and dried in air for 30 minutes. The solvent-exchanged crystals were placed in a vacuum oven for 1 hr at 300 ^oC to obtain the final porous material MOF-5. Nitrogen adsorption experiment gives the BET surface area larger than 3000 m^2/g.

CuBTC was synthesized from the following chemicals: copper nitrate trihydrate, $Cu(NO_3)_2 \cdot 3H_2O$; trimesic acid, H_3BTC; ethanol, EtOH; deionized water, H_2O. A mixture of $Cu(NO_3)_2 \cdot 3H_2O$ (0.875 g, 3.62 mmol), H_3BTC (0.42 g, 2.00 mmol), EtOH (15 mL), and H_2O (15 mL) was placed into a Teflon-lined 45 mL reactor. The mixture was heated for 16 hrs at 110 ^oC. After cooling to room temperature, blue crystals were obtained, and then washed with EtOH three times. The crystals were then filtered and dried in air. The air-dried crystals were placed in a vacuum oven for 1 hr at 200 ^oC to obtain the activated porous material CuBTC. Nitrogen adsorption experiment gives the surface area larger than 1200 m^2/g.

UMCM-1 was synthesized from the following chemicals as received without further purification: zinc nitrate tetrahydrate, $Zn(NO_3)_2 \cdot 4H_2O$; 1,3,5-tris(4-carboxyphenyl)benzene, H_3BTB; terephthalic acid, H_2BDC; diethylformamide, DEF; dimethylformamide, DMF; dichloromethane, CH_2Cl_2. A mixture of $Zn(NO_3)_2 \cdot 4H_2O$ (0.85g, 3.25mmol), H_2BDC (0.135g, 0.813mmol), H_3BTB (0.32g, 0.73mmol), and DEF (30mL) was placed into a Teflon-lined 45 mL reactor. The mixture was heated for 3 days at 80 ^oC. After cooling to room temperature, needle-shaped colorless crystals were obtained, and then washed with DMF three times. The crystals were then immersed in 50 mL CH_2Cl_2. During the following one week, CH_2Cl_2 was replaced once per day. The crystals were then filtered and dried in air. The solvent-exchanged crystals were placed in a vacuum oven for 1 hr at 300 ^oC to obtain the activated porous material UMCM-1. Nitrogen adsorption experiment gives the surface area larger than 4000 m^2/g.

2.1 RATIONALE FOR SYNTHESIS OF NOVEL MOFS

After finishing all needed experimental practices and theoretical preparation, searching proper MOF materials and synthesizing new MOFs are my main goals. Besides identifying known MOFs according to the pore size and functional group, how to synthesize novel MOF structures with desired topology framework and chemical properties are a major focus.

In materials such as those assembled from the paddle-wheel structure, as-synthesized MOFs have solvent molecules attached as ligands to the metal centers. Removal of these solvent ligands by thermal activation generates unsaturated metal centers (UMC) or open metal sites. Thus, the metal atoms are exposed on the interior surfaces of the material and are open to direct approach by sorbate molecules. These exposed metal sites can be seen as analogous to entatic metal centers in bioinorganic chemistry, in which metal ions are forced into unusual coordination geometry like the iron in hemoglobin.[6] Open metal sites greatly increase the ability of the material to selectively adsorb particular molecules. Consequently, the incorporation of UMCs into MOFs is a practical strategy for manipulating the adsorption behavior.

There have been a number of reports in recent years of MOFs with UMCs.[6-14] Many of these materials possess 3D structures with channels or interconnected pores. The adsorption properties of a particular material will depend on this structure dimensionality in combination with porosity and pore size, surface area, and presence or absence of open metal sites. Thus, it is necessary to understand the complex interplay of these factors in affecting adsorption behavior to move towards a rational design of these materials for adsorption applications. One classic MOF with UMCs is CuBTC or HKUST-1.[1] The

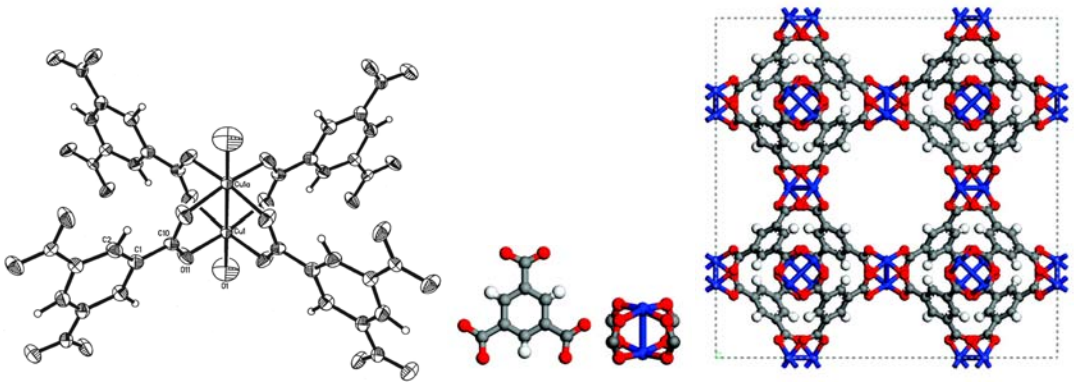

Figure 2.1 Paddel-wheel unites and crystal structure of CuBTC

structure of CuBTC is defined by $Cu_2(CO_2)_4$ paddle-wheel unites connected by 1,3,5-benzene tricarboxylate groups, forming a sequence of square cages, as shown in Figure 2.1. Unsaturated copper sites (blue spheres) become available after removing coordinated water molecules by thermal activation procedures. A series of studies involving both of simulations and experiments explored the role of unsaturated copper sites of CuBTC in the interaction with adsorbates, and confirmed the positive effect of UMCs on the improved adsorption performances.[10,15-18] We also realize that if high surface area and large pore volume benefit the total adsorption capacity, only the presence of a large number of strong adsorption sites can decrease the energy barrier for adsorption and particularly, improve the filter performance for high vapor pressure chemicals.

Based on the above mentioned recognition of adsorption mechanism, MOF materials which possess available exposed metal sites or organic functional groups, high surface area, and large pore volume would be good candidates for our adsorption applications. To examine the structure-property relations and host-guest interactions, and finally to achieve our goals, the idea of reticular chemistry is introduced into the synthesis work. The concept of *Reticular Chemistry* or *Reticular Synthesis* was

introduced by Yaghi and O'Keeffe only a few years ago,[19] and means the practice of logical synthesis must begin with knowledge of the target network "blueprint" and identification of the required building blocks for its assembly. Thus, reticular synthesis can be defined as the process of assembling judiciously designed rigid molecular building blocks into predetermined ordered structures (networks), which are held together by strong bonding.

Since CuBTC was reported first about ten years ago, a variety of studies about its structure-property relations have been explored, and 1,3,5-benzene tricarboxylate acid (H_3BTC) has been regarded as the most classic example of three-connected ligands. Thus, one logical question will be what if we use similar three-connected ligand but with longer chain. We can imagine that frameworks with large pores can be realized if vertices in a network are spaced apart by longer links to give expanded structures. For example, the 1,3,5-carbon atoms in H_3BTC could be extended with varied length of alkanes or benzene rings; and the latter case may be easier to achieve in chemistry. Thus, the two-connected benzene rings space apart the central benzene ring from the carboxylate carbon atoms in H_3BTC, which produces another famous three-connected ligand, 1,3,5-tris(4-carboxyphenyl) benzene (H_3BTB) as an expanded version of H_3BTC (Figure. 2.2). At the

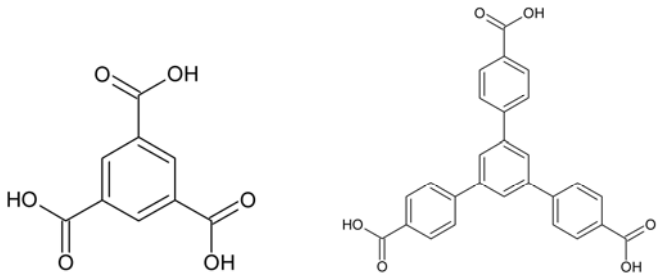

Figure 2.2 Structures of H_3BTC (left) and H_3BTB (right)

same time, if the implementation of reticular synthesis can yield the same copper paddle wheel units, then a novel MOF structure with the similar open metal sites as in CuBTC, higher surface area, and larger pore volume is feasible. Thus, H_3BTB is employed as the major ligand to synthesize novel porous MOFs with different metal sources.

2.2 SIGNIFICANT RESULTS

Based on the results of literature and Cambridge Structural Database (CSD) investigation, the synthesis progress of MOFs with H_3BTB as ligand is summarized here. The second row of Table 2.1 lists the electronegativity of examined metal elements, while other numbers represent the number of crystal structures reported from literature and CSD including the results of this work. Up to date, 30 coordination polymer structures have been reported totally. The coordination polymers combing Zn and H_3BTB are the most widely explored, including 5 structures using H_3BTB as the single ligand, 6 structures using H_3BTB and a secondary ligand, and 6 structures using H_3BTB as the single ligand and coordinated with another metal besides Zn. Other metals have also been investigated including transition metals (Cd, Fe, Co, Cu, Ni), alkali earth metals (Mg, Be), and lanthanides (La, Tb). From Chapter 3 to 7, we will first discuss 5 new MOF structures synthesized in our lab, including one Cu-BTB, one Cd-BTB, two Zn-BTB, and one La-BTB, and their crystal structures, characterization results, and gas adsorption properties are presented respectively.

Table 2.1 Synthesis progress of coordination polymers using H_3BTB as ligand

		Zn	Cd	Fe	Co	Cu	Ni	Mg	Be	La	Tb
Electronegativity of metals		1.65	1.66	1.83	1.88	1.90	1.91	1.31	1.57	1.1	1.1
H_3BTB		5	2	2	1	2		1	1	1	1
H_3BTB	Other Metals	6									
H_3BTB	Bipy						2				
H_3BTB	BDC	3									
H_3BTB	NH_2-BDC	1									
H_3BTB	2, 6-NDC	1									
H_3BTB	T^2DC	1									

Secondary Ligands	Structure
4,4'-Bipyridine (Bipy)	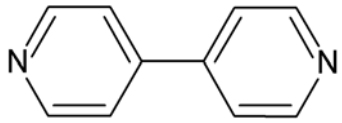
Terephthalic acid (BDC)	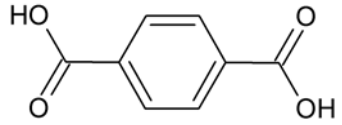
2-Aminoterephthalic acid (NH_2-BDC)	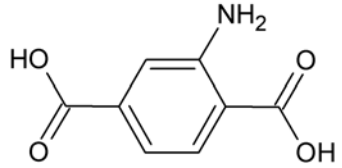
2,6-Naphthalenedicarboxylic acid (2, 6-NDC)	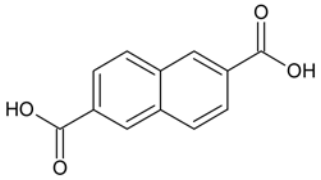
Thieno[3,2-b]thiophene-2,5-dicarboxylate (T^2DC)	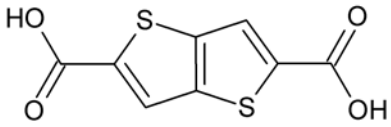

2.3 REFERENCES

(1) Chui, S. S. Y.; Lo, S. M. F.; Charmant, J. P. H.; Orpen, A. G.; Williams, I. D. *Science* **1999**, *283*, 1148.

(2) Li, H.; Eddaoudi, M.; O'Keeffe, M.; Yaghi, O. M. *Nature* **1999**, *402*, 276.

(3) Kaye, S. S.; Dailly, A.; Yaghi, O. M.; Long, J. R. *J Am Chem Soc* **2007**, *129*, 14176.

(4) Lee, J. Y.; Olson, D. H.; Pan, L.; Emge, T. J.; Li, J. *Adv Funct Mater* **2007**, *17*, 1255.

(5) Koh, K.; Wong-Foy, A. G.; Matzger, A. J. *Angew Chem Int Edit* **2008**, *47*, 677.

(6) Ma, S. Q.; Zhou, H. C. *J Am Chem Soc* **2006**, *128*, 11734.

(7) Mu, B.; Huang, Y. G.; Walton, K. S. *Crystengcomm* **2010**, *12*, 2347.

(8) Park, M.; Moon, D.; Yoon, J. W.; Chang, J. S.; Lah, M. S. *Chem Commun* **2009**, 2026.

(9) Hong, D. Y.; Hwang, Y. K.; Serre, C.; Ferey, G.; Chang, J. S. *Adv Funct Mater* **2009**, *19*, 1537.

(10) Liu, Y.; Kabbour, H.; Brown, C. M.; Neumann, D. A.; Ahn, C. C. *Langmuir* **2008**, *24*, 4772.

(11) Dietzel, P. D. C.; Johnsen, R. E.; Blom, R.; Fjellvag, H. *Chem-Eur J* **2008**, *14*, 2389.

(12) Moon, H. R.; Kobayashi, N.; Suh, M. P. *Inorg Chem* **2006**, *45*, 8672.

(13) Forster, P. M.; Eckert, J.; Heiken, B. D.; Parise, J. B.; Yoon, J. W.; Jhung, S. H.; Chang, J. S.; Cheetham, A. K. *J Am Chem Soc* **2006**, *128*, 16846.

(14) Dinca, M.; Dailly, A.; Liu, Y.; Brown, C. M.; Neumann, D. A.; Long, J. R. *J Am Chem Soc* **2006**, *128*, 16876.

(15) Karra, J. R.; Walton, K. S. *Langmuir* **2008**, *24*, 8620.

(16) Dinca, M.; Long, J. R. *Angew Chem Int Edit* **2008**, *47*, 6766.

(17) Vitillo, J. G.; Regli, L.; Chavan, S.; Ricchiardi, G.; Spoto, G.; Dietzel, P. D. C.; Bordiga, S.; Zecchina, A. *J Am Chem Soc* **2008**, *130*, 8386.

(18) Prestipino, C.; Regli, L.; Vitillo, J. G.; Bonino, F.; Damin, A.; Lamberti, C.; Zecchina, A.; Solari, P. L.; Kongshaug, K. O.; Bordiga, S. *Chem Mater* **2006**, *18*, 1337.

(19) Yaghi, O. M.; O'Keeffe, M.; Ockwig, N. W.; Chae, H. K.; Eddaoudi, M.; Kim, J. *Nature* **2003**, *423*, 705.

CHAPTER 3

INTRODUCING OPEN METAL SITES AND ORGANIC FUNCTIONAL GROUP INTO MOF

Porous coordination polymers or metal-organic frameworks (MOFs) have attracted great interest recently for potential applications in adsorption separations, gas storage, sensing, and catalysis.[1-5] In contrast to conventional microporous materials, these organic-inorganic hybrids have the potential for synthesis using a rational design approach by flexible control of the architecture and functional group.[6] In materials such as those assembled from the paddle-wheel structure, as-synthesized MOFs have solvent molecules attached as ligands to the metal centers. Removal of these solvent ligands by thermal activation generates unsaturated metal centers (UMC) or open metal sites. Thus, the metal atoms are exposed on the interior surfaces of the material and are open to direct approach by sorbate molecules. These exposed metal sites can be seen as analogous to entatic metal centers in bioinorganic chemistry, in which metal ions are forced into unusual coordination geometry like the iron in hemoglobin.[7] Open metal sites greatly increase the ability of the material to selectively adsorb particular molecules. Consequently, the incorporation of UMCs into MOFs is a practical strategy for manipulating the adsorption behavior.

There have been a number of reports in recent years of MOFs with UMCs.[8-16] Many of these materials possess 3D structures with channels or interconnected pores. The adsorption properties of a particular material will depend on this structure dimensionality in combination with porosity and pore size, surface area, and presence or absence of open

metal sites. Thus, it is necessary to understand the complex interplay of these factors in affecting adsorption behavior to move towards a rational design of these materials for adsorption applications.

In this chapter, we describe the first new MOF material reported by our lab. $[Cu_2(HBTB)_2(H_2O)(EtOH)]\cdot H_2O\cdot EtOH$[17] (**1**) is a unique interpenetrating two-dimensional network structure with uncoordinated carboxylic functional groups and unsaturated Cu^{2+} ions which display a Jahn-Teller distortion. The as-synthesized material was harvested from the reaction of H_3BTB (H_3BTB=1,3,5-tris(4-carboxyphenyl) benzene) with $Cu(NO_3)_2.3H_2O$ in a mixture of ethanol and water at 110 ^oC. This material assembles in 2D sheets that are stacked through hydrogen bonding. Channels resembling coils are formed by the helical chains. The composition of **1** was confirmed by single-crystal X-ray diffraction, and the phase purity of the bulk sample was confirmed by powder XRD. TGA analysis presents that the compound **1** is stable up to 300 ^oC. The BET surface area is calculated from nitrogen adsorption at 77 K to be approximately 600 m^2/g.

3.1 SYNTHESIS AND CHARACTERIZATION

3.1.1 Materials and Synthesis Method

All chemicals are purchased from commercial companies and used as received without further purification: copper nitrate trihydrate, $Cu(NO_3)_2\cdot 3H_2O$ (Acros Organics, 99%); 1,3,5-tris(4-carboxyphenyl)benzene, H_3BTB (Sigma-Aldrich, ≥98%); ethanol, EtOH (Acros Organics, 99.5%). Exact amounts of $Cu(NO_3)_2.3H_2O$ (0.2g) and H_3BTB (0.1g) were dissolved in a 50mL digestion bomb reactor using (1:1) water-ethanol (15mL:15mL). The mixture solution was heated at 110 ℃ for 16 hours. Then the green

diamond-shaped crystal $[Cu_2(HBTB)_2(H_2O)(EtOH)]\cdot H_2O\cdot EtOH$ (**1)** was obtained. The as-synthesized sample was obtained by filtration, washed with ethanol and then dried in air.

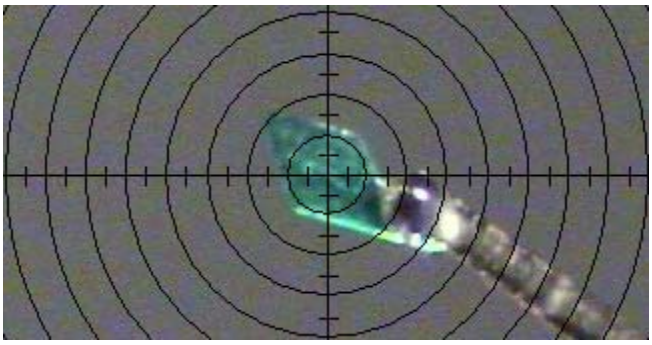

Figure 3.1 Green diamond-shaped crystal of $[Cu_2(HBTB)_2(H_2O)(EtOH)]\cdot H_2O\cdot EtOH$

3.1.2 Scanning electron microscope (SEM) characterization

The SEM images were conducted on a Hitachi SEM S-3500N equipped with a model S-6542 absorbed electron detector.

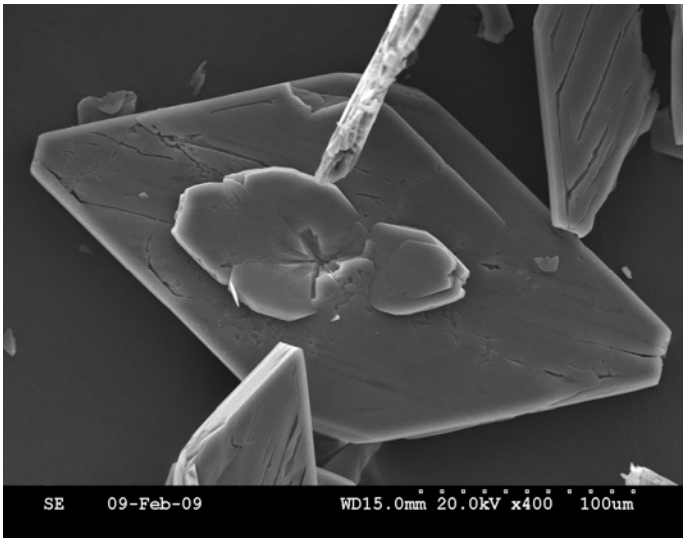

Figure 3.2 Diamond-shaped crystal of $[Cu_2(HBTB)_2(H_2O)(EtOH)]\cdot H_2O\cdot EtOH$

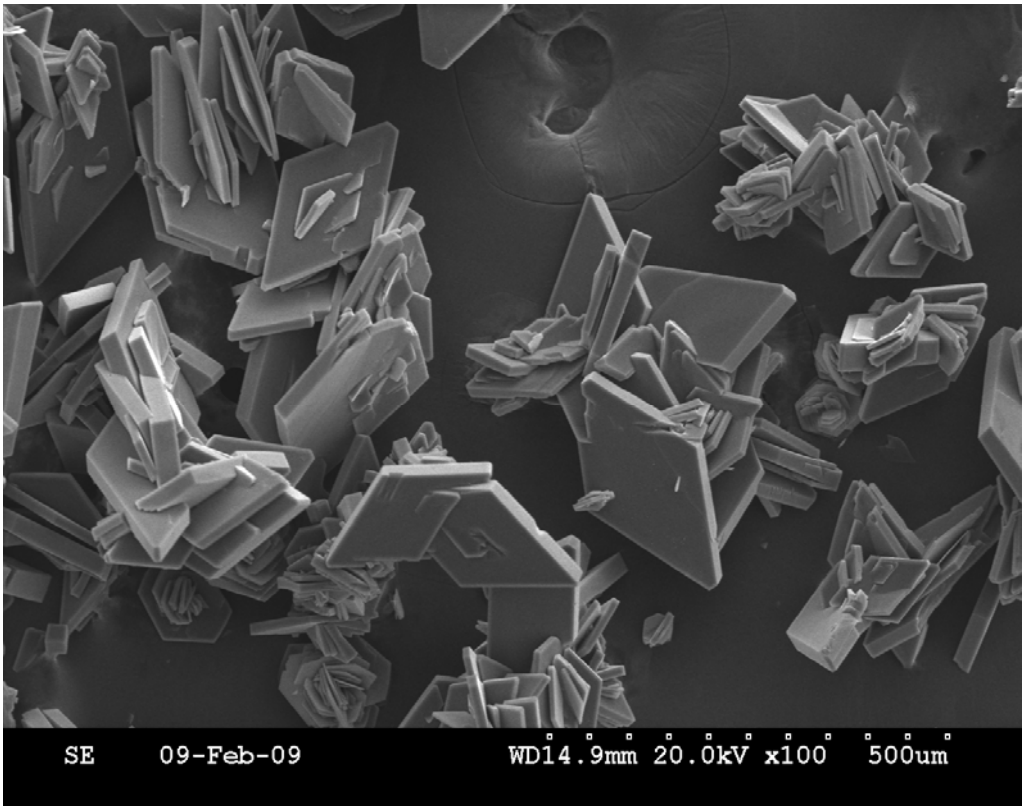

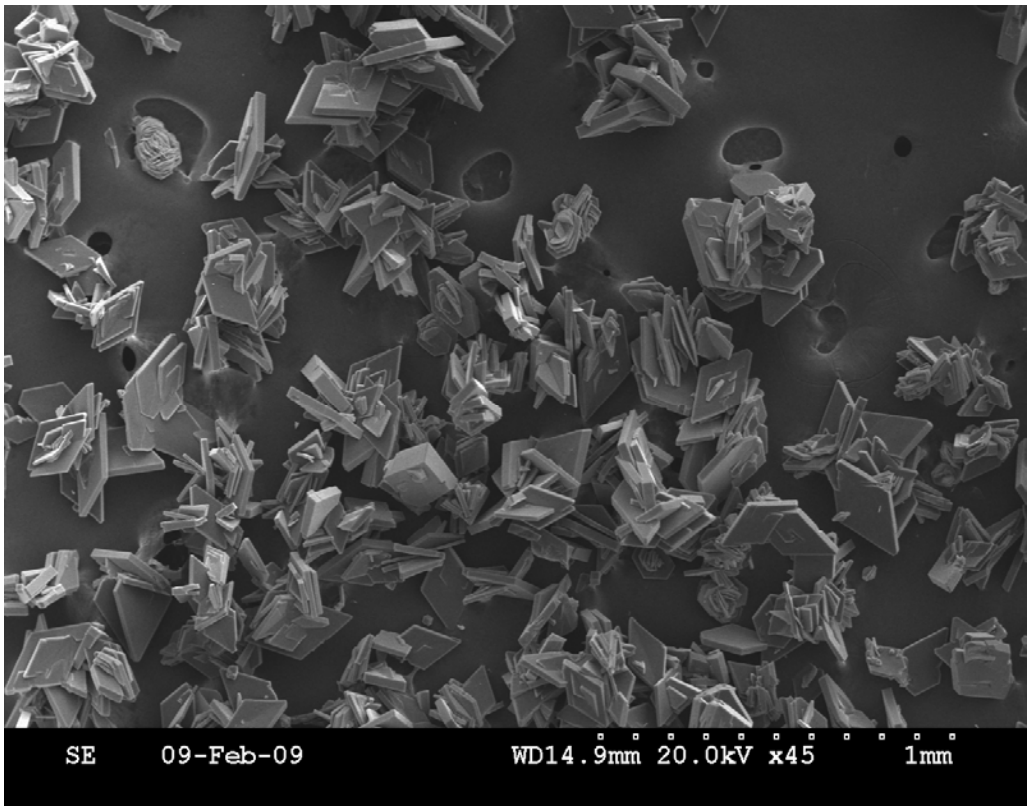

Figure 3.2 continued

3.1.3 Single-Crystal X-Ray Diffraction Characterization

Single-crystal XRD data of compound **1** (CCDC 708312) was collected on a Bruker SMART APEX CCD single crystal diffraction system with MoKα radiation (λ= 0.71073 Å). The structures were solved by direct methods with the help of SHELX-97 and refined by full-matrix least-squares techniques using SHELXL-97. X-ray diffraction analysis reveals that **1** is a two parallel interpenetrating (4,4) 2D network. As shown in Figure 3.3, four crystallographically independent copper atoms are present, which are all five-coordinated in square pyramid coordination geometry. Cu1(Cu2) is coordinated by one water molecule and four oxygen atoms from four carboxyl groups. Cu3(Cu4) is coordinated by one ethanol molecule and four oxygen atoms from four carboxyl groups. Four carboxyl groups link Cu1 and Cu2 (Cu3 and Cu4) into the paddle-wheel cluster motif with a Cu1-Cu2 distance of 2.589(4) Å (Cu3-Cu4 2.618(4) Å).

Due to the different coordination environment between Cu1(Cu2) and Cu3(Cu4), the respective paddle-wheel units also display some differences (Figure 3.3). In **1**, the H_3BTB ligands are partially deprotonated. Two carboxyl groups of this ligand are deprotonated and coordinated to the copper ions with bidentate coordination mode. The third carboxyl group is protonated and does not take part in the coordination. Thus, each $HBTB^{2-}$ connects two adjacent Cu1-Cu2 and Cu3-Cu4 paddle-wheel clusters into 2_1 helical chains along the *b* axis. Each unit of the helical chain contains one Cu1-Cu2 and one Cu3-Cu4 paddle-wheel cluster (the helical pitch, given by one full rotation around the 2_1 helical axis, is 12.56 Å). As mentioned above, four carboxyl groups link two copper atoms into one paddle-wheel cluster. Two of four carboxyl groups of each paddle-wheel cluster link Cu1-Cu2 and Cu3-Cu4 clusters into one left-handed helical chain, and

the other two carboxyl groups of each cluster compose one unit of a right-handed helical chain. In compound **1**, left- and right-handed helical chains coexist and array alternately. Through sharing Cu-Cu paddle-wheel clusters, adjacent helical chains are linked into (4,4) 2D layers at the [100] plane (Figure 3.5). Such change in dimensionality and crystal structure is due to partial deprotonation of the H_3BTB ligand, which produces significant alterations in functionality compared to another known Cu-BTB crystal, MOF-14[18]. Yaghi *et. al* synthesized MOF-14 by solvothermal reaction of H_3BTB and $Cu(NO_3)_2$ in a mixture of ethanol, DMF, water and pyridine. In MOF-14, three carboxyl groups of H_3BTB are all deprotonated and coordinated to copper centers, which results in a 3D interwoven metal-organic framework with extra-large pores. A sphere 16.4 Å in diameter can fit inside each cavity. Due to the absence of DMF and pyridine in this work, H_3BTB ligands are only partially deprotonated in **1**, which results in a 2D network containing helical chains (Figure 3.7). Though the helical channels are smaller than the cavities of MOF-14, the smaller channels may be more suitable for selective adsorption.

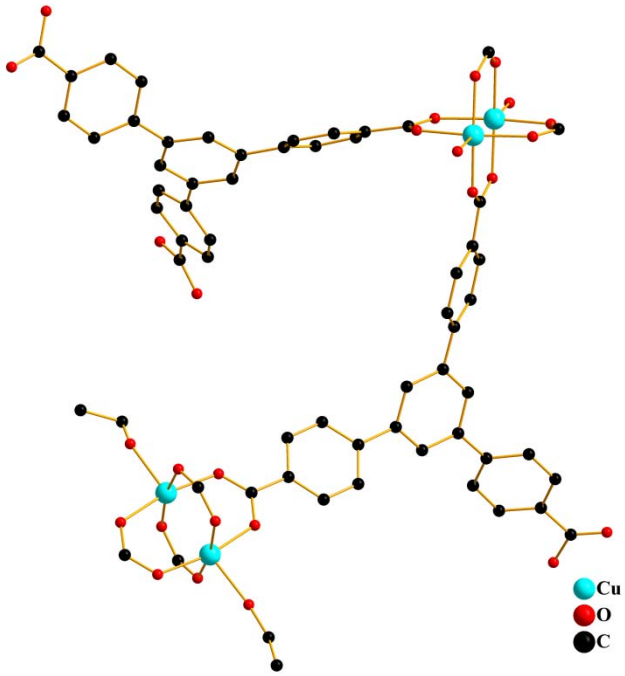

Figure 3.3 View of the coordination about the Cu atoms.
(All solvent molecules and hydrogen atoms are omitted for clarity)

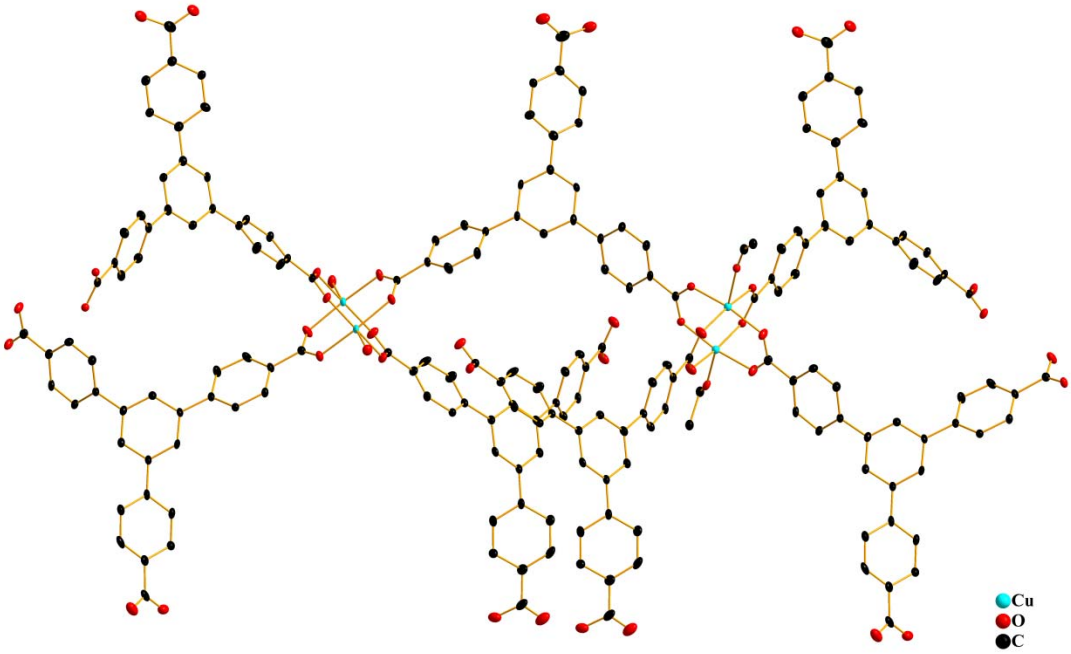

Figure 3.4 ORTEP diagram of compound **1**
(All solvent molecules and hydrogen atoms are omitted for clarity)

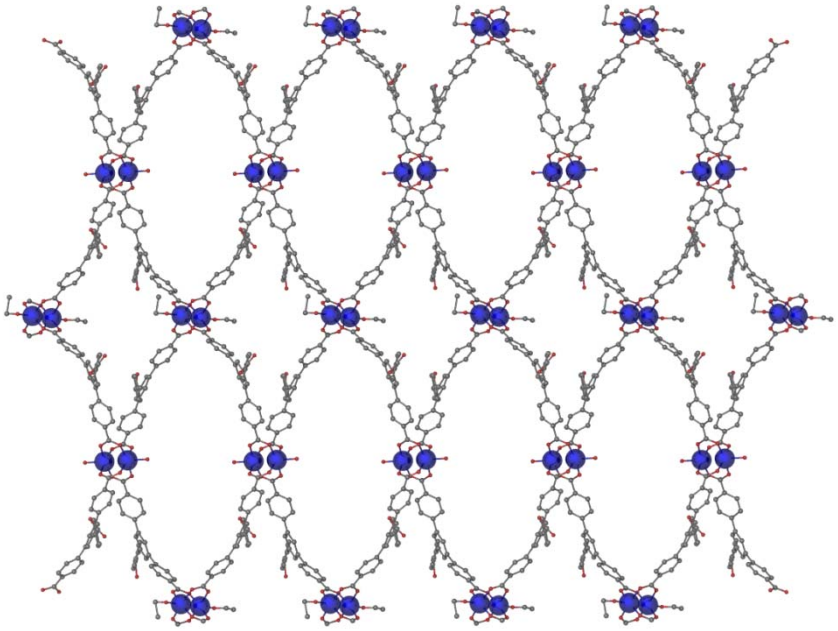

Figure 3.5 (4, 4) 2D network composed of copper paddle-wheel clusters and $HBTB^{2-}$ ligands at the [100] plane. (All solvent molecules and hydrogen atoms are omitted for clarity)

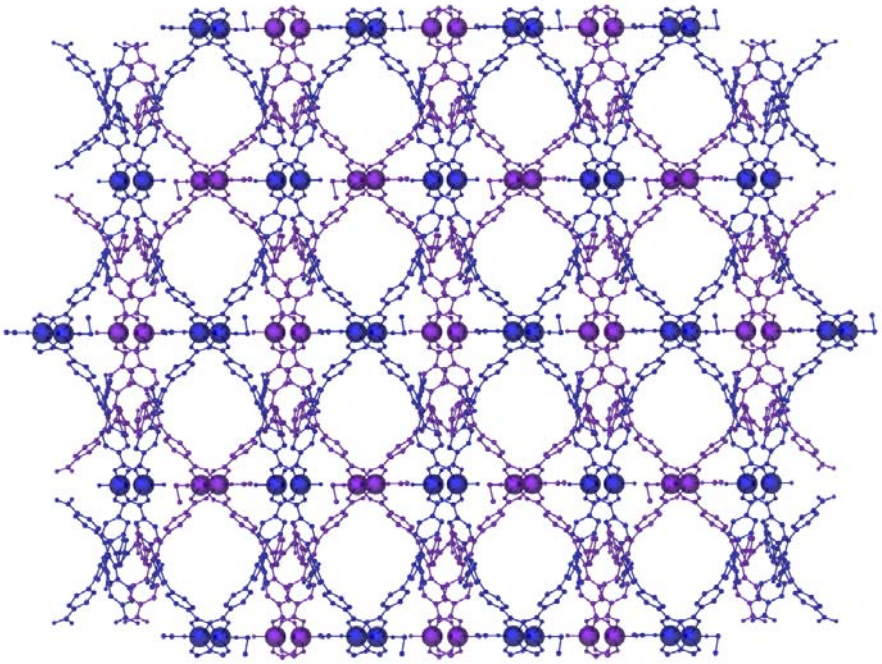

Figure 3.6 Interpenetrating (4, 4) 2D networks.
(All solvent molecules and hydrogen atoms are omitted for clarity)

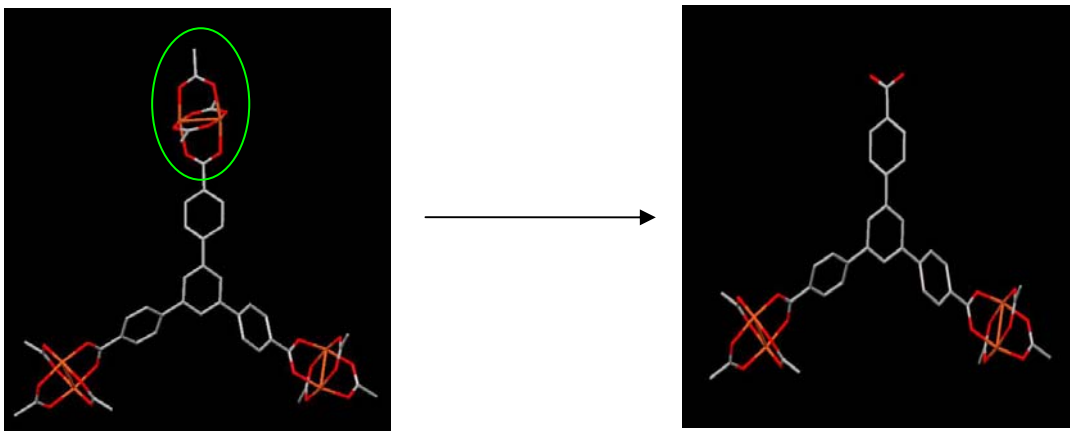

Figure 3.7 3D to 2D dimensional change coming from partial deprotonation of H_3BTB ligand

When exploring the acting forces that exist between sheets, weak hydrogen bonding interactions were observed between the coordinated water oxygen atoms from one layer and the coordinated carboxyl oxygen atoms from the second neighboring layer (3.091 Å and 3.043 Å). Through hydrogen bonds, two helical chains from two individual nets are linked into a double-stranded helical chain. The weak hydrogen bonds between sheets result in a 2-fold parallel interpenetrating 2D layer (Figure 3.6). In previous reports of such networks, the individual networks involved in 2D interpenetration are usually based on the (4,4) or (6,3) net with one exception ($8^2$10).[19] However, it is seldom that dinuclear metal species have been introduced into a two parallel interpenetrating (4,4) net.[20] To make parallel interpenetration possible, the individual 2D networks must be corrugated or possess some appropriate element of undulation.[21] In **1**, each side of the rhombus windows of the 2D net is actually one repeating unit of the helical chain. The undulation and flexibility of the helical chain makes one 2D net pass through the other an infinite number of times, which is different from the corrugation of the whole 2D network.

At the [010] plane, like two open arms, the dangling phenyl rings with uncoordinated carboxyl groups protrude perpendicularly from both sides of the sheets . The effective length of each arm is *ca*. 7.13 Å (from the centroid of the central benzyl group to the uncoordinated carboxyl carbon atom). Along the *a* axis, all the layers are stacked on top of each other. However, the layers are not arrayed at the same distance. As shown in Figure 3.8, the distance between layer A and layer B (9.601 Å) is short enough that the uncoordinated carboxyl arms of layer A are threaded into the helical channels of layer B in a mutual relationship. The helical channels are then partially occupied by these arms, and the threading results in the formation of bilayers (AB). The arms between two bilayers (AB-AB) are not threaded into each other. The distance between two bilayers (AB-AB) is longer (15.491 Å) than the distance between sheets within a bilayer (A-B).

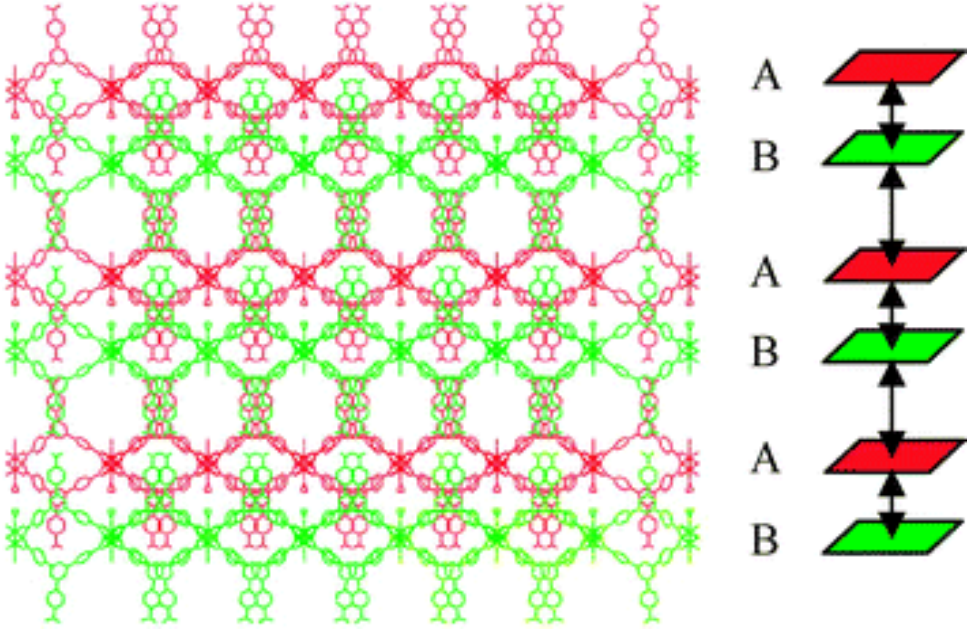

Figure 3.8 The stack of different layers **A** (red), **B** (green) at [010] plane (all solvent molecules and hydrogen atoms are omitted for clarity)

Table 3.1 Crystallographic Data for $[Cu_2(HBTB)_2(H_2O)(EtOH)]\cdot H_2O\cdot EtOH$

Empirical formula	$C_{456}\ H_{308}\ Cu_{16}O_{142}$
Molecular weight	9075.84
Temperature (K)	100(2)
Crystal system	Orthorhombic
Space group	Pbcm
a(Å)	28.0524(17)
b(Å)	14.8658(9)
c(Å)	28.7818(18)
α(º)	90
β(º)	90
γ(º)	90
$V(A^3)$	12002.6(13)
Z	1
D_{calcd}(g cm^{-3})	1.255
F(000)	4608
μ (mm^{-1})	0.774
Reflection (collected/unique)	104053/ 12040
R_{int}	0.0891
Goodness-of-fit on F^2	1.012
Final R indices [I>2σ(I)]	$R_1 = 0.0468$, $wR_2 = 0.1425$
R indices (all data)	$R_1 = 0.1021$, $wR_2 = 0.1536$
Max, min $\Delta\rho$ (e $Å^{-3}$)	1.629, -1.653

3.1.4 Powder X-Ray Diffraction Characterization and Elemental Analysis

The powder-XRD pattern of samples were collected on a Bruker D8 powder diffraction system with Cu radiation (λ= 1.5406 Å) to determine the phase purity. Elemental analyses were carried out on an Elementar Vario EL III analyzer. Calculated for $C_{456}Cu_{16}O_{142}H_{308}$: C, 60.29%; Cu, 11.28%; O, 25.03%; H, 3.39%. Found: C, 60.18%; Cu, 11.25%; O, 25.10%; H, 3.47%.

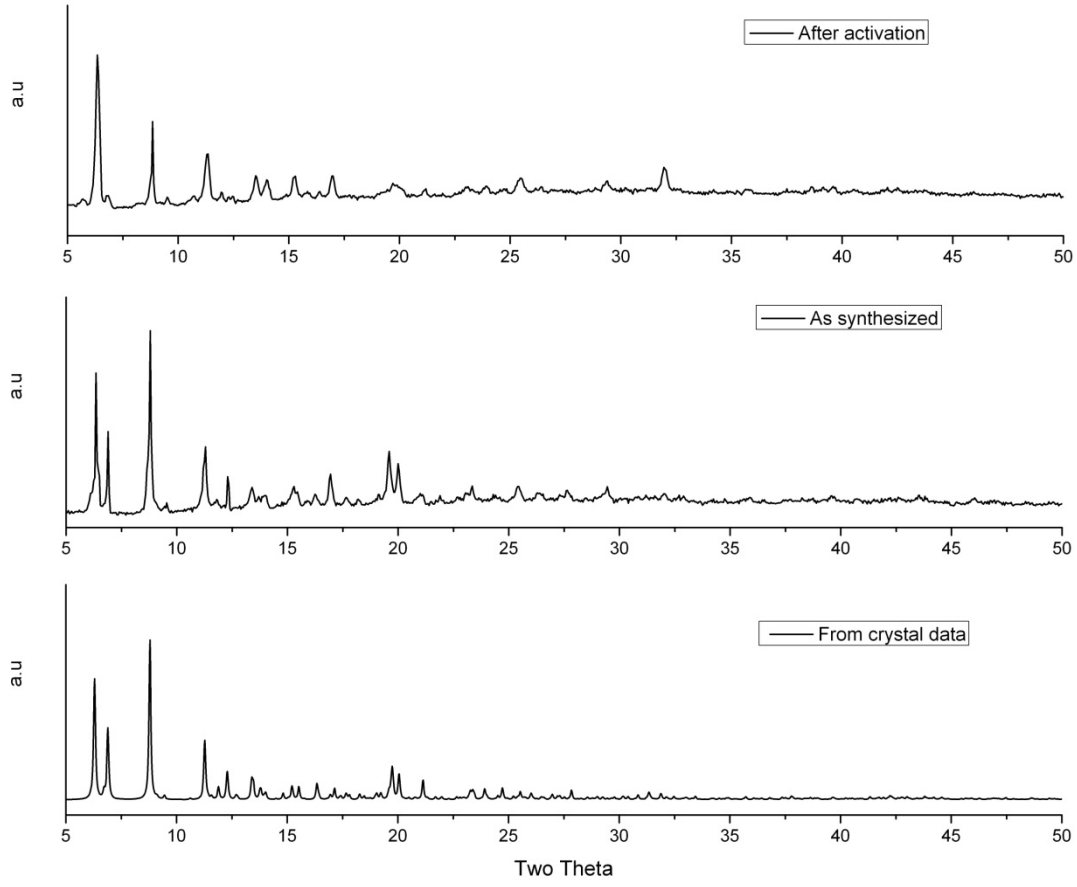

Figure 3.9 A comparison of experimental powder-XRD pattern of **1** after activations to remove guest molecules (top), as synthesized (middle) and theoretical pattern from the single crystal data (bottom).

3.1.5 Thermogravimetric Analyses (TGA)

Thermogravimetric analyses were carried out with a NETZSCH STA 449C unit at a heating rate of 10 ^{o}C/min under nitrogen atmosphere. TGA results show that MOF **1** is thermally stable up to 300 ^{o}C.

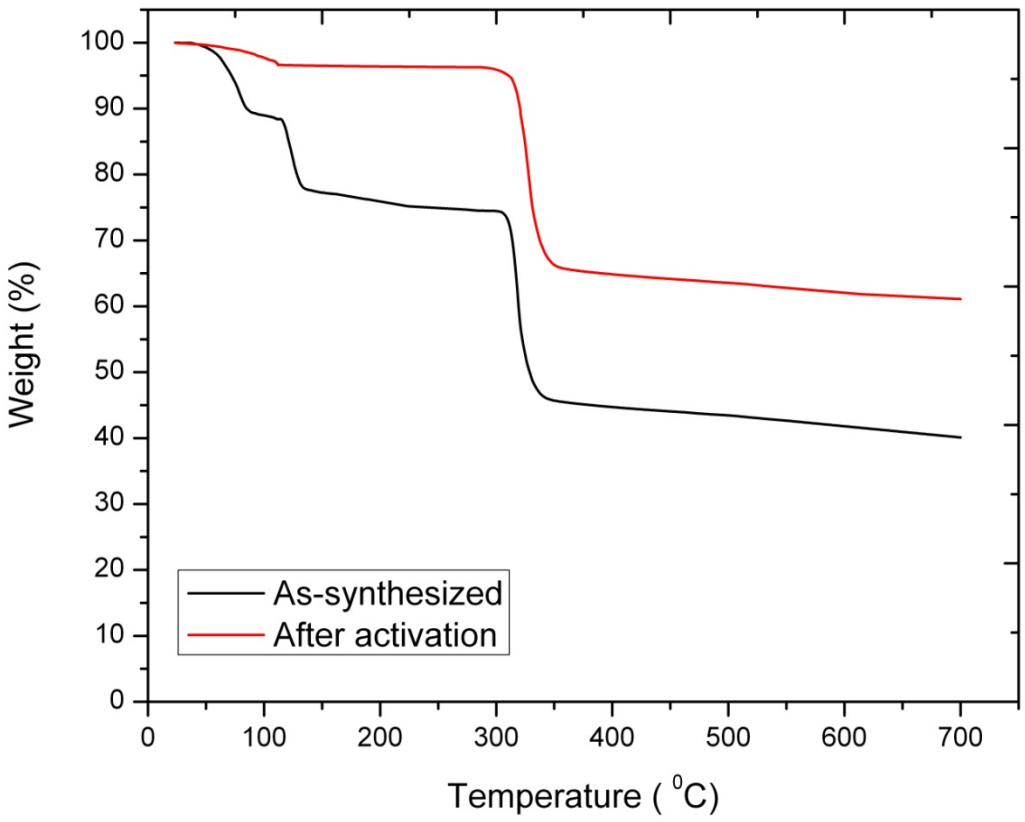

Figure 3.10 TGA trace of compound **1**.

3.1.6 Specific Surface Area and Porosity Characterization

Nitrogen adsorption isotherm of activated product at 77 K was measured with Autosorb-1 from Quantachrome Corporation to calculate the surface area. The BET surface area is calculated to be 600 m^2/g. The Langmuir surface area is calculated to be 900 m^2/g. However, it should be noted that these surface areas should be considered with some caution because low measurements at low relative pressures could not be obtained due to the absence of the facility for low pressure measurement. Thus, the BET analysis was performed near the saturation point.

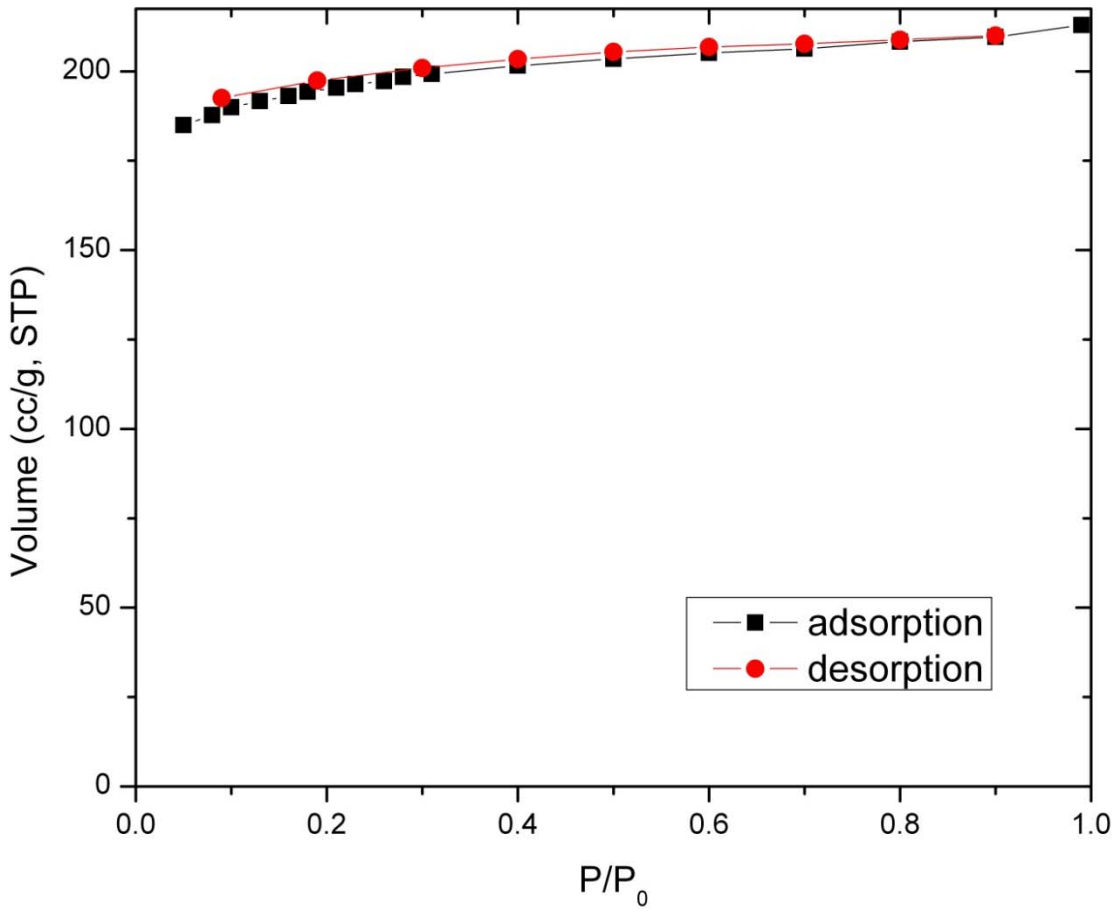

Figure 3.11 N_2 isotherm of activated samples of **1** at 77 K.

3.1.7 Fourier Transform Infrared Spectroscopy Characterization (FTIR)

To provide the spectroscopy information for this new MOF as a reference characterization, infrared (IR) spectra were recorded with PerkinElmer Spectrum One as KBr pellets in the range 4000 - 400cm^{-1}.

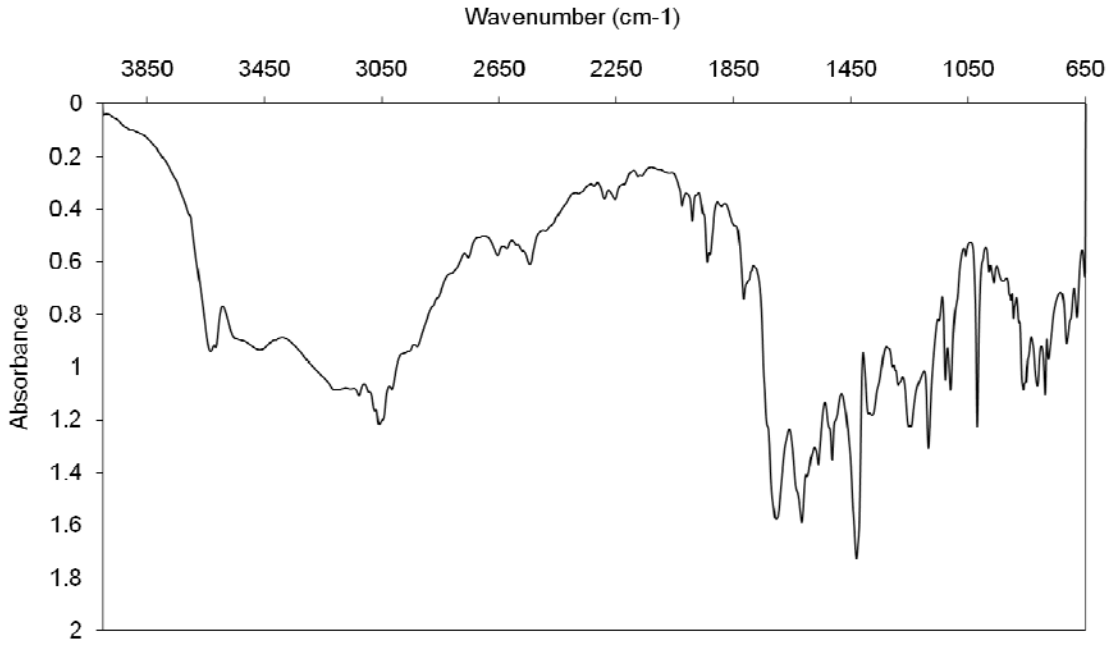

Figure 3.12 FT-IR pattern of the compound **1**

3.2 HIGH PRESSURE GAS ADSORPTION STUDY

A gravimetric adsorption apparatus (the GHP-100 gravimetric high pressure analyzer with C. I. microbalance from the VTI Corporation) was employed to measure the single-component adsorption isotherms. All adsorbate gases were purchased from the Linweld Company including carbon dioxide (LW617, bone dry 99.8 %), methane (LW913, ultra-high purity 99.99 %), and helium (LW800, UHP/ZERO). Before the adsorption measurement, the sample **1** was activated by heating at 200 ^{o}C in vacuum for 2 h to remove associated guest molecules and coordinated solvent molecules. A 150 mg

sample was placed in the sample cartridge of the GHP-100 gravimetric high pressure analyzer to undergo continued outgassing at 200 ^{o}C in a vacuum for 2 h. The sample weight was recorded every 2 minutes or per 0.01 % by mass. After outgassing, the system temperature was adjusted to the adsorption temperature of interest, and the sample cell was kept under vacuum for 30 min before starting the first adsorption point. All adsorption equilibrium data were collected after maintaining a given stable pressure for 30 min. After finishing the adsorption and desorption runs at the given temperature, the sample was regenerated by heating at 110 ^{o}C in a vacuum for 12 h until a constant sample weight was achieved. The sample was then reused in subsequent adsorption experiments.

3.2.1 Carbon Dioxide and Methane Isotherms

Upon activation of **1**, the copper atoms become coordinatively unsaturated, which should be expected to enhance the adsorption of dipolar or quadrupolar molecules. Because **1** presents 2D sheets without interconnected pores, this material provides an ideal system for examining the impact of open metal sites or unsaturated metal centers (UMCs) on adsorption. CO_2/CH_4, which is a difficult and important separation in biogas upgrading and natural gas purification, was chosen as a model mixture for examining the separation capability of **1**.

High-pressure single-component adsorption measurements were performed with a gravimetric system. Figure 3.13 displays the single-component adsorption isotherms of these gases in **1** at 298 K. CO_2 is more strongly adsorbed than CH_4, which is expected because CO_2 has a significant quadrupole moment, whereas CH_4 is essentially nonpolar. Neither molecule reaches its saturation loading over the pressure range examined (up to

25 bar). It is shown in Figure 3.13 that the adsorption isotherms are reversible, and there is no hysteresis.

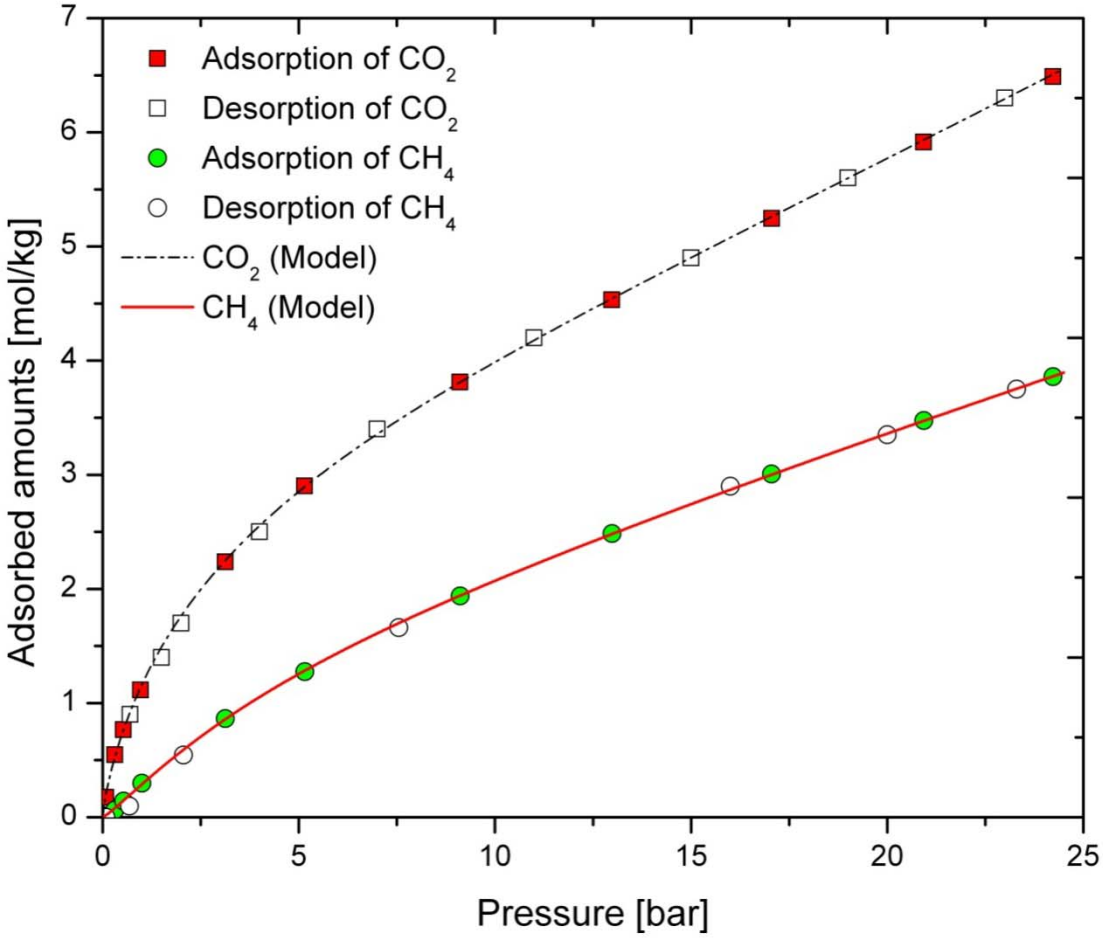

Figure 3.13 Single-component isotherms of CO_2, CH_4 in **1** at 298 K.

3.2.2 Multi-Component Adsorption Selectivity

Multi-component adsorption equilibrium data are essential for designing adsorption-based separation processes. Components often experience competitive adsorption from mixtures, which results in mixture adsorption isotherms that differ

significantly from pure-component behavior. To examine mixture behavior, multi-component isotherms and selectivities for CO_2/CH_4 mixture adsorption were calculated using the ideal adsorbed solution theory (IAST).[22] The ideal adsorbed solution theory (IAST) assumes the adsorbed phase is thermodynamically ideal, and thus derives the equilibrium relationship for an adsorbed mixture directly from the pure-component isotherms.

Before using IAST, an accurate isotherm model must be applied to represent single-component adsorption isotherms. Here, the dual-site Langmuir-Freundlich model provided an excellent fit of the adsorption data as shown in Figure 3.13. The fitted isotherm parameters were then used to predict the mixture adsorption in **1** using IAST. The predicted adsorption selectivities for equimolar CO_2/CH_4 mixture in **1** as a function of total bulk pressure are presented in Figure 3.14. As shown in the figure, this material displays very high selectivities for CO_2 at low pressure. At 298 K, the calculated selectivity for equimolar CO_2/CH_4 in activated **1** is near 12.4 at 1 bar. This is much higher than the reported values in Cu-BTC and MOF-5 which displayed selectivities of 6 and 2, respectively, independent of gas-phase composition under the same conditions by GCMC simulation.[23] The selectivities here are also higher than the values in MFI zeolite and nanoporous carbon membranes, which were reported as 2.5 and 5.2, respectively.[24] The selectivity decreases with increasing bulk pressure as copper sites become inaccessible. However, even at a total pressure of 20 bar, the selectivity is still close to 5.

Comparing IAST selectivities with those calculated from the pure-component isotherms (Figure 3.14), we find that **1** adsorbs CO_2 preferentially from the mixture with methane. Thus, methane adsorbs less than its pure-component loadings due to

competition with CO_2. If competitive adsorption did not exist between CO_2 and methane, then the IAST selectivities would match the selectivities calculated from pure-component loadings.

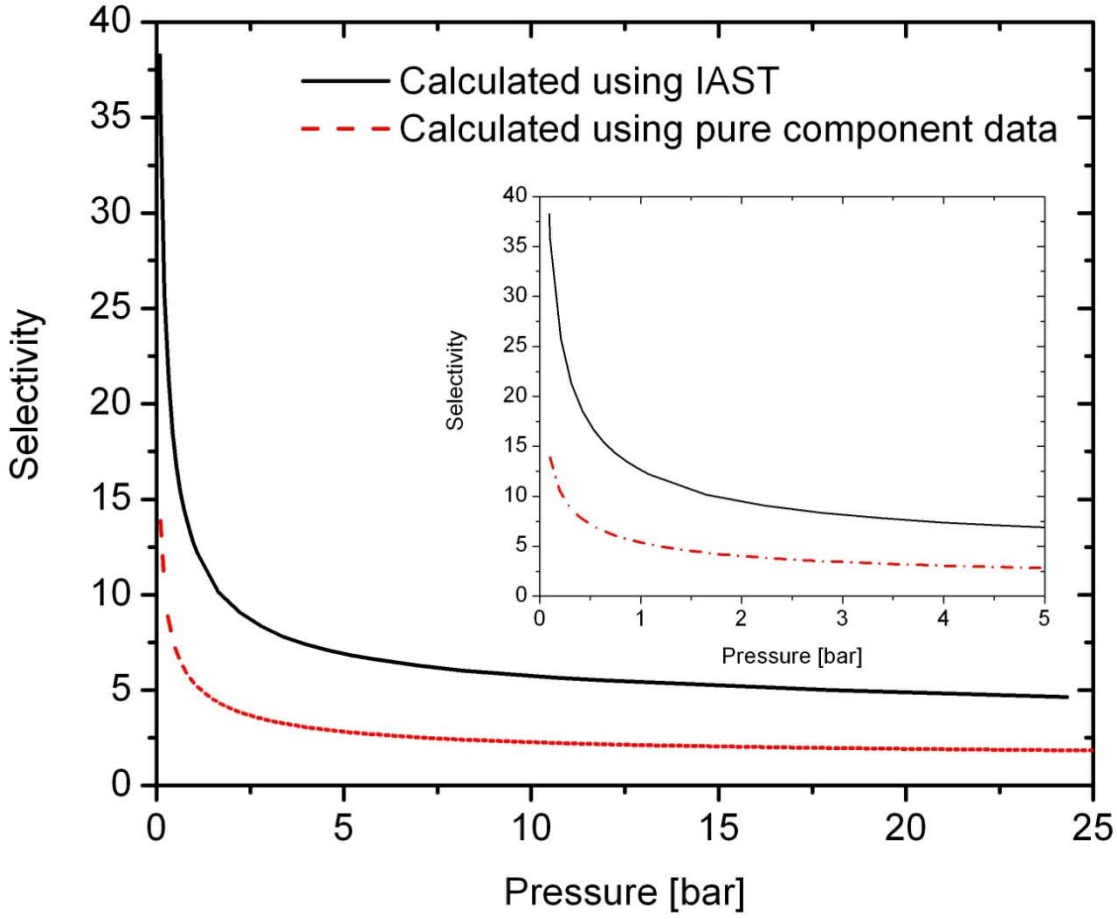

Figure 3.14 Selectivity of CO_2 over CH_4 in **1** for equimolar mixture of CO_2 and CH_4 at 298 K.

As a contrast, consider the results of Cu-BTC, which possesses UMCs and 3D interconnected pores. In that material we see that methane is quite attracted to the 3D pore space, which competes with the attraction of CO_2 to UMCs. Thus, selectivities are relatively low (~6). Our material **1** possesses no comparable pores but an abundance of

open copper sites. Thus, we have decreased the adsorption potential for methane and increased the selectivity for CO_2 (~13).

3.3 CONCLUSIONS

In summary, experiments and IAST calculations have shown that activated product **1** is a promising material for the separation and purification of CO_2 from CO_2/CH_4 mixtures. From a design standpoint, these results imply that constructing MOFs with unsaturated metal centers is of paramount importance for selective adsorption of polar molecules over nonpolar molecules. Furthermore, while somewhat counterintuitive, it appears that for CO_2/CH_4 and similar mixtures, the presence of 3D interconnected pores can actually be detrimental to adsorption selectivities due to the increase in van der Waals interactions for both polar and nonpolar molecules.

3.4 REFERENCES

(1) Bae, Y.-S.; Mulfort, K. L.; Frost, H.; Ryan, P.; Punnathanam, S.; Broadbelt, L. J.; Hupp, J. T.; Snurr, R. Q. *Langmuir* **2008**, *24*, 8592.

(2) Millward, A. R.; Yaghi, O. M. *J Am Chem Soc* **2005**, *127*, 17998.

(3) Chen, B.; Yang, Y.; Zapata, F.; Lin, G.; Qian, G.; Lobkovsky, E. B. *Adv Mater* **2007**, *19*, 1693.

(4) Zou, R.-Q.; Sakurai, H.; Xu, Q. *Angew Chem Int Edit* **2006**, *45*, 2542.

(5) Chen, B.; Eddaoudi, M.; Hyde, S. T.; O'Keeffe, M.; Yaghi, O. M. *Science* **2001**, *291*, 1021.

(6) Zou, R.-Q.; Jiang, L.; Senoh, H.; Takeichi, N.; Xu, Q. *Chem Commun* **2005**, 3526.

(7) Ma, S.; Zhou, H.-C. *J Am Chem Soc* **2006**, *128*, 11734.

(8) Xiang, S. C.; Zhou, W.; Zhang, Z. J.; Green, M. A.; Liu, Y.; Chen, B. L. *Angew Chem Int Edit* **2010**, *49*, 4615.

(9) Dietzel, P. D. C.; Georgiev, P. A.; Eckert, J.; Blom, R.; Strassle, T.; Unruh, T. *Chem Commun* **2010**, *46*, 4962.

(10) Yazaydin, A. O.; Benin, A. I.; Faheem, S. A.; Jakubczak, P.; Low, J. J.; Willis, R. R.; Snurr, R. Q. *Chem Mater* **2009**, *21*, 1425.

(11) Wu, H.; Zhou, W.; Yildirim, T. *J Am Chem Soc* **2009**, *131*, 4995.

(12) Park, M.; Moon, D.; Yoon, J. W.; Chang, J. S.; Lah, M. S. *Chem Commun* **2009**, 2026.

(13) Dietzel, P. D. C.; Besikiotis, V.; Blom, R. *J Mater Chem* **2009**, *19*, 7362.

(14) Britt, D.; Furukawa, H.; Wang, B.; Glover, T. G.; Yaghi, O. M. *P Natl Acad Sci USA* **2009**, *106*, 20637.

(15) Vitillo, J. G.; Regli, L.; Chavan, S.; Ricchiardi, G.; Spoto, G.; Dietzel, P. D. C.; Bordiga, S.; Zecchina, A. *J Am Chem Soc* **2008**, *130*, 8386.

(16) Dinca, M.; Dailly, A.; Liu, Y.; Brown, C. M.; Neumann, D. A.; Long, J. R. *J Am Chem Soc* **2006**, *128*, 16876.

(17) Mu, B.; Li, F.; Walton, K. S. *Chem Commun* **2009**, 2493.

(18) Chen, B. L.; Eddaoudi, M.; Hyde, S. T.; O'Keeffe, M.; Yaghi, O. M. *Science* **2001**, *291*, 1021.

(19) Thurn, H.; Krebs, H. *Acta Crystallographica Section B-Structural Crystallography and Crystal Chemistry* **1969**, *B 25*, 125.

(20) Qin, C.; Wang, X. L.; Carlucci, L.; Tong, M. L.; Wang, E. B.; Hua, C. W.; Xua, L. *Chem Commun* **2004**, 1876.

(21) Batten, S. R.; Robson, R. *Angew Chem Int Edit* **1998**, *37*, 1460.

(22) Myers, A. L.; Prausnitz, J. M. *Aiche J* **1965**, *11*, 121.

(23) Yang, Q. Y.; Zhong, C. L. *J Phys Chem B* **2006**, *110*, 17776.

(24) Babarao, R.; Hu, Z. Q.; Jiang, J. W.; Chempath, S.; Sandler, S. I. *Langmuir* **2007**, *23*, 659.

CHAPTER 4

MOF WITH OPEN METAL SITES AND SURFACE NANOPORES

A variety of porous MOFs featuring 2D or 3D nets have been reported recently. Usually these nets are constructed from clusters[1] or inorganic chains[2]. The reported clusters are considerably diverse, containing paddle wheel dinuclear, triangle cluster, tetrahedron, etc.[3-5] In this chapter, we describe the second new MOF material reported by our lab, which is an unique 2D porous framework $[Cd_3(BTB)_2(DEF)_4]_n \cdot 3nDEF$ (**2**) based on linear $\{Cd_3\}$ building blocks with bilayer honeycomb structure. After solvent exchange and activation under vacuum and heating, this material contains coordinatively unsaturated Cd centers which can be observed by IR spectra, thermogravimetric analysis (TGA), and powder X-ray diffraction. The activated material possesses high porosity demonstrated from N_2 adsorption isotherm. Scanning electron microscope (SEM) characterization of as-synthesized compound **2** revealed an interesting microporous structure.

4.1 SYNTHESIS AND CHARACTERIZATION

4.1.1 Materials and Synthesis Method

Solvothermal reactions were carried out in digestion bomb reactors. All chemicals are purchased from commercial companies and used as received without further purification: cadmium nitrate tetrahydrate, $Cd(NO_3)_2 \cdot 4H_2O$ (Acros Organics, 99+%); 1,3,5-tris(4-carboxyphenyl)benzene, H_3BTB (Sigma-Aldrich, ≥98%); N,N-diethylformamide, DEF (Acros Organics, 99%); N,N-dimethylformamide, DMF (Acros

Organics, 99.8+%). Exact amounts of $Cd(NO_3)_2.4H_2O$ (0.1g) and H_3BTB (0.1g) were dissolved in a 50 mL digestion bomb reactor using DEF. The mixture solution was heated at 110 ^oC for 35 hours. Then the light cubic-like crystal $[Cd_3(BTB)_2(DEF)_4]\cdot 3DEF$ (**2**) was obtained. The as-synthesized sample was obtained by filtration, washed with DMF and then dried in air.

4.1.2 Single-Crystal X-Ray Diffraction Characterization

Single-crystal XRD data of compound **2** (CCDC 763063)[6] was collected on a Rigaku Mercury CCD area-detector single crystal diffraction system with MoKα radiation ($\lambda = 0.71073$ Å). The structures were solved by direct methods with the help of SHELX-97 and refined by full-matrix least-squares techniques using SHELXL-97. Due to highly disordered solvent pockets, the data were corrected by PLATON Squeeze program.

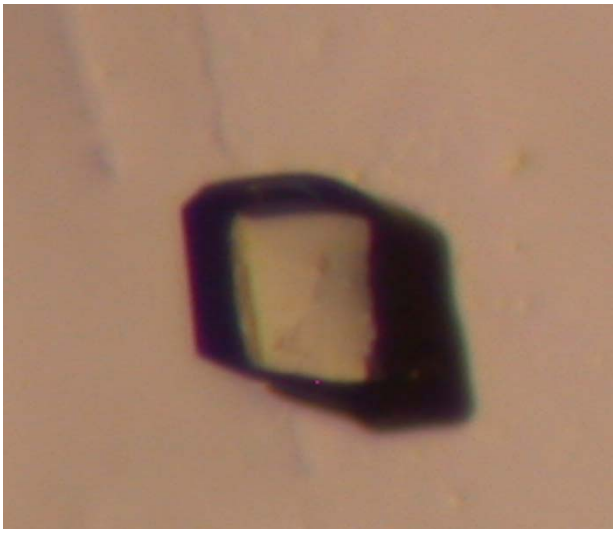

Figure 4.1 Crystal particle used to obtain the single-crystal structure.

Table 4.1 Crystallographic Data for $[Cd_3(BTB)_2(DEF)_4]_n \cdot 3nDEF$ (**2**)

Empirical formula	$C_{74}Cd_3O_{16}N_4H_{74}$
Molecular weight	1612.57
Temperature (K)	193(2)
Crystal system	triclinic
Space group	P-1
a(Å)	10.4595(9)
b(Å)	14.3920(13)
c(Å)	14.7634(13)
α(º)	69.608(1)
β(º)	82.476(1)
γ(º)	88.043(1)
$V(A^3)$	2065.0(3)
Z	1
D_{calcd}(g cm^{-3})	1.297
F(000)	818
μ (mm^{-1})	0.825
Reflection (collected/unique)	22830 / 11602
R_{int}	0.03
Goodness-of-fit on F^2	1.04
Final R indices [I>2σ(I)]	$R_1 = 0.0556$, $wR_2 = 0.1364$
R indices (all data)	$R_1 = 0.0693$, $wR_2 = 0.1444$
Max, min $\Delta\rho$ (e $Å^{-3}$)	1.496, -0.526

The X-ray crystallographic analysis of compound **2** reveals a porous 2D bilayer structure constructed from two identical Cd^{2+} ions bridged honeycomb sheets. There are one and a half Cd^{2+} ions, a BTB ligand and two coordinated DEF molecules in the asymmetric unit. Both the crystallographically unique Cd^{2+} ions are six coordinated by oxygen atoms. Cd1 atom lies on an inversion center, which is coordinated by two BTB ligands and their inversion-related species as well as by one DEF molecule and its inversion-related molecule. Thus, Cd1 is coordinated by four oxygen atoms from four BTB ligands and two oxygen atoms from two DEF molecules with an octahedral geometry. Cd2 is coordinated by five oxygen atoms from three BTB lignds and an oxygen atom of a DEF molecule with distorted octahedral geometry (Figure 4.2). The Cd-O bond lengths range from 2.177 Å to 2.378 Å. The BTB ligand acts as a μ5-bridge to link five Cd^{2+} ions together, in which three carboxylate groups adopt a chelating, μ2-η1:η1-bridging mode and μ2-η2:η1-bridging mode, respectively (Figure 4.3).

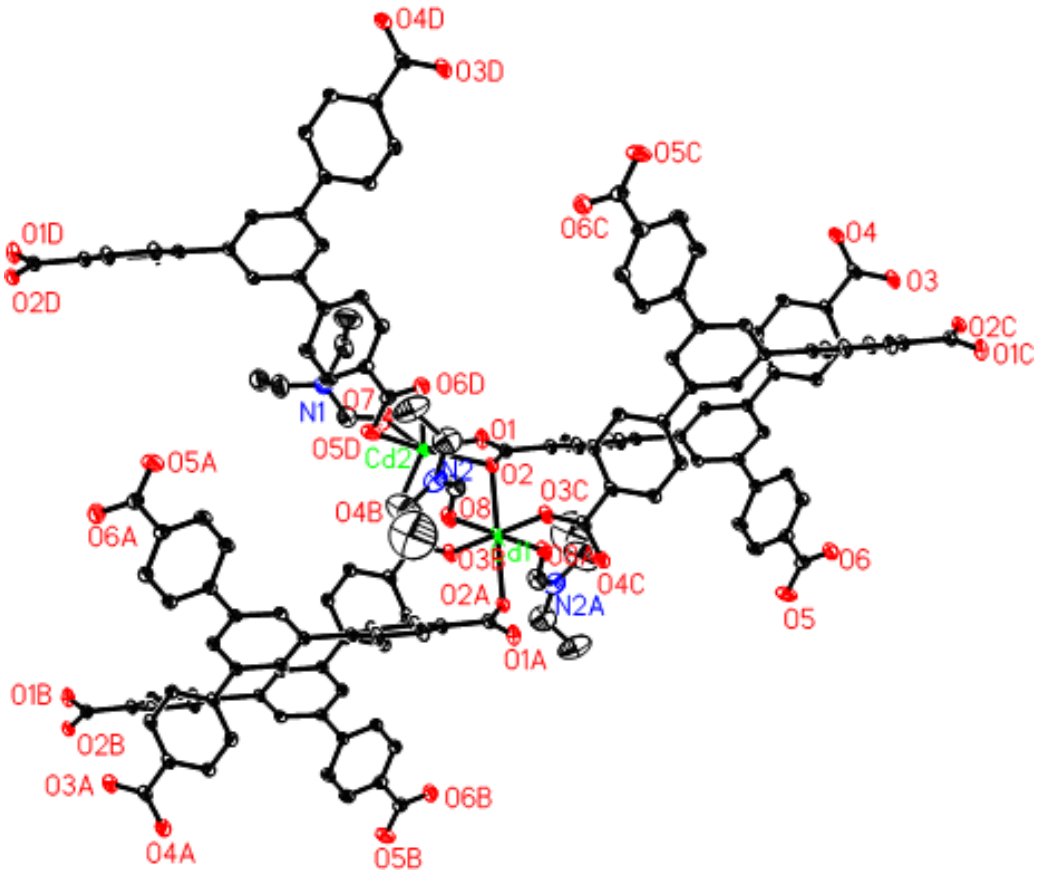

Figure 4.2 The coordination environments of metal ions in **2**. Displacement ellipsoids are plotted at 30% probability level. Symmetry codes: A: -x, -y, -z; B: x, 1+y, z-1; C: -x, -y-1, 1-z, D: 1+x, y, z-1, respectively.

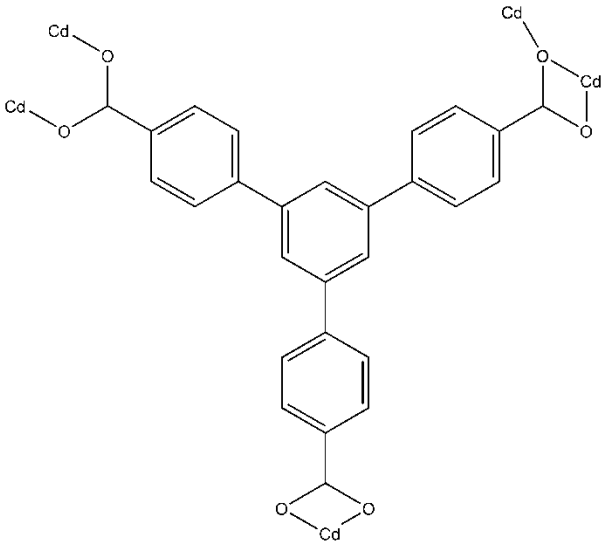

Figure 4.3 Coordination mode of BTB^{3-} ligand in the structure of **2**.

In the framework of compound **1**, the Cd2 centers are linked by BTB ligands to give rise to a 2D honeycomb layer with large hexagonal cavities (Figure 4.4 (a)). In the view of topology, this layer can be simplified as a (6, 3) net (Figure 4.4 (b)), treating the Cd2 centers and BTB ligands as nodes. Two parallel honeycomb layers are further bridged to generate a bilayer structure by Cd1-O2 bonds (Figure 4.4 (c)). Each honeycomb layer is offset from the next layer by appoximately half of the hexagonal width. Notably, the bilayer structure is based on symmetric carboxylate bridged $\{Cd_3\}$ clusters with Cd···Cd distance of 3.878 Å. Each $\{Cd_3\}$ cluster connects to six BTB ligands while each BTB ligand connects to three $\{Cd_3\}$ clusters. Therefore, treating the $\{Cd_3\}$ clusters and BTB ligands as nodes, the bilayer sheet can be specified as a 2D (3, 6) connected $CdCl_2$-type net with $(4^3 \cdot 4^6)$ symbol (Figure 4.4 (d)). Comparing against this 2D $CdCl_2$ topology type, MOF-177 displays 3D (6,3) net regarding Zn_4O clusters and BTB ligands as nodes, which was termed as **qom** type, related to the **pyr** type[7]; while MOF-39 produces a 3D (3,4) network or a decorated-expanded (3,6) network considering Zn_3O clusters and BTB ligands as nodes.[8]

These 2D bilayer sheets are further stacked together in a repeating fashion to form a 3D supramolecular structure with two kinds of rhombus channels along the *a*-axis: the large one (A) has approximate dimensions of 8.45 × 8.45 Å and the small one (B) has approximate dimensions of 8.16 × 8.16 Å after removing coordinated DEF molecules (Figure 4.5).

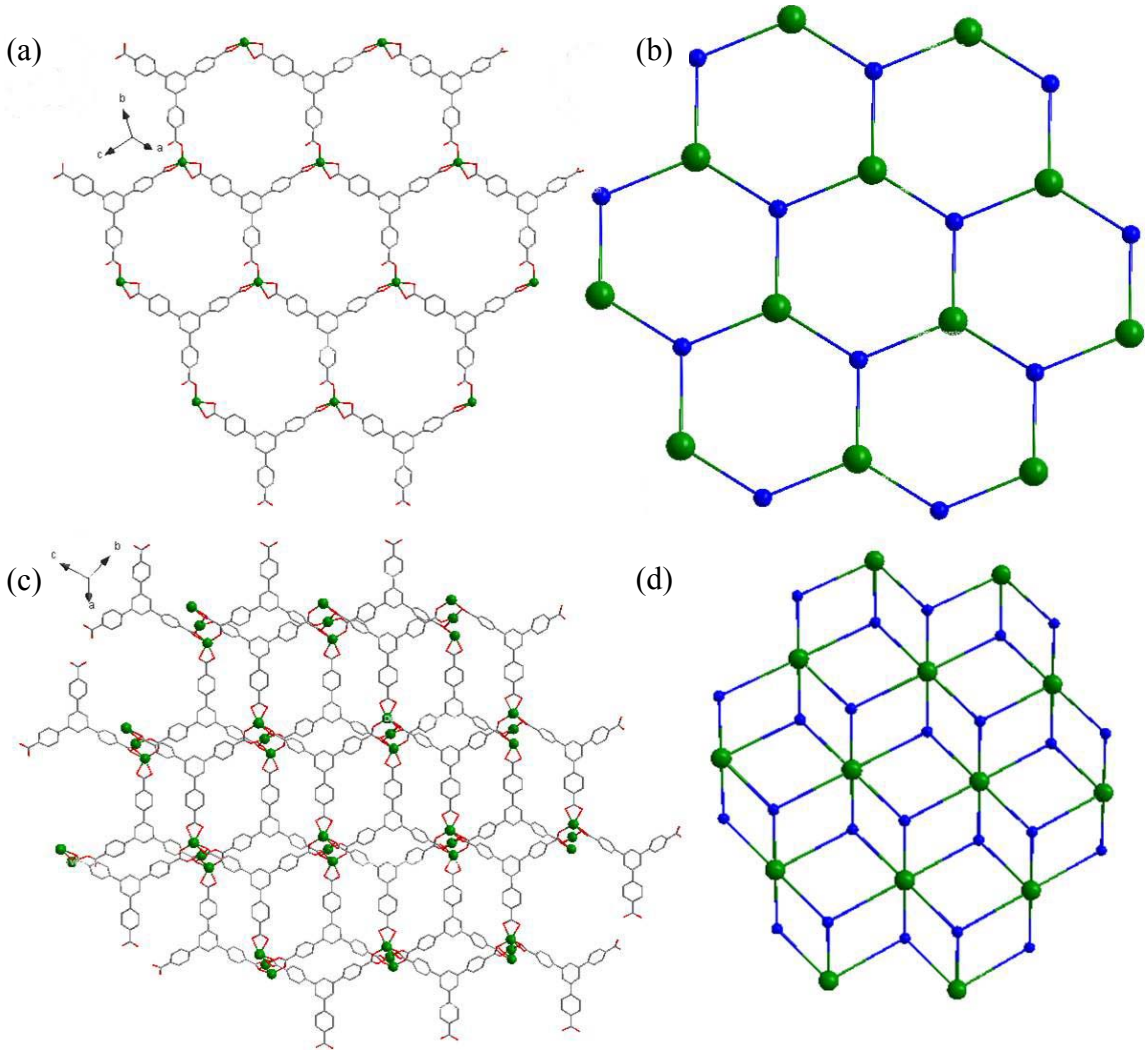

Figure 4.4 (a) The honeycomb layer with hexagonal cavities in **2**; (b) topology view of the honeycomb layer with (6,3) net; (c) the bilayer structure based on $\{Cd_3\}$ clusters; (d) topology view of the bilayer treating the $\{Cd_3\}$ cluster and BTB ligands as nodes.

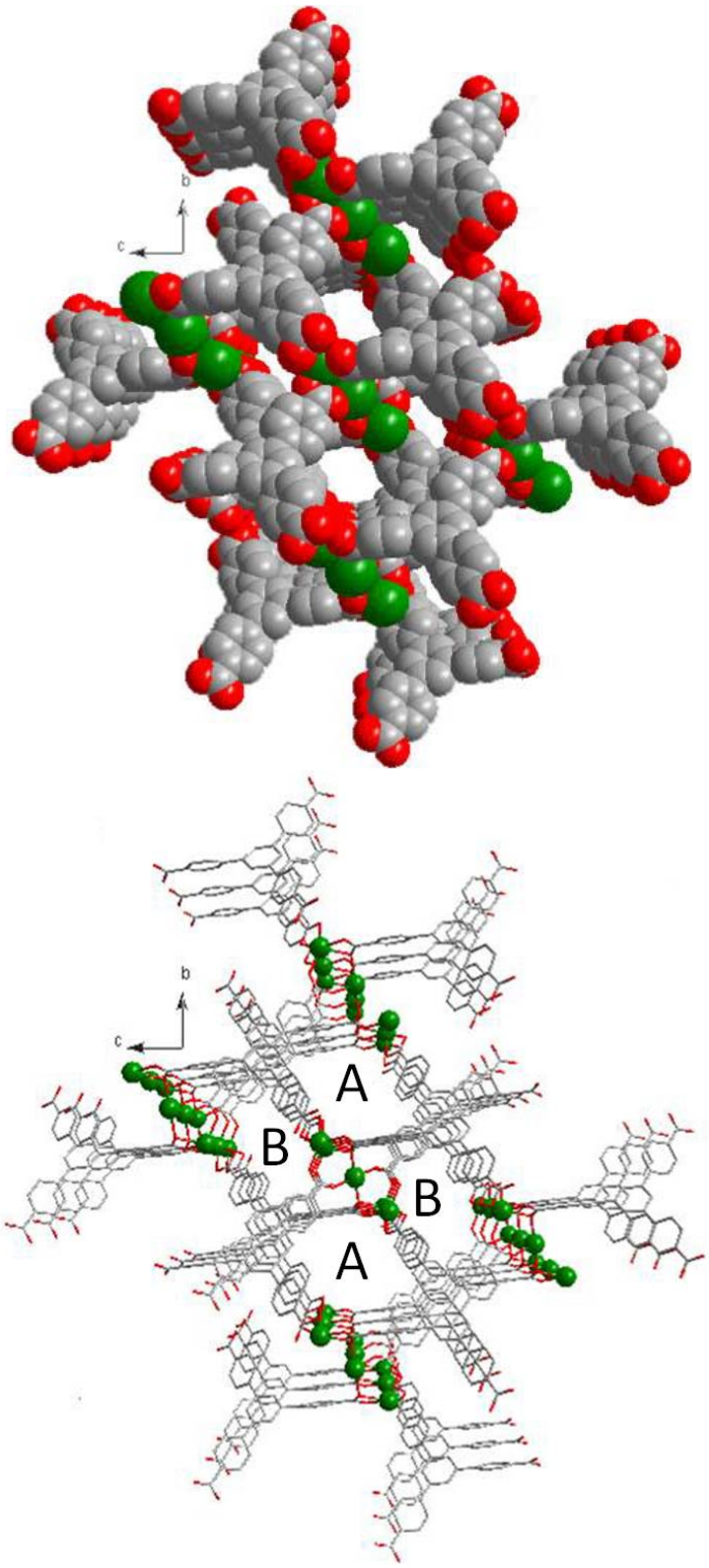

Figure 4.5 The 3D supramolecular structure of compound **2** showing two kinds of channels (A and B).

4.1.3 Scanning electron microscope (SEM) characterization

The SEM images were conducted on a Hitachi SEM S-3500N equipped with a model S-6542 absorbed electron detector. SEM characterization of as-synthesized compound **2** revealed an interesting microporous structure. In Figure 4.6, the SEM image exhibits cubic-shaped crystal particles with average diameter of 50 μm. In Figure 4.7, the top image shows the macroporous structure observed from a section of a broken crystal particle, while the bottom image provides further detail of pores with an average diameter of 500 nm, which indicates the potential of this MOF material as a catalyst support. Such interesting microporous structure is not often visible in MOFs.

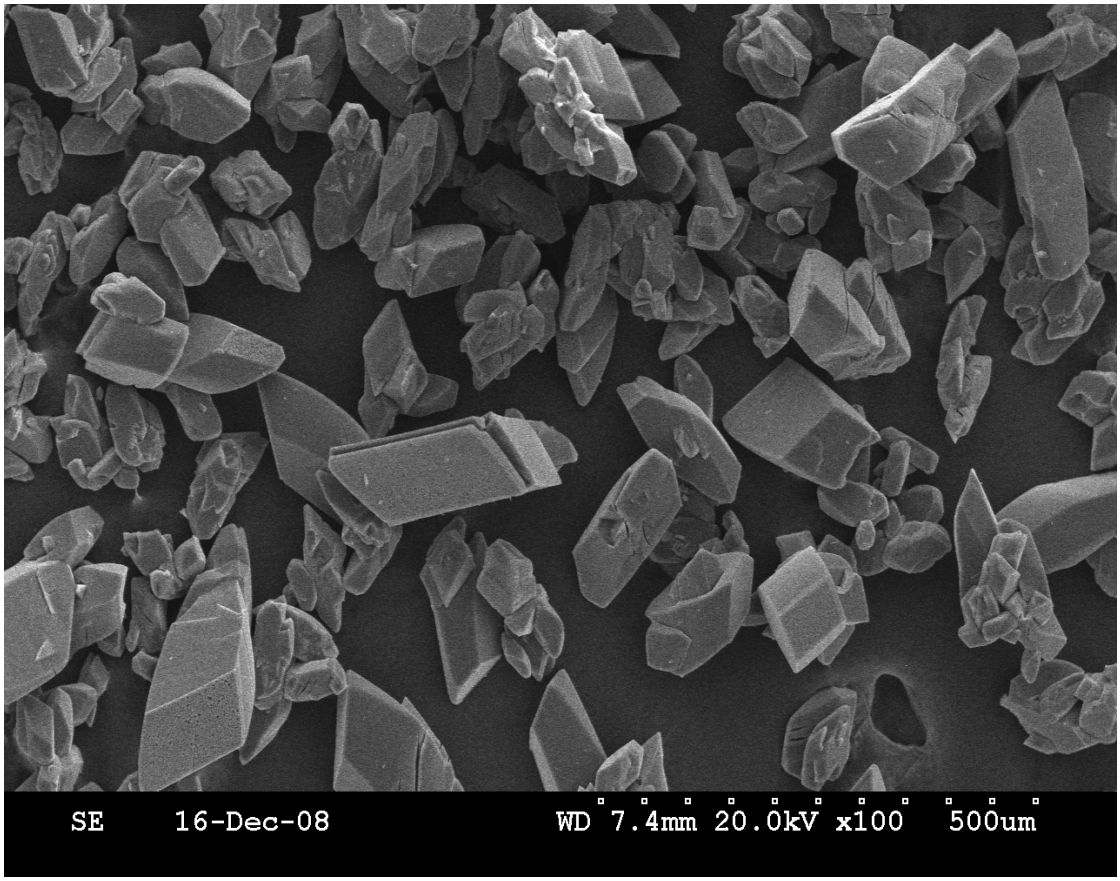

Figure 4.6 SEM of **2** presenting the cubic-shaped crystal particles.

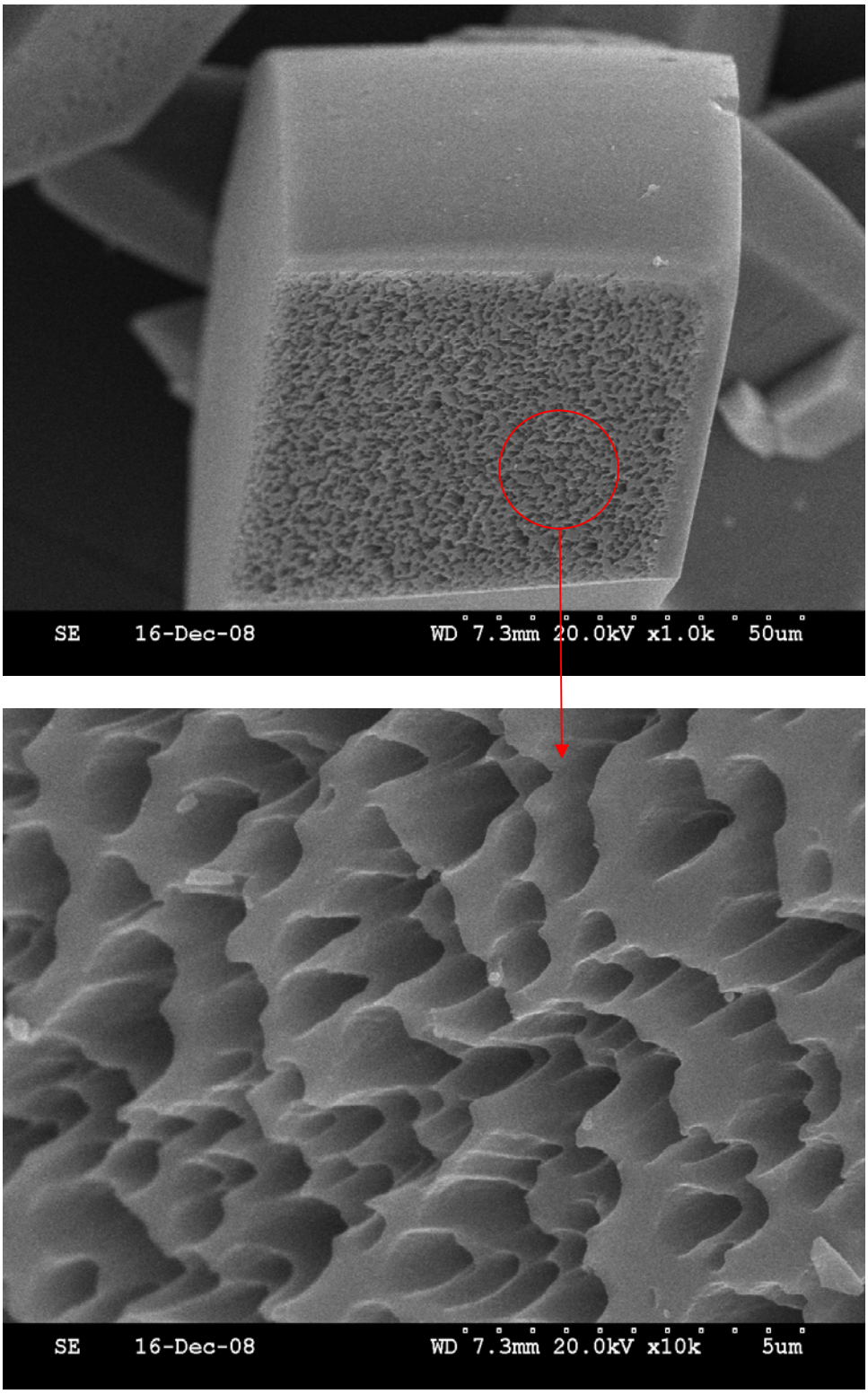

Figure 4.7 Surface characterization of **2** demonstrating nanopores on the surface of MOF

4.1.4 Powder X-Ray Diffraction Characterization

The powder-XRD pattern of samples were collected on a Bruker D8 powder diffraction system with Cu radiation (λ= 1.5406 Å).

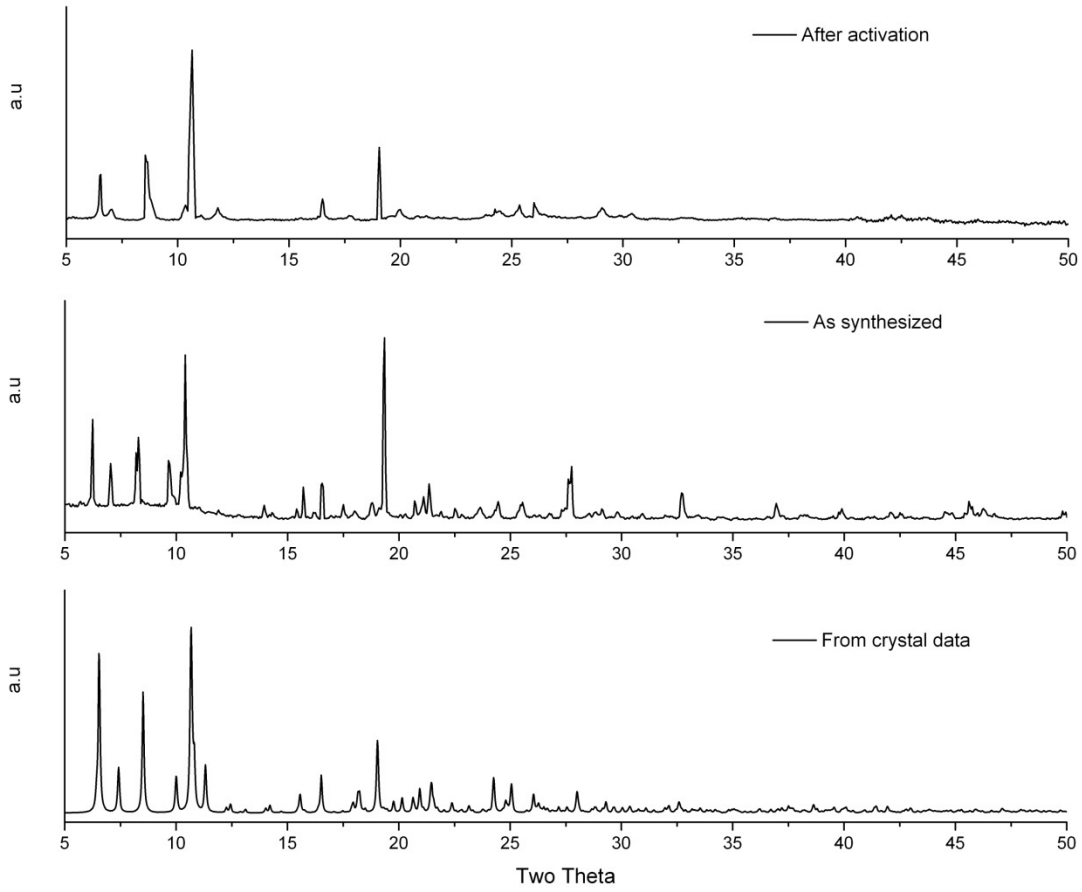

Figure 4.8 A comparison of experimental powder-XRD pattern of **2** after activations to remove guest molecules (top), as synthesized (middle) and theoretical pattern from the single crystal data (bottom).

4.1.5 Thermogravimetric Analyses (TGA) and Elemental Analysis

Thermogravimetric analyses were carried out with a SHIMADZU TGA-50 at a heating rate of 5 ^{o}C/min under helium atmosphere with 25 mL/min flow rate. Elemental analyses were carried out on an Elementar Vario EL III analyzer. Combined with the result of TGA analysis, we can confirm that there are one and half DEF molecules associated in an asymmetric unit. Therefore, the molecular formula with associated DEF will be $C_{89}Cd_3O_{19}N_7H_{107}$: C, 55.79%; Cd, 17.62%; O, 15.88%; N, 5.12%; H, 5.59%. Found: C, 55.81%; Cd, 17.60%; O, 15.89%; N, 5.10%; H, 5.60%.

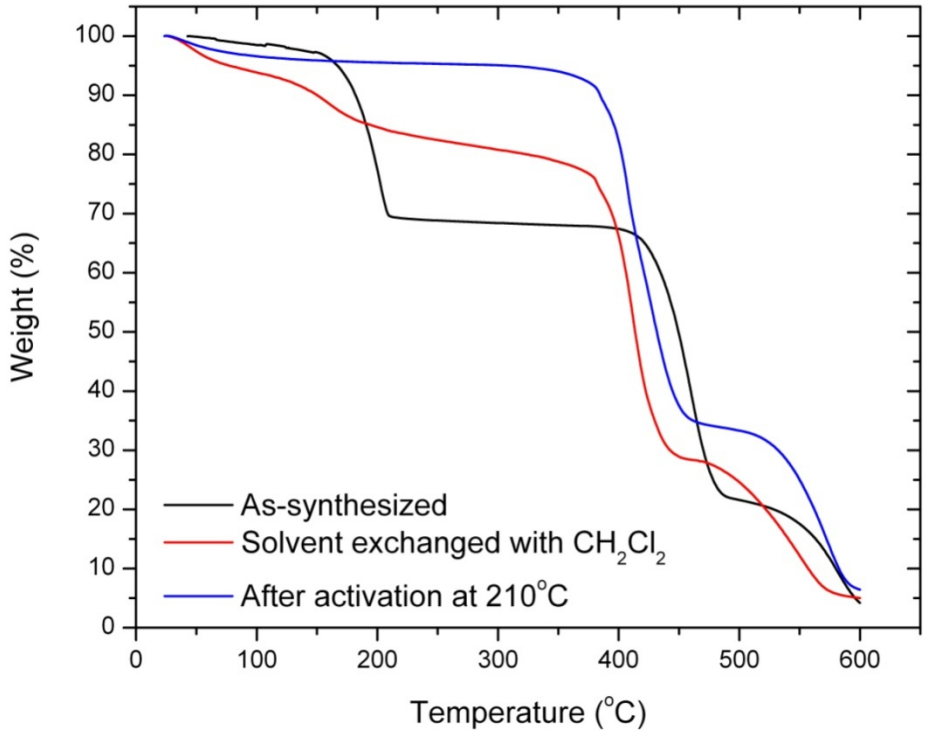

Figure 4.9 TGA trace of compound **2**.

4.1.6 Fourier Transform Infrared Spectroscopy Characterization (FTIR)

To remove the coordinated DEF molecules, **2** was immersed in a mixture of acetone and dichloromethane for a few days, then filtered and activated in a vacuum oven. TGA data indicate that all coordinated DEF molecules can be removed from **1** at 210 ^{o}C, and thermal stability of the crystal is up to 410 ^{o}C as shown in Figure 4.9. The comparison of FT-IR patterns (Figure 4.10) for as-synthesized compound **2** and activated sample confirms the successful removal of DEF molecules as well. The C=O bond in a DEF molecule has a reduced bond order compared to the carboxylic group due to the nitrogen atom. The stretching frequency of C=O in DEF is lower than that of an unsubstituted C=O bond, which is usually around 1710 cm^{-1} for saturated carboxylic acids. Thus, for as-synthesized compound **2**, the existence of a strong peak at 1650 cm^{-1} indicates C=O in DEF molecule. Furthermore, the disappearance of the peak at 1650 cm^{-1} in the FT-IR pattern of activated compound **2** confirms the removal of DEF molecules after activation. This FT-IR pattern change can also be seen in $[Zn_9O_3(2,7\text{-ndc})_6(DMF)_3]$[9] and $[Mn(NDC)(DEF)]_n$.[10] After DEF molecules are successfully removed, the Cd centers have open coordination sites that are accessible to incoming sorbate molecules and can influence gas storage, adsorption separations, and catalysis.

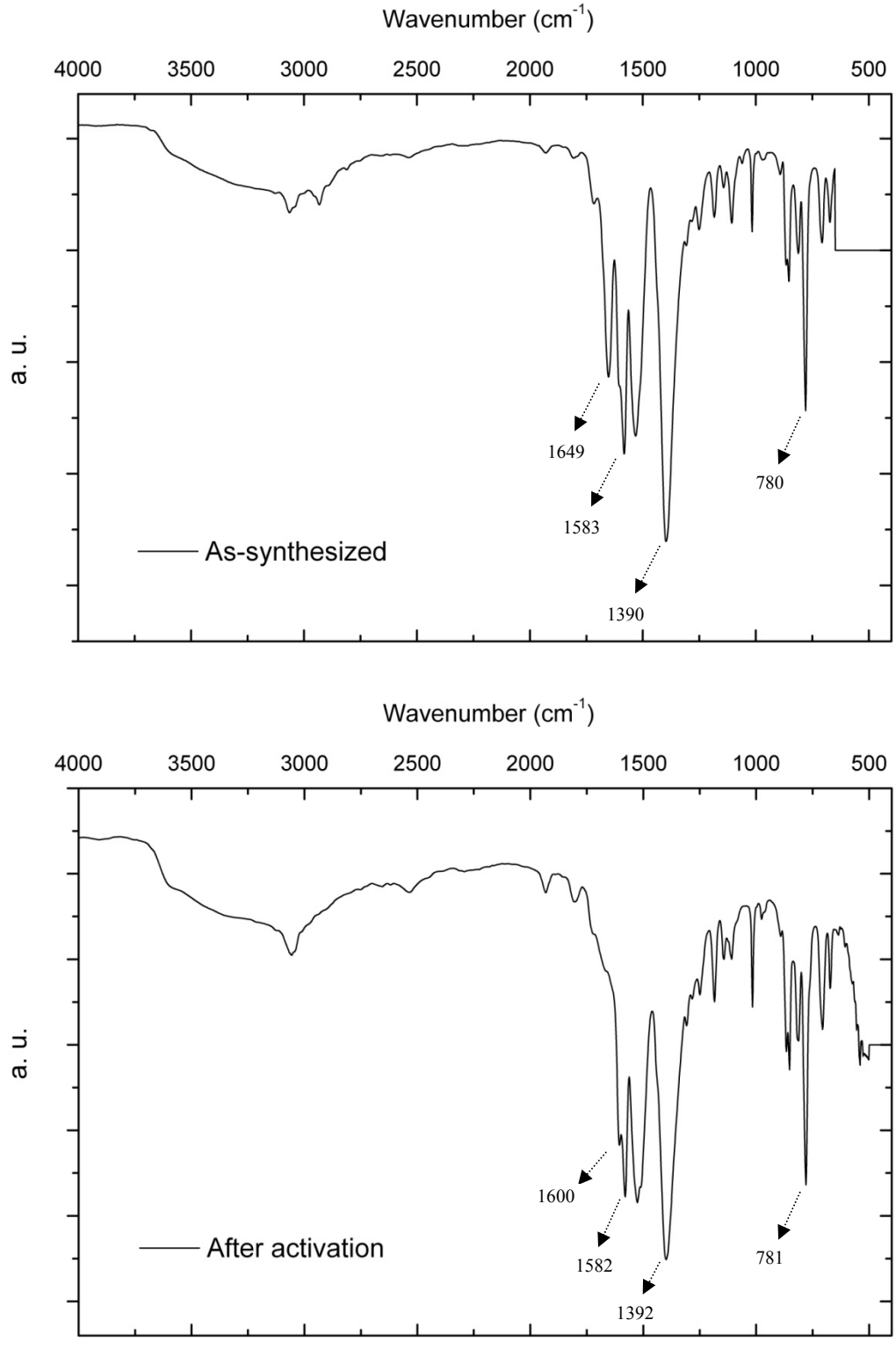

Figure 4.10 FT-IR pattern of compound **2** (top, as-synthesized; bottom, after activation).

4.1.7 Specific Surface Area and Porosity Characterization

Nitrogen adsorption isotherm of activated product at 77 K was measured with Autosorb-1 from Quantachrome Corporation to calculate the surface area. The adsorption isotherm for nitrogen at 77 K in activated compound **2** is presented in Figure 4.11. The isotherm is similar to the type-IV isotherm according to BDDT classification. As shown in the figure, the micropore is filled quickly at low pressure. From the second to third adsorption points (relative pressure of 0.05 to 0.075), a steep slope on the isotherm indicates that capillary condensation is occurring in the mesopores. With further increase in pressure, a reproducible, step-style adsorption isotherm develops, which indicates the existence of mesopore and macropore size distribution in the crystals. The N_2 isotherm demonstrated a hysteresis loop upon desorption, which is often attributed to the presence of mesopores and nanosized pores. Such hysteresis phenomena have also been observed in other porous MOFs.[10] The BET surface area is calculated as 504 m^2/g, while total pore volume is 0.35 cm^3/g. The Langmuir surface area is calculated to be 661 m^2/g.

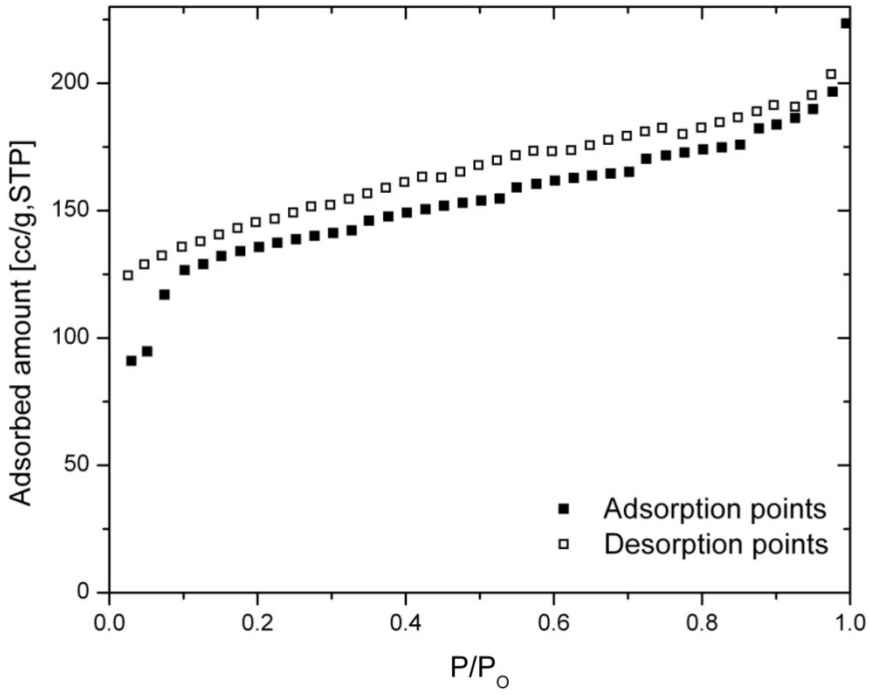

Figure 4.11 N_2 isotherm of activated compound **2** at 77 K.

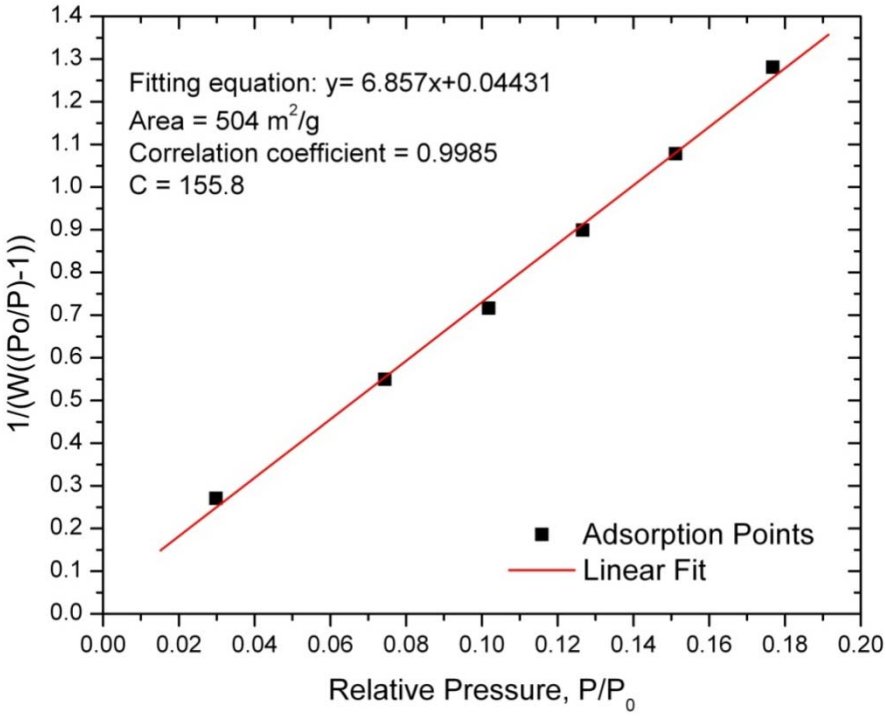

Figure 4.12 Multipoint BET analysis of N_2 isotherm at 77 K.

4.2 CONCLUSIONS

In conclusion, a novel MOF material $[Cd_3(BTB)_2(DEF)_4]_n \cdot 2nDEF$ (**2**) with open metal sites has been synthesized. This material exhibited an interesting nanoporous structure as shown by SEM characterization. TGA trace confirmed that the thermal stability is up to 410 ^oC. In addition, after activation under heating and vacuum conditions, coordinated DEF molecules on Cd metal sites can be removed to obtain open metal sites or unsaturated metal centers (UMCs) which is confirmed from TGA data and FT-IR patterns. Finally, N_2 isotherm at 77 K demonstrated the porosity of this material which possesses BET surface area of 504 m^2/g and total pore volume of 0.35 cm^3/g.

4.3 REFERENCES

(1) Park, M.; Moon, D.; Yoon, J. W.; Chang, J.-S.; Lah, M. S. *Chem Commun* **2009**, 2026.

(2) Zhang, X.-M.; Hao, Z.-M.; Zhang, W.-X.; Chen, X.-M. *Angew Chem Int Edit* **2007**, *46*, 3456.

(3) Wang, X.-S.; Ma, S.; Sun, D.; Parkin, S.; Zhou, H.-C. *J Am Chem Soc* **2006**, *128*, 16474.

(4) Wang, Z.; Zhang, B.; Fujiwara, H.; Kobayashi, H.; Kurmoo, M. *Chem Commun* **2004**, 416.

(5) Huang, Y.-Q.; Ding, B.; Song, H.-B.; Zhao, B.; Ren, P.; Cheng, P.; Wang, H.-G.; Liao, D.-Z.; Yan, S.-P. *Chem Commun* **2006**, 4906.

(6) Mu, B.; Huang, Y. G.; Walton, K. S. *Crystengcomm* **2010**, *12*, 2347.

(7) Chae, H. K.; Siberio-Perez, D. Y.; Kim, J.; Go, Y.; Eddaoudi, M.; Matzger, A. J.; O'Keeffe, M.; Yaghi, O. M. *Nature* **2004**, *427*, 523.

(8) Kim, J.; Chen, B. L.; Reineke, T. M.; Li, H. L.; Eddaoudi, M.; Moler, D. B.; O'Keeffe, M.; Yaghi, O. M. *J Am Chem Soc* **2001**, *123*, 8239.

(9) Park, M.; Moon, D.; Yoon, J. W.; Chang, J. S.; Lah, M. S. *Chem Commun* **2009**, 2026.

(10) Moon, H. R.; Kobayashi, N.; Suh, M. P. *Inorg Chem* **2006**, *45*, 8672.

CHAPTER 5

A NEW POLYMORPH OF ZN-BTB MOF FOR ADSORPTION APPLICATION

For adsorption technologies ranging from gas separations to gas storage, selection of the proper solid adsorbent is the key step to designing an efficient adsorption process. To examine the practicality of a solid adsorbent, the following characteristics must be considered: porosity, structural stability, reversible uptake and release, and capability for surface modification for creating molecule-specific adsorption sites. Adsorbents such as activated carbons and zeolites have been used in adsorption separations for decades. However, it is difficult to modify these materials to enhance selectivities, and it can be difficult to regenerate them without significant heating, which leads to low productivity and great expense[1]. Metal-organic frameworks (MOFs) have emerged as a new class of porous materials possessing ordered structures, high surface areas, modifiable surfaces, and tunable pore sizes [2-7]. MOFs are promising solid adsorbents for gas storage and separation, but such materials have not yet reached an applied level.

On the other hand, polymorphism in materials science is the ability of a solid material to exist in more than one form or crystal structure, which was first described by Mitscherlich in 1822.[8] This phenomenon could be found in any crystalline material including polymers, minerals, and metals. With the increasing report of MOFs structure, many polymorphic frameworks are recognized in some MOFs, in which each compound is composed of the same secondary building unit (SBU) and linker but differ in topology and thus pore structure.[9] Thus, it is because of not only the interests in science but also

practical application that we would like to investigate the impact of different polymorphs of MOFs on adsorption properties.

In this paper, we present pure-component adsorption equilibrium data for methane and carbon dioxide at different temperatures on a new three-dimensional Zn-MOF material built from the ligand 1,3,5-tris(4-carboxyphenyl) benzene (H_3BTB) with Zn metal, which is a new polymorphic framework of Zn-BTB as MOF-177. The adsorption data are described by the Toth equation and Dubinin-Astakhov (D-A) equation. Thermodynamic properties including isosteric heat of adsorption are estimated based on the two models, and comparisons are made with other adsorbents.

5.1 SYNTHESIS AND CHARACTERIZATION

5.1.1 Materials and Synthesis Method

Solvothermal reactions were carried out in digestion bomb reactors. All chemicals are purchased from commercial companies and used as received without further purification: zinc nitrate hexahydrate, $Zn(NO_3)_2 \cdot 6H_2O$ (EMD Chemicals); 1,3,5-tris(4-carboxyphenyl)benzene, H_3BTB (Sigma-Aldrich, ≥98%); Thiophene-3,4-dicarboxylic acid, T1828 (Frontier Scientific, 98%); N,N-dimethylformamide, DMF (Acros Organics, 99.8+%). A mixture of $Zn(NO_3)_2 \cdot 6H_2O$ (0.15g, 0.5mmol), T1828 (0.04g, 0.23mmol), H_3BTB (0.1g, 0.23mmol), and DMF (30mL) was placed into a Teflon-lined 45 mL reactor. The mixture was heated for 58 hr at 373 K. After cooling to room temperature, colorless crystals $[Zn_4O(BTB)_2(DMF)_2] \cdot 3DMF$ (**3**)were obtained and then washed with DMF three times. The crystals were then filtered and dried in air. The yield is approximately 80% based on H_3BTB.

5.1.2 Single-Crystal X-Ray Diffraction Characterization

Single-crystal XRD data of compound **3** was collected on a Rigaku Mercury CCD area-detector single crystal diffraction system with MoKα radiation (λ = 0.71073 Å). The structures were solved by direct methods with the help of SHELX-97 and refined by full-matrix least-squares techniques using SHELXL-97.

Zn-MOF (**3**) is composed of Zn_4O cluster and BTB ligand, which is the similar secondary building unit (SBUs) that appears in MOF-177.[10] However, Zn-MOF possesses a pore structure and topology that are distinct from MOF-177 due to the different coordination number of Zn atoms. As shown in Figure 5.1, there are three 4-coordinated Zn atoms and one 6-coordinated Zn atom in one Zn-O cluster of Zn-MOF, while all Zn atoms are 4-coordinated in MOF-177. It is due to the different reaction conditions that local coordination environment around metal oxide cluster causes different pore structure and topology. As shown in Figure 5.2, Zn-MOF possesses rectangular pores with diameters of 9.0Å × 7.5Å, which are interconnected to each other by inside channels (about 5.0 Å in diameter), while MOF-177 has two different pore sizes, which are around 8.4 Å and 3.0 Å in diameter at [001] plane, and these pores are interconnected to each other by inside channels (about 8 Å in diameter). Such variation in pore structure can have a significant impact on adsorption properties.

In the topological structure, the tetrahedral $[Zn_4O(CO_2)_6]$ clusters are connected by the tritopic BTB linkers to form (6,3)-connected **ant** net with large DMF filled channels. The actual net here is two-fold interpenetrated, leaving the channels along *c*-axis. This structure is similar to MOF **Zn/BTB ant** reported by Matzger's group.[9] However, all Zn atoms are 4-coordinated in MOF **Zn/BTB ant** as appeared in MOF-177.

In the crystallographic report of MOF **Zn/BTB ant**, a = 26.3857 Å, b = 28.3859 Å, c = 31.6139 Å, $\alpha = 90^{o}$, $\beta = 113.567^{o}$, $\gamma = 90^{o}$, while in the single-crystal measurement of Zn-MOF (**3**), a = 23.5243 Å, b = 29.3483 Å, c = 31.8203 Å, $\alpha = 90^{o}$, $\beta = 110.836^{o}$, $\gamma = 90^{o}$.

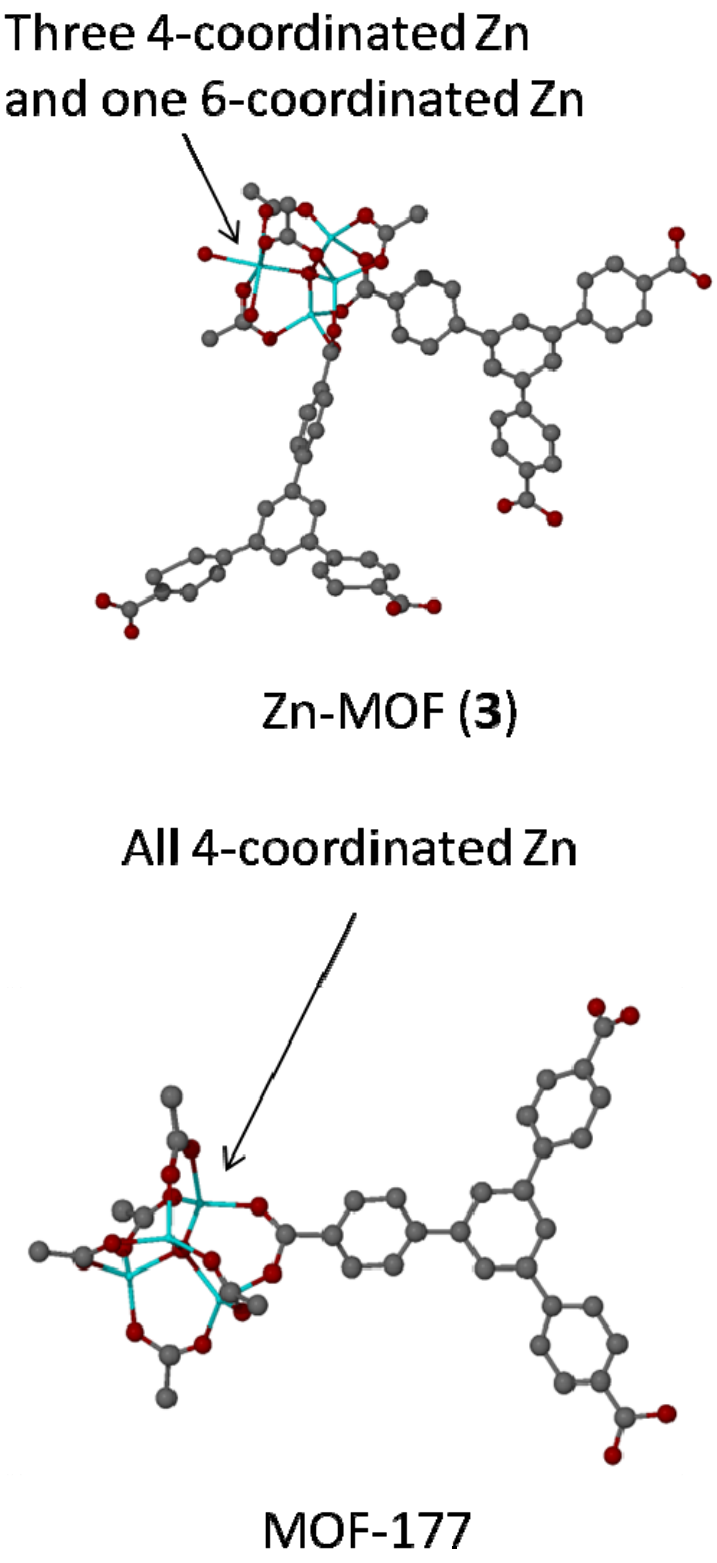

Figure 5.1 Coordination environment comparison between Zn-MOF (**3**) and MOF-177.

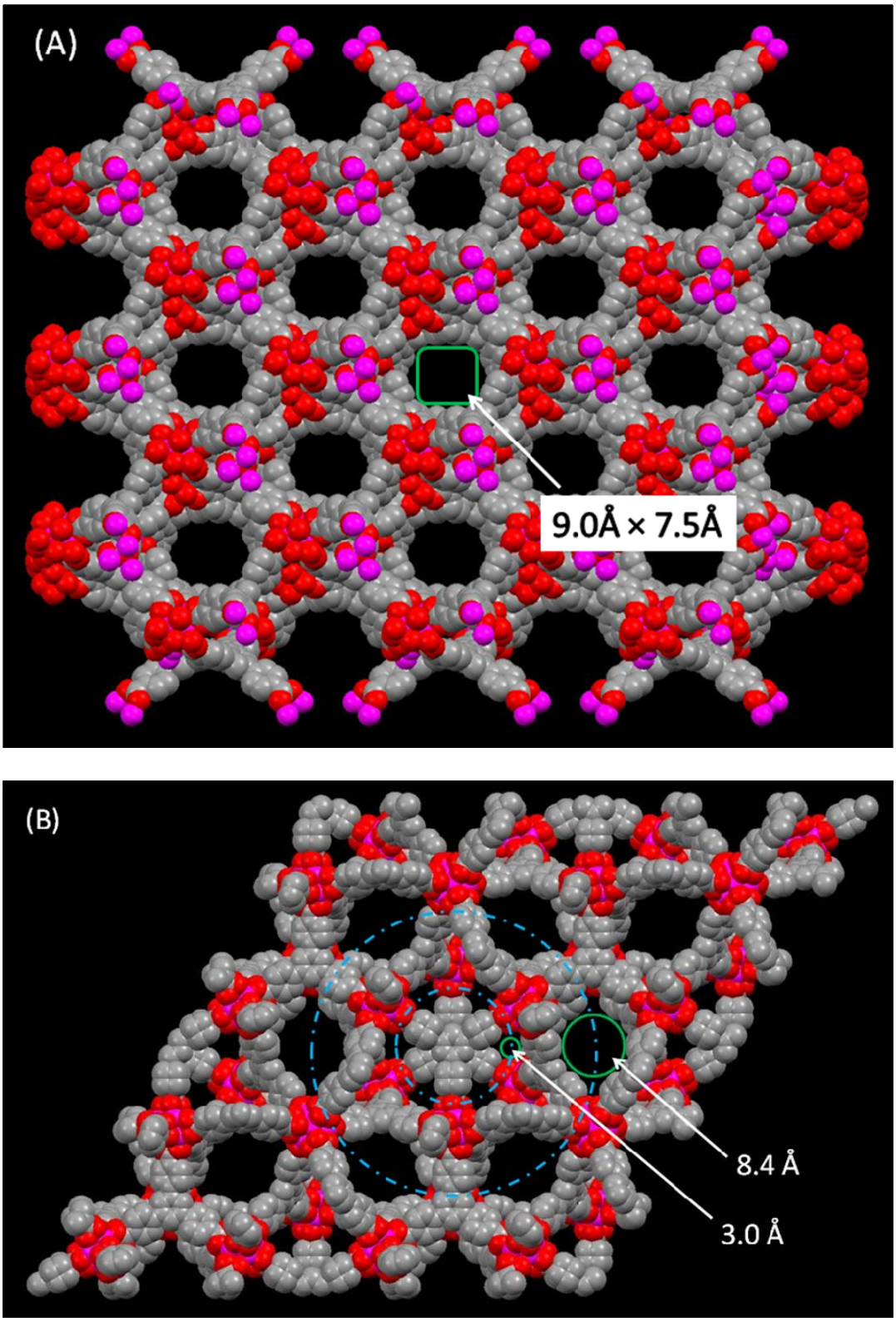

Figure 5.2 Comparison of pore structure between Zn-MOF (A) and MOF-177 (B)

5.1.3 Scanning electron microscope (SEM) characterization

The SEM images were conducted on a Hitachi SEM S-3500N equipped with a model S-6542 absorbed electron detector. SEM characterization of as-synthesized compound **3** presents bulk-shaped crystal particles.

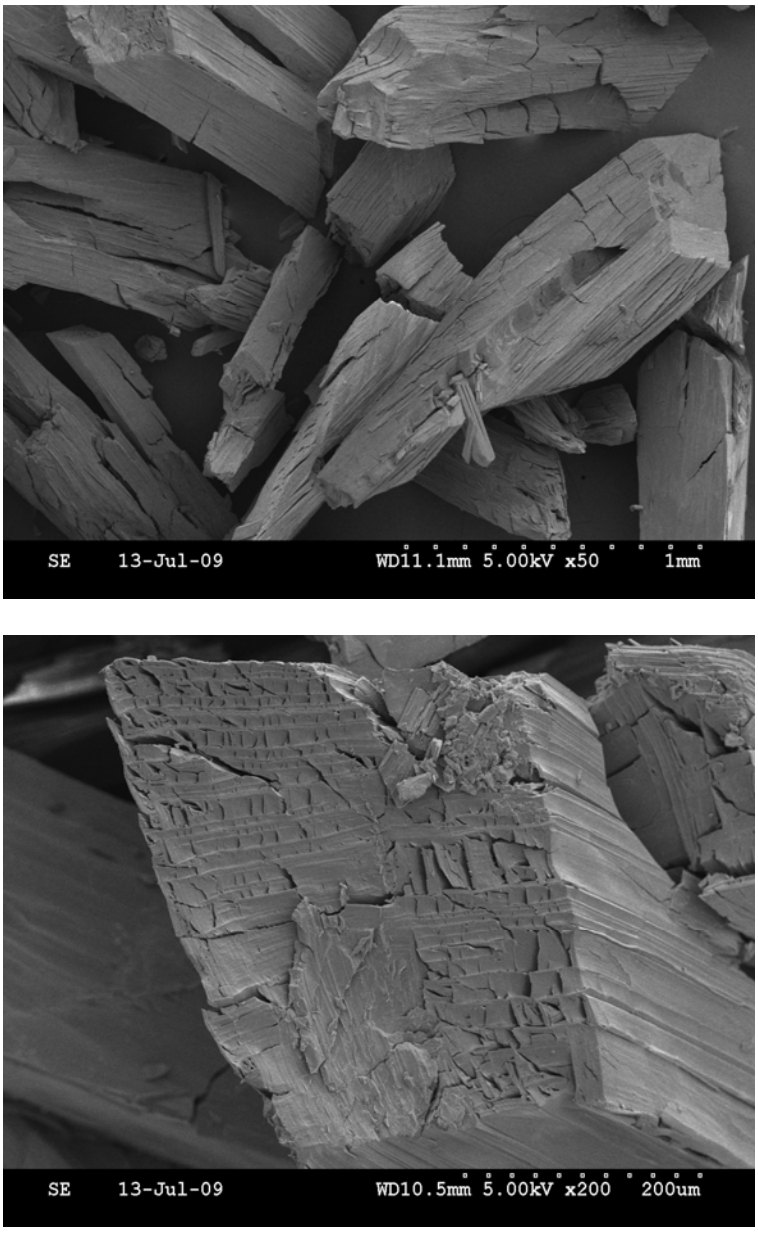

Figure 5.3 SEM of Zn-MOF (**3)** presenting the bulk-shaped crystal particles.

5.1.4 Powder X-Ray Diffraction Characterization

The powder-XRD pattern of samples were collected on a Bruker D8 powder diffraction system with Cu radiation (λ= 1.5406 Å).

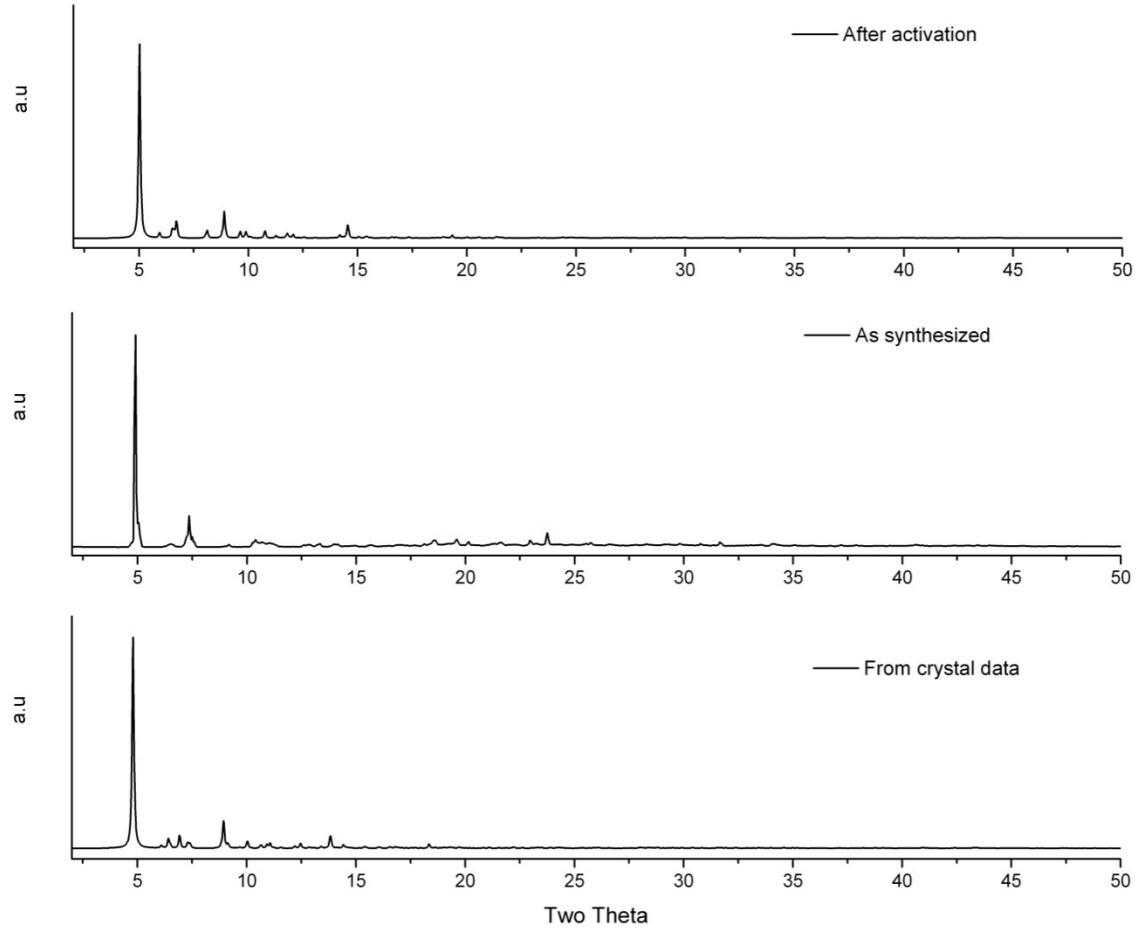

Figure 5.4 A comparison of experimental powder-XRD pattern of **3** after activations to remove guest molecules (top), as synthesized (middle) and theoretical pattern from the single crystal data (bottom).

5.1.5 Thermogravimetric Analyses (TGA)

Thermogravimetric analyses were carried out with a SHIMADZU TGA-50 at a heating rate of 5 ^{o}C/min under helium atmosphere with 25 mL/min flow rate. The thermal stability of Zn-MOF (**3**) is up to 420 ^{o}C.

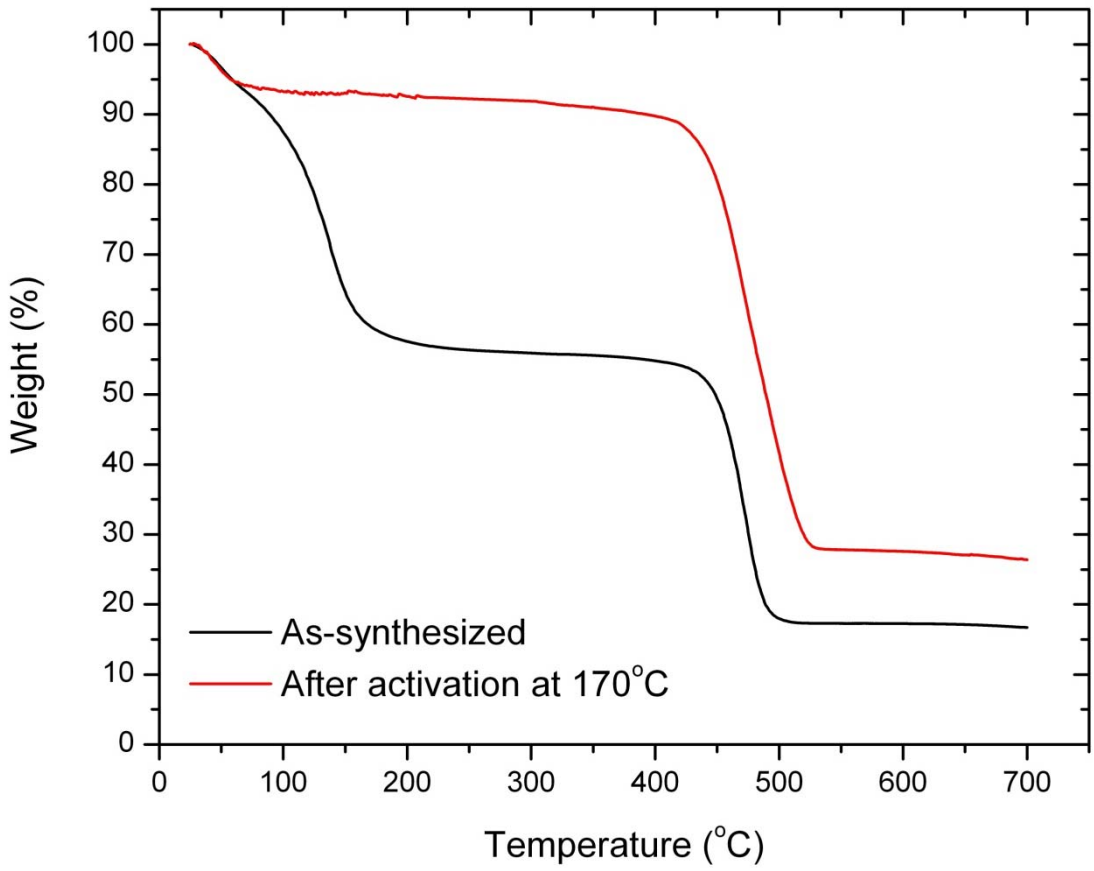

Figure 5.5 TGA trace of compound **3**.

5.1.6 Fourier Transform Infrared Spectroscopy Characterization (FTIR)

To remove the coordinated DMF molecules, Zn-MOF (**3**) was activated at 170 ^{o}C for 2 hrs under vacuum. TGA data indicate that all coordinated DEF molecules can be removed from **3** at 170 ^{o}C, and thermal stability of the crystal is up to 420 ^{o}C as shown in Figure 5.5. The comparison of FT-IR patterns (Figure 5.6) for as-synthesized compound **3** and activated sample confirms the successful removal of DMF molecules as well. The C=O bond in a DMF molecule has a reduced bond order compared to the carboxylic group due to the nitrogen atom. The stretching frequency of C=O in DMF is lower than that of an unsubstituted C=O bond, which is usually around 1710 cm^{-1} for saturated carboxylic acids. Thus, for as-synthesized compound **3**, the existence of a strong peak at 1650 cm^{-1} indicates C=O in DMF molecule. Furthermore, the disappearance of the peak at 1650 cm^{-1} in the FT-IR pattern of activated compound **3** confirms the removal of DMF molecules after activation. Such FT-IR pattern change can also be seen in the last MOF $[Cd_3(BTB)_2(DEF)_4]\cdot 2DEF$ (**2**)[7], $[Zn_9O_3(2,7\text{-ndc})_6(DMF)_3]$[11] and $[Mn(NDC)(DEF)]_n$.[12] After DMF molecules are successfully removed, the Zn centers have open coordination sites that are accessible to incoming sorbate molecules and can influence gas storage, adsorption separations, and catalysis.

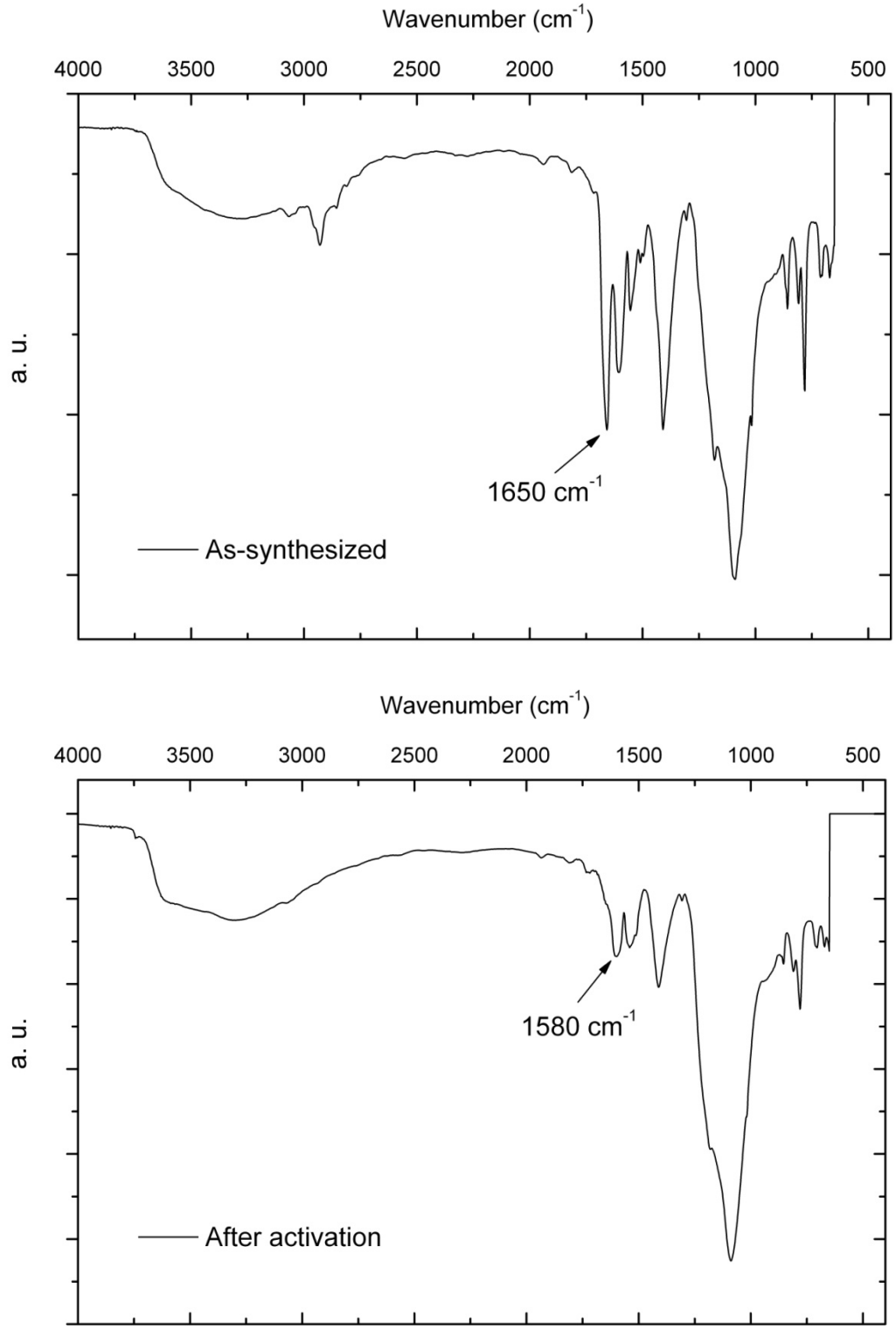

Figure 5.6 FT-IR pattern of compound **3** (top, as-synthesized; bottom, after activation).

5.1.7 Specific Surface Area and Porosity Characterization

Nitrogen adsorption isotherm of activated product at 77 K was measured with Autosorb-1 from Quantachrome Corporation to calculate the surface area. The adsorption isotherm for nitrogen at 77 K in activated Zn-MOF (**3)** is presented in Figure 5.7. The isotherm is similar to the type-I isotherm according to BDDT classification. As shown in the figure, the micropore is filled quickly at low pressure. The BET surface area is calculated as 2155 m^2/g, while total pore volume is 1.20 cm^3/g. The Langmuir surface area is calculated to be 3178 m^2/g (Figure 5.8).

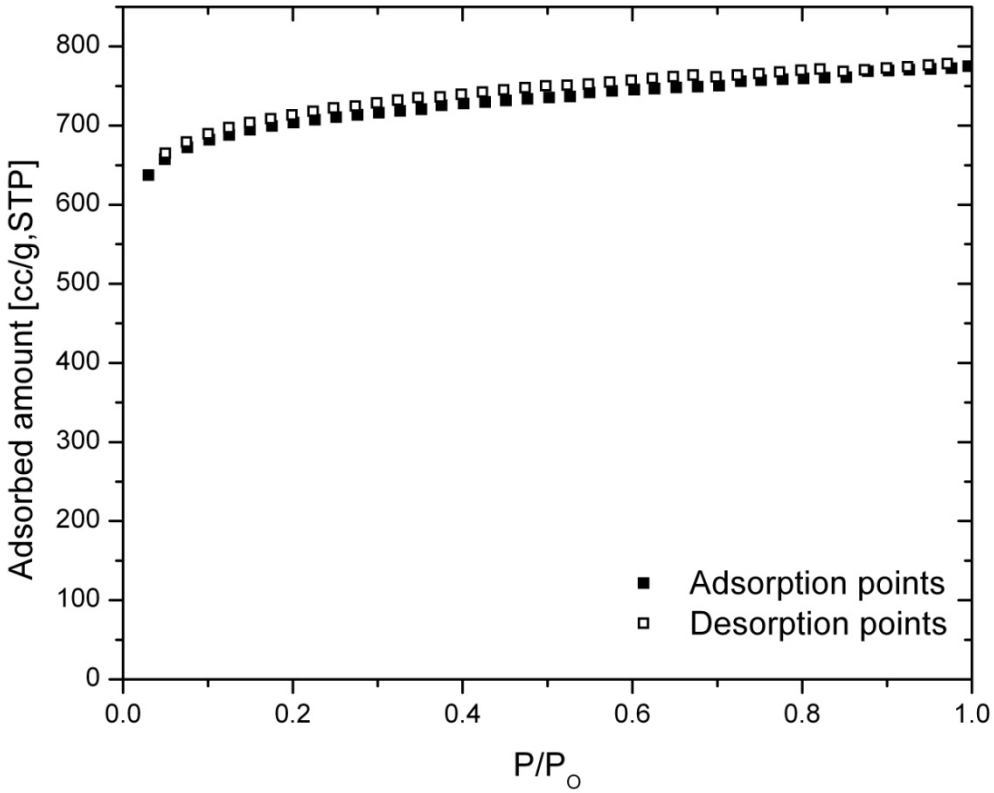

Figure 5.7 N_2 isotherm of activated compound **3** at 77 K.

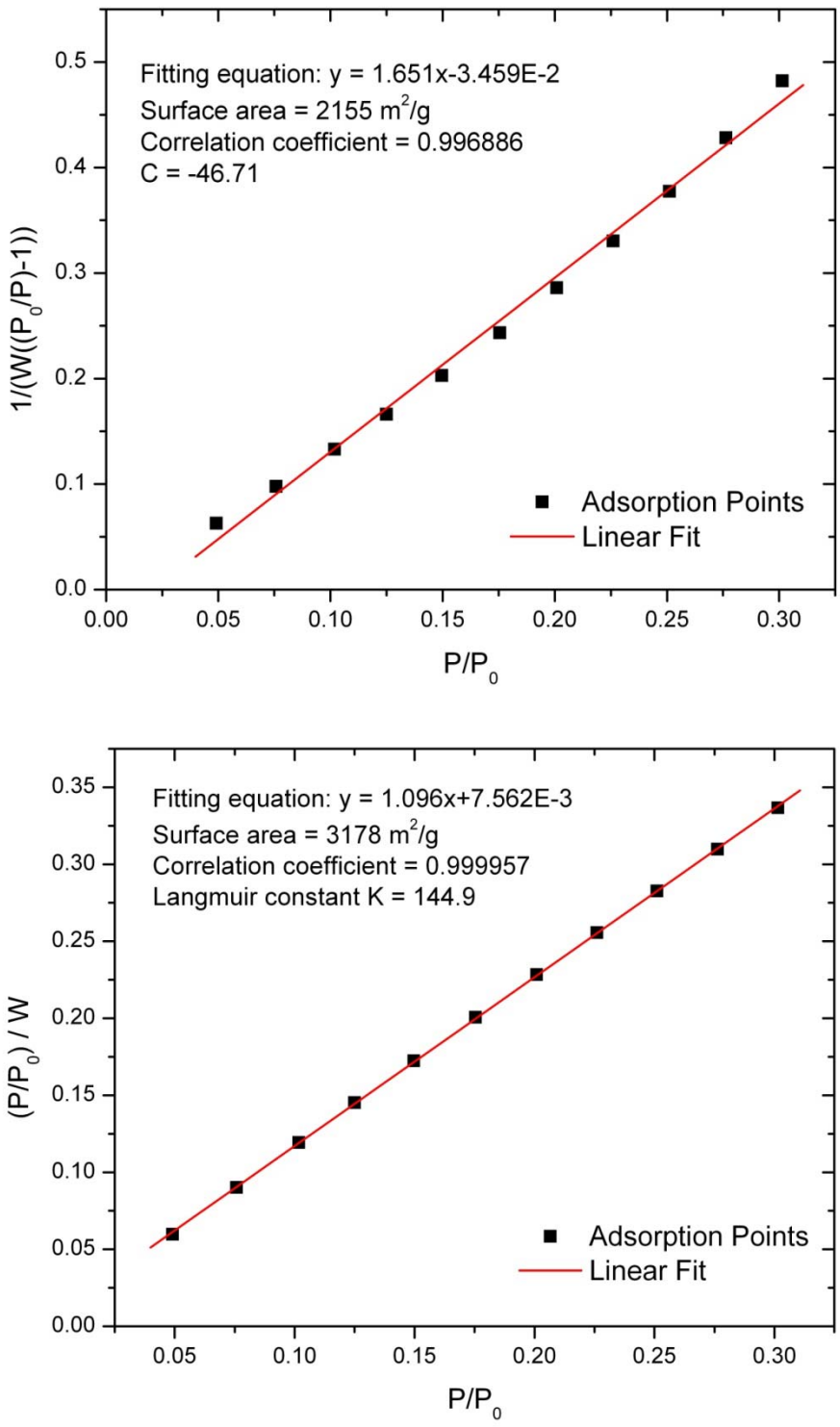

Figure 5.8 Specific surface area of activated compound **3** according to the BET method (top) and Langmuir method (bottom).

5.2 HIGH PRESSURE GAS ADSORPTION STUDY

A gravimetric adsorption apparatus (the GHP-100 gravimetric high pressure analyzer with C. I. microbalance from the VTI Corporation) was employed to measure the single-component adsorption isotherms. All adsorbate gases were purchased from the Linweld Company including carbon dioxide (LW617, bone dry 99.8 %), methane (LW913, ultra-high purity 99.99 %), and helium (LW800, UHP/ZERO). Before the adsorption measurement, the sample Zn-MOF (**3)** was activated by heating at 170 ^{o}C in vacuum for 2 h to remove associated guest molecules and coordinated solvent molecules. A 150 mg sample was placed in the sample cartridge of the GHP-100 gravimetric high pressure analyzer to undergo continued outgassing at 120 ^{o}C in a vacuum for 2 h. The sample weight was recorded every 2 minutes or per 0.01 % by mass. After outgassing, the system temperature was adjusted to the adsorption temperature of interest, and the sample cell was kept under vacuum for 30 min before starting the first adsorption point. All adsorption equilibrium data were collected after maintaining a given stable pressure for 30 min. After finishing the adsorption and desorption runs at the given temperature, the sample was regenerated by heating at 120 ^{o}C in a vacuum for 6 h until a constant sample weight was achieved. The sample was then reused in subsequent adsorption experiments.

5.2.1 Pure-Component Adsorption Models

Because of the simplicity of the Toth equation in form and its correct thermodynamic consistency at low and high pressures, it is often applied to fit the adsorption isotherms of hydrocarbons on activated carbon [13] and zeolites [14]. The Toth equation is given by [14]

$$N = \frac{N_S bP}{\left[1 + (bP)^m\right]^{1/m}} \quad 5.1$$

where N_s is the monolayer capacity, b is related to the adsorption affinity at low pressure, and m characterizes the system heterogeneity, The more the parameter m deviates from unity, the more heterogeneous is the system. When m = 1, the Toth equation reduces to the Langmuir equation.

For physical adsorption of gases and vapors on porous solids, the theory of volume filling of micropores (TVFM) contributed mainly by Dubinin and coworkers has been of long-standing importance for both data modeling and gaining physical insight [15]. Thus, Dubinin-Astakhov (D-A) equation was also chosen to fit the adsorption isotherms. The D-A equation can be expressed as [16]

$$W = W_0 \exp\left[-\left(\frac{A}{E}\right)^m\right] - W_g \quad 5.2$$

$$W_g = \rho_g V_p \quad 5.3$$

where W is the measured excess adsorption amount. W_0 is the modeled maximum amount adsorbed (cm^3/g), which does not necessarily agree with the physical maximum amount adsorbed. E is the characteristic energy of adsorption. W_g is a correction term to fit the D-A equation to experimental excess adsorption data, and ρ_g is the gas-phase density as a function of temperature and pressure calculated from solving the Peng-Robinson equation of state. V_p is the total pore volume of the adsorbent Zn-MOF, which is obtained from nitrogen adsorption as 1.20 cm^3/g. A is the adsorption potential, also called the differential molar work of adsorption, which represents the negative differential Gibbs free energy, and P_s is the virtual saturation vapor pressure of the adsorbate for supercritical isotherms. These parameters are defined as:

$$A = -\Delta G = RT \ln\left(\frac{P_s}{P}\right) \tag{5.4}$$

$$P_s = \left(\frac{T}{T_c}\right)^r P_c \tag{5.5}$$

where r is determined by fitting experimental data and is specific to the adsorbent-adsorbate pair. When $r = 2$, the expression of virtual saturation vapor pressure reduces to the Dubinin empirical equation. R and T are the universal gas constant and adsorption temperature, respectively, and T_c and P_c are the critical temperature and pressure of the adsorbate.

To fit the experimental excess adsorption data, the gravimetrically measured adsorption amounts are multiplied by the adsorbed phase specific volume V_a to obtain the adsorbed phase volume. V_a is estimated according to the method proposed by Ozawa et al. [17] to account for the thermal expansion of the liquid:

$$V_a = V_b(T_b) \cdot \exp[0.0025(T - T_b)] \tag{5.6}$$

where V_b is the specific volume of the adsorbate at the boiling point T_b.

5.2.2 Results and Discussion

Pure-component adsorption isotherms with Toth and D-A equation fits are shown in Figures 5.9 and 5.10. Under the examined temperatures, all isotherms presented no adsorption hysteresis. Thus, only adsorption data are shown in the figures. Zn-MOF demonstrated remarkable gravimetric capacity for CH_4 and CO_2. The adsorption capacity of methane in Zn-MOF at 298 K is 5.2 mmol/g at 25.8 bar and 6.3 mmol/g at 273 K and 25.8 bar. The adsorption capacity of carbon dioxide in Zn-MOF at 298 K is 10.3 mmol/g at 25.8 bar and increases to 12.0 mmol/g at 273 K and 25.6 bar.

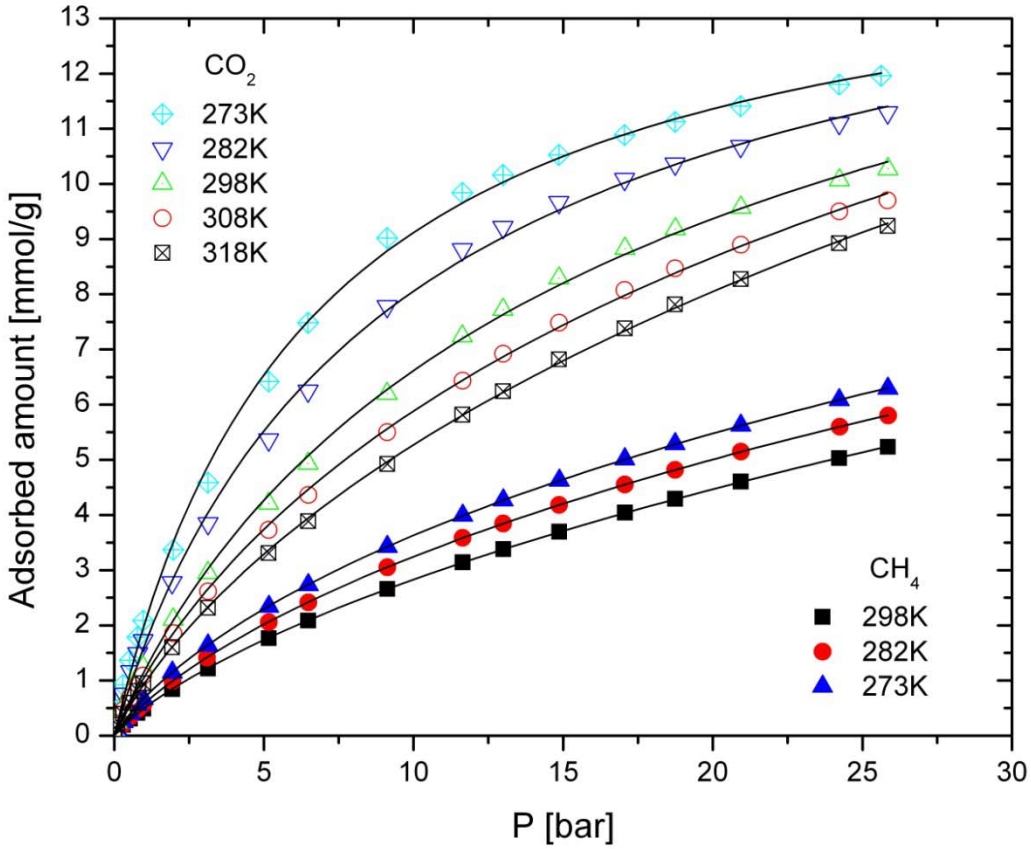

Figure 5.9 Toth equation fit of pure-component gas adsorption isotherms on Zn-MOF. Solid curves are Toth model predictions.

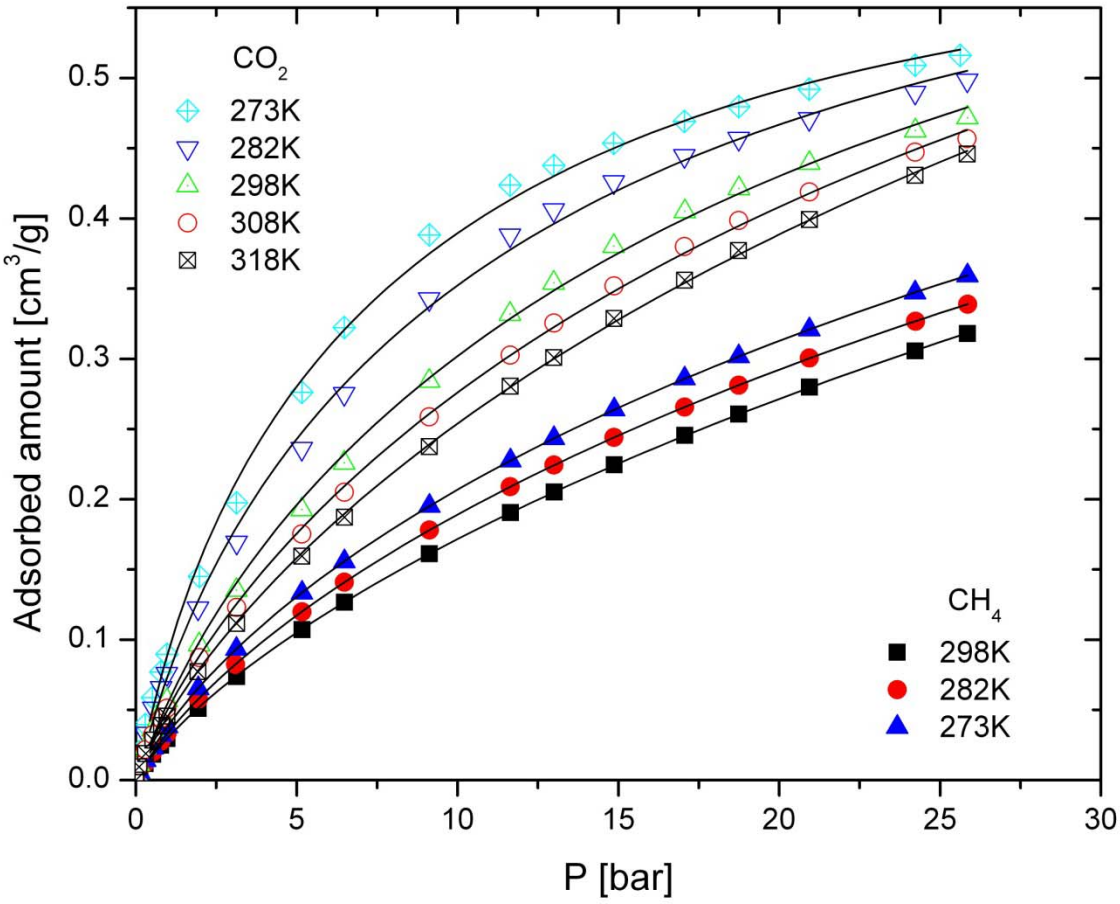

Figure 5.10 D-A equation fit of pure-component gas adsorption isotherms on Zn-MOF. Solid curves are D-A model predictions.

The Toth equation parameters are provided in Table 5.1. For CH_4, the Toth model provides good fitting consistency at the examined temperature and pressure. However, the monolayer capacity for CH_4 is overestimated and increases unrealistically with increasing temperature. For CO_2, the situation is more complex in that the model provides good fitting consistency at the supercritical temperature (higher than 304 K) but some inconsistency at subcritical temperature. Although the monolayer capacity for CO_2 is reasonable at 273 K, it also keeps increasing with increasing temperature, finally approaching two times larger than the value at 273 K. Thus, these model parameters demonstrate that a layering process is not good enough to explain the adsorption mechanism of supercritical fluids in microporous MOFs, even when the model fits the data very well.

Table 5.1 Toth model parameters for adsorption isotherms on Zn-MOF

	T (K)	N_s (mmol/g)	b	m	K_H
CH_4	273	40.315	0.0279	0.4109	1.125
	282	48.445	0.0193	0.3960	0.936
	298	109.563	0.0087	0.3142	0.952
CO_2	273	15.086	0.1538	0.9963	2.320
	282	16.288	0.1156	0.8950	1.883
	298	19.193	0.0702	0.7918	1.347
	308	29.518	0.0469	0.5811	1.384
	318	54.553	0.0257	0.4454	1.401

Table 5.2 D-A model parameters for adsorption isotherms on Zn-MOF

	T (K)	W_0 (cm^3/g)	En (J/mol)	m	r
CH_4	273	0.597	4877.01	1.34	2
	282	0.607	4815.48	1.34	2
	298	0.605	5057.10	1.32	2
CO_2	273	0.578	6938.19	1.94	1
	282	0.591	6561.04	1.76	1
	298	0.620	6045.05	1.57	1
	308	0.661	5704.93	1.42	2
	318	0.714	5380.71	1.31	2

In contrast to the Toth equation, the D-A equation based on Polanyi adsorption potential theory assumes that the mechanism for adsorption in micropores is that of pore-filling rather than layer-by-layer surface coverage. This theory is widely applied to describe adsorption on activated carbon and zeolites [18-19]. Recently, hydrogen adsorption data on MOFs were also studied using the D-A equation [20-22]. The D-A model parameters for CH_4 and CO_2 adsorption in Zn-MOF are shown in Table 5.2. For CH_4, the D-A model provides better fitting consistency than the Toth equation at the examined temperature and pressure and gives a consistent maximum capacity $W_0 \approx 0.60$ cm^3/g. For CO_2, the fitting results are better than that of the Toth equation, although some inconsistency still exists at the subcritical temperature range. All parameters present reasonable values. The characteristic curves for CH_4 and CO_2 are presented in Figures 5.11 and 5.12. It can be

seen that the adsorption potential decreases with the increasing uptake, which also means less molar work is required for adsorption by micropore-filling when the gas is approaching the bulk vapor pressure. The experimental data for various temperatures fall on the characteristic curve, which indicates that Dubinin's micropore-filling mechanism works well, especially for CH_4 on Zn-MOF.

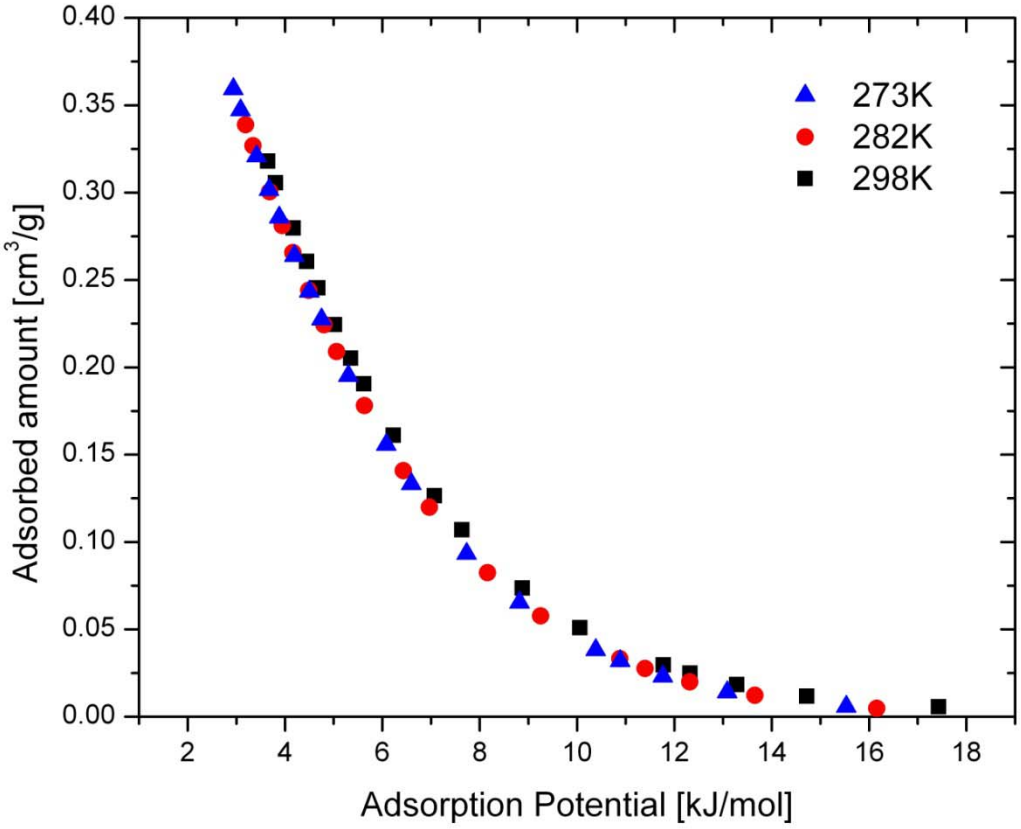

Figure 5.11 Characteristic curve for methane on Zn-MOF

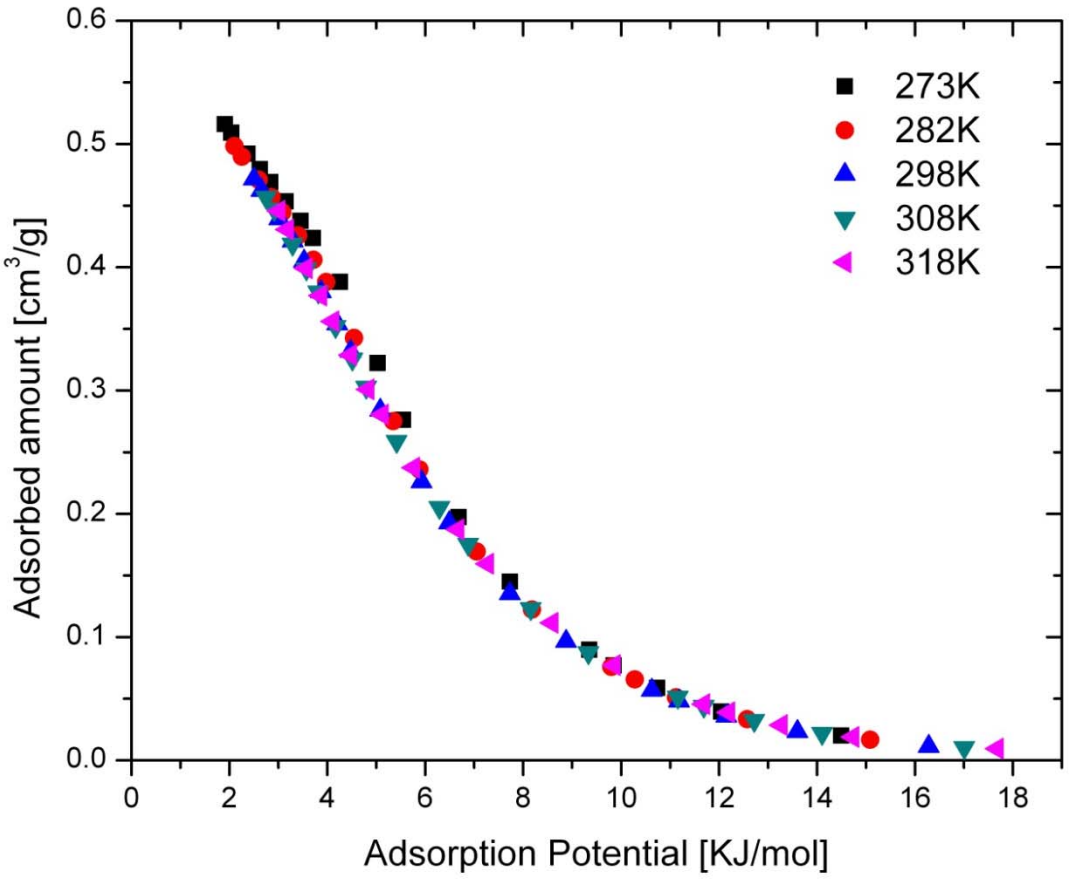

Figure 5.12 Characteristic curve for carbon dioxide on Zn-MOF

The adsorption loadings for Zn-MOF are compared with other MOFs at 1 bar and 25 bar in Table 5.3. At 1 bar, Zn-MOF adsorbs more methane than the other BTB MOFs (MOF-177, Cu-BTB, UMCM-1) due to its smaller channel size. The open metal site MOFs (Cu-BTC, MOF-505) have among the highest methane loadings at 1 bar due to enhanced van der Waals interactions with the copper sites. IRMOF-6 possesses no open metal sites but displays comparable uptake as a result of alkyl functional groups that decrease the pore size compared with IRMOFs -1 and -3 and provide preferred adsorption sites [23]. At higher pressure, high free volume of the framework and low

framework density play an important role for CH_4 storage which explains the high capacity of MOF-177 [24]. As for CO_2 adsorption, open copper sites have a strong influence on CO_2 molecules such that Cu-BTC and MOF-505 adsorb 3-4 times the amount of CO_2 at 1 bar compared to the other MOFs. However, Zn-MOF displays the highest uptake at 1 bar compared to all examined MOFs with no open metal sites. At higher pressure, the packing effect and electrostatic self-attraction of CO_2 molecules[25] are important and high free volume of the framework is desired.

Table 5.3 Gravimetric CH_4 and CO_2 capacity at 298 K on different MOF materials.

	CH_4 [mmol/g]		CO_2 [mmol/g]	
MOFs	1 bar	25 bar	1 bar	25 bar
IRMOF-1 [23,26]	0.57	7.85	1.0	20.5
IRMOF-3 [24]	0.37	6.95	1.2	18.0
IRMOF-6 [23,26]	0.97	8.10	1.0	18.3
CuBTC [26-27]	0.8	6.19	4.1	10.6
MOF2 [24]	0.05	3.02	0.57	2.98
MOF505 [24]	0.92	5.87	3.27	9.78
MOF-177 [24]	0.07	8.31	0.8	31.0
CuBTB [4]	0.29	4.0	1.16	6.60
UMCM-1[28]	0.37	8.10	1.0	23.6
Zn-MOF	0.50	5.15	1.25	10.17

The isosteric heat of adsorption Q_{st} is independent of adsorbate loading for homogeneous adsorbents but can be strong and complex functions of loading for heterogeneous adsorbents. Q_{st} can be calculated from adsorption isotherms using the Clausius-Clapeyron equation:

$$Q_{st} = -R\left[\frac{\partial \ln (P)}{\partial (\frac{1}{T})}\right]_{n^a} \qquad 5.7$$

The isosteric heat of adsorption of CH_4 and CO_2 on Zn-MOF was calculated from the original experimental data using Eq. 5.7. The isosteric heats of adsorption of CH_4 and CO_2 on Zn-MOF are 6.7 kJ/mol and 9.2 kJ/mol, respectively, at a loading of 0.01mmol/g. These values are similar to the isosteric heats for these gases in UMCM-1.[17]

5.3 CONCLUSIONS

A three-dimensional porous MOF material obtained in our lab demonstrates high surface area and remarkable adsorption capacity for CH_4 and CO_2. Seven isotherms were obtained in this study. The data are described by the Toth equation and Dubinin-Astakhov equation, which represent two adsorption mechanisms, layering process and micropore filling. The results indicate that the pore-filling theory can better explain the adsorption behavior on this microporous MOF material. Isosteric heats of adsorption at low coverage are relatively low for both molecules. The comparison of adsorption loadings demonstrates that MOFs with open metals sites and pore size comparable with that of gas molecules provide better affinity at lower pressure, while the capacity at higher pressure is dependent on the free volume of the framework.

5.4 REFERENCES

(1) Yang, R. T. *Adsorbents : fundamentals and applications*; Wiley-Interscience: Hoboken, N.J., 2003.

(2) Ma, S. Q.; Zhou, H. C. *Chem Commun* **2010**, *46*, 44.

(3) Aakeroy, C. B.; Champness, N. R.; Janiak, C. *Crystengcomm* **2010**, *12*, 22.

(4) Mu, B.; Li, F.; Walton, K. S. *Chem Commun* **2009**, 2493.

(5) Kitagawa, S.; Kitaura, R.; Noro, S. *Angew Chem Int Edit* **2004**, *43*, 2334.

(6) Maji, T. K.; Kitagawa, S. *Pure Appl Chem* **2007**, *79*, 2155.

(7) Mu, B.; Huang, Y. G.; Walton, K. S. *Crystengcomm* **2010**, *12*, 2347.

(8) Soldatov, D. V.; Enright, G. D.; Ripmeester, J. A. *Cryst Growth Des* **2004**, *4*, 1185.

(9) Caskey, S. R.; Wong-Foy, A. G.; Matzger, A. J. *Inorg Chem* **2008**, *47*, 7751.

(10) Chae, H. K.; Siberio-Perez, D. Y.; Kim, J.; Go, Y.; Eddaoudi, M.; Matzger, A. J.; O'Keeffe, M.; Yaghi, O. M. *Nature* **2004**, *427*, 523.

(11) Park, M.; Moon, D.; Yoon, J. W.; Chang, J. S.; Lah, M. S. *Chem Commun* **2009**, 2026.

(12) Moon, H. R.; Kobayashi, N.; Suh, M. P. *Inorg Chem* **2006**, *45*, 8672.

(13) Himeno, S.; Komatsu, T.; Fujita, S. *J Chem Eng Data* **2005**, *50*, 369.

(14) Walton, K. S.; Abney, M. B.; LeVan, M. D. *Micropor Mesopor Mat* **2006**, *91*, 78.

(15) Jaroniec, M. *Adsorption* **1997**, *3*, 187.

(16) Hutson, N. D.; Yang, R. T. *Adsorption* **1997**, *3*, 189.

(17) Ozawa, S.; Kusumi, S.; Ogino, Y. *J Colloid Interf Sci* **1976**, *56*, 83.

(18) Gil, A. *Adsorption* **1998**, *4*, 197.

(19) Richard, M. A.; Benard, P.; Chahine, R. *Adsorption* **2009**, *15*, 43.

(20) Poirier, E.; Chahine, R.; Benard, P.; Lafi, L.; Dorval-Douville, G.; Chandonia, P. A. *Langmuir* **2006**, *22*, 8784.

(21) Poirier, E.; Dailly, A. *J Phys Chem C* **2008**, *112*, 13047.

(22) Poirier, E.; Dailly, A. *Nanotechnology* **2009**, *20*.

(23) Duren, T.; Sarkisov, L.; Yaghi, O. M.; Snurr, R. Q. *Langmuir* **2004**, *20*, 2683.

(24) Millward, A. R. *PhD Thesis* **2006**.

(25) Walton, K. S.; Millward, A. R.; Dubbeldam, D.; Frost, H.; Low, J. J.; Yaghi, O. M.; Snurr, R. Q. *J Am Chem Soc* **2008**, *130*, 406.

(26) Millward, A. R.; Yaghi, O. M. *J Am Chem Soc* **2005**, *127*, 17998.

(27) Wang, Q. M.; Shen, D. M.; Bulow, M.; Lau, M. L.; Deng, S. G.; Fitch, F. R.; Lemcoff, N. O.; Semanscin, J. *Micropor Mesopor Mat* **2002**, *55*, 217.

(28) Mu, B.; Schoenecker, P. M.; Walton, K. S. *J Phys Chem C* **2010**, *114*, 6464.

CHAPTER 6

GAS ADSORPTION STUDY ON A MESOPOROUS MOF UMCM-1

Porous metal-organic frameworks (MOFs) have become the focus of intense study over the past decade due to their potential for advancing a variety of applications including gas storage, adsorption separation, catalysis, and gas sensing. These materials have some distinct advantages over traditional porous materials such as their well-defined structures, uniform pore sizes, chemically functionalized sorption sites, and potential for post-synthetic modification. Adsorption studies in MOFs have increased substantially in recent years, but full structure-property relations have yet to be developed. Information on host-guest interactions at low pressure, the effect of uncoordinated metal sites, pore structure and volume, chemical functionality, and surface area is crucial to elevate MOFs to an applied level in the adsorption field.

Methane and hydrogen have been the most extensively studied gases for adsorption in MOFs, and gas storage for alternative fuel vehicles continues to be an important driver for this research area. Yaghi et al.[1] demonstrated a series of MOF materials with remarkable methane storage capacity, among which IRMOF-6 is impressive with an uptake of 240 cm^3/g at 298 K and 36 atm. Düren et al.[2] used molecular modeling to analyze the roles played by the surface area, free volume, heats of adsorption, and pore size distribution for methane storage in porous materials. Their simulation results confirmed that high surface area, high free volume, low adsorbent density, uniform pore size distribution, and strong interaction energy between adsorbate and adsorbent will facilitate high methane storage capacity. Wang et al.[3] used grand

canonical Monte Carlo (GCMC) simulations to examine a series of ten MOFs and reached similar conclusions.

MOFs have also been studied for hydrogen storage, and several reviews on current progress are available.[4-13] Frost et al.[14] studied the influences of surface area, free volume, and heat of adsorption on hydrogen adsorption in a series of MOFs. Their GCMC simulation results indicated that the predominant factors affecting hydrogen uptake depend on heat of adsorption at low pressure, surface area at intermediate pressure, and free volume at high pressure. It has also been shown that structural properties such as unsaturated metal centers can be incorporated into materials to increase the magnitude of hydrogen interaction with the framework.[11,15]

In addition to gas storage, the capture of carbon dioxide has become one of the most urgent research topics in fields related to energy and the environment. The removal of CO_2 from raw products to purify biogas is the most expensive step in biofuel upgrading.[16-17] The removal of CO_2 from natural gas is also an important process to help prevent pipeline corrosion. The concentration of CO_2 in natural gas should be as low as 2%.[16] Yaghi and coworkers reported the adsorption capacity of CO_2 on a series of ten MOF materials at room temperature, among which MOF-177 had the highest capacity of 34 mmol/g at 40 bar.[18] Zhong et al.[19] and Jiang et al.[20] studied CO_2 storage capacity on different MOF materials using grand canonical Monte Carlo (GCMC) simulations and found that IRMOF-16 has the highest capacity of 64 mmol/g at 50 bar. Walton et al.[21] studied the inflections in CO_2 adsorption isotherms on MOFs with no open metal sites and found that attractive electrostatic interactions between CO_2 molecules are responsible for the unusual shape of the adsorption isotherms.

Oxygen or nitrogen generation from air is an important industrial process. The applied technologies include three major types: cryogenic distillation, which has the longest application history, especially for large volumes of high-purity gas; air separation at ambient temperatures using polymeric membranes or porous zeolites; and high-temperature air separation using specialized ceramic ion transport membranes (ITM).[22] For many applications that require a smaller volume of oxygen or nitrogen daily (i.e. < 1 ton) and do not need very high purity (i.e. < 99%), ambient-temperature pressure-swing adsorption (PSA) separation of air has proven more economical than other technologies.[23] Since the adsorbent units are often the key part of the capital cost of adsorption separation technology, research on improved adsorbent materials has high value. With the large variety of MOFs that are available, one can expect these novel porous materials to be capable of increasing selectivity, improving energy efficiency, and reducing the costs of the system. However, reports on N_2 and O_2 adsorption in MOF materials are relatively rare,[24-28] especially at ambient temperature.

A variety of MOFs with very high surface areas, large pore diameters, and giant pore volumes have been synthesized in recent years including MOF-177,[28] MIL-100 and MIL-101,[29-30] and UMCM-1.[31] Among these, UMCM-1 reported by Matzger and coworkers[31] in 2008 has many advantages including easily-obtained reactants, simple synthesis routes, and high yields. The high surface area (4100 m^2/g) and giant pore volume (2.141 cm^3/g) of UMCM-1 should lead to excellent adsorption properties, particularly at high pressures. To date, however, there have been no reports on the adsorption characteristics of UMCM-1. Here we report adsorption isotherms for CH_4, H_2, CO_2, O_2, and N_2 in UMCM-1 at various temperatures. The Dubinin-Astakhov

equation adsorption model was applied to fit the experimental adsorption isotherms and to obtain thermodynamic properties including adsorption potential and isosteric heats of adsorption.

6.1 SYNTHESIS AND CHARACTERIZATION

6.1.1 Materials and Synthesis Method

Solvothermal reactions were carried out in digestion bomb reactors. All chemicals are purchased from commercial companies and used as received without further purification: zinc nitrate hexahydrate, $Zn(NO_3)_2 \cdot 4H_2O$ (EMD Chemicals); 1,3,5-tris(4-carboxyphenyl)benzene, H_3BTB (Sigma-Aldrich, ≥98%); N,N-diethylformamide, DEF (Acros Organics, 99%); N,N-dimethylformamide, DMF (Acros Organics, 99.8+%); dichloromethane, CH_2Cl_2 (Acros Organics, 99.5%). A mixture of $Zn(NO_3)_2 \cdot 4H_2O$ (0.85g, 3.25mmol), H_2BDC (0.135g, 0.813mmol), H_3BTB (0.32g, 0.73mmol), and DEF (30mL) was placed into a Teflon-lined 45 mL reactor. The mixture was heated for 3 days at 358 K. After cooling to room temperature, needle-shaped colorless crystals were obtained, and then washed with DMF three times. The crystals were then immersed in 50 mL CH_2Cl_2. During the following one week, CH_2Cl_2 was replaced once per day. The crystals were then filtered and dried in air. The yield is approximately 80% based on H_3BTB. The solvent-exchanged crystals were placed in a vacuum oven for 1 hr at 573 K to obtain the activated porous material UMCM-1.

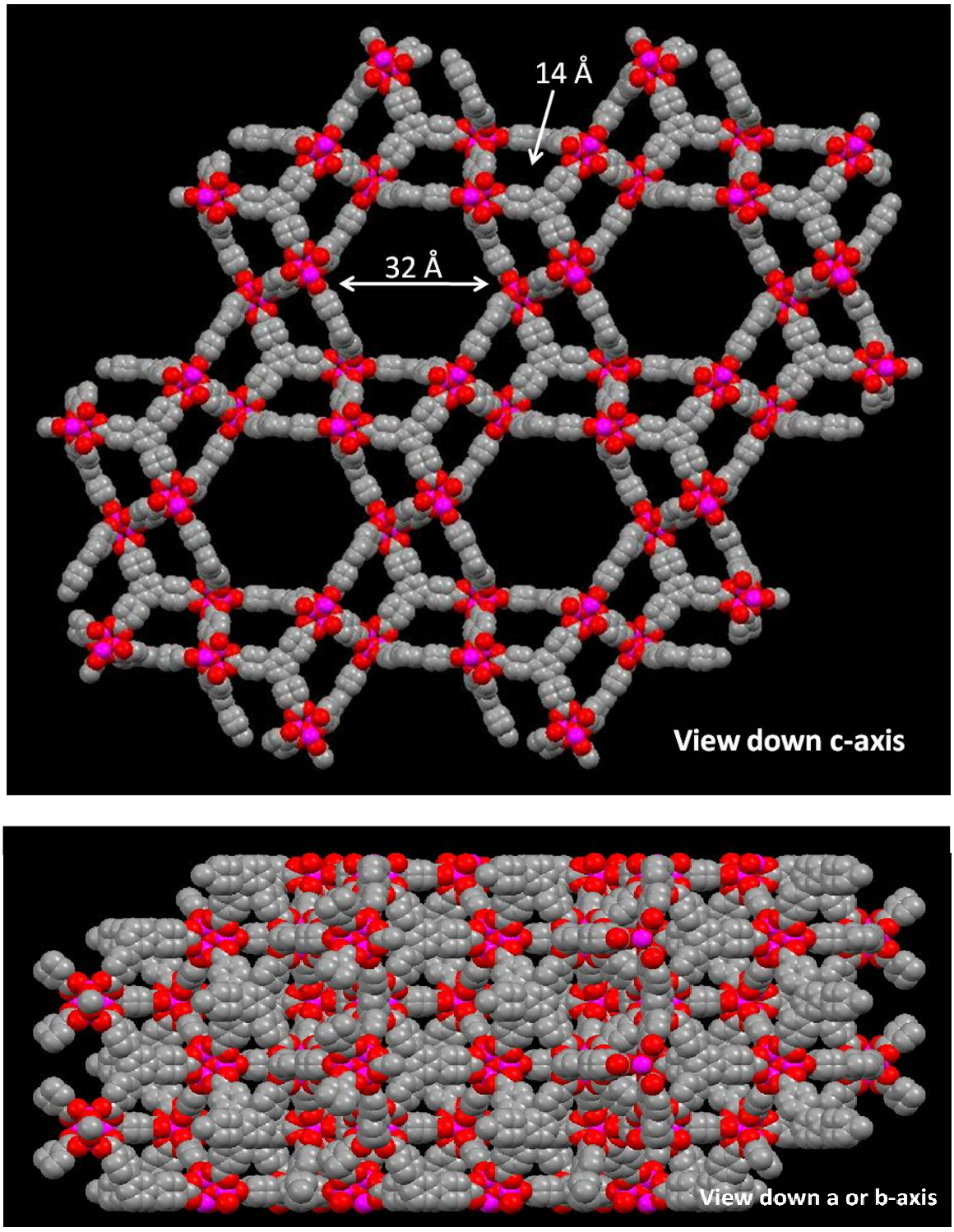

Figure 6.1 Crystal Structure of Mesoporous UMCM-1.

6.1.2 Scanning electron microscope (SEM) characterization

The SEM images were conducted on a Hitachi SEM S-3500N equipped with a model S-6542 absorbed electron detector. It was reported previously that UMCM-1 possesses needle-shaped crystals. As shown in Figure 6.2, UMCM-1 samples retained their needle shape after activation and presented a stable surface structure.

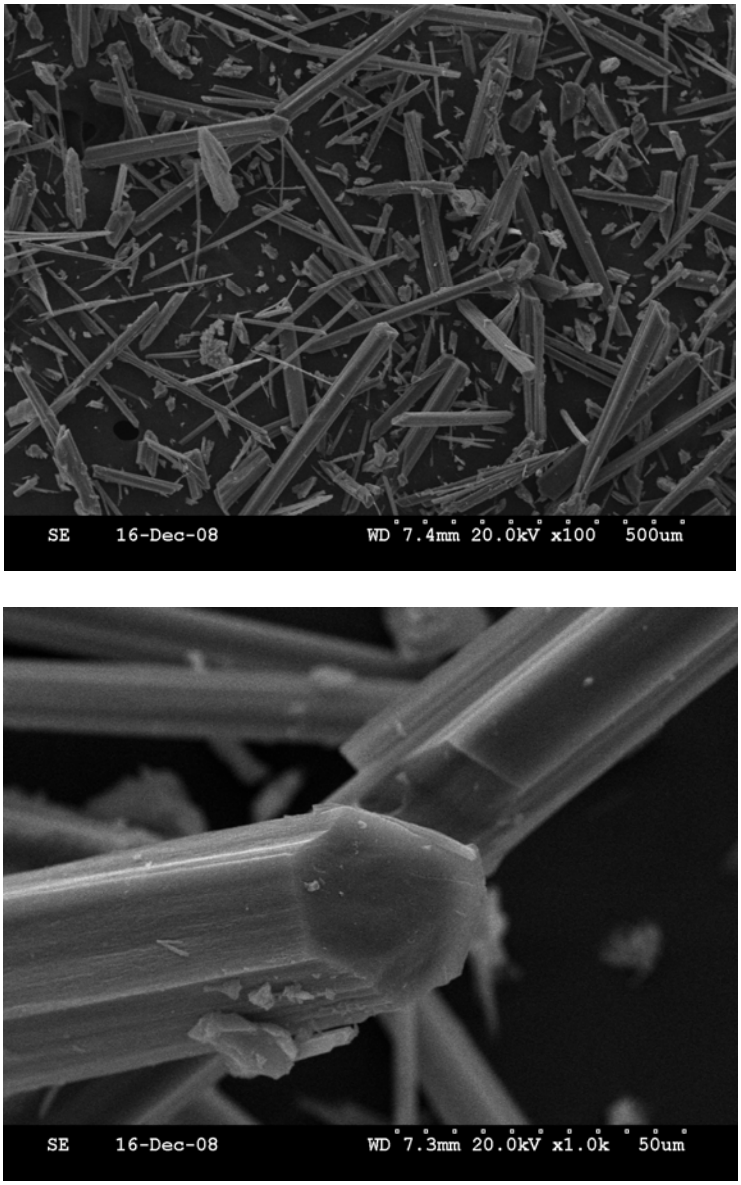

Figure 6.2 SEM of UMCM-1 presenting the needle-shaped crystal particles.

6.1.3 Powder X-Ray Diffraction Characterization

The powder-XRD patterns were collected on a Bruker D8 powder diffraction system with Cu radiation (λ= 1.5406 Å). From those experimental patterns, the phase purity of as-synthesized and after-activation samples can be confirmed by comparison with the simulated pattern.

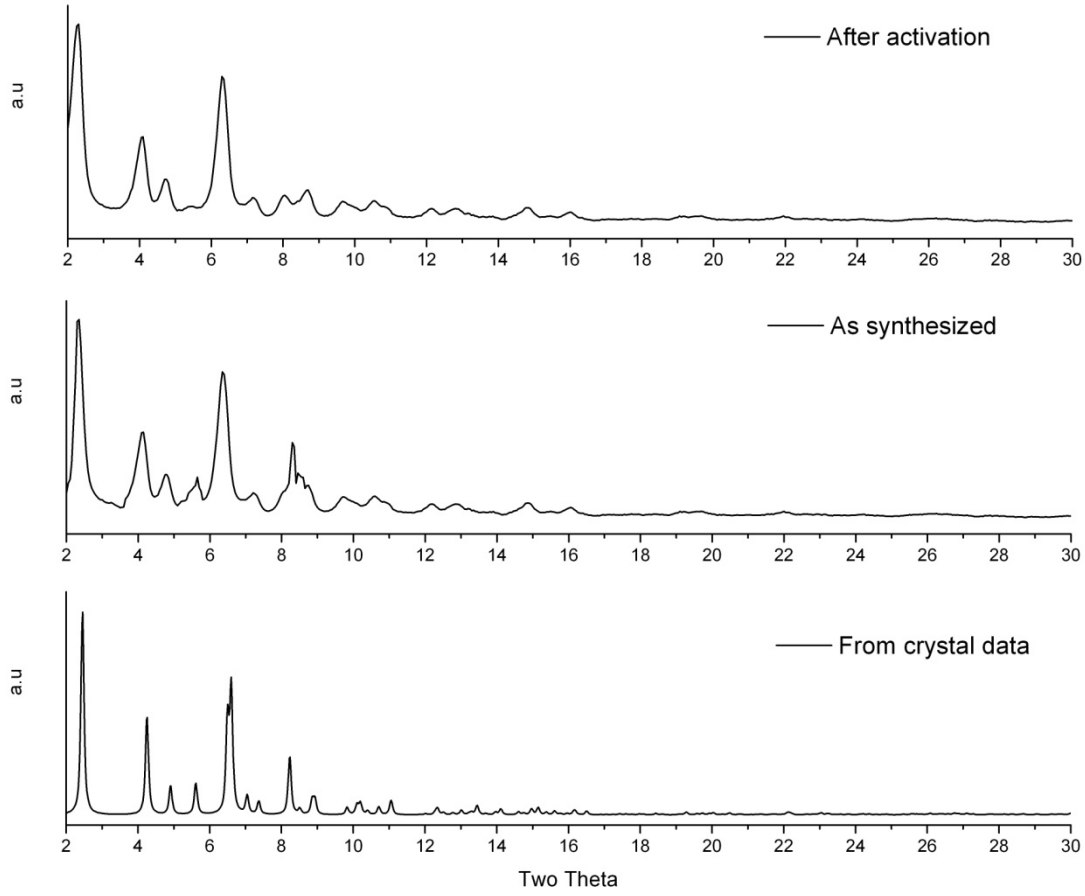

Figure 6.3 Comparison of experimental powder-XRD pattern of UMCM-1 after activations to remove guest molecules (top), as synthesized (middle) and theoretical pattern from the single crystal data (bottom).

6.1.4 Fourier Transform Infrared Spectroscopy Characterization (FTIR)

Infrared (IR) spectra of activated UMCM-1 were recorded with PerkinElmer Spectrum One as KBr pellets in the range 400 – 4000 cm^{-1}. According to the discussion in Chapter 5 about the FTIR pattern, the absence of a peak at 1650 cm^{-1} in the FTIR pattern of this activated UMCM-1 confirms the removal of DEF molecules after activation.

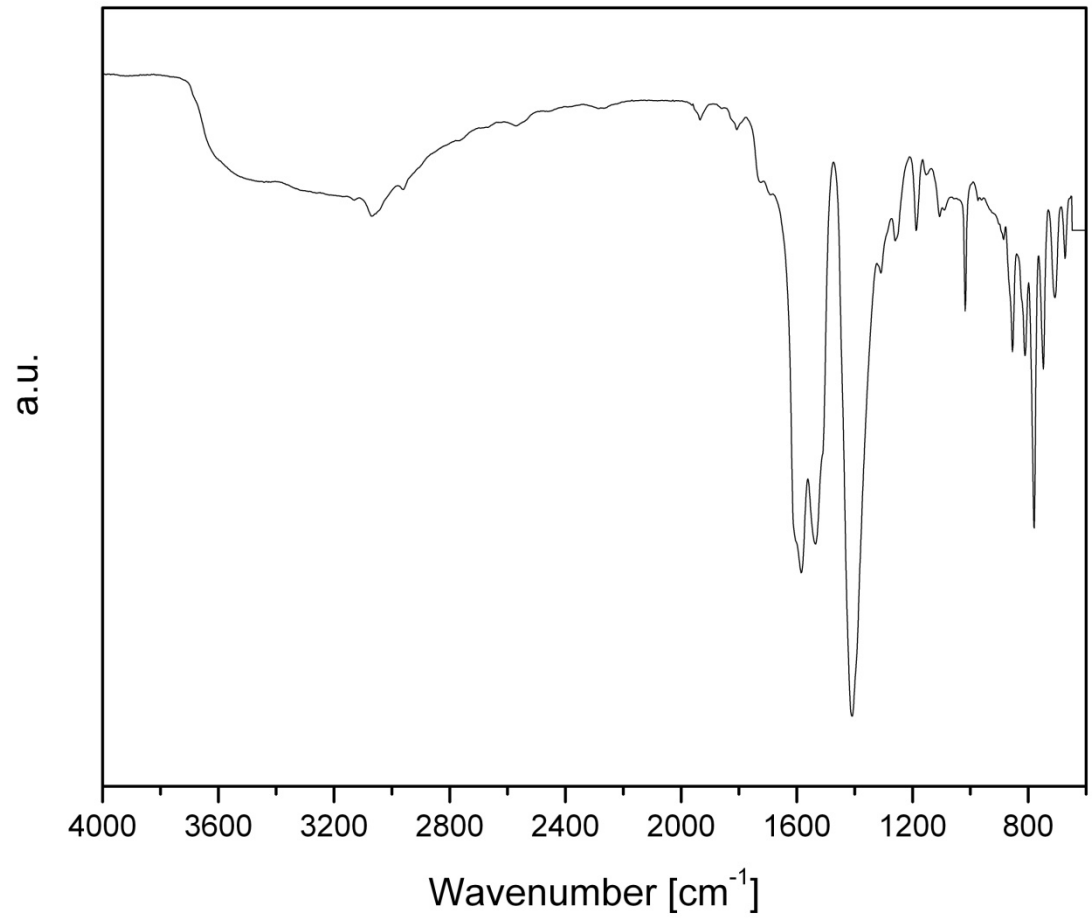

Figure 6.4 Infrared spectra of UMCM-1 (after activation)

6.1.5 Specific Surface Area and Porosity Characterization

Nitrogen adsorption on the activated product at 77 K was measured with Autosorb-1 from Quantachrome Corporation to calculate the surface area and total pore volume. A total of 79 points, including adsorption and desorption, were obtained for a relative pressure range of 0.025 to 1.00 (Figure 6.5). The BET and Langmuir surface areas were calculated to be 4100 m^2/g and 6500 m^2/g respectively, which are very close to the reported values. The total pore volume was calculated to be 2.141 cm^3/g using nitrogen as the probe molecule.

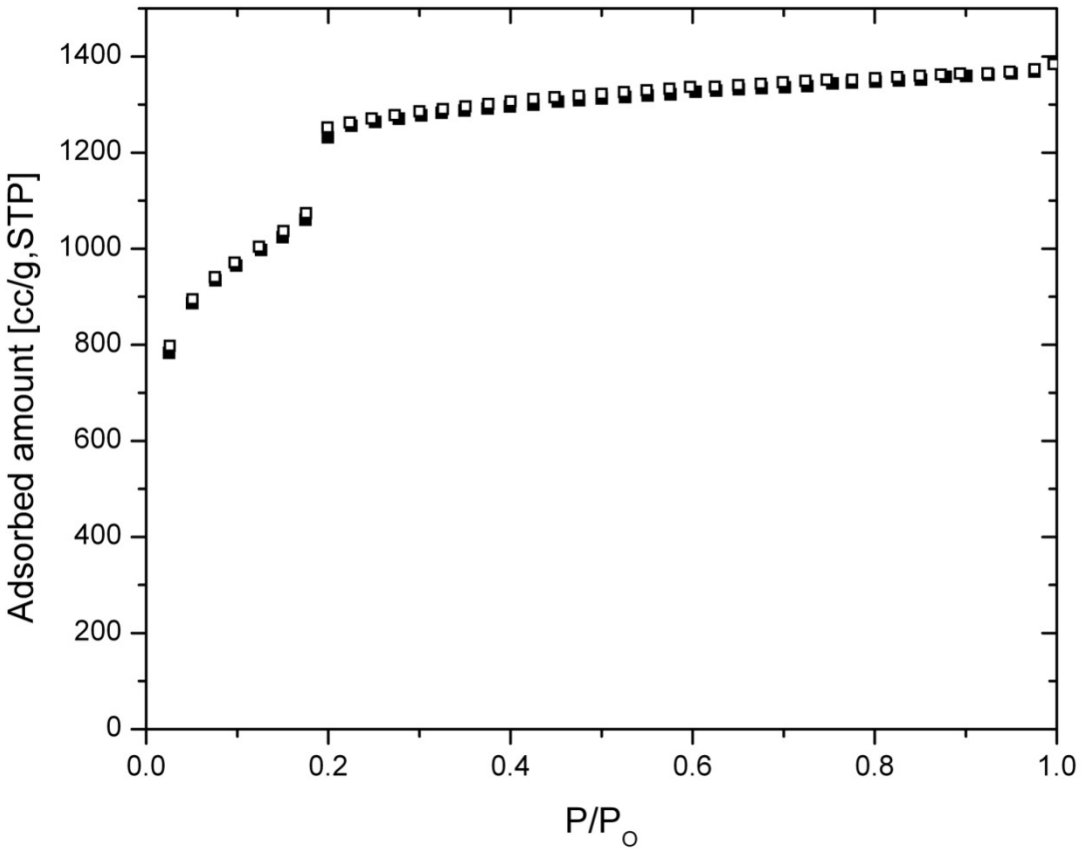

Figure 6.5 N_2 isotherm of activated UMCM-1 at 77 K.

6.2 HIGH PRESSURE GAS ADSORPTION STUDY

A high-pressure gravimetric adsorption apparatus was used to measure single-component adsorption isotherms. Before adsorption measurement, 150 mg of activated UMCM-1 were placed in the sample cartridge of the adsorption apparatus and outgassed at 393 K under vacuum for 2 hr. The sample weight was recorded every 2 minutes or 0.01 wt% change. After outgassing, the system temperature was adjusted to the desired adsorption temperature, and the sample cell was kept under vacuum for 30 min before the first adsorption measurement was taken. Adsorption equilibrium data were collected after maintaining a stable pressure and weight for 30 minutes at each point along the isotherm. All isotherms are reversible. After finishing the adsorption and desorption runs at the given temperature, UMCM-1 was regenerated by heating at 393 K in vacuum for 2 hr until the sample weight was no longer changing. The porosity of UMCM-1 is sensitive to the regeneration conditions. After various trials, we found that regeneration at temperatures higher than 393 K and at times longer than 2 hrs will cause a decrease in porosity. If applying proper regeneration conditions, all isotherms are reversible, and the sample can be reused.

UMCM-1 has two different pore diameters, 1.4 and 3.2 nm, and possesses no unsaturated metal centers (Figure 6.1). Because of this, it is expected that relatively small gas molecules will interact weakly with the pore walls at low pressure, leading to low loadings and linear isotherms in this region. However, UMCM-1 should have very high saturation capacities for these same molecules due to the large total pore volume of approximately 2.14 cm^3/g. Adsorption isotherms were measured for methane, hydrogen, carbon dioxide, nitrogen, and oxygen at three different temperatures. For all gases, the

isotherms are almost linear over the pressure range tested (up to 25 bar). This behavior is indicative of mesoporous materials with non-specific adsorption sites.

6.2.1 Methane and Hydrogen Adsorption

UMCM-1 demonstrated remarkable gravimetric capacity for methane storage. Figure 6.6 shows adsorption and desorption curves of methane on UMCM-1 at three different temperatures using gravimetric and volumetric based units. Under the examined temperatures, all isotherms presented no adsorption hysteresis, which means all methane stored in UMCM-1 is deliverable by simply reducing the pressure of gas. The adsorption capacity of methane in UMCM-1 at 298 K is 8.0 mmol/g or 180 cm^3 (STP)/g at 24.2 bar, which is among the highest reported methane adsorption capacities under the same conditions. However, because of the lighter density (0.39 g/cm^3 crystallographically) of UMCM-1, its volumetric uptake of 70 cm^3(STP)/cm^3 is still far from the storage target (180 v/v) set by DOE.[2]

The 2010 energy density targets for hydrogen storage systems are 6.0 wt% and 45 kg H_2/m^3, while the goals for 2015 are 9.0 wt% and 81 kg H_2/ m^3.[32] Hydrogen adsorption in UMCM-1 at room temperature and pressure up to 26 bar is shown in Figure 6.7. The maximum storage capacity of hydrogen in UMCM-1 at 298 K and 26 bar is 3.4 mmol/g (0.68 wt%). This result further confirms that large pore volume alone is not enough to effectively store H_2 at room temperature.

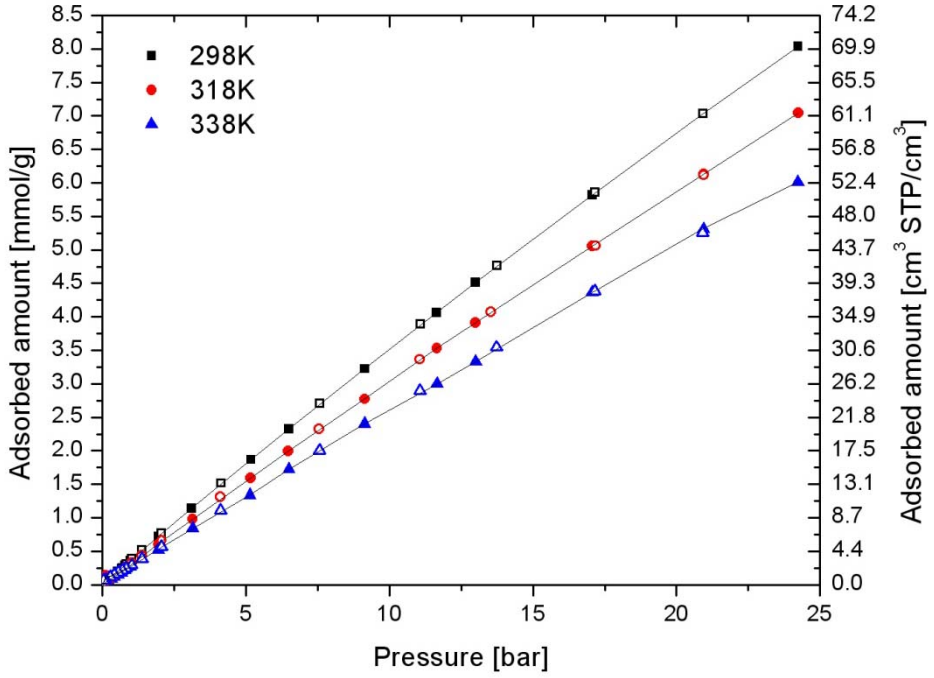

Figure 6.6 CH_4 isotherms for UMCM-1 at 298, 318, and 338 K. (line&solid symbols, adsorption; open symbols, desorption).

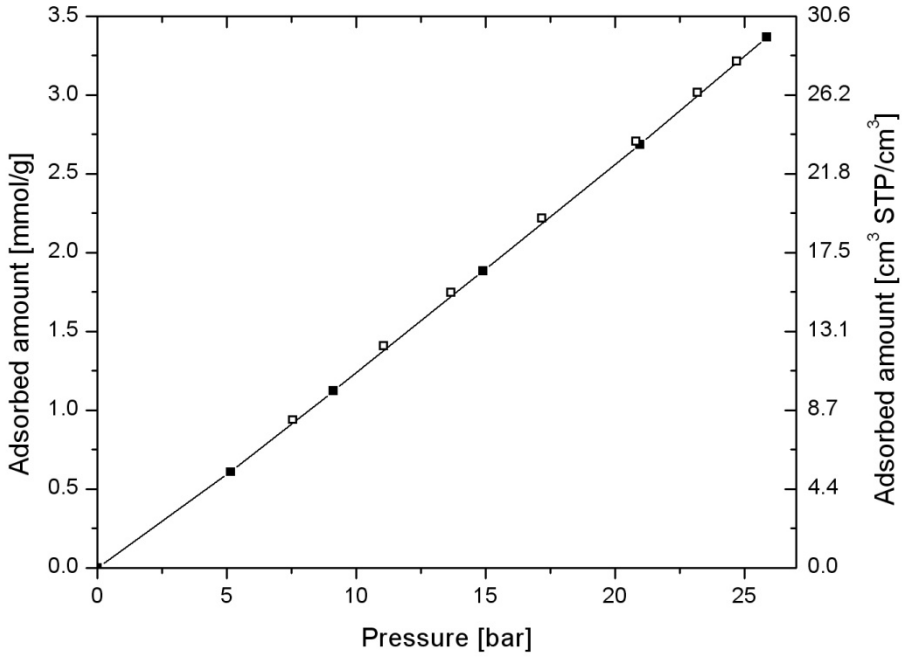

Figure 6.7 H_2 storage capacity of UMCM-1 at 298 K. (line&solid symbols, adsorption; open symbols, desorption)

6.2.2 CO_2 Adsorption

CO_2 isotherms at three different temperatures are shown in Figure 6.8 with loadings expressed in both gravimetric and volumetric units. The maximum gravimetric uptake capacities at 24 bar are 23.5, 18.7, and 14.0 mmol/g, corresponding to 298 K, 318 K, and 338 K. All three isotherms are linear at low pressure (< 5 bar). At 298 K, the CO_2 isotherm presents a slight inflection around 10-15 bar. With an increase in the adsorption temperature, this curved shape becomes obscure and totally disappears at higher temperature. The isotherm at 338 K is almost entirely linear over the pressure range studied. These isotherm shapes are consistent with those reported for CO_2 adsorption in IRMOF-1. It could likewise be expected here that a sharpening of the isotherm inflection would occur at temperatures lower than 298 K.

The CO_2 capacity of UMCM-1 is compared with the capacity of various sorbents at 298 K and five different pressures in Figure 6.9. Data are included for mesoporous silicas (MCM-41, SBA-15), mesoporous carbons (FMCK-3, CMK-3), Maxsorb activated carbon, and mesoporous MOF-177, in order of increasing pore volume. Physical properties of the selected materials are listed in Table 6.1. At lower pressure (<10 bar), Maxsorb activated carbon exhibits the greatest uptake of CO_2 due to the pore size distribution. With an increase of pressure, UMCM-1 and MOF-177 demonstrated the greatest capacities due to their higher surface area and pore volume. However, MOF-177 finally exceeds UMCM-1 at 15-25 bar. UMCM-1 has a larger pore volume than MOF-177 and should have greater adsorption capacities for CO_2 at saturation, but this will occur at pressures much higher than those examined here. The other mesoporous materials demonstrated poor CO_2 capacity due to lower surface area and large pore size.

In general, the trends show that for mesoporous materials, pore volume controls loadings at high pressure, and pore size controls uptake at pressures less than 5 bar.

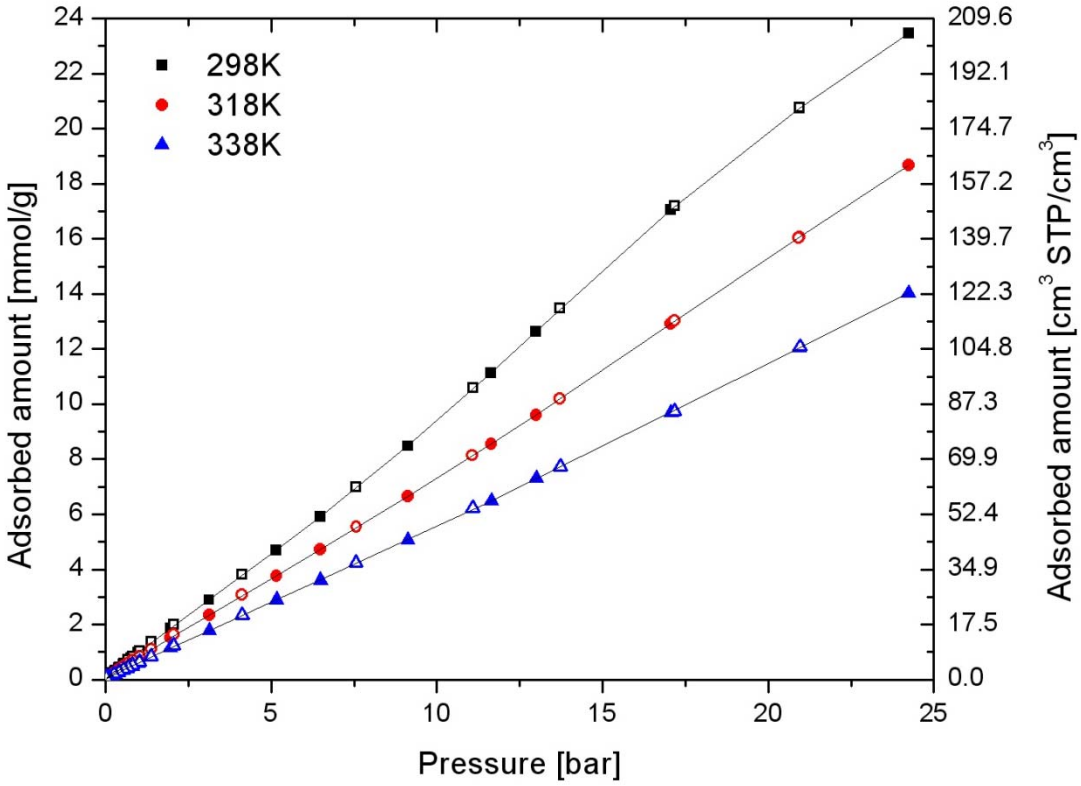

Figure 6.8 CH_4 isotherms for UMCM-1 at 298, 318, and 338 K. (line&solid symbols, adsorption; open symbols, desorption).

Table 6.1 Physical characteristics of the selected CO_2 adsorbents

Materials	Pore volume (cc/g)	S_{BET} (m^2/g)	Pore diameter (nm)
MCM-41[33]	0.99	1490	3.32
SBA-15[34]	1	700	6.1
FCMK-3[34]	1.3	1258	5.3
CMK-3[34]	1.3	1491	3.8
Maxsorb AC[35]	1.79	3250	2.0 (mean)
MOF-177[36]	1.75	4508	1.1-1.7
UMCM-1	2.14	4100	1.4-3.2

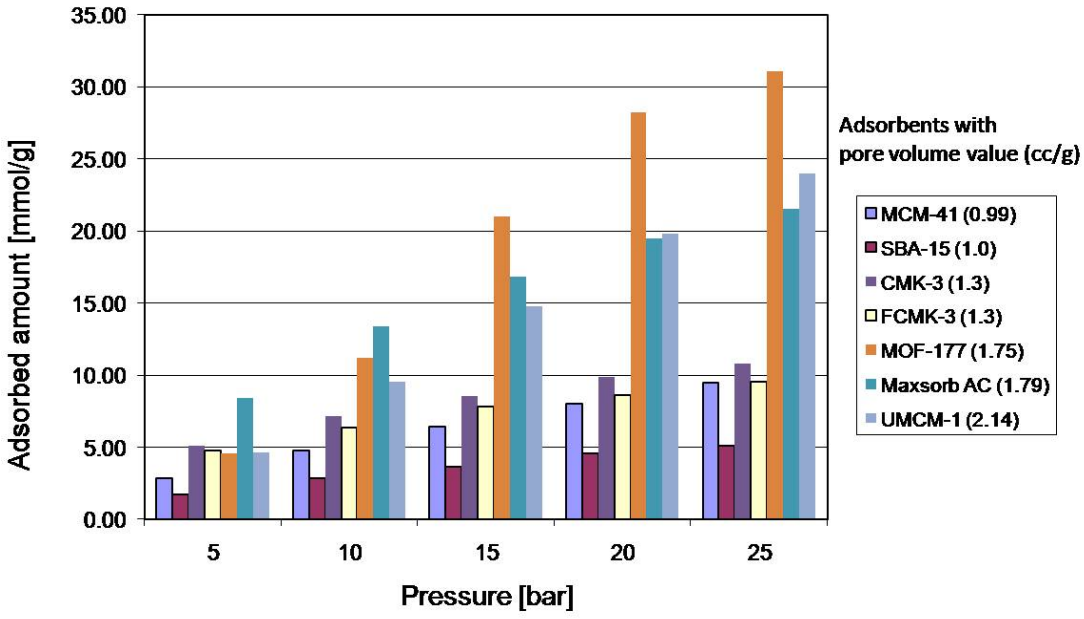

Figure 6.9 Gravimetric CO_2 capacity on different porous materials.

6.2.3 O_2 and N_2 Adsorption

Single-component isotherms for O_2 and N_2 on UMCM-1 at three different temperatures are shown in Figure 6.10 and Figure 6.11. Isotherms for both gases present no adsorption hysteresis. A comparison of O_2 and N_2 adsorption equilibrium isotherms at 298 K is shown in Figure 6.12. O_2 is shown to be adsorbed slightly more favorably than N_2 on UMCM-1, which is the same experimental result observed for MOF-177.[28] This preference was attributed to the higher magnetic susceptibility of O_2 over N_2. The same reasoning can be applied to UMCM-1, which possesses the same coordination environment as MOF-177.

The preference for O_2 over N_2 is an interesting result compared to the adsorption behavior observed for zeolites and carbons.[23,37-38] Zeolites have the ability to adsorb N_2 more strongly than O_2 because of the stronger interaction between the quadrupole moment of N_2 and the cation that is attached to the zeolite framework.[37] Figure 6.13 compares N_2 selectivity over O_2 for several materials. Zeolite LiX has the highest N_2/O_2 selectivity, which decreases with increasing pressure. CMS has slight preference to adsorb more N_2 than O_2 at the examined pressure from the equilibrium capacity.[38] However, due to the different kinetic diameters of nitrogen (3.64 Å) and oxygen (3.46 Å) molecules, oxygen diffuses more rapidly in the CMS than nitrogen which is the fundamental for kinetic separation of N_2 and O_2 on CMS.[23] UMCM-1 and MOF-177[28] demonstrated the reverse equilibrium capacity. At approximately 0.96 bar, the equilibrium capacities for O_2 and N_2 on UMCM-1 at 298 K are 0.23 and 0.14 mmol/g, respectively, and the pure-component O_2/N_2 selectivity is 1.64. At about 24.2 bar, the equilibrium capacities for O_2 and N_2 on UMCM-1 at 298 K are 4.47 and 4.05 mmol/g

respectively, and the pure-component selectivity decreases to 1.1. In contrast, MOF Cu-BTC exhibits adsorption preference similar to zeolites.[24] The reason for this difference from UMCM-1 and MOF-177 is most likely due to the existence of unsaturated copper centers, which play a similar role in the adsorption mechanism as the cations in zeolites.

It is not surprising to see low selectivity between O_2 and N_2 in UMCM-1 considering the large mesopore diameters (3.2 nm), which are much larger than the kinetic diameters of O_2 and N_2. A material with smaller pores will be much more effective in adsorbing N_2 or O_2. However, these results coupled with previous work suggest that O_2/N_2 selectivities in MOFs can be reversed based on the presence or absence of open metal sites. This information could prove very useful in designing new materials for air separation.

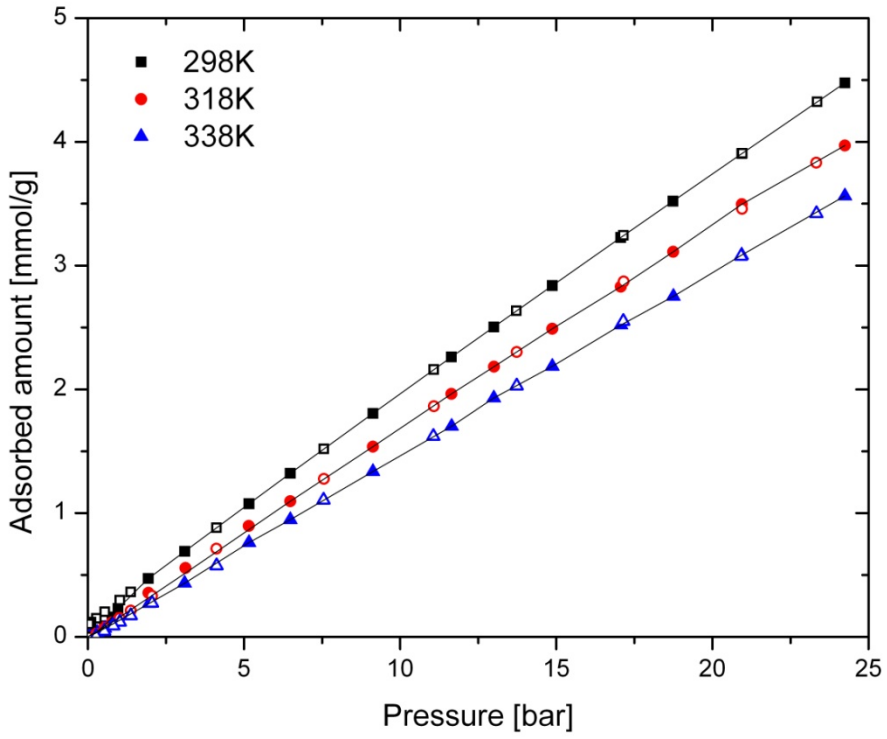

Figure 6.10 O_2 isotherms for UMCM-1 at 298, 318, and 338 K. (line&solid symbols, adsorption; open symbols, desorption)

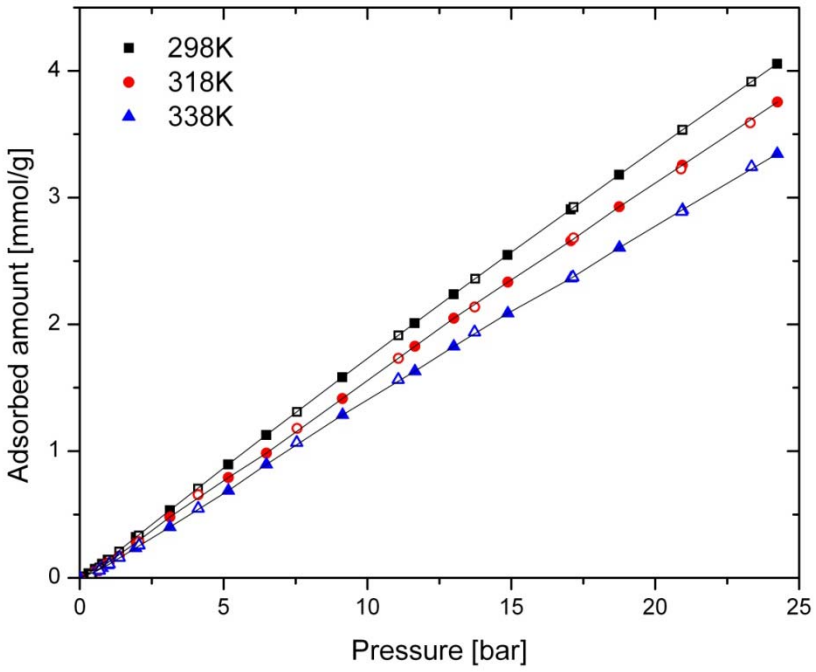

Figure 6.11 N_2 isotherms for UMCM-1 at 298, 318, and 338 K. (line&solid symbols, adsorption; open symbols, desorption)

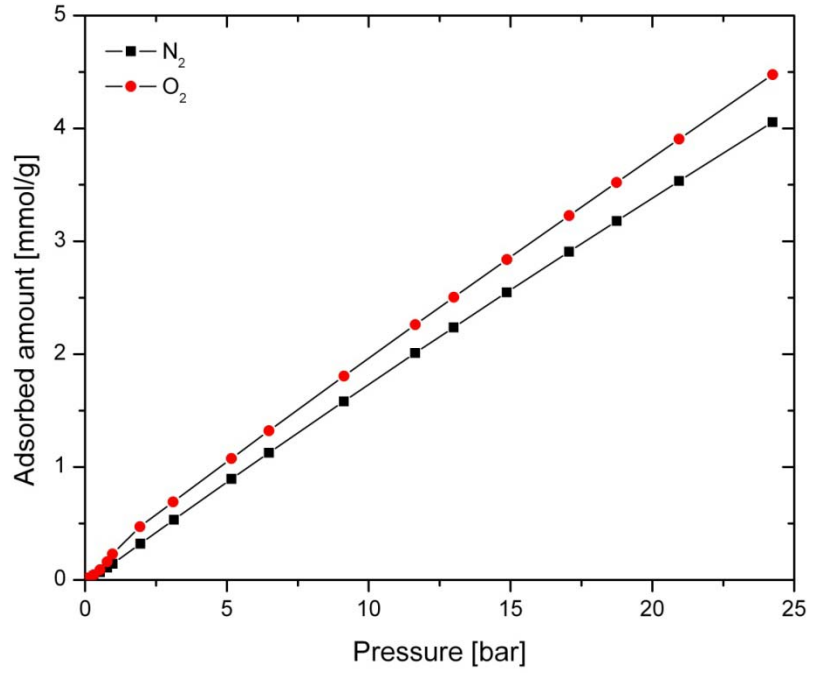

Figure 6.12 N_2 and O_2 adsorption isotherms on UMCM-1 at 298 K and pressures up to 25 bar

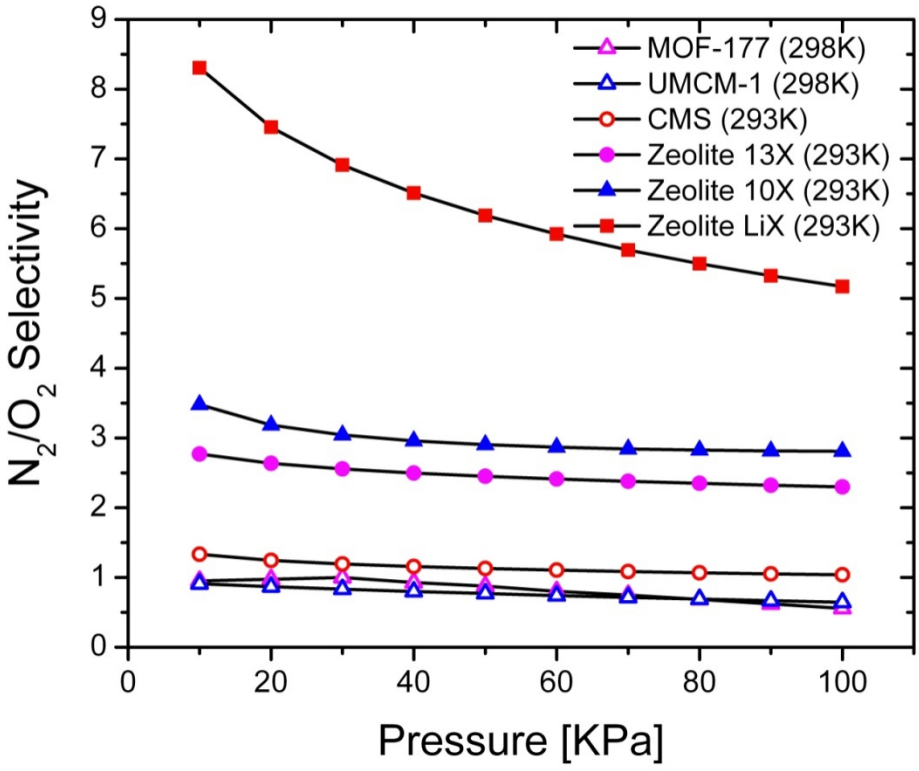

Figure 6.13 N_2/O_2 selectivity comparison on the selected adsorbents at room temperature and pressure up to 1 bar

6.2.4 Dubinin-Astakhov Model Analysis

The Dubinin-Astakhov (D-A) equation was chosen to fit the multi-temperature adsorption isotherms and is expressed as:[39-40]

$$W = W_0 \exp\left[-\left(\frac{A}{E}\right)^m\right] \qquad 6.1$$

where W is the measured volumetric adsorption amount. W_0 is the calculated limiting pore volume for a certain adsorbate, which does not necessarily agree with the actual total pore volume, m is the structural heterogeneity parameter, and E is the characteristic energy of adsorption. A is the adsorption potential given by

$$A = -\Delta G = RT \ln\left(\frac{P_s}{P}\right) \tag{6.2}$$

$$P_s = \left(\frac{T}{T_c}\right)^r P_c \tag{6.3}$$

where P_s is the virtual saturation vapour pressure of the adsorbate for supercritical isotherms. The parameter *r* is determined by fitting experimental data, which is specific to the adsorbent-adsorbate pair. When $r = 2$, the expression of virtual saturation vapour pressure is reduced to Dubinin empirical equation. *R* and *T* are the universal gas constant and adsorption temperature respectively. T_c and P_c are critical temperature and pressure of the adsorbate.

To fit the experimental adsorption data, the gravimetrically measured adsorption amounts are multiplied by the adsorbed phase specific volume V_a to obtain the adsorbed phase volume. V_a is estimated according to the method proposed by Ozawa et al.[41] to account for the thermal expansion of the liquid:

$$V_a = V_b(T_b) \cdot \exp[0.0025(T - T_b)] \tag{6.4}$$

where V_b is the specific volume of the adsorbate at the boiling point T_b. All adsorption isotherms with D-A equation fits are presented in Figure 6.14-6.17 as a plot of volumetric adsorbed amounts vs. relative pressure.

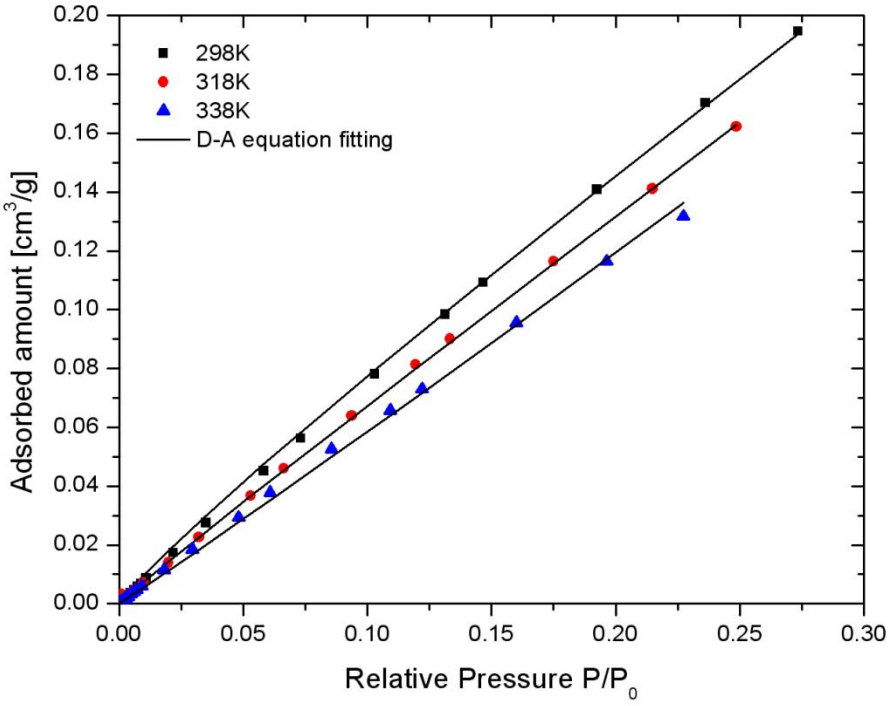

Figure 6.14 CH_4 adsorption isotherms with D-A equation fitting

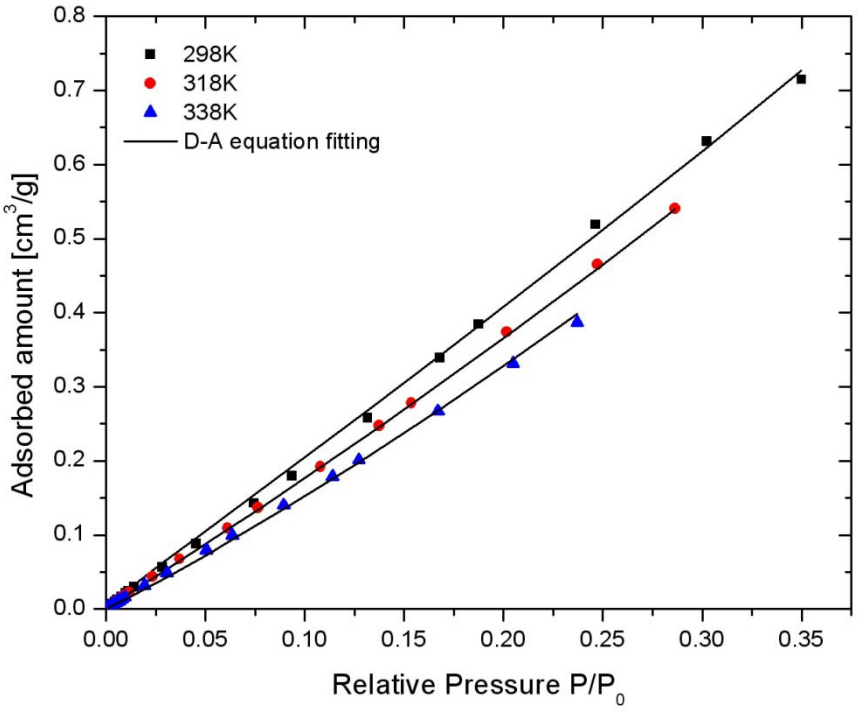

Figure 6.15 CO_2 adsorption isotherms with D-A equation fitting

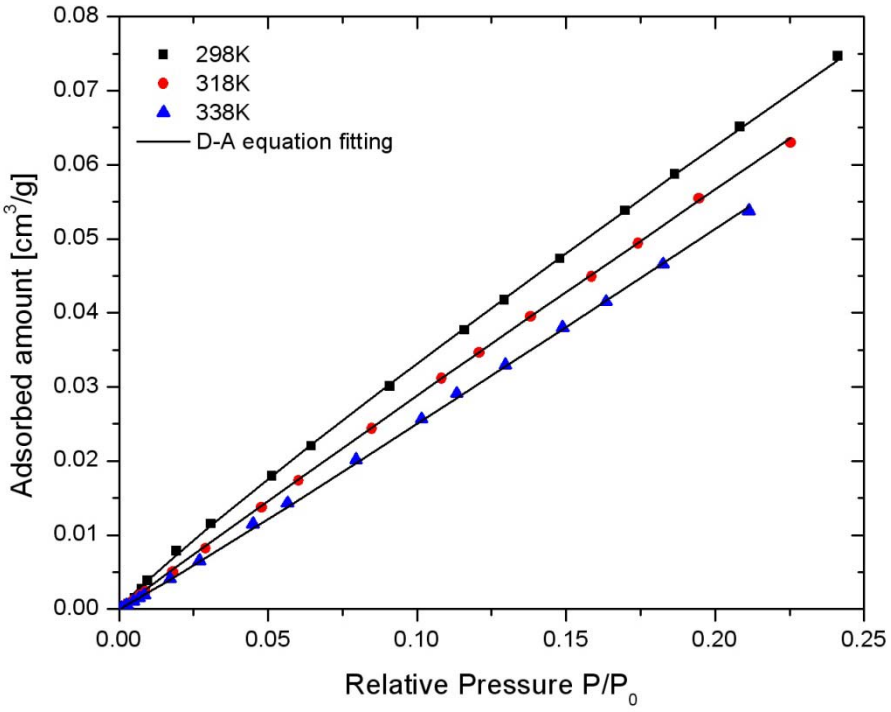

Figure 6.16 O_2 adsorption isotherms with D-A equation fitting

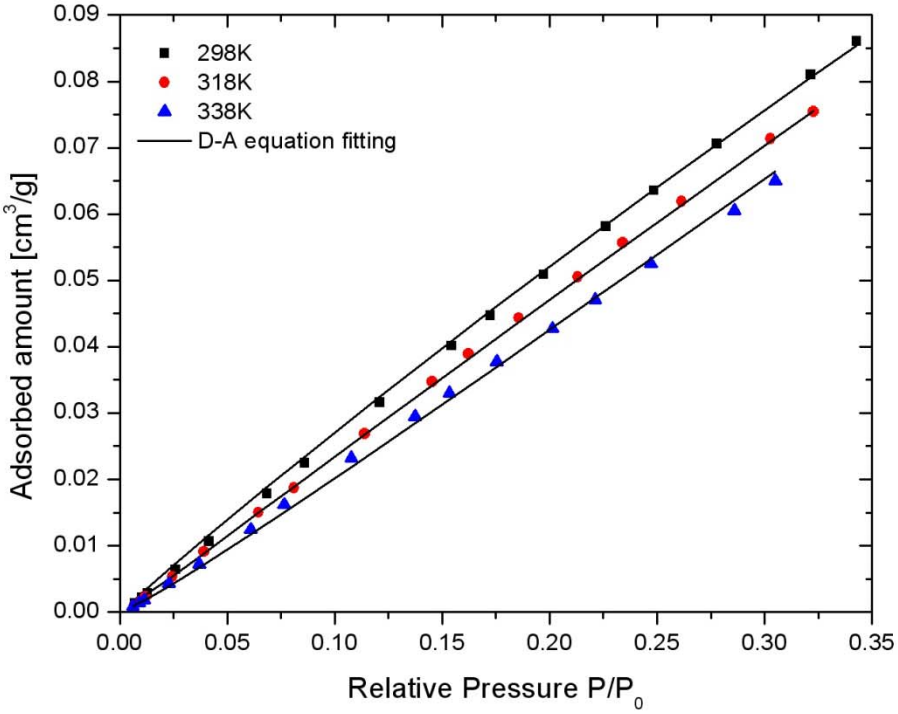

Figure 6.17 N_2 adsorption isotherms with D-A equation fitting

6.2.5 Determination of Characterization Curve and Heat of Adsorption

An essential parameter of the D-A equation is the adsorption potential A, which represents the negative differential Gibbs free energy. A significant step for the successful application of D-A equation is to obtain characteristic curves, which are plots of the adsorbed phase volume versus the adsorption potential. As shown in Figure 6.18, all characteristic curves for CH_4, CO_2, O_2, N_2 on UMCM-1 presented adequate temperature invariance, which demonstrates the successful application of the D-A equation. The characteristic curves can be used to predict adsorption equilibrium data at other temperatures. However, the model parameters were obtained for data within a relatively narrow temperature range, so extrapolation should proceed with caution. The model parameters for the D-A equation are given in Table 6.2. All isotherms were fit very well with a correlation coefficient $R^2 > 0.999$.

As can be seen from the table, the value of W_0 for different adsorbates on the same adsorbent presented obvious variance. This has also been noted in previous studies.[35,40] If we regard the total pore volume obtained from nitrogen adsorption at 77 K ($2.141 cm^3/g$) as the maximum accessible pore volume, then the value of W_0 for CO_2 is closest to the actual pore volume compared to the other gases. One possible explanation is that the narrow adsorption temperature range examined here (298 K – 338 K) includes the critical temperature of CO_2 (304.2 K). However, this range is well above the critical temperature of CH_4 (190.6 K), O_2 (154.58 K), and N_2 (126.19 K). The order of W_0 followed the order of the critical temperature for all gases, which means N_2 with the lowest critical temperature among all examined adsorbates will give the lowest W_0, as shown in the table. This trend has also been observed in other studies.[35]

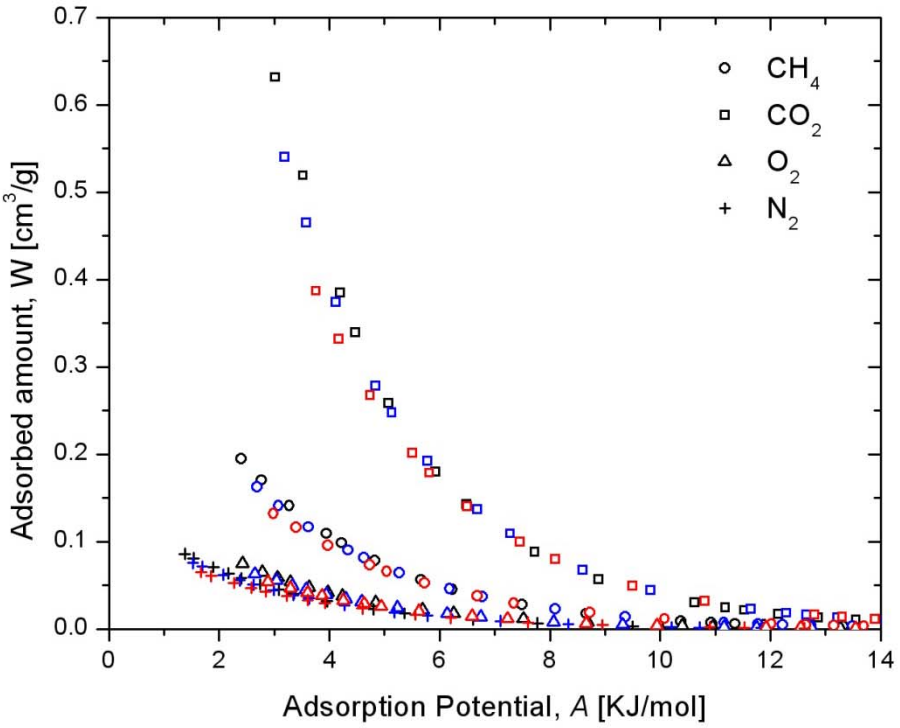

Figure 6.18 Characteristic curves for CH_4, CO_2, O_2, N_2 on UMCM-1 with D-A equation fitting: 298 K (black symbol), 318 K (blue symbol), 338 K (red symbol)

Table 6.2 Model Parameters for the D-A Equation

Adsorbate	W_0 (cm^3/g)	E (J/mol)	m	r	R^2
CH_4	0.653	2633	0.979	1.466	0.99931
CO_2	2.535	2026	0.890	3.087	0.99917
O_2	0.266	2766	1.013	1.051	0.99978
N_2	0.212	2898	1.065	0.928	0.99927

The isosteric heat of adsorption (ΔH) is another fundamentally interesting property of adsorption systems.[34] Isosteric heats were calculated for each molecule using the Clausius-Clapeyron equation. Figure 6.19 shows the isosteric heat of CH_4, CO_2, O_2, N_2 on UMCM-1 as a function of adsorption uptake. As shown in the figure, CO_2 demonstrated the highest isosteric heat of adsorption, while N_2 is the lowest one. The CO_2 and CH_4 isosteric heats are approximately constant at 11 kJ/mol and 7 kJ/mol, respectively, within the examined pressure region. The CO_2 isosteric heat is slightly lower than the reported simulation value of 14.90 kJ/mol.[20] The isosteric heat of O_2 was calculated to be 10.9 kJ/mol at 0.5 mmol/g loading, however, it decreased rapidly with increasing loading ending at 4.9 kJ/mol at 4.5 mmol/g. N_2 isosteric heat also demonstrated a decreasing isosteric heat with increasing loading with values in the range of 5.5-3.3 kJ/mol.

Isosteric heats of adsorption for CO_2 and CH_4 at zero coverage on selected materials are listed in Table 6.3 for comparison with UMCM-1. The isosteric heat for CO_2 is larger than that of CH_4 adsorption with the exception of Maxsorb AC, which has almost equal values of isosteric heat of adsorption. Among the listed materials, 5A zeolite, MIL-100, and MIL-101 demonstrated remarkably high isosteric heats of adsorption for CO_2. The zeolite possesses calcium cations and small pores of approximately 5 Å, so high heats of adsorption are not surprising. MIL-100 and -101 are mesoporous MOFs, but both possess open metal sites that are available for interaction with CO_2 molecules. As for isosteric heat of adsorption for CH_4, most materials have a value less than 20 kJ/mol except for multi-walled carbon nanotube, whose isosteric heat

for CH_4 is up to 40 kJ/mol measured experimentally.[42] In sharp contrast to the CO_2 results, open metal sites have little effect on the isosteric heat for methane.

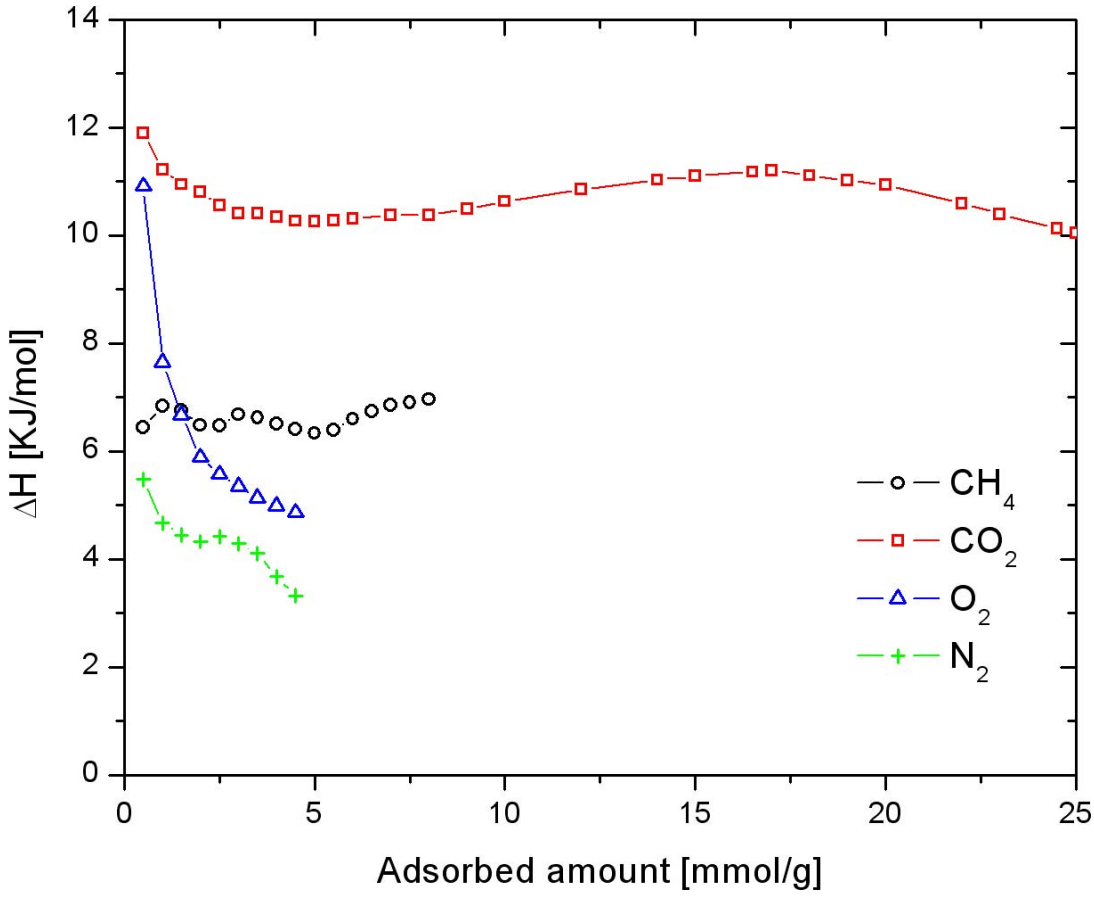

Figure 6.19 Isosteric heats of adsorption for CH_4, CO_2, O_2, and N_2 on UMCM-1

Table 6.3 Isosteric heat of adsorption for CO_2 and CH_4 near zero coverage

Materials	S (m^2/g)	Pore volume (cc/g)	ΔH_{CO2} (kJ/mol)	ΔH_{CH4} (kJ/mol)
MWCNT[43]	250	0.43	-	40.0
SWNT[20,44]	693	0.39	22.89	18.3
SWNT bundles[45]	-	-	22.5	18.3
MFI zeolite[20]	691	0.21	23.86	-
DD3R zeolite[46]	304	0.153	32.0	18.8
5A zeolite[42]	699	-	62.0	19.0
13X zeolite[47]	685	-	37.2	15.3
MCM-41[2,33]	1490	0.99	21.6	8.5
Maxsorb AC[35]	3250	1.79	16.2	16.3
BPL AC[35]	1150	0.43	25.7	16.1
MIL-100[29]	1900	1.1	62	19
MIL-101[29]	4230	2.15	44	18
IRMOF-1[2,20]	3558	1.37	15.65	10.6
IRMOF-14[2,19]	4800	2.30	13.28	10.0
Cu-BTC[3,19]	2368	0.82	25.60	18.7
MOF-177[19]	4688	1.96	14.43	-
UMCM-1	4100	2.14	11.9	6.5

6.3 CONCLUSIONS

In this chapter, adsorption equilibrium data were reported for CH_4, H_2, CO_2, O_2, and N_2 at three different temperatures on mesoporous MOF UMCM-1. The multi-temperature isotherms were modeled using the Dubinin-Astakhov isotherm equation to obtain useful thermodynamic properties including adsorption potential and isosteric heats of adsorption. Several conclusions can be drawn from comparison of these experiments with results from a variety of mesoporous and microporous materials. Large-pore materials are shown to exhibit very high heats of adsorption for CO_2 when open metal sites are present. This phenomenon is not observed for methane, which indicates the importance of the CO_2 quadrupole in influencing binding strength. Adsorption results for N_2 and O_2 show that selectivities in MOFs can be manipulated by the presence or absence of open metal sites. UMCM-1 and MOF-177 show a slight preference for O_2 over N_2. However, open metal site MOFs such as Cu-BTC show the opposite adsorption preference, which is similar to zeolite selectivities. This experimental study reveals interesting adsorption information about a novel mesoporous MOF within the context of other MOFs and traditional mesoporous adsorbents. These results can be used to advance the development of structure-property relationships for metal-organic frameworks.

6.4 REFERENCES

(1) Eddaoudi, M.; Kim, J.; Rosi, N.; Vodak, D.; Wachter, J.; O'Keeffe, M.; Yaghi, O. M. *Science* **2002**, *295*, 469.

(2) Duren, T.; Sarkisov, L.; Yaghi, O. M.; Snurr, R. Q. *Langmuir* **2004**, *20*, 2683.

(3) Wang, S. Y. *Energ Fuel* **2007**, *21*, 953.

(4) Zhao, D.; Yuan, D. Q.; Zhou, H. C. *Energ Environ Sci* **2008**, *1*, 222.

(5) Frost, H.; Snurr, R. Q. *J Phys Chem C* **2007**, *111*, 18794.

(6) Morris, R. E.; Wheatley, P. S. *Angew Chem Int Edit* **2008**, *47*, 4966.

(7) Hu, Y. H.; Zhang, L. *Adv Mater* **2010**, *22*, E117.

(8) Lin, X.; Jia, J. H.; Hubberstey, P.; Schroder, M.; Champness, N. R. *Crystengcomm* **2007**, *9*, 438.

(9) Murray, L. J.; Dinca, M.; Long, J. R. *Chem Soc Rev* **2009**, *38*, 1294.

(10) Rosi, N. L.; Eckert, J.; Eddaoudi, M.; Vodak, D. T.; Kim, J.; O'Keeffe, M.; Yaghi, O. M. *Science* **2003**, *300*, 1127.

(11) Dinca, M.; Long, J. R. *Angew Chem Int Edit* **2008**, *47*, 6766.

(12) Jia, C.; Yuan, X. X.; Ma, Z. F. *Prog Chem* **2009**, *21*, 1954.

(13) Hirscher, M.; Panella, B.; Schmitz, B. *Micropor Mesopor Mat* **2010**, *129*, 335.

(14) Frost, H.; Duren, T.; Snurr, R. Q. *J Phys Chem B* **2006**, *110*, 9565.

(15) Lochan, R. C.; Khaliullin, R. Z.; Head-Gordon, M. *Inorg Chem* **2008**, *47*, 4032.

(16) Bae, Y.-S.; Mulfort, K. L.; Frost, H.; Ryan, P.; Punnathanam, S.; Broadbelt, L. J.; Hupp, J. T.; Snurr, R. Q. *Langmuir* **2008**, *24*, 8592.

(17) Mu, B.; Li, F.; Walton, K. S. *Chem Commun* **2009**, 2493.

(18) Millward, A. R.; Yaghi, O. M. *J Am Chem Soc* **2005**, *127*, 17998.

(19) Yang, Q. Y.; Zhong, C. L.; Chen, J. F. *J Phys Chem C* **2008**, *112*, 1562.

(20) Babarao, R.; Jiang, J. W. *Langmuir* **2008**, *24*, 6270.

(21) Walton, K. S.; Millward, A. R.; Dubbeldam, D.; Frost, H.; Low, J. J.; Yaghi, O. M.; Snurr, R. Q. *J Am Chem Soc* **2008**, *130*, 406.

(22) Shelley, S. *Chem. Eng. Prog.* **2009**, *105*, 6.

(23) Yang, R. T. *Gas separation by adsorption processes*; Butterworths: Boston, 1987.

(24) Wang, Q. M.; Shen, D. M.; Bulow, M.; Lau, M. L.; Deng, S. G.; Fitch, F. R.; Lemcoff, N. O.; Semanscin, J. *Micropor Mesopor Mat* **2002**, *55*, 217.

(25) Noguchi, H.; Kondo, A.; Hattori, Y.; Kajiro, H.; Kanoh, H.; Kaneko, K. *The Journal of Physical Chemistry C* **2006**, *111*, 248.

(26) Garcia-Perez, E.; Gascon, J.; Morales-Florez, V.; Castillo, J. M.; Kapteijn, F.; Calero, S. *Langmuir* **2009**, *25*, 1725.

(27) Humphrey, S. M.; Chang, J.-S.; Jhung, S. H.; Yoon, J. W.; Wood, P. T. *Angew Chem Int Edit* **2007**, *46*, 272.

(28) Li, Y.; Yang, R. T. *Langmuir* **2007**, *23*, 12937.

(29) Llewellyn, P. L.; Bourrelly, S.; Serre, C.; Vimont, A.; Daturi, M.; Hamon, L.; De Weireld, G.; Chang, J. S.; Hong, D. Y.; Hwang, Y. K.; Jhung, S. H.; Ferey, G. *Langmuir* **2008**, *24*, 7245.

(30) Latroche, M.; Surblé, S.; Serre, C.; Mellot-Draznieks, C.; Llewellyn, P. L.; Lee, J.-H.; Chang, J.-S.; Jhung, S. H.; Férey, G. *Angew Chem Int Edit* **2006**, *45*, 8227.

(31) Koh, K.; Wong-Foy, A. G.; Matzger, A. J. *Angew Chem Int Edit* **2008**, *47*, 677.

(32) Rowsell, J. L. C.; Yaghi, O. M. *Angew Chem Int Edit* **2005**, *44*, 4670.

(33) Belmabkhout, Y.; Serna-Guerrero, R.; Sayari, A. *Chem Eng Sci* **2009**, *64*, 3721.

(34) Chandrasekar, G.; Son, W.-J.; Ahn, W.-S. *J Porous Mat* **2009**, *16*, 545.

(35) Himeno, S.; Komatsu, T.; Fujita, S. *J Chem Eng Data* **2005**, *50*, 369.

(36) Millward, A. R.; Yaghi, O. M. *J Am Chem Soc* **2005**, *127*, 17998.

(37) Rege, S. U.; Yang, R. T. *Ind Eng Chem Res* **1997**, *36*, 5358.

(38) Park, Y.-J.; Lee, S.-J.; Moon, J.-H.; Choi, D.-K.; Lee, C.-H. *Journal of Chemical & Engineering Data* **2006**, *51*, 1001.

(39) Chen, S. G.; Yang, R. T. *Langmuir* **1994**, *10*, 4244.

(40) Amankwah, K. A. G.; Schwarz, J. A. *Carbon* **1995**, *33*, 1313.

(41) Ozawa, S.; Kusumi, S.; Ogino, Y. *J Colloid Interf Sci* **1976**, *56*, 83.

(42) Sievers, W.; Mersmann, A. *Chem Eng Technol* **1994**, *17*, 325.

(43) Lee, J.-W.; Kang, H.-C.; Shim, W.-G.; Kim, C.; Moon, H. *Journal of Chemical & Engineering Data* **2006**, *51*, 963.

(44) Muris, M.; Dufau, N.; Bienfait, M.; Dupont-Pavlovsky, N.; Grillet, Y.; Palmari, J. P. *Langmuir* **2000**, *16*, 7019.

(45) Bienfait, M.; Zeppenfeld, P.; Dupont-Pavlovsky, N.; Muris, M.; Johnson, M. R.; Wilson, T.; DePies, M.; Vilches, O. E. *Phys Rev B* **2004**, *70*, 035410.

(46) Himeno, S.; Tomita, T.; Suzuki, K.; Yoshida, S. *Micropor Mesopor Mat* **2007**, *98*, 62.

(47) Cavenati, S.; Grande, C. A.; Rodrigues, A. E. *J Chem Eng Data* **2004**, *49*, 1095.

CHAPTER 7

BREATHING EFFECTS OF CO_2 ADSORPTION ON FLEXIBLE 3D LANTHANIDE MOF

Carbon dioxide capture, storage and separation (CCS) has been at the center of interest in the scientific and engineering community in recent years due to increasing attention to climate change. Traditional technologies for CO_2 capture and separation from flue gases include the employment of alkyl amine solution ("scrubbers") and cryogenic coolers.[1] However, these existing methods are energy intensive and are far from cost-effective for CO_2 abatement. Thus, CO_2 adsorptive storage and separation on porous materials have been proposed as an alternative. In particular, metal-organic frameworks (MOFs) have attracted much attention in the past two decades owing to their abundant structural and chemical diversity and their potential applications in gas storage and separation,[2-5] heterogeneous catalysis,[6-8] and drug delivery.[9-10]

More recently, the discovery of flexible and dynamic MOFs has changed many of our ideas of crystalline porous solids.[11-12] These so-called "third generation MOFs" exhibit extraordinary structure flexibility on adsorption/desorption of specific gases or liquids. Such structural transformation is often directly related to the functionality of these frameworks, such as pore size/shape change, gate-opening effects, and controlled molecular diffusion. Related potential applications may involve selective separation,[13-14] molecular sensing,[15] controlled drug storage and delivery,[11,16] and as nanoreactors for polymerization.[17] For the interest of application, selective separation of CO_2 over CH_4

and N_2 will be the center of our study.[18-20] However, there are relatively few reported studies about CO_2 capture and separation using flexible MOFs.[13,21-28]

A major group of flexible MOFs involve pillared layer coordination polymers, in which rigid layer and flexible ligand could be compared to solid roof and expandable pillar.[29-33] Another source of the flexibility comes from the interpenetration, in which weak interactions including hydrogen bonds and π-π bonds play an important role for the framework's dynamic behavior.[21,23,34-35] One of the most studied flexible MOFs is MIL-53[36-37] and a series of modified versions,[38] which are made of terephthalic acids and different metal ions. Their structures are not pillared layers or interpenetrating ones, but 3D frameworks with 1D channels, whose flexibility is possibly from the "kneecap" connection between the inorganic chain and the carboxylic function of the terephthalate.[39] However, breathing effects of 3D flexible MOFs are still far from clear, and exploring the mechanism and potential application of flexibility in MOFs are of high fundamental interest.

On the other hand, those using d-block transition metal-based systems among the porous MOFs, demonstrated significant success because of easier predictability and control of the coordination environment compared to f-block rare-earth metal-based systems. However, rare-earth elements with 4f valence electrons exhibit a number of features that differentiate them from the d-block metals and make them especially attractive in catalysis, magnetism, and luminescence. Thus, porous lanthanide MOFs combining porosity with other unique physical properties are obtaining more attention as potential multifunctional hybrid materials. However, MOFs with f-block metals still have been far less studied to date than their d-block counterparts.[40]

In this chapter, we present a new three-dimensional flexible lanthanide metal-organic framework $[La(BTB)(H_2O)\cdot 3DMF]_n$ (BTB = 1,3,5-tris(4-carboxyphenyl) benzene). This MOF possesses a rare chiral space group, very high thermal stability up to 560 ^oC and demonstrates a large adsorption hysteresis loop on the N_2 isotherm at 77K after activation at 300 ^oC. Among common 3-connected ligands, extensively investigated 1,3,5-benzenetricarboxylic acid (H_3BTC) has been regarded as a rigid ligand, while BTB is considered an expanded version of BTC. As far as we know, lanthanide MOFs composed of 3-connected ligands which demonstrate breathing effects are very rare. In order to further explore the mechanism and potential application of flexibility in the lanthanide MOF, a detailed equilibrium and kinetics study of the breathing effect of LaBTB upon adsorption of three important gases CO_2, CH_4, N_2 by high pressure gravimetric adsorption equipment was performed. It is very surprising that LaBTB presents a very large adsorption hysteresis loop on the CO_2 isotherm near room temperature and also demonstrates highly selective CO_2 capacity compared with CH_4 and N_2. In addition, thermogravimetric analysis (TGA), differential scanning calorimetry (DSC), and powder X-ray thermodiffraction studies were performed to help explain the possible structural transformation and obtain useful thermodynamic information. The meaning of this study is 2-fold: (1) experimentally confirming large breathing effects in LaBTB, which is composed of traditionally regarded rigid 3-connected ligand and f-block rare-earth metal; (2) exploring possible mechanism of breathing effects in LaBTB by adsorption equilibrium and kinetics investigation.

7.1 SYNTHESIS AND CHARACTERIZATION

7.1.1 Materials and Synthesis Method

All chemicals are purchased from commercial companies and used as received without further purification: lanthanum nitrate hexahydrate, $La(NO_3)_2 \cdot 6H_2O$ (EMD Chemicals); 1,3,5-tris(4-carboxyphenyl)benzene, H_3BTB (Sigma-Aldrich, ≥98%); N,N-dimethylformamide, DMF (Acros Organics, 99.8+%); dichloromethane, CH_2Cl_2 (Acros Organics, 99.5%). Solvothermal reactions were carried out in digestion bomb reactors. Exact amounts of $La(NO_3)_2 \cdot 6H_2O$ (1.8 mmol) and H_3BTB (0.6 mmmol) were dissolved in 30 mL DMF. The mixture solution was heated at 95 ^oC for 48 hours. Then the colorless crystal $[La(BTB)(H_2O) \cdot 3DMF]_n$ was obtained. The as-synthesized sample (**5**) was obtained by filtration, and dried in air for one day. The solvent-exchanged sample (**5'**) was obtained by immersing **5** in dichloromethane for two weeks. The activated sample (**5"**) was obtained by heating **5'** at 300 ℃ under vacuum for 1 hrs.

7.1.2 Single-Crystal X-Ray Diffraction Characterization

Single-crystal XRD data of compound **5** was collected on a Rigaku Mercury CCD area-detector single crystal diffraction system with CuKα radiation ($\lambda = 1.54178$ Å). The structure was solved by the Direct Method of SHELXS-97 and refined by full-matrix least-squares techniques using the SHELXL-97 program. Non-hydrogen atoms were refined with anisotropic temperature parameters.

Table 7.1 Crystallographic Data for [La(BTB)(H_2O)]·3DMF (**5**)

Compound	**5**
Chemical Formula	$C_{36}H_{38}N_3O_{10}La$
Formula weight	811.61
Crystal system	hexagonal
Space group	P6522
a (Å)	16.5428(4)
b (Å)	16.5428(4)
c (Å)	24.3988(15)
α (°)	90.00
β (°)	90.00
γ (°)	120.00
V (Å3)	5782.5(4)
Dc (g/cm3)	1.017
Abso. coef. (mm-1)	8.806
Z	6
T (K)	296(2)
Wavelength (Å)	1.54178
F(000)	1740
Goodness-of-fit on F2	1.080
R1 indices [I>2.0σ(I)]	0.0550
wR2 indices[I>2.0σ(I)]	0.1508
R1 indices (all data)	0.0565
wR2 indices (all data)	0.1522

$$R_1 = \Sigma(\,|Fo| - |Fc|\,) / \Sigma\,|Fo|\,;\; wR_2 = [\,\Sigma w(Fo^2 - Fc^2)^2 / \Sigma w(Fo^2)^2]^{1/2}$$

Single-crystal X-ray analysis shows that compound **5** crystallizes in the chiral space group $P6_522$. Considering H_3BTB ligand is an achiral building block, the successful synthesis of compound **5** is non-trivial, and will help elucidate the synthesis mechanism of chiral MOFs from achiral building blocks.[41] Among important porous lanthanide MOFs,[42-50] only very few structures possess chirality. These include MIL-103[46] and MOF-76[50], but only compound **5** belongs to the $P6_522$ space group.

Each La^{3+} ion is nine coordinated by eight oxygen atoms from six carboxyl groups and one water molecule with tricapped trigonal prism geometry (Figure 7.1). The La-O bond lengths range from 2.428 Å to 2.758 Å. The BTB ligand acts as a μ6-bridge linking six La^{3+} ions, in which one carboxylate group adopts μ2-η1: η1-bridging, and two μ2-η2: η1-bridging mode, respectively (Figure 7.2).

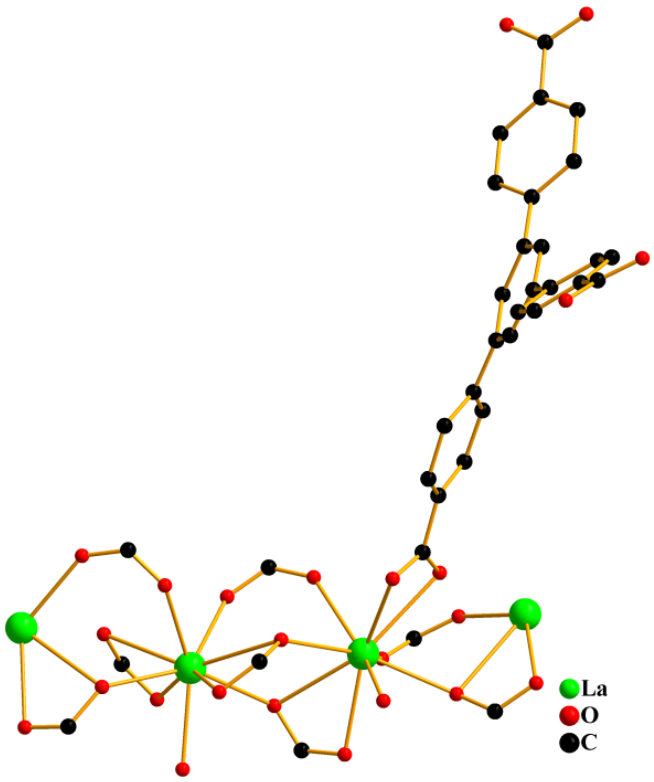

Figure 7.1 Coordination Environment of La atoms in compound **5**.

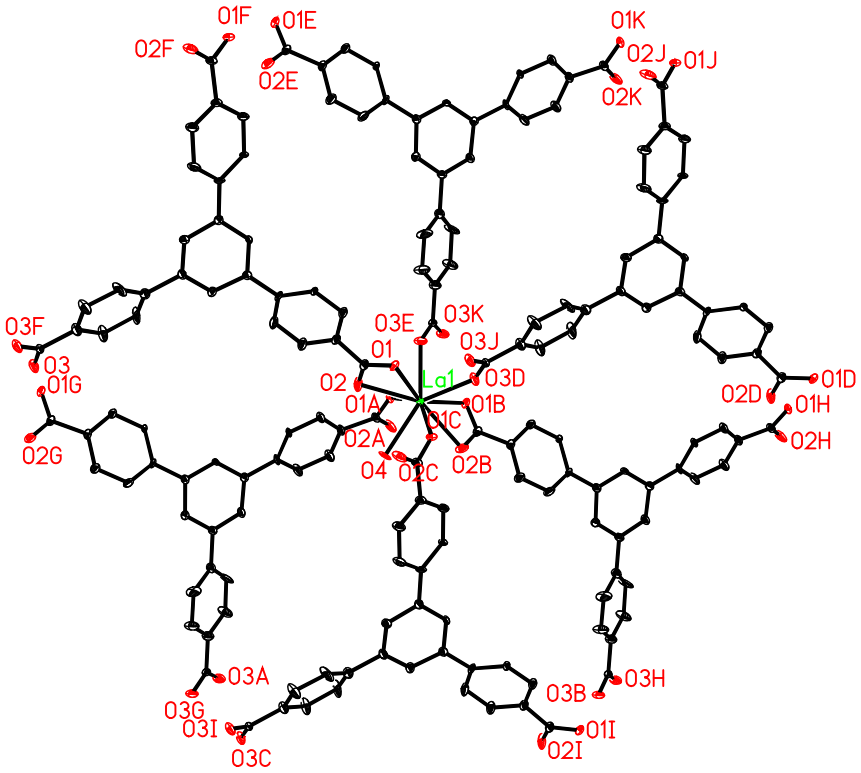

Figure 7.1 continued

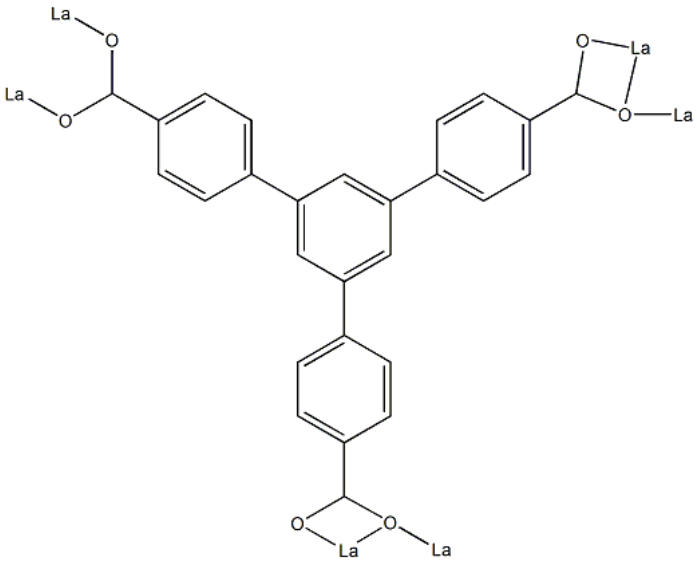

Figure 7.2 Connecting mode of BTB ligand in compound **5**.

The structure of **5** is a complicated 3D net constructed from carboxyl bridged helices. The carboxyl groups from BTB ligands first bridge the La ions into an inorganic helical chain with La…La distance of 4.281 Å along the *c* axis (Figure 7.3). The adjacent La^{3+} ions are bridged by three carboxyl groups from BTB ligands. The pitch of the helix is 20.376 Å. In the plane [001], each helix is linked to six neighboring helices by BTB ligands to form the complicated 3D framework (Figure 7.4), with each BTB ligand linking three helices. The water molecules coordinate to La^{3+} ions as terminal ligands to finish the final framework.

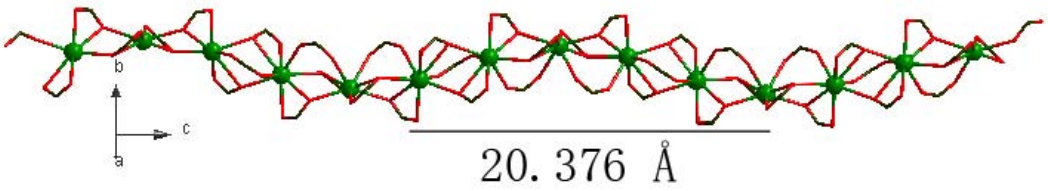

Figure 7.3 Inorganic helical chain composed of La and O atoms.

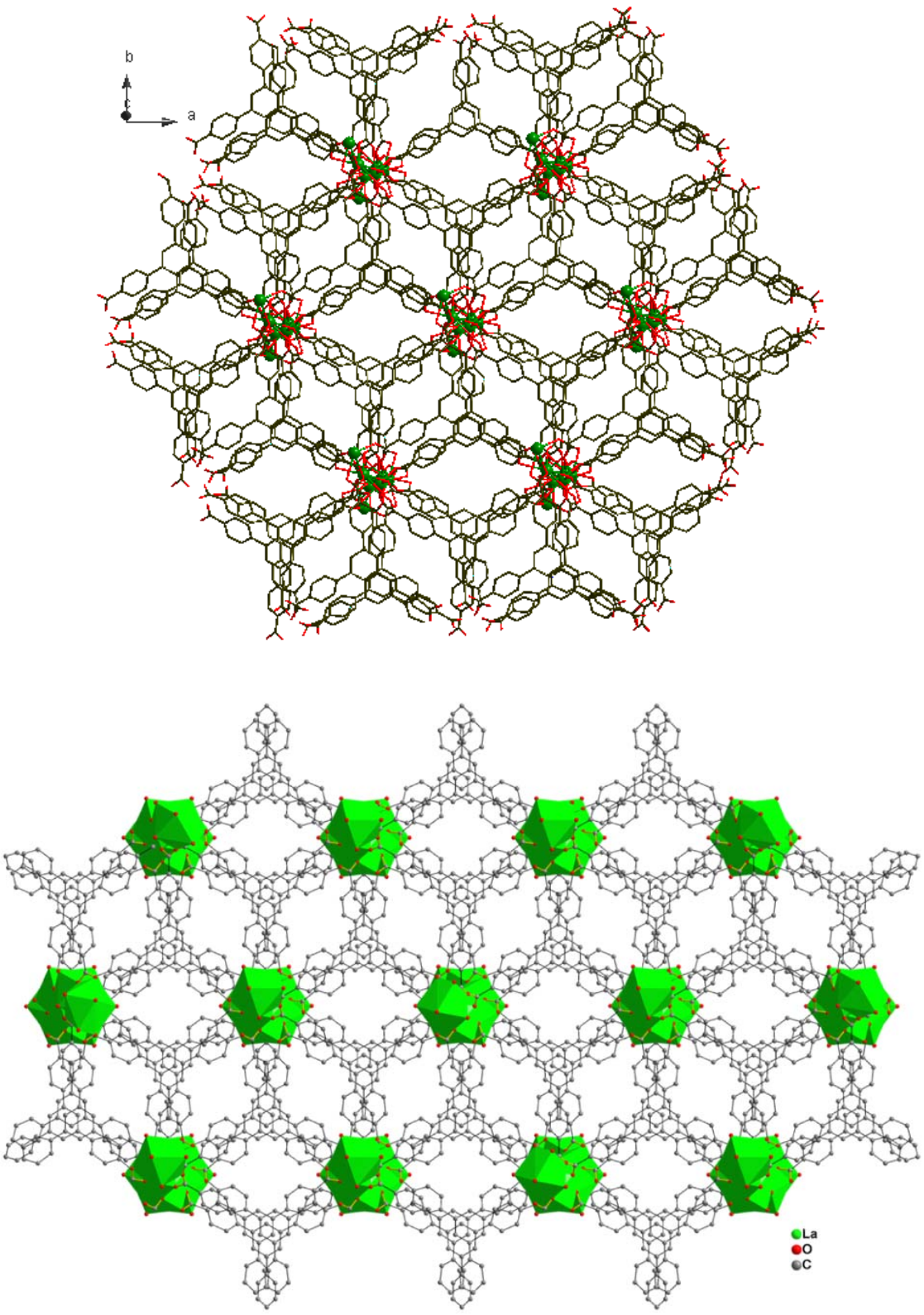

Figure 7.4 3D framework in compound **5** along c axis (hydrogen atoms removed for clarity); carbon atoms (black), oxygen atoms (red), lanthanum atoms (green).

Better insight into the nature of this intricate framework can be achieved by the application of the topological approach. According to the classification of RCSR,[51] the overall structure of **5** can be simplified to be a binodal 6-connected **nia** net with a $(4^{12}\cdot6^3)(4^9\cdot6^6)$ Schläfli symbol, where La and BTB nodes possess $(4^{12}\cdot6^3)$ and $(4^9\cdot6^6)$ topology, respectively (Figure 7.5).

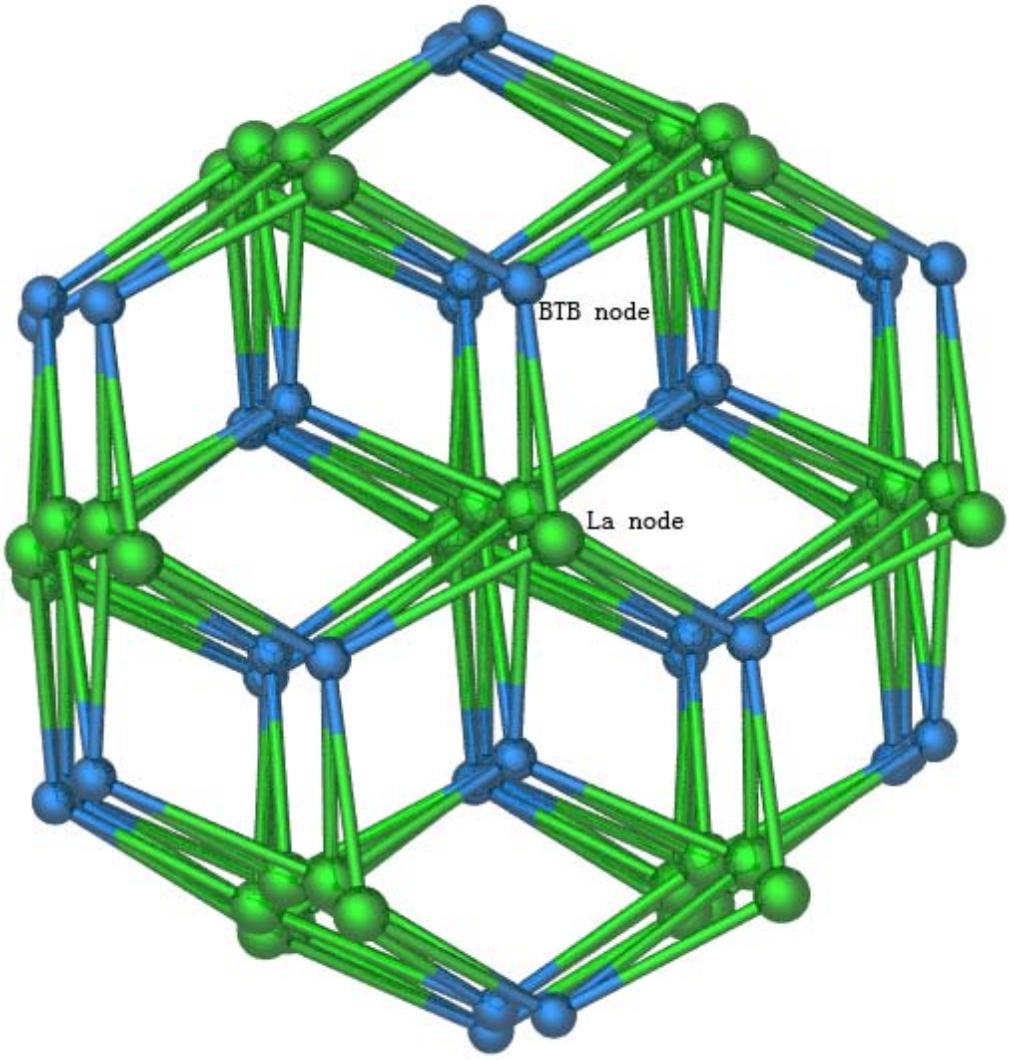

Figure 7.5 Three-periodic binodal **nia** net composed of BTB and La nodes.

7.1.3 Thermogravimetric Analysis (TGA)

Thermogravimetric analysis was carried out with a NETZSCH STA 449 F1 Jupiter® at a heating rate of 10 ^{o}C/min under helium atmosphere with 20 mL/min flow rate. The examined temperature ranges from 30 ^{o}C to 750 ^{o}C. The as-synthesized sample (**5**) was exposed to air for 1 day before test. The solvent-exchanged sample (**5**') was exposed to air less than 6 hours before test, while the activated sample (**5**") was exposed to air less than 30 mins before test.

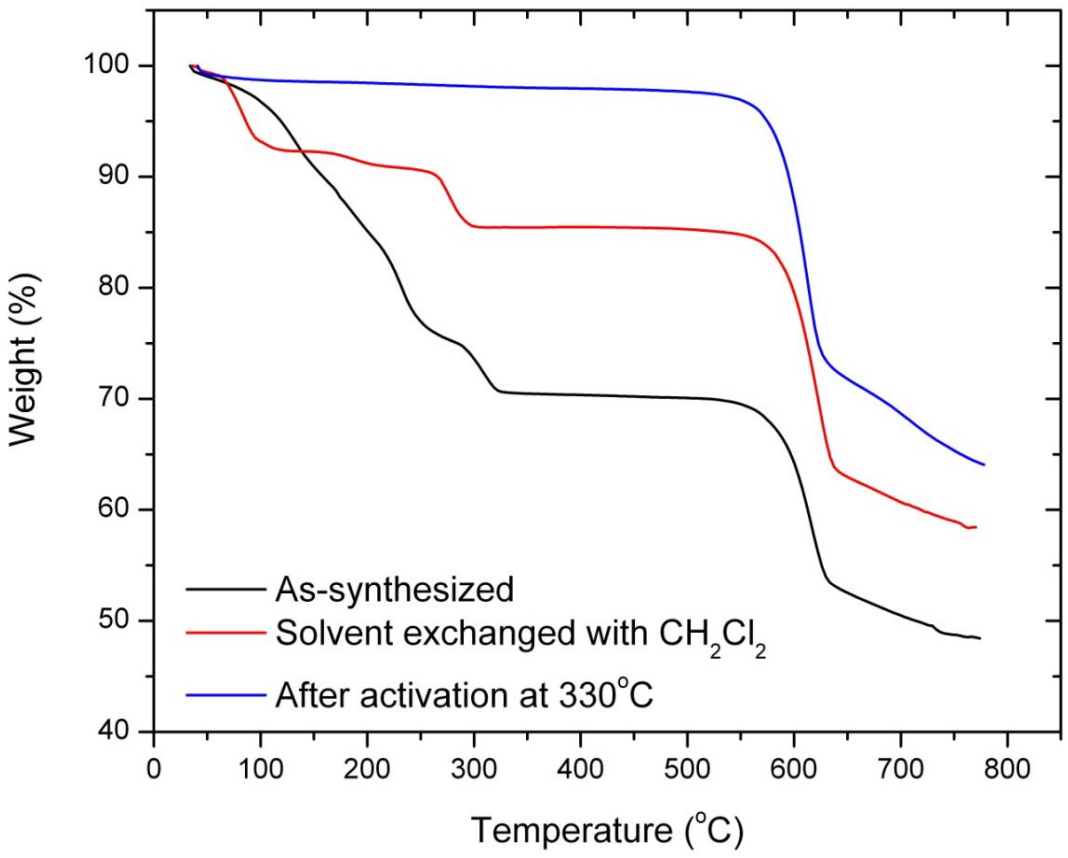

Figure 7.6 TGA curve demonstrates high thermal stability of compound **5**.

TGA data (Figure 7.6) indicates that **5** is stable up to 560 ^{o}C, which is much higher than the decomposition temperature (400 ^{o}C) of MIL-103[46]. The first weight loss of 29.66% from 20 to 325 ^{o}C corresponds to the loss of three DMF molecules and one coordinated water molecule (calcd. 29.24%). After the loss of solvent molecules, compound **5** shows thermal stability until 560 ^{o}C. A gradual weight loss of 21.81% is observed at the temperature range of 560-750 ^{o}C, which is attributed to the decomposition of BTB ligand (calcd. 20.67%). Without the support of any interpenetration, compound **5** keeps its framework until 560 ^{o}C. To our knowledge, the thermal stability temperature of **5** is the highest among the reported porous lanthanide MOFs[42-49]. The TG curve of **5** demonstrates a wide-range stage without any weight loss, which shows the framework of **5** is stable within the wide temperature range (325-560 ^{o}C) after guest removal. The wide temperature range of compound **5** makes it suitable for adsorption processes with various amounts of heat liberation. In addition, TGA results of the solvent-exchanged sample (**5'**) and the activated sample (**5"**) demonstrated consistent thermal stability. Thus, we believe the strong coordination bond between carboxyl oxygen and lanthanide ions has a significant impact on the high thermal stability.

7.1.4 Powder X-Ray Thermodiffraction

Powder X-ray thermodiffraction experiment was carried out at an X'Pert Pro work station equipped with high-speed RTMS detector and TTK-450 temperature/environment control chamber provided by PANalytical Company. The examined temperature ranges from 25 ^{o}C to 350 ^{o}C. At increasing temperature stage, each scanning was performed every 20 ^{o}C until 200 ^{o}C, and then scanning was intensified to every 10 ^{o}C until 350 ^{o}C. After the temperature was kept at 350 ^{o}C for 30 mintutes,

scanning started for the decreasing stage and was recorded every 50 °C until arriving to room temperature.

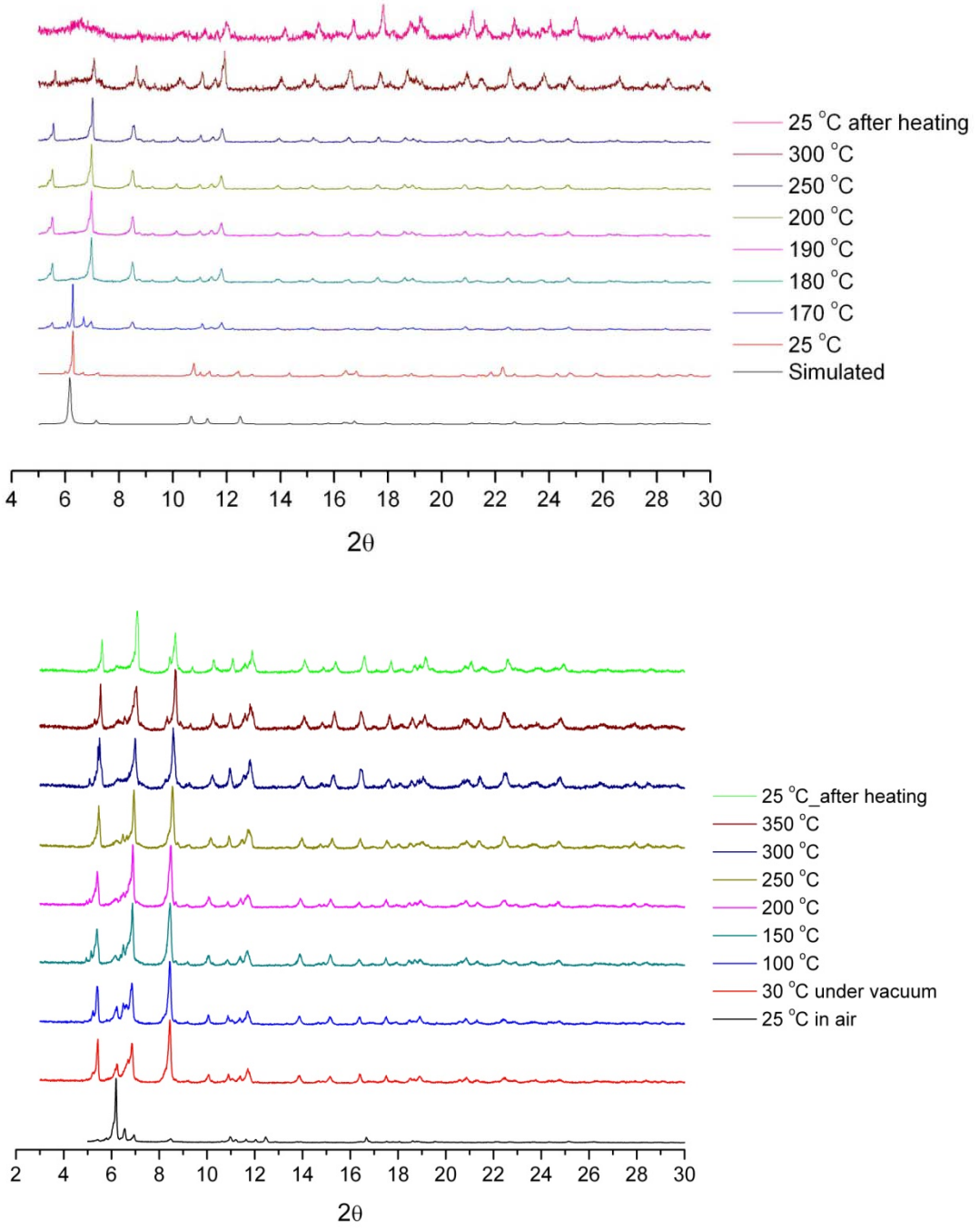

Figure 7.7 Powder X-ray thermodiffraction pattern of the as-synthesized sample (**5,** top) and the solvent-exchanged sample (**5',** bottom)

7.2 BREATHING EFFECT OF GAS ADSORPTION ON FLEXIBLE MOF

7.2.1 Structural Transformation

Powder X-ray pattern was collected from 5^o to 50^o of 2 theta for the as-synthesized sample (**5**), which presented good phase purity compared with the simulated pattern from single-crystal structure. Powder X-ray thermodiffraction of **5** in air indicated an irreversible structure transformation occurred at around 180 ^oC. As shown in Figure 7.7, the crystal structure **5** is maintained until 170 ^oC. However, a major peak at $2\Theta = 6.16$ totally disappears in the conditions of $T \geq 180\ ^oC$, and three peaks predominate at $2\Theta = 5.52, 6.95, 8.55$ respectively. Such apparent change in XRD pattern indicates the formation of a new crystal structure. A possible explanation is that the removal of guest molecules associated in the pores results in the structure transformation of **5**. Considering the boiling temperature of DMF molecules is 153 ^oC, above 170 ^oC is a reasonable temperature range to release DMF molecules within the nanopores in this case. With the further increase of the temperature, thermolysis begins to take places due to oxygen and moisture in air. After a heating and cooling cycle in air, the as-synthesized sample finally loses its crystallinity as shown in the last XRD scan on the top of Figure 7.7. In order to further understand the mechanism of the structure transformation, powder X-ray thermodiffraction of the solvent-exchanged sample (**5'**) was carried out as well. First XRD scans were performed in air for **5'**, which is exposed to air less than 12 hours after filtered from CH_2Cl_2. Then, the **5'** was put under a vacuum in situ for 1 hour before XRD scanning. As shown in Figure 7.7 (bottom), XRD pattern of **5'** in air at 25 ^oC is the same as the as-synthesized sample (**5**). However, after vacuuming for 1 hour, structure transformation occurs due to the removal of dichloromethane molecules. From 30 ^oC to

350 ^{o}C, the major peak at 2θ = 6.16 eventually disappears with the increase of temperature, and three new peaks predominate finally at 2θ = 5.48, 6.91, 8.50 respectively, which are almost the same as the peaks appearing in XRD pattern of the as-synthesized sample (**5**) in the conditions of T ≥ 180 ^{o}C. In addition, the transformed crystal structure (**5"**) stays intact during the heating activation process. Thus, we believe that the removal of guest molecules play an important role for the structural transformation. Combined with TGA results, we can confirm that such structure transformation does not break the basic crystal framework since thermal stability remains the same after structural transformation.

7.2.2 Low Temperature N_2 Sorption Properties

The nitrogen adsorption properties of **5”** at lower temperature were investigated first, which presented very interesting adsorption behavior. The adsorption measurement was performed at 77 K using nitrogen as the adsorbate. As shown in Figure 7.8, **5”** exhibits a large step in adsorption within 0.3-0.45 relative pressure, and then develops a hysteresis loop upon desorption. This behavior has been called a “breathing effect”[11], or “gate phenomenon”[52]. Combined with the results of powder X-ray thermodiffraction in the above section, we believe that the breathing effect in this MOF involve the transformation of the crystal structure from **5"** to **5**. In other words, the crystal from the shrinking form (**5"**) recovered to the expanded form (**5**) once the crystal obtains sufficient energy from gas adsorbate molecules to overcome the energy barrier required to open the "gate". Thus, the crystal presents the shrinking form (**5"**) before the 0.3 relative pressure on the adsorption branch, while the expanded form (**5**) is achieved after the 0.45 relative pressure and maintained through desorption until very low pressure.

Thus, the surface area of the structures of **5"** and **5** can be calculated by using BET method on adsorption and desorption branches, respectively. Under the same pressure range from 0.01 to 0.05 relative pressure, the BET surface area is around 393 m^2/g for the shrinking form (**5"**) and 1014 m^2/g for the expanded form (**5)**, which is the highest among the reported porous lanthanide MOFs[42-50]. The accessible surface area of the expanded form (**5)** was also calculated from the crystal structure using the geometric method[53] based on the crystal structure of the as-synthesized sample without guest molecules. Assuming the kinetic diameter of the probe molecule (N_2) to be 3.681 Å, the resulting surface area is 1385.17 m^2/g. The experimental total pore volume is 0.48 cc/g at P/P_0 = 0.99 using nitrogen as the probe, which is also the largest among the reported porous lanthanide MOFs[42-50].

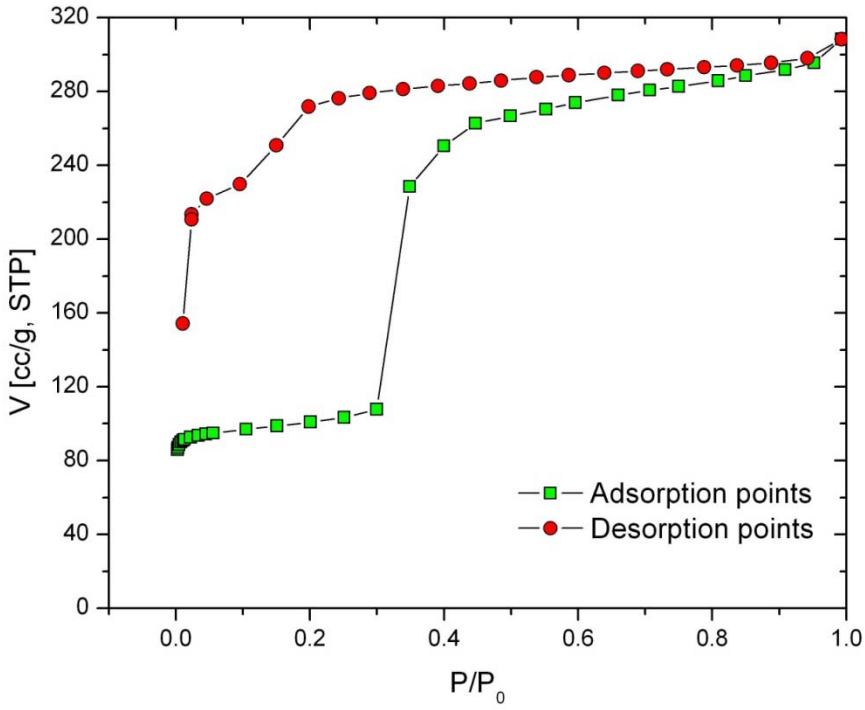

Figure 7.8 Nitrogen adsorption isotherm at 77 K for the activated sample **5"**

In addition, the energy required for transformation between two crystal structures is estimated according to the following pressure-volume work equation without considering the dissipated heat energy:

$$W = \int_{V_1}^{V_2} PdV = P\Delta V \quad 7.1$$

At the 0.2 relative pressure, the adsorbed amount of nitrogen are assumed as the volume of pore so that the calculating the work at this point gives 17.1 J/g. This value is in the similar amplitude compared with the reported transition free energy (14 J/g) of MIL-53(Cr), , which is obtained from mercury porosimetry experiment.[54]

7.2.3 High Pressure Gas Adsorption Studies

The CO_2, CH_4, N_2 adsorption properties of **5"** at ambient temperature were investigated by gravimetric adsorption experiments (Figure 7.9). From 278 K to 298 K, N_2 and CH_4 adsorption present almost linear reversible isotherms without hysteresis; the maximum capacities are 0.5mmol/g and 0.76 mmol/g at 20 bar, respectively. Meanwhile, the adsorption of CO_2 on **5"** is quite different under the examined range of temperature and pressure. The discussion of the results is listed here according to the adsorption temperature:

CO_2 adsorption at 298 K produces a typical Langmuir-type reversible isotherm without hysteresis, in which linear increase of capacity from 4 bar to 20 bar can be observed producing a rate of 0.055 mmol/bar. The capacity at 20 bar is 1.47 mmol/g. It is worth noting that although the hysteresis loop does not form under the examined pressure range, it does not mean that breathing effect would not occur at higher pressure at 298 K, and further analysis will be given later.

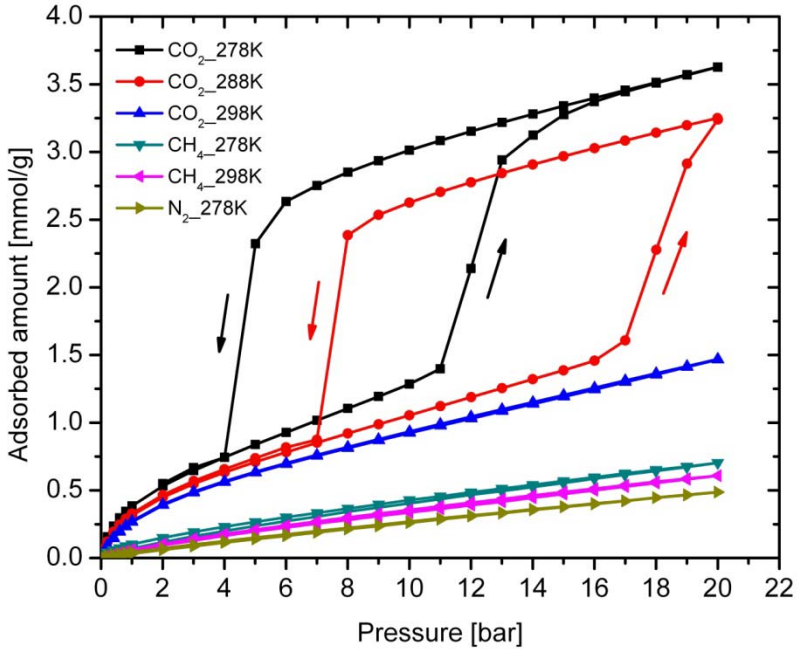

Figure 7.9 Gas adsorption isotherms at room temperature for the activated sample **5"**

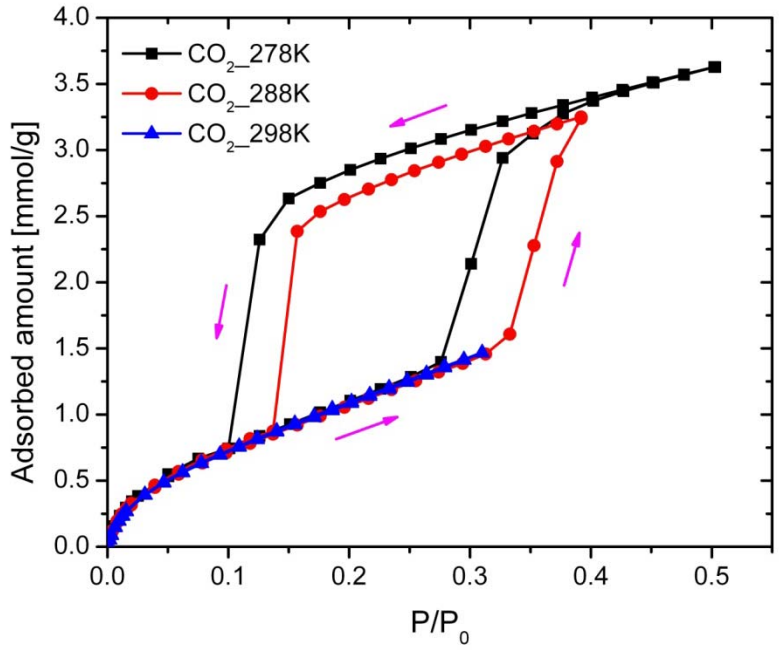

Figure 7.10 CO_2 adsorption isotherms with relative pressure for the activated sample **5"**

At 288 K, linear increase of capacity from 4 bar to 16 bar can be observed producing a rate of 0.068 mmol/bar; however, the adsorption capacity quickly jumps to 3.25 mmol/g at 20 bar from 1.61 mmol/g at 17 bar, with a rate of 0.55 mmol/bar, and the capacity increases to more than double within 3 bar. At desorption branch, linear decrease of capacity from 20 bar to 9 bar can be observed producing a rate of 0.063 mmol/bar; however, the adsorption capacity quickly drops to 0.87 mmol/g at 7 bar from 2.38 mmol/g at 8 bar, with a rate of 1.51 mmol/bar, and the capacity decreases to almost one third within 1 bar. Thus, a breathing cycle starts from 17 bar on adsorption branch, and ends at 7 bar on desorption branch.

At 278 K, similar hysteresis can be observed again. Linear increase of capacity from 2 bar to 11 bar gives a rate of 0.093 mmol/bar, and then the adsorption capacity quickly jumps to 2.94 mmol/g at 13 bar from 1.40 mmol/g at 11 bar, with a rate of 0.77 mmol/bar, and the capacity increases to more than double within 2 bar. After that, the capacity slowly increases to 3.63 mmol/g at 20 bar. At desorption branch, linear decrease of capacity from 20 bar to 6 bar can be observed producing a rate of 0.065 mmol/bar; however, the adsorption capacity quickly drops to 0.74 mmol/g at 4 bar from 2.32 mmol/g at 5 bar, with a rate of 1.57 mmol/bar, and the capacity decreases to almost one third within 1 bar. Thus, a breathing cycle starts from 11 bar on adsorption branch, and ends at 4 bar on desorption branch.

To better understand the internal relationship between breathing effect and adsorption pressure and temperature, we redraw the CO_2 isotherms using the relative pressure. As shown in Figure 7.10, it is surprising that the isotherms at different temperatures overlap each other very well until the beginning of breathing effect, and

then they come back to the single curve again after the finishing of breathing cycle. Lower adsorption temperature results in that the whole breathing cycle takes place at lower relative pressure. For example, the breathing effect at 278 K starts from 0.28 of relative pressure ending at 0.1 of relative pressure, while that at 288 K starts from 0.33 of relative pressure ending at 0.14 of relative pressure. Considering 298 K is still under the critical temperature of CO_2, we believe the breathing effect at 298 K will start from 0.38 of relative pressure (around 25 bar), and end at 0.18 of relative pressure (around 11 bar).

The above analysis is further presented in the plots of adsorption capacity gradient versus pressure or relative pressure. As shown in Figure 7.11, the peak values in the plots indicate the possible opening or closing rate of "gate" in the microstructure of this flexible MOF. Comparing adsorption points and desorption points, we found the closing rate of "gate" is larger than the opening rate no matter what temperature. In addition, lower temperature produces higher opening or closing rate covering both cases of CO_2 and N_2 isotherms.

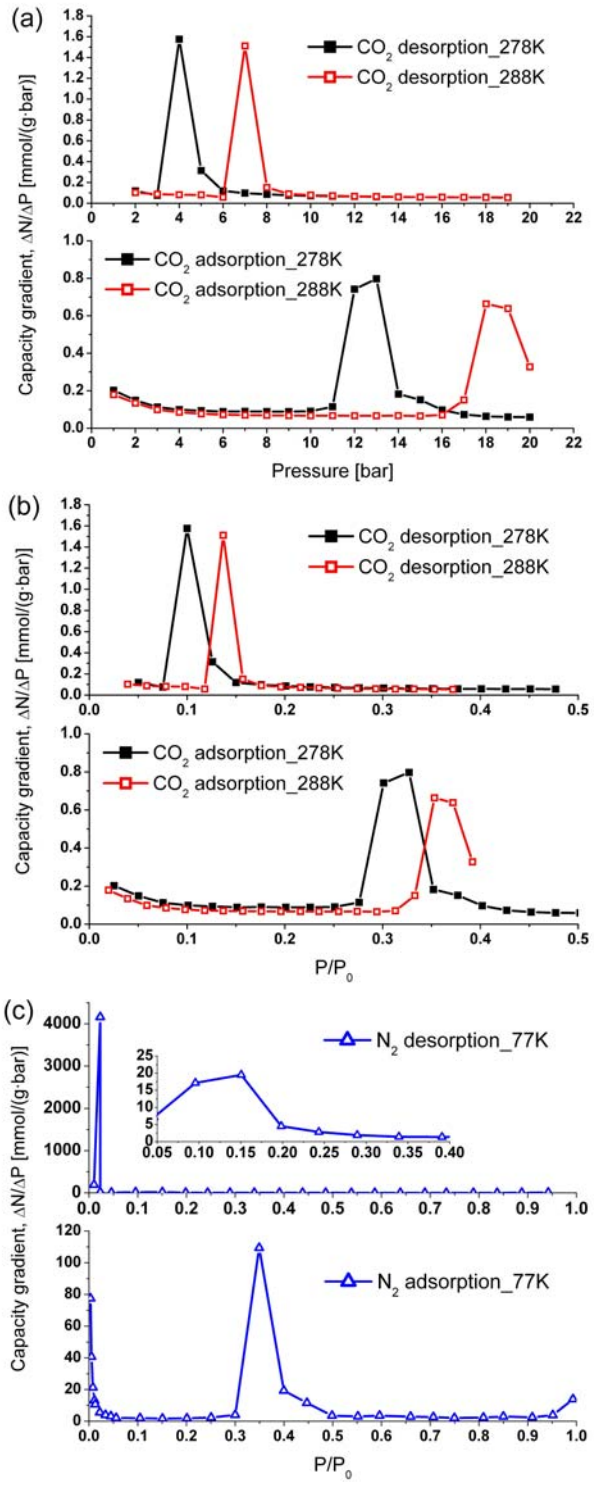

Figure 7.11 CO_2 and N_2 adsorption capacity gradients for the activated sample **5"**

7.2.4 Adsorption Kinetics

Linear driving force (LDF) model is one of the simplest kinetic models, which provide satisfactory descriptions, in most cases, of the adsorption kinetics of various gases on carbon molecular sieves and activated carbons.[55] Recently, LDF model and its derivative version double exponential (DE) model were chosen to describe the kinetic profiles for gases or vapors adsorption on flexible MOFs.[29,31,55-56] In our case, DE model with two parameters does not provide better fitting precision than LDF model with just a single parameter, so we employ LDF model to provide a simple kinetic profile. Although the application LDF model does not indicate that the diffusion barrier through pore entrance is the only diffusion barrier during adsorption process, the single kinetic rate constant provides the most direct comparison among sorption points. The LDF model is expressed by the following equation:

$$\frac{M_t}{M_e} = 1 - exp(-kt) \qquad 7.2$$

where M_t is the adsorption amount at time t, M_e is the mass or molar capacity at equilibrium, and k is the kinetic rate constant.

Figure 7.12 shows the kinetic rate constant k changing with relative pressure for CO_2 adsorption at different temperature on activated sample **1”**. At 298 K, k does not change much with the pressure except in the very low range of pressure, which indicates that adsorption capacity of CO_2 develops just with the increase of pressure, without involving “gate” opening process. In other words, 20 bar of pressure at 298 K for CO_2 is not high enough to open the “gate” due to the energy barrier. At 288 K and 278 K, the examined pressure range involves “gate” opening and closing processes, and apparent variety in k could be observed. The lower k values indicate the slower kinetic process.

Thus, compared with normal adsorption process, the adsorption or desorption points on isotherms involving "gate" opening or closing take much longer time to arrive at equilibrium so that "gate" opening or closing is the rate-determining step compared with molecular diffusion.

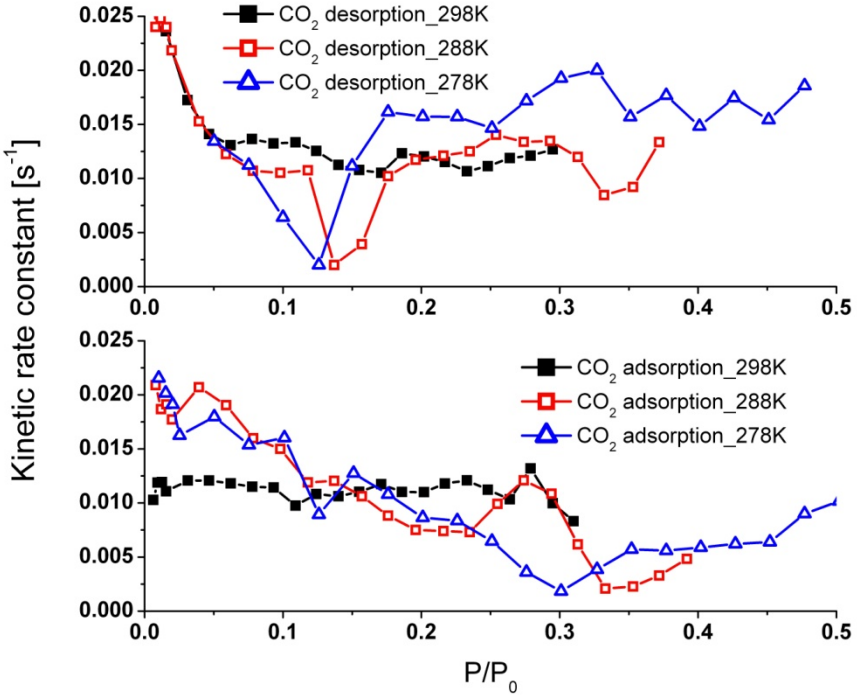

Figure 7.12 CO_2 adsorption kinetic rate constant *k* with relative pressure (P/P_0) for the activated sample **5"**

7.3 CONCLUSIONS

In summary, we present here a unique three-dimensional lanthanide MOF ($[La(BTB)(H_2O)\cdot 3DMF]_n$), which possesses rare chiral space group ($P6_522$) and the highest thermal stability (up to 560 ^oC) among the reported porous MOFs so far. Powder X-ray thermodiffraction experiments indicate the structural transformation results from removal of guest molecules. After solvent exchange and activation, N_2 adsorption isotherms of the activated sample present an interesting breathing effect, and yield the highest surface area (experimental 1014 m^2/g and calculated 1385.17 m^2/g) among the reported porous lanthanide MOFs so far. Furthermore, high pressure adsorption experiments of CO_2, CH_4 and N_2 were performed at ambient temperature. Particularly, equilibrium and kinetic investigation of CO_2 adsorption provided deeper information about the mechanism and potential application of adsorption breathing effects. The following conclusions about breathing effects could be drawn from this work:

1. Breathing effects could be observed on N_2 and CO_2 isotherms at undercritical adsorption temperature, and the desorption is completely reversible at reduced pressure, demonstrating that gas sorption involves a pressure-dependent “gate” opening and closing process. The energy required for "gate" opening is estimated from pressure-volume work equation and gives 17.1 J/g.
2. Lower adsorption temperature results in that the whole breathing cycle of CO_2 starts at lower relative pressure, but still at approximately the same range of N_2 adsorbed. Basically, the “gate” opening process occurs at

around 0.3-0.45 of relative pressure, while the "gate" closing process occurs at less than 0.15 of relative pressure.

3. Although lower adsorption temperature causes faster "gate" opening and closing rate, it seems that "gate" opening process is slower than "gate" closing process.
4. The adsorption or desorption points on isotherms involving "gate" opening or closing take much longer time to arrive at equilibrium so that "gate" opening or closing is the rate-determining step compared with molecular diffusion.

7.4 REFERENCES

(1) Choi, S.; Drese, J. H.; Jones, C. W. *Chemsuschem* **2009**, *2*, 796.

(2) Ma, S. Q. *Pure Appl Chem* **2009**, *81*, 2235.

(3) Ma, S. Q.; Zhou, H. C. *Chem Commun* **2010**, *46*, 44.

(4) Zou, R. Q.; Abdel-Fattah, A. I.; Xu, H. W.; Zhao, Y. S.; Hickmott, D. D. *Crystengcomm* **2010**, *12*, 1337.

(5) Snurr, R. Q.; Hupp, J. T.; Nguyen, S. T. *Aiche J* **2004**, *50*, 1090.

(6) Lin, W. B. *Top Catal* **2010**, *53*, 869.

(7) Ma, L. Q.; Abney, C.; Lin, W. B. *Chem Soc Rev* **2009**, *38*, 1248.

(8) Lee, J.; Farha, O. K.; Roberts, J.; Scheidt, K. A.; Nguyen, S. T.; Hupp, J. T. *Chem Soc Rev* **2009**, *38*, 1450.

(9) An, J. Y.; Geib, S. J.; Rosi, N. L. *J Am Chem Soc* **2009**, *131*, 8376.

(10) Horcajada, P.; Chalati, T.; Serre, C.; Gillet, B.; Sebrie, C.; Baati, T.; Eubank, J. F.; Heurtaux, D.; Clayette, P.; Kreuz, C.; Chang, J. S.; Hwang, Y. K.; Marsaud, V.; Bories, P. N.; Cynober, L.; Gil, S.; Ferey, G.; Couvreur, P.; Gref, R. *Nat Mater* **2010**, *9*, 172.

(11) Ferey, G.; Serre, C. *Chem Soc Rev* **2009**, *38*, 1380.

(12) Bureekaew, S.; Shimomura, S.; Kitagawa, S. *Science and Technology of Advanced Materials* **2008**, *9*.

(13) Hamon, L.; Llewellyn, P. L.; Devic, T.; Ghoufi, A.; Clet, G.; Guillerm, V.; Pirngruber, G. D.; Maurin, G.; Serre, C.; Driver, G.; van Beek, W.; Jolimaitre, E.; Vimont, A.; Daturi, M.; Ferey, G. *J Am Chem Soc* **2009**, *131*, 17490.

(14) Millange, F.; Guillou, N.; Medina, M. E.; Ferey, G.; Carlin-Sinclair, A.; Golden, K. M.; Walton, R. I. *Chem Mater* **2010**, *22*, 4237.

(15) Millange, F.; Serre, C.; Guillou, N.; Ferey, G.; Walton, R. I. *Angew Chem Int Edit* **2008**, *47*, 4100.

(16) Horcajada, P.; Serre, C.; Maurin, G.; Ramsahye, N. A.; Balas, F.; Vallet-Regi, M.; Sebban, M.; Taulelle, F.; Ferey, G. *J Am Chem Soc* **2008**, *130*, 6774.

(17) Uemura, T.; Yanai, N.; Kitagawa, S. *Chem Soc Rev* **2009**, *38*, 1228.

(18) Mu, B.; Huang, Y. G.; Walton, K. S. *Crystengcomm* **2010**, *12*, 2347.

(19) Mu, B.; Li, F.; Walton, K. S. *Chem Commun* **2009**, 2493.

(20) Mu, B.; Schoenecker, P. M.; Walton, K. S. *J Phys Chem C* **2010**, *114*, 6464.

(21) Kitaura, R.; Seki, K.; Akiyama, G.; Kitagawa, S. *Angew Chem Int Edit* **2003**, *42*, 428.

(22) Llewellyn, P. L.; Bourrelly, S.; Serre, C.; Filinchuk, Y.; Ferey, G. *Angew Chem Int Edit* **2006**, *45*, 7751.

(23) Chen, B. L.; Ma, S. Q.; Hurtado, E. J.; Lobkovsky, E. B.; Zhou, H. C. *Inorg Chem* **2007**, *46*, 8490.

(24) Bourrelly, S.; Llewellyn, P. L.; Serre, C.; Millange, F.; Loiseau, T.; Ferey, G. *J Am Chem Soc* **2005**, *127*, 13519.

(25) Suh, M. P.; Cheon, Y. E.; Lee, E. Y. *Chem-Eur J* **2007**, *13*, 4208.

(26) Couck, S.; Denayer, J. F. M.; Baron, G. V.; Remy, T.; Gascon, J.; Kapteijn, F. *J Am Chem Soc* **2009**, *131*, 6326.

(27) Thallapally, P. K.; Tian, J.; Kishan, M. R.; Fernandez, C. A.; Dalgarno, S. J.; McGrail, P. B.; Warren, J. E.; Atwood, J. L. *J Am Chem Soc* **2008**, *130*, 16842.

(28) Choi, H. S.; Suh, M. P. *Angew Chem Int Edit* **2009**, *48*, 6865.

(29) Fletcher, A. J.; Cussen, E. J.; Prior, T. J.; Rosseinsky, M. J.; Kepert, C. J.; Thomas, K. M. *J Am Chem Soc* **2001**, *123*, 10001.

(30) Maji, T. K.; Uemura, K.; Chang, H. C.; Matsuda, R.; Kitagawa, S. *Angew Chem Int Edit* **2004**, *43*, 3269.

(31) Culp, J. T.; Smith, M. R.; Bittner, E.; Bockrath, B. *J Am Chem Soc* **2008**, *130*, 12427.

(32) Kitaura, R.; Fujimoto, K.; Noro, S.; Kondo, M.; Kitagawa, S. *Angew Chem Int Edit* **2002**, *41*, 133.

(33) Seo, J.; Matsuda, R.; Sakamoto, H.; Bonneau, C.; Kitagawa, S. *J Am Chem Soc* **2009**, *131*, 12792.

(34) Seki, K. *Phys Chem Chem Phys* **2002**, *4*, 1968.

(35) Ma, S. Q.; Wang, X. S.; Manis, E. S.; Collier, C. D.; Zhou, H. C. *Inorg Chem* **2007**, *46*, 3432.

(36) Millange, F.; Serre, C.; Ferey, G. *Chem Commun* **2002**, 822.

(37) Serre, C.; Millange, F.; Thouvenot, C.; Nogues, M.; Marsolier, G.; Louer, D.; Ferey, G. *J Am Chem Soc* **2002**, *124*, 13519.

(38) Devic, T.; Horcajada, P.; Serre, C.; Salles, F.; Maurin, G.; Moulin, B.; Heurtaux, D.; Clet, G.; Vimont, A.; Greneche, J. M.; Le Ouay, B.; Moreau, F.; Magnier, E.; Filinchuk, Y.; Marrot, J.; Lavalley, J. C.; Daturi, M.; Ferey, G. *J Am Chem Soc* **2010**, *132*, 1127.

(39) Serre, C.; Bourrelly, S.; Vimont, A.; Ramsahye, N. A.; Maurin, G.; Llewellyn, P. L.; Daturi, M.; Filinchuk, Y.; Leynaud, O.; Barnes, P.; Ferey, G. *Adv Mater* **2007**, *19*, 2246.

(40) Hill, R. J.; Long, D. L.; Hubberstey, P.; Schroder, M.; Champness, N. R. *J Solid State Chem* **2005**, *178*, 2414.

(41) Morris, R. E.; Bu, X. H. *Nat Chem* **2010**, *2*, 353.

(42) Luo, J. H.; Xu, H. W.; Liu, Y.; Zhao, Y. S.; Daemen, L. L.; Brown, C.; Timofeeva, T. V.; Ma, S. Q.; Zhou, H. C. *J Am Chem Soc* **2008**, *130*, 9626.

(43) Guo, X. D.; Zhu, G. S.; Li, Z. Y.; Sun, F. X.; Yang, Z. H.; Qiu, S. L. *Chem Commun* **2006**, 3172.

(44) Harbuzaru, B. V.; Corma, A.; Rey, F.; Atienzar, P.; Jorda, J. L.; Garcia, H.; Ananias, D.; Carlos, L. D.; Rocha, J. *Angew Chem Int Edit* **2008**, *47*, 1080.

(45) Ma, S. Q.; Yuan, D. Q.; Wang, X. S.; Zhou, H. C. *Inorg Chem* **2009**, *48*, 2072.

(46) Devic, T.; Serre, C.; Audebrand, N.; Marrot, J.; Ferey, G. *J Am Chem Soc* **2005**, *127*, 12788.

(47) Wang, G.; Song, T. Y.; Fan, Y.; Xu, J. N.; Wang, M.; Wang, L. P.; Zhang, L. R.; Wang, L. *Inorg Chem Commun* **2010**, *13*, 95.

(48) Pan, L.; Adams, K. M.; Hernandez, H. E.; Wang, X. T.; Zheng, C.; Hattori, Y.; Kaneko, K. *J Am Chem Soc* **2003**, *125*, 3062.

(49) Chen, J. X.; Chen, Z. X.; Yu, T.; Weng, L. H.; Tu, B.; Zhao, D. Y. *Micropor Mesopor Mat* **2007**, *98*, 16.

(50) Rosi, N. L.; Kim, J.; Eddaoudi, M.; Chen, B. L.; O'Keeffe, M.; Yaghi, O. M. *J Am Chem Soc* **2005**, *127*, 1504.

(51) O'Keeffe, M.; Peskov, M. A.; Ramsden, S. J.; Yaghi, O. M. *Accounts Chem Res* **2008**, *41*, 1782.

(52) Kondo, A.; Noguchi, H.; Carlucci, L.; Proserpio, D. M.; Ciani, G.; Kajiro, H.; Ohba, T.; Kanoh, H.; Kaneko, K. *J Am Chem Soc* **2007**, *129*, 12362.

(53) Duren, T.; Millange, F.; Ferey, G.; Walton, K. S.; Snurr, R. Q. *J Phys Chem C* **2007**, *111*, 15350.

(54) Beurroies, I.; Boulhout, M.; Llewellyn, P. L.; Kuchta, B.; Ferey, G.; Serre, C.; Denoyel, R. *Angew Chem Int Edit* **2010**, *49*, 7526.

(55) Fletcher, A. J.; Cussen, E. J.; Bradshaw, D.; Rosseinsky, M. J.; Thomas, K. M. *J Am Chem Soc* **2004**, *126*, 9750.

(56) Choi, H. J.; Dinca, M.; Long, J. R. *J Am Chem Soc* **2008**, *130*, 7848.

CHAPTER 8

HIGH PRESSURE GAS ADSORPTION EQUILIBRIUM ON AN IMPREGNATED ACTIVATED CARBON

Understanding adsorption in porous materials is a fundamental step in designing adsorption processes including gas separation, purification, and storage.[1-4] Adsorption equilibrium data over a wide range of pressures and temperatures are needed to effectively develop new adsorption processes, understand adsorption mechanisms, and simulate fixed-bed systems. The need for single-component adsorption data is still most important in this regard. Single-component adsorption equilibrium experiments are used to characterize different adsorbent surfaces and investigate the nature of their interactions with the adsorbate molecules. Thanks to high-quality adsorption equilibrium data, various adsorption models can be developed more accurately to elucidate the adsorption mechanism and simplify the design process. Furthermore, thermodynamic properties, which can be derived from isotherm data, including Henry's law constants, isosteric heats, heat capacities, and the entropy change on adsorption are required for simulating cyclic non-isothermal adsorption processes such as temperature and pressure swing adsorption. Thus, it is difficult or even impossible without the knowledge of the adsorption equilibrium to simulate and design an adsorption process.[5]

Among the porous materials used commercially, activated carbon is one of the most complex and also one of the most widely studied. However, single-component adsorption isotherms measured over ranges of pressure and temperature on impregnated activated carbons (I-AC) are relatively scarce in the literature. The I-AC studied here is

BPL activated carbon (manufactured by Calgon Carbon Corporation) impregnated primarily with copper and zinc. Water isotherms have been reported for a similar material,[6] but no studies have been published on the adsorption of carbon dioxide, carbon monoxide, and methane. This paper presents experimental adsorption and desorption isotherms of CO_2, CH_4, and CO on I-AC over the temperature range 25 ^oC to 45 ^oC and a wide range of pressure from (0 to 24) bar. Furthermore, the adsorption isotherms on the I-AC are compared with the isotherms from BPL and other activated carbons by fitting the data to the Toth equation.

8.1 MATERIALS, METHODS, AND CHARACTERIZATION

BPL Carbon (Calgon Carbon Corporation) is produced from bituminous coal and is highly activated to give a surface area and pore volume of approximately 1250 m^2/g and 0.56 cm^3/g, respectively.[7] The carbon has substantial meso- and macroporosity to provide for rapid internal mass transfer and to accommodate the application of the reactive impregnates. Scanning electron microscopy (SEM) images (Figure 8.1) were conducted on a Hitachi SEM S-3500N equipped with a model S-6542 absorbed electron detector, and the compositional analysis was obtained by energy dispersive spectroscopy (EDS, Oxford-INCA). SEM results present apparent irregularity of the I-AC in shape, and particle size is around millimeters to micrometers. Such roughness of surface is favorable to increase inter-space among particles and to increase adsorption amount on adsorbent's surface. The compositional analysis given in Figure 8.2 shows that the primary impregnate loadings are 4.4 wt% copper and 4.1 wt% zinc.

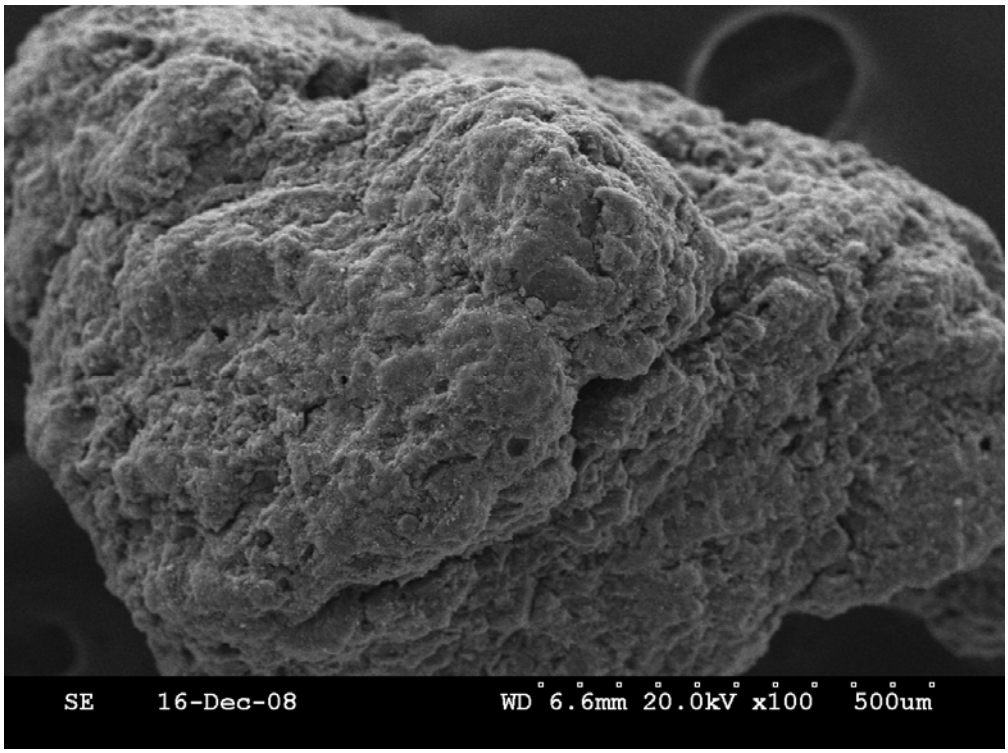

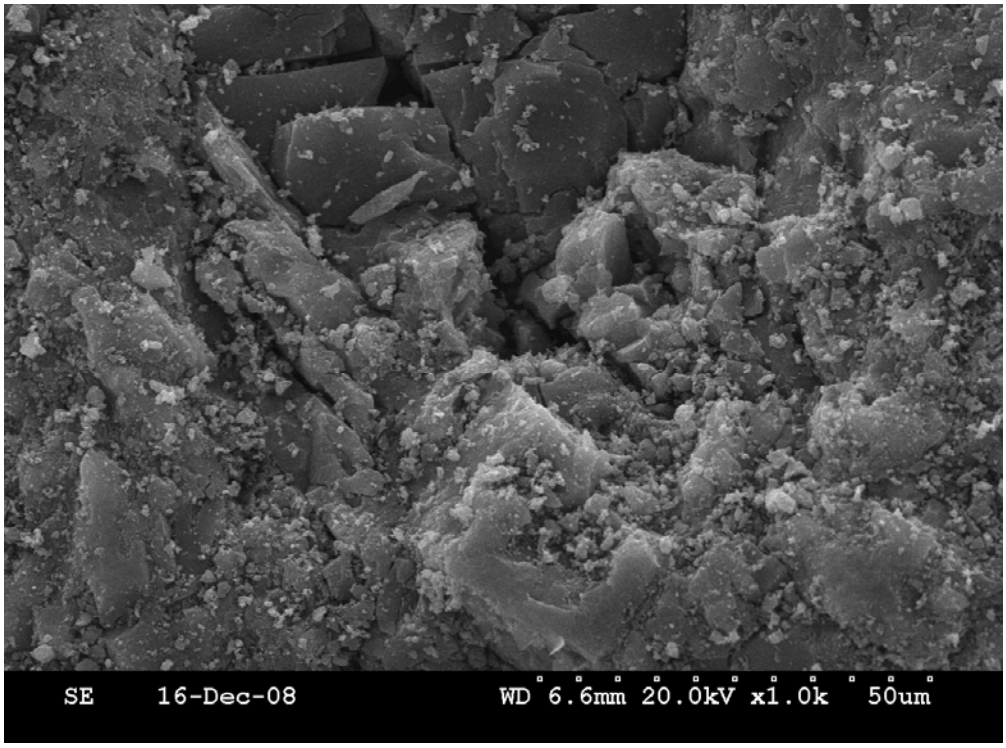

Figure 8.1 SEM images of the I-AC.

Element	Weight %	Atomic %
C K	78.01	87.09
O K	12.29	10.29
Al K	0.29	0.14
Si K	0.38	0.18
S K	0.45	0.19
Cu K	4.43	0.94
Zn K	4.15	0.85
Totals	100.00	

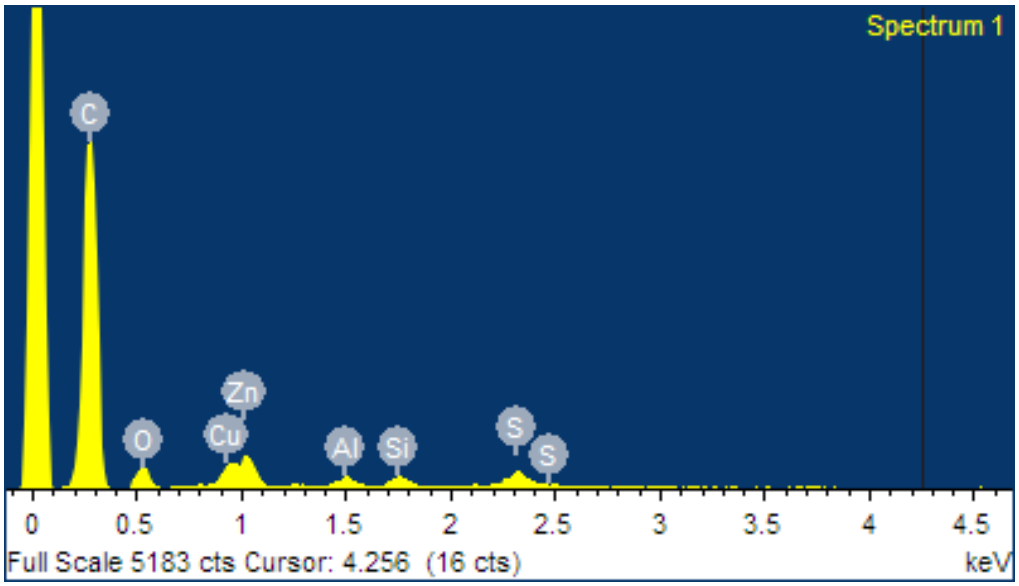

Figure 8.2 Compositional analysis of the I-AC using energy dispersive spectroscopy (EDS, Oxford-INCA).

A nitrogen adsorption isotherm (Figure 8.3) of the I-AC at 77 K was measured with Autosorb-1 from the Quantachrome Corporation. The isotherm presents a major type-I Langmuir isotherm together with a minor type-II isotherm near the saturated vapor pressure, indicating monolayer coverage may be complete. In addition, a slight hysteresis loop appears at higher pressure, which was closed at about $P/P_0 = 0.4$. Specific surface area calculated using the BET and Langmuir models are 922 m^2/g and 1238 m^2/g, respectively. The BET constant and Langmuir constant are 799.4 and 38.5, respectively, in which the linear BET region for the I-AC occurs at relative pressures lower than 0.12, while the linear Langmuir region for the I-AC occurs at relative pressures lower than 0.70. The total pore volume is 0.51 mL/g at $P/P_0 = 0.99513$, while the average pore diameter is 2.22 nm. A t-plot was fitted with the de Boer equation (Figure 8.4). The pore size distribution was calculated using the Dubinin-Astakhov (DA) method, as shown in Figure 8.5, and the micropore structure analysis results are listed in Table 8.1.

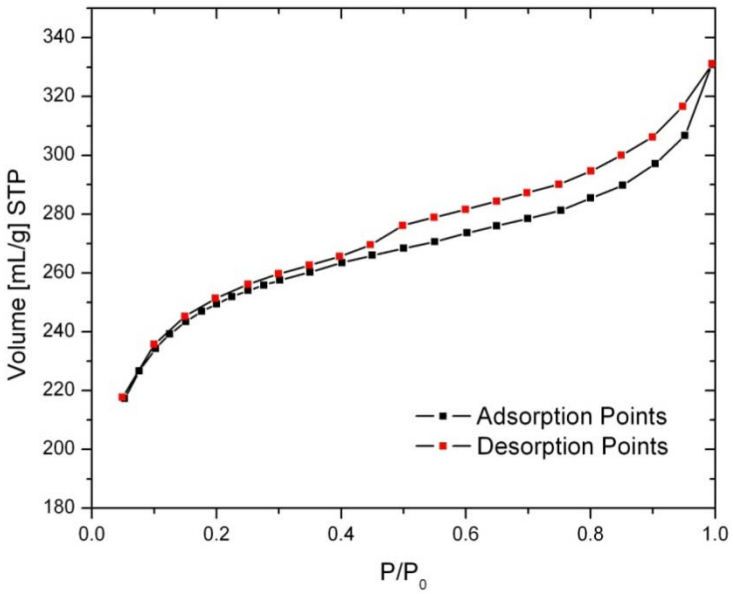

Figure 8.3 Nitrogen isotherm at 77K.

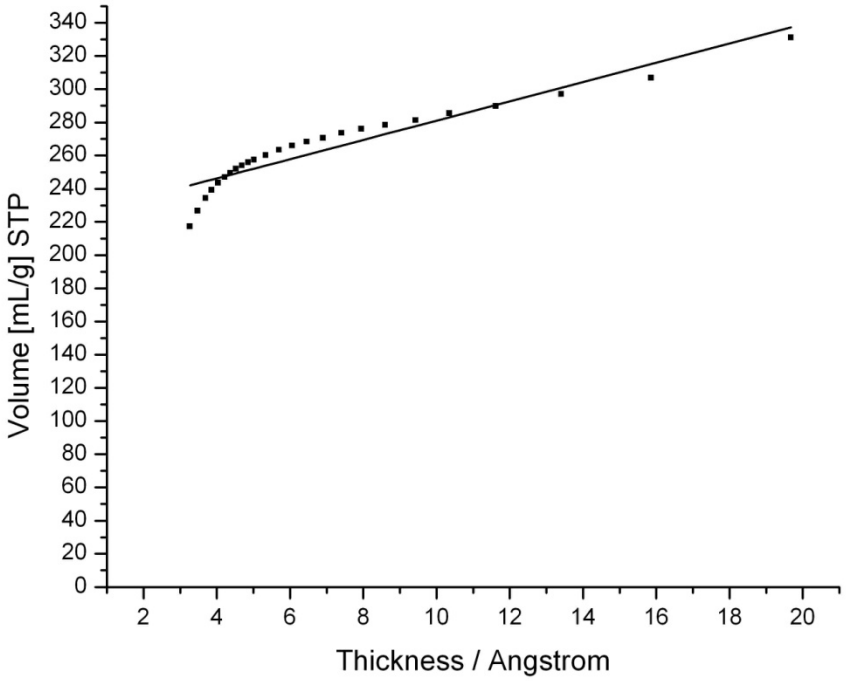

Figure 8.4 t-plot of the I-AC.

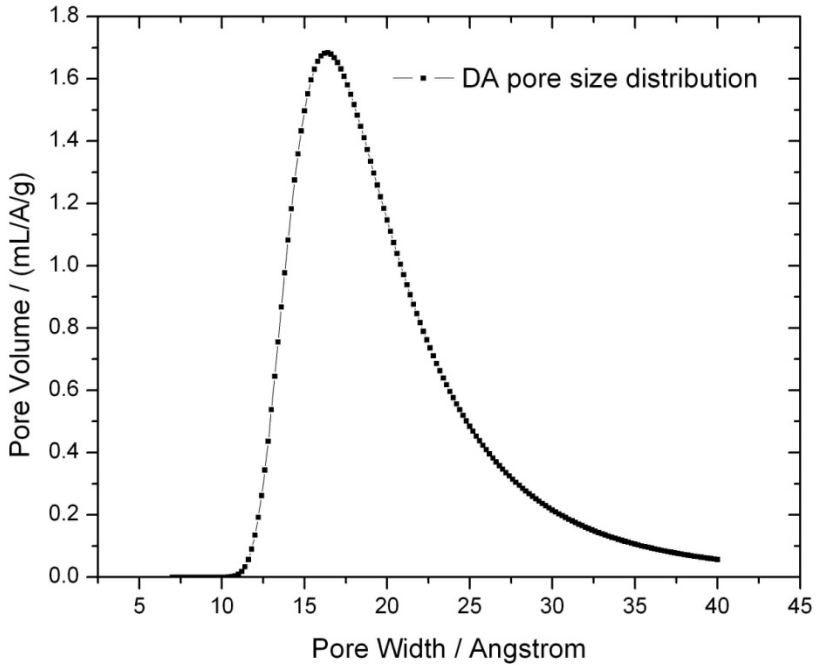

Figure 8.5 DA pore size distribution plot.

Table 8.1 Micropore structure analysis of I-AC.

N_2 isotherm	Total pore volume / (mL/g)	0.51
	Average Pore Diameter / (nm)	2.22
	Hysteresis loop rang (P/P_0)	0.4 - 1.0
BET method	Surface Area / (m^2/g)	922
	BET Constant	799.4
	Linear range	0.05 – 0.12
Langmuir method	Surface Area / (m^2/g)	1238
	Langmuir Constant	38.5
	Linear range	0.05 – 0.70
t-plot (de Boer equation)	Slope	5.801
	Y - Intercept	223.036
	External Surface Area / (m^2/g)	89.7
	Micro-pore volume / (mL/g)	0.345
	Micro-pore area / (m^2/g)	831.9
D-A method	Characteristic energy / (kJ/mol)	6.00
	n	1.90
	pore diameter / (nm)	1.64

8.2 HIGH PRESSURE GAS ADSORPTION STUDY

A gravimetric adsorption apparatus (the GHP-100 gravimetric high pressure analyzer with C. I. microbalance from the VTI Corporation) was employed to measure the single-component adsorption isotherms. All adsorbate gases were purchased from the Linweld Company including carbon dioxide (LW617, bone dry 99.8 %), methane (LW913, ultra-high purity 99.99 %), carbon monoxide (LW609, CP 99.5 %), helium (LW800, UHP/ZERO), and nitrogen (LW411, UHP/ZERO). Before the adsorption measurement, the I-AC was activated by heating at 120 ^{o}C in vacuum for 24 h to remove moisture and other adsorbed gases. A 150 mg sample was placed in the sample cartridge of the GHP-100 gravimetric high pressure analyzer to undergo continued outgassing at 110 ^{o}C in a vacuum for 12 h. The sample weight was recorded every 2 minutes or per 0.01 % by mass. After outgassing, the system temperature was adjusted to the adsorption temperature of interest, and the sample cell was kept under vacuum for 30 min before starting the first adsorption point. All adsorption equilibrium data were collected after maintaining a given stable pressure for 30 min. After finishing the adsorption and desorption runs at the given temperature, the I-AC was regenerated by heating at 110 ^{o}C in a vacuum for 12 h until a constant sample weight was achieved. The sample was then reused in subsequent adsorption experiments.

8.2.1 Adsorption Isotherms.

The data for adsorption and desorption of methane, carbon dioxide, and carbon monoxide on the I-AC were obtained for temperatures ranging from 298 K to 318 K and pressures up to 24 bar. The maximum adsorption capacities of CH_4 on the I-AC at 298 K, 308 K, and 318 K are (3.26, 3.16, and 3.07) mmol/g, respectively, at 24.2 bar. The

maximum capacities of CO_2 at 298 K, 308 K, and 318 K are (6.15, 5.83, and 5.59) mmol/g, respectively, at 24.2 bar, and the capacities of CO at these temperatures are (2.01, 2.06, and 2.21) mmol/g, respectively, at 17.1 bar. For CH_4 and CO_2, the adsorption isotherms are reversible, and there is no hysteresis in the range of examined temperature and pressure (Figure 8.6-8.7). However, CO appears to undergo chemisorption and displays a hysteresis loop upon desorption that becomes more pronounced with increasing temperature (Figure 8.8-8.9).

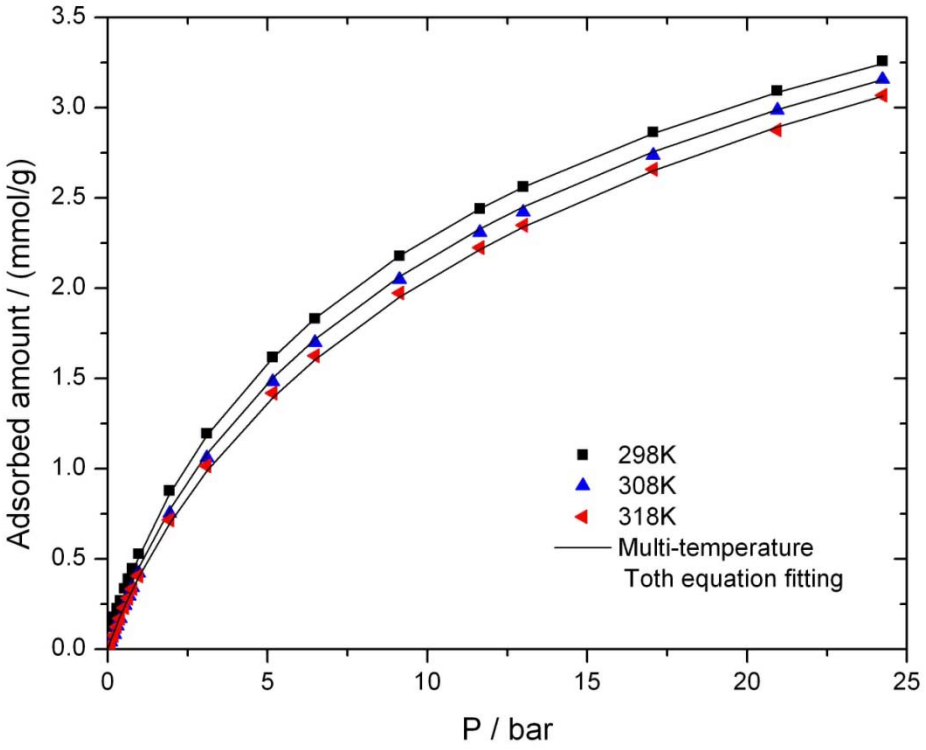

Figure 8.6 CH_4 isotherms on the I-AC at different temperatures.

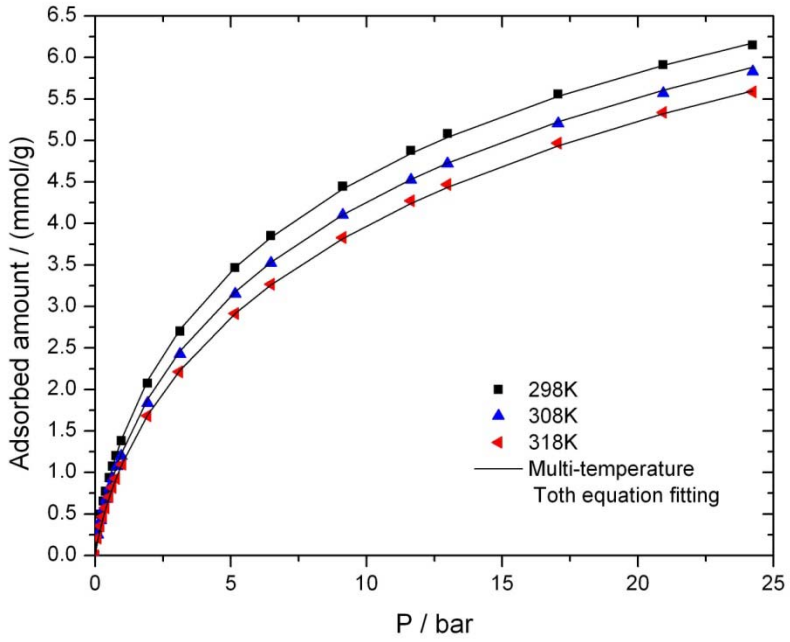

Figure 8.7 CO_2 isotherms on the I-AC at different temperatures.

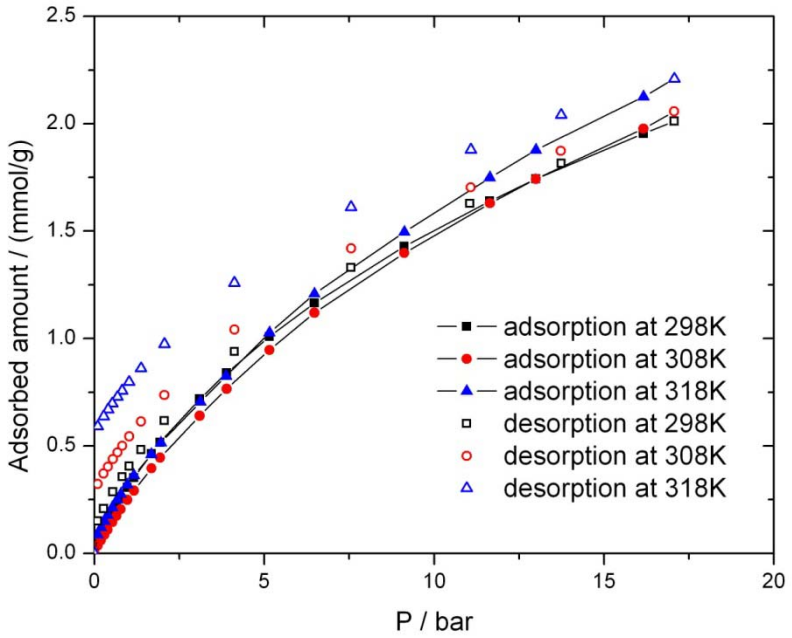

Figure 8.8 CO isotherms on I-AC at different temperatures.

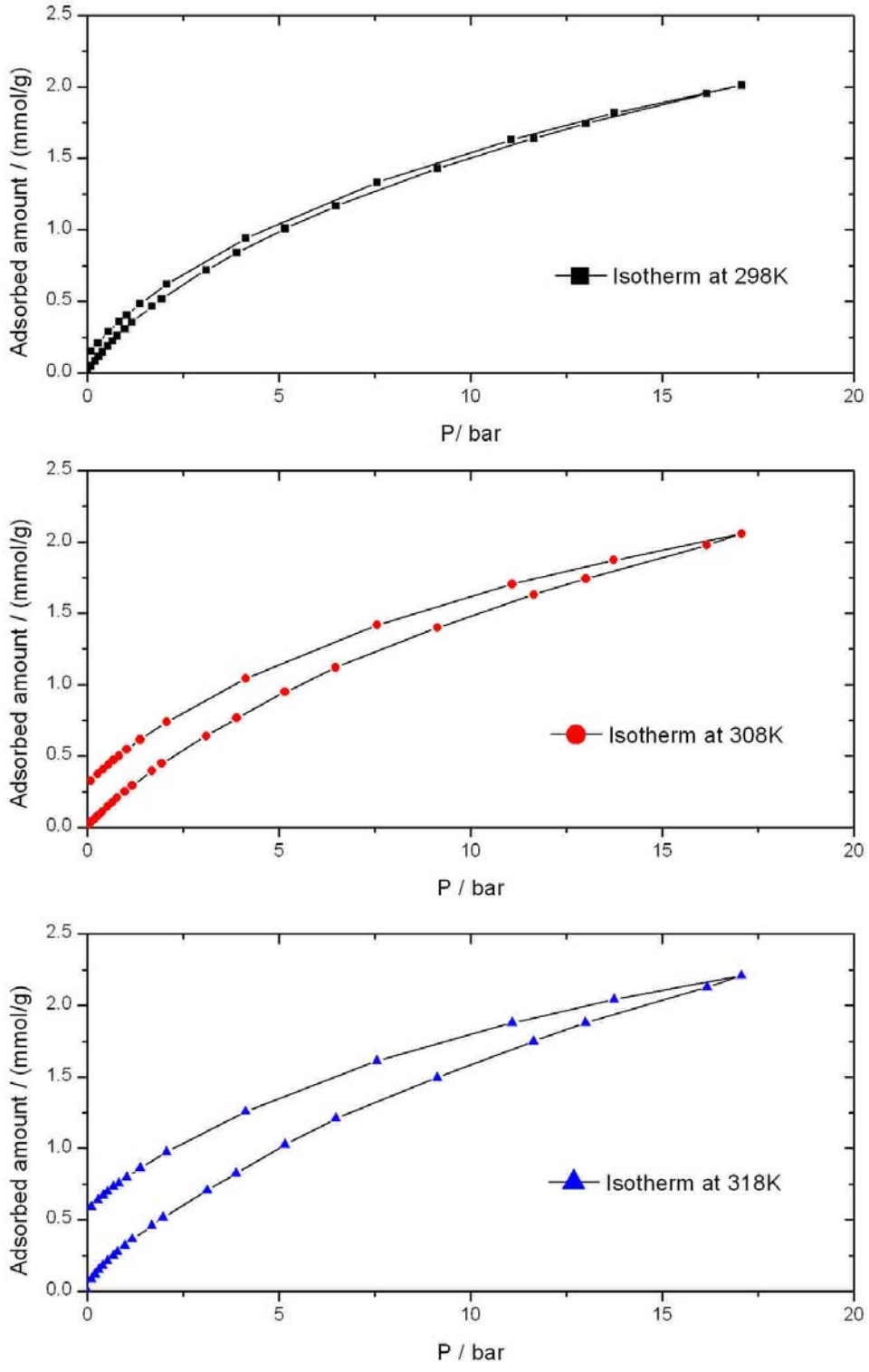

Figure 8.9 Development of CO hysteresis loop with increasing temperature**.**

Because of the simplicity of the Toth equation in form and its correct thermodynamic consistency at low and high pressures, it has been recommended for fitting the adsorption isotherms of hydrocarbons on activated carbon.[8] The Toth equation has also been used successfully to fit CO_2 and CH_4 adsorption data in a variety of activated carbons (Table 8.2).[9-14] The Toth equation is given by:

$$N = \frac{N_S bP}{\left[1 + (bP)^m\right]^{1/m}} \qquad 8.1$$

where N_s is the monolayer capacity, b is related to the adsorption affinity at low pressure, and m characterizes the system heterogeneity. The deviation of m from unity indicates the heterogeneity of the system. When m = 1, the Toth equation reduces to the Langmuir equation. Using the Toth equation parameters listed in Table 8.2, CH_4 and CO_2 isotherms of various activated carbons at 298 K are graphically presented in Figure 8.10 and Figure 8.11 for direct comparison with I-AC. The BET surface area and total pore volume of the various activated carbons are listed in Table 8.3 for further comparison.

Among the examined activated carbons, Maxsorb has the highest surface area and the largest total pore volume. Thus, it is not surprising for it to present the highest adsorption capacities for CH_4. As shown in Table 8.2, the parameter m from Calgon-AC is the closest to unity at room temperature, which indicates that Calgon-AC is more homogeneous than other activated carbons. Activated carbon obtained from coconut shells (Coconut-AC) demonstrates unexpectedly low CH_4 capacity considering its high surface area. However, at low pressure, it presents higher adsorption loadings compared to I-AC and BPL, which is consistent with the higher adsorption affinity parameter b of Coconut-AC. With an increase in pressure, its capacity does not increase significantly and is much less than that of BPL and I-AC at 24 bar due to the low monolayer capacity.

These experimental results also confirm the conclusion of Bhatia and Myers.[15] They studied the effect of heterogeneity on adsorptive storage of H_2 and CH_4 on activated carbon from a thermodynamic viewpoint, and demonstrated that heterogeneity is less helpful and even detrimental for CH_4 storage on activated carbon. The impregnated activated carbon has less surface area and total pore volume than BPL, which is responsible for the decreased adsorption capacities of CH_4. For CO_2 adsorption equilibrium, the isotherms followed the order of increasing capacity with increasing surface area.

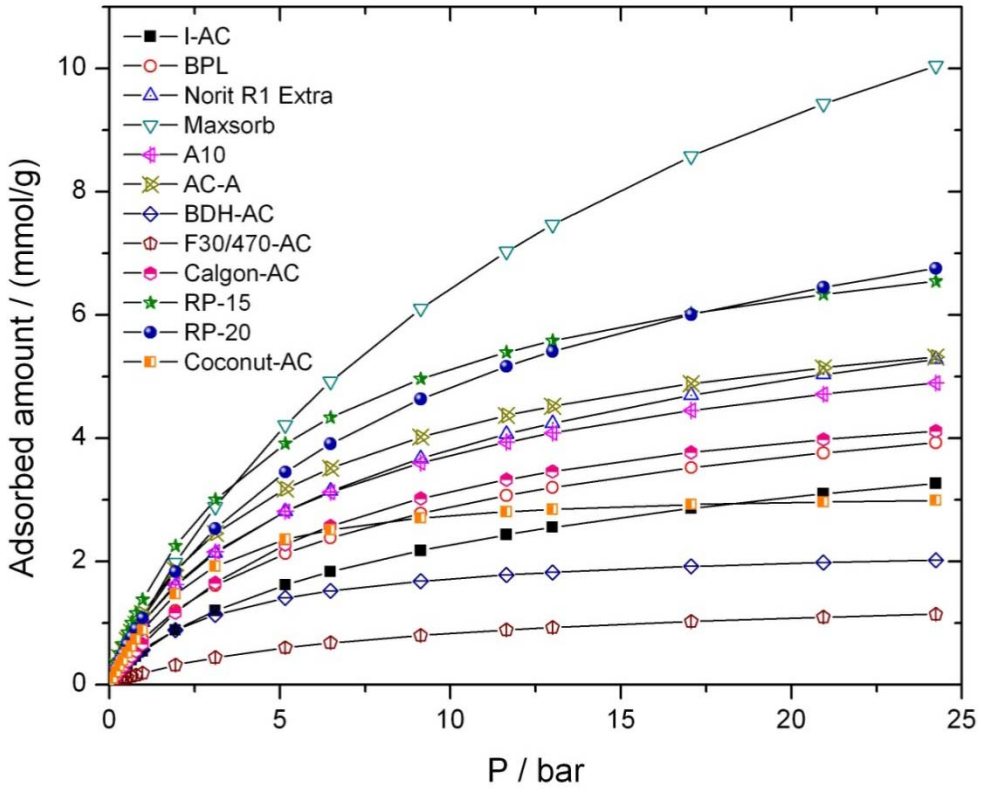

Figure 8.10 Comparison of CH_4 isotherms at 298 K on varied activated carbons calculated using Toth Equation (the data of BDH-AC, F30/470-AC, Calgon-AC, RP-15, and RP-20 are at 303 K, while others are at 298 K).

Table 8.2 Toth equation parameters for different activated carbons.

Adsorbents	T	CH_4			CO_2			CO		
		N_s /	b /	m	N_s /	b /	m	N_s /	b /	m
	K	mmol g^{-1}	bar^{-1}		mmol g^{-1}	bar^{-1}		mmol g^{-1}	bar^{-1}	
I-AC	298	7.509	0.128	0.527	13.79	0.296	0.439	10.36	0.053	0.437
	308	5.624	0.094	0.744	14.14	0.232	0.437	9.391	0.035	0.553
	318	5.741	0.091	0.714	14.65	0.186	0.436	10.20	0.044	0.496
BPL[9]	273	6.813	0.300	0.647	13.70	0.540	0.561			
	298	6.809	0.180	0.616	12.00	0.384	0.533			
	323	7.686	0.095	0.578	9.438	0.134	0.77			
Norit R1 Extra[9]	298	10.80	0.184	0.525	16.8	0.223	0.583			
Maxsorb[9]	298	20.35	0.064	0.768	41.88	0.058	0.827			
A10[9]	298	7.573	0.220	0.658	11.07	0.330	0.744			
AC-A[9]	298	7.524	0.241	0.717	10.43	0.384	0.817			
Coconut-AC[10]	298	3.109	0.336	1.382						
BDH-AC[12]	303	2.367	0.361	0.878						
F30/470-AC[13]	303	1.767	0.14	0.761						
Calgon-AC[11]	293	5.812	0.173	0.998						
	303	5.272	0.147	1.085						
RP-15[14]	293	8.688	0.217	0.776						
	303	8.904	0.232	0.773						
	313	9.563	0.153	0.665						
RP-20[14]	293	11.67	0.173	0.694						
	303	11.514	0.136	0.693						
	313	12.484	0.101	0.650						

Table 8.3 Surface area and total pore volume of activated carbons.

Adsorbent	I-AC	BPL[7]	Norit R1 Extra[9]	Maxsorb[9]
BET (m^2/g)	922	1250	1450	3250
V (mL/g)	0.51	0.56	0.47	1.79
Adsorbent	BDH-AC[12]	F30/470-AC[13]	Coconut-AC[10]	RP-15[14]
BET (m^2/g)	1220	994	2100	1493
V (mL/g)	0.534	0.497	-	0.658
Adsorbent	A10[9]	AC-A[9]	RP-20[14]	Calgon_AC[11]
BET (m^2/g)	1200	1207	1853	1200
V (mL/g)	0.53	0.54	0.765	0.72

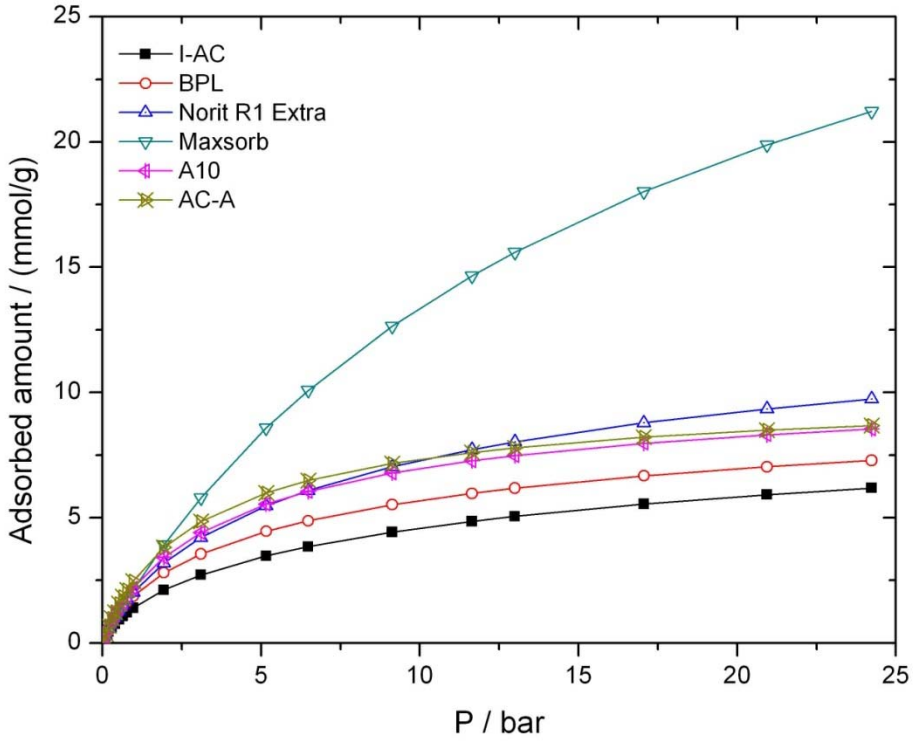

Figure 8.11 Comparison of CO_2 isotherms at 298 K on various activated carbons calculated using the Toth Equation.

8.2.2 Henry's Law Constants and Heat of Adsorption.

Henry's law constants k_H were calculated from the product of the Toth equation parameters $N_s \times b$, which indicates the affinity between the sorbate and sorbent surface at low coverage. The Henry's law constants are listed in Table 8.4,[9-14,16] and the values from I-AC and BPL are graphically presented as a function of temperature in Figure 8.12. From Table 8.4 and Figure 8.12, we can observe that Henry's law constants of CH_4 for I-AC are slightly smaller than the corresponding values for BPL within the examined temperature range, and k_H for both CH_4 and CO_2 decrease with an increase of temperature.

The isosteric heat of adsorption on the I-AC is calculated by the Clausius-Clapeyron equation combined with the multi-temperature Toth equation, given by:

$$N = \frac{N_S bP}{\left[1 + (bP)^m\right]^{1/m}} \tag{8.2}$$

$$b = b_0 \cdot \exp\left[\frac{Q}{RT_0}\left(\frac{T_0}{T} - 1\right)\right] \tag{8.3}$$

$$m = m_0 + a\left(1 - \frac{T_0}{T}\right) \tag{8.4}$$

$$N_S = N_{S,0} \cdot \exp\left[c\left(1 - \frac{T}{T_0}\right)\right] \tag{8.5}$$

where T_0 is the reference temperature, 318 K; b_0 is the adsorption affinity at the reference temperature; Q is the heat of adsorption at zero coverage; $N_{S,0}$ is the monolayer capacity at the reference temperature; m_0 indicates heterogeneity of the system at the reference temperature; and *a, c* are fitting parameters that do not have a sound theoretical basis.[8] The comparison of experimental adsorption data and the multi-temperature Toth

equation fitting are graphically displayed in Figure 8.6 and Figure 8.7, and the parameters are given in Table 8.5. The multi-temperature Toth equation provides a very successful fit of our experimental data. Thus, the isosteric heat of adsorption for CH_4 and CO_2 can be calculated from the fitting parameters. As presented in Figure 8.13, the isosteric heat of adsorption for CO_2 increases substantially with an increase in the loading, which demonstrates that adsorbate interactions between CO_2 molecules are becoming more significant. As for CH_4, the negligible intermolecular interaction between CH_4 molecules causes a decrease in the isosteric heat of adsorption as a result of the disappearance of favorable adsorption sites. The heats of adsorption near zero coverage for various activated carbons are listed in Table 8.6.[9-14,16-18] Among all examined activated carbons, Calgon-AC has the highest heat of adsorption for CH_4, while BPL AC has the highest heat of adsorption for CO_2. The heats of adsorption for CO_2 are consistent with the Henry's constants, but no clear correlation is observed for methane. Compared with BPL AC, the heats of adsorption for CH_4 and CO_2 on the I-AC decrease 7.5 % and 29.2 % respectively, implying a negative effect of the impregnated form to CH_4 and CO_2 adsorption.

Table 8.4 Henry's law constants.

Adsorbents	T / K	CH_4	CO_2
		k_H / mol·kg^{-1}·bar^{-1}	k_H / mol·kg^{-1}·bar^{-1}
I-AC	298	0.961	4.082
	308	0.529	3.280
	318	0.522	2.725
BPL[9]	273	2.044	7.398
	298	1.226	4.608
	323	0.730	1.265
Norit R1 Extra[9]	298	1.987	3.746
Norit R1 Extra[16]	298	1.724	4.737
Maxsorb[9]	298	1.302	2.429
A10[9]	298	1.666	3.653
AC-A[9]	298	1.813	4.005
Coconut-AC[10]	298	1.045	
BDH-AC[12]	303	0.854	
F30/470-AC[13]	303	0.247	
Calgon-AC[11]	293	1.005	
	303	0.775	
RP-15[14]	293	1.885	
	303	2.066	
	313	1.463	
RP-20[14]	293	2.019	
	303	1.566	
	313	1.261	

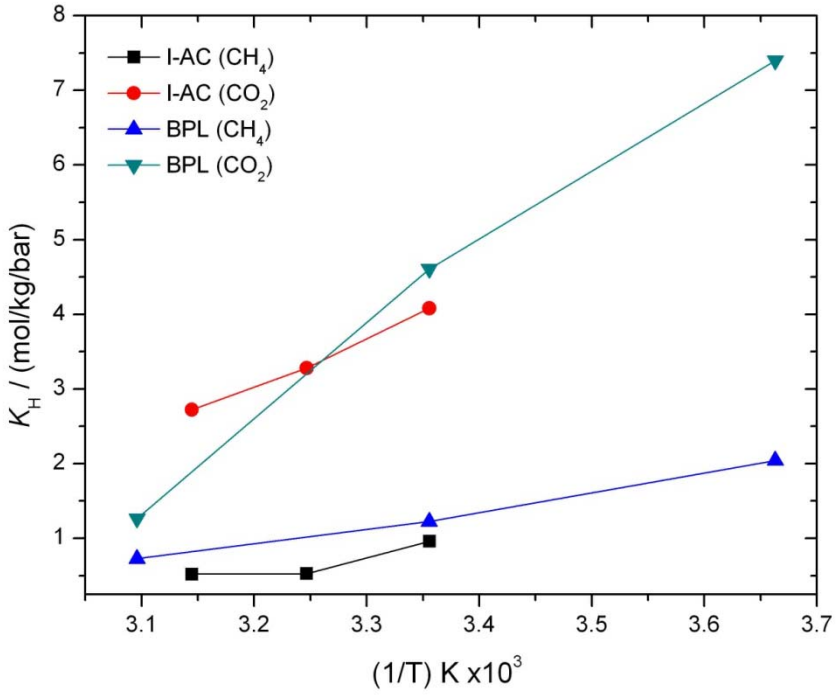

Figure 8.12 Henry's law constants at different temperatures.

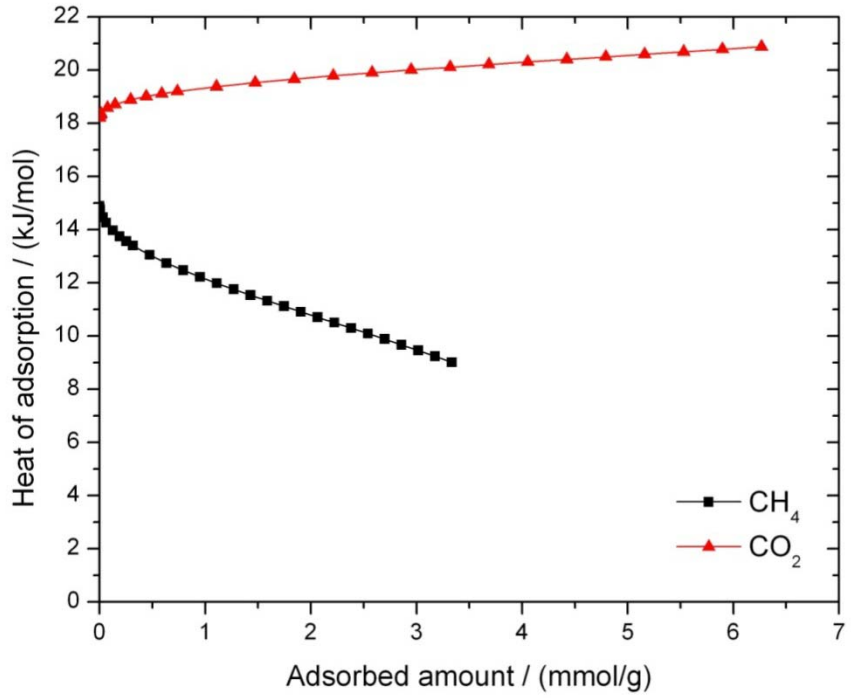

Figure 8.13 The isosteric heat of adsorption of CH_4 and CO_2 on the I-AC.

Table 8.5 Multi-temperature Toth equation parameters for describing CH_4 and CO_2 isotherms on the I-AC.

	CH_4	CO_2
$N_{S,0}$	6.35457	14.74364
b_0	0.08403	0.18622
$Q/(RT_0)$	5.65244	6.8373
m_0	0.66427	0.43307
a	0.47176	-0.10344
c	-0.4773	-1.13972
T_0	318	318
Chi^2/DoF	0.00056	0.00062
R^2	0.99958	0.99986
ARE, %	9.19	1.92

Table 8.6 Comparison of heats of adsorption for various activated carbons at zero coverage.

Adsorbents	Heat of Adsorption / (kJ/mol)	
	CH_4	CO_2
I-AC	14.9	18.2
BPL[9]	16.1	25.7
Norit R1 Extra[9]	20.6	22
Maxsorb[9]	16.3	16.2
A10[9]	16.2	21.6
AC-A[9]	18.3	17.8
Norit RB1[18]	19.5	23.5
Coconut-AC[10]	18.6	
BDH-AC[12]	25.4	
BAX-1100[17]	24.5	
Calgon-AC[11]	27.5	
RP-15[14]	11.4	
RP-20[14]	18.3	

8.3 CONCLUSIONS

A detailed micropore structure analysis and surface characterization of an impregnated activated carbon (I-AC) were presented with the help of a nitrogen adsorption isotherm and SEM technique. Adsorption equilibrium data of methane, carbon dioxide, and carbon monoxide on the I-AC were obtained at 298 K, 308 K, and 318 K and pressures up to 24 bar. CH_4 and CO_2 presented reversible adsorption isotherms, while CO displayed strong chemisorption that became more pronounced at higher temperatures. The adsorption data of CH_4 and CO_2 were correlated by the Toth equation and further by the multi-temperature Toth equation. The fitting details demonstrated that the multi-temperature Toth equation is a powerful tool to mathematically represent the CH_4 and CO_2 isotherms on the I-AC. In addition, the experimental data confirmed the conclusion of Bhatia and Myers that the impregnation method is harmful to adsorption capacity of CH_4. Finally, the Henry's law constants and heat of adsorption near zero coverage of the I-AC were calculated and compared with the values from various activated carbons.

8.4 REFERENCES

(1) Ma, S. Q. *Pure Appl Chem* **2009**, *81*, 2235.

(2) Li, J. R.; Kuppler, R. J.; Zhou, H. C. *Chem Soc Rev* **2009**, *38*, 1477.

(3) Mu, B.; Schoenecker, P. M.; Walton, K. S. *J Phys Chem C* **2010**, *114*, 6464.

(4) Mu, B.; Li, F.; Walton, K. S. *Chem Commun* **2009**, 2493.

(5) Yang, R. T. *Gas separation by adsorption processes*; Butterworths: Boston, 1987.

(6) Sullivan, P. D.; Stone, B. R.; Hashisho, Z.; Rood, M. J. *Adsorption* **2007**, *13*, 173.

(7) Furukawa, H.; Yaghi, O. M. *J Am Chem Soc* **2009**, *131*, 8875.

(8) Duong, D. D. *Adsorption analysis : equilibria and kinetics*; Imperial College Press: London, 1998.

(9) Himeno, S.; Komatsu, T.; Fujita, S. *J Chem Eng Data* **2005**, *50*, 369.

(10) Walton, K. S.; Cavalcante, C. L.; Levan, M. D. *Braz. J. Chem. Eng.* **2006**, *23*, 555.

(11) Choi, B. U.; Choi, D. K.; Lee, Y. W.; Lee, B. K.; Kim, S. H. *J Chem Eng Data* **2003**, *48*, 603.

(12) Al-Muhtaseb, S. A.; Abu Al-Rub, F. A.; Al Zarooni, M. *J Chem Eng Data* **2007**, *52*, 60.

(13) Frere, M. G.; De Weireld, G. F. *J Chem Eng Data* **2002**, *47*, 823.

(14) Lee, J. W.; Balathanigaimani, M. S.; Kang, H. C.; Shim, W. G.; Kim, C.; Moon, H. *J Chem Eng Data* **2007**, *52*, 66.

(15) Bhatia, S. K.; Myers, A. L. *Langmuir* **2006**, *22*, 1688.

(16) Dreisbach, F.; Staudt, R.; Keller, J. U. *Adsorption* **1999**, *5*, 215.

(17) Holland, C. E.; Al-Muhtaseb, S. A.; Ritter, J. A. *Ind Eng Chem Res* **2001**, *40*, 338.

(18) Van der Vaart, R.; Huiskes, C.; Bosch, H.; Reith, T. *Adsorption* **2000**, *6*, 311.

CHAPTER 9

THERMAL ANALYSIS AND HEAT CAPACITY STUDY OF MOFS AND ORGANIC LIGANDS

Metal-organic frameworks (MOFs) have attracted much attention in the last decade as a new class of porous materials because of their perspective applications in many areas, especially for adsorptive storage and separation.[1-4] The adsorption and diffusion of different molecules in MOFs have been studied intensely, in which capacity[5], selectivity[6], and heats of adsorption[7] have been reported from many research groups. However, our knowledge about the thermodynamic properties of MOFs is still far from sufficient; in particular, very little information is known about the heat capacity of MOFs. There have been no systematic investigations on this topic, but many experimental and simulation studies have shown the importance of understanding thermal effects in various adsorption systems, as shown in the following energy balance equation for a simplified fixed-bed adsorption process[8]:

$$\rho_b \frac{\partial u_s}{\partial t} + \epsilon' \frac{\partial (ch_f)}{\partial t} + \epsilon \frac{\partial (vch_f)}{\partial z} = 0 \qquad 9.1$$

where u_s is the internal energy of the stationary phase, given by

$$u_s = u_{ref}^{sol} + C_{sol}(T - T_{ref}) + nh_a \qquad 9.2$$

in which C_{sol} is the heat capacity of the solid adsorbent. A larger heat capacity of a solid adsorbent will contribute to decreasing undesired thermal effects.

Differential scanning calorimetry (DSC) is an effective analytical tool to characterize the thermal properties of materials. In this work, a thermal gravimetric

analyzer coupled with DSC was employed to determine the heat capacities of typical MOF materials, covering three different ligands and five different metals with or without open metal sites, including CuBTC, IRMOF-1, and UMCM-1. The heat capacity of MOFs is very important thermodynamic data not only for characterizing adsorbent material itself, but also for optimizing adsorption processes. The impact of the coordination environment and metal content and type on the heat capacity values will be discussed, and comparisons will be made with heat capacities of traditional porous materials.

9.1 EXPERIMENTAL SECTION

9.1.1 Synthesis

Nine MOFs were synthesized from the following chemicals as received without further purification: copper nitrate trihydrate, $Cu(NO_3)_2 \cdot 3H_2O$ (Acros Organics, 99%); zinc nitrate tetrahydrate, $Zn(NO_3)_2 \cdot 4H_2O$ (EMD Chemicals); zinc nitrate hexahydrate, $Zn(NO_3)_2 \cdot 6H_2O$ (EMD Chemicals); lanthanum nitrate hexahydrate, $La(NO_3)_2 \cdot 6H_2O$ (EMD Chemicals); cadmium nitrate tetrahydrate, $Cd(NO_3)_2 \cdot 4H_2O$ (Acros Organics, 99+%); nickel nitrate hexahydrate, $Ni(NO_3)_2 \cdot 6H_2O$ (Acros Organics, 99%); terephthalic acid, H_2BDC (Acros Organics, 99+%); trimesic acid, H_3BTC (Acros Organics, 99%); 1,3,5-tris(4-carboxyphenyl)benzene, H_3BTB (Sigma-Aldrich, ≥98%); N,N-diethylformamide, DEF (Acros Organics, 99%); N,N-dimethylformamide, DMF (Acros Organics, 99.8+%), ethanol, EtOH (Acros Organics, 99.5%). The synthesis methods are given in the Scheme 9.1. The crystal structures of the examined MOFs are listed in Figure 9.1.

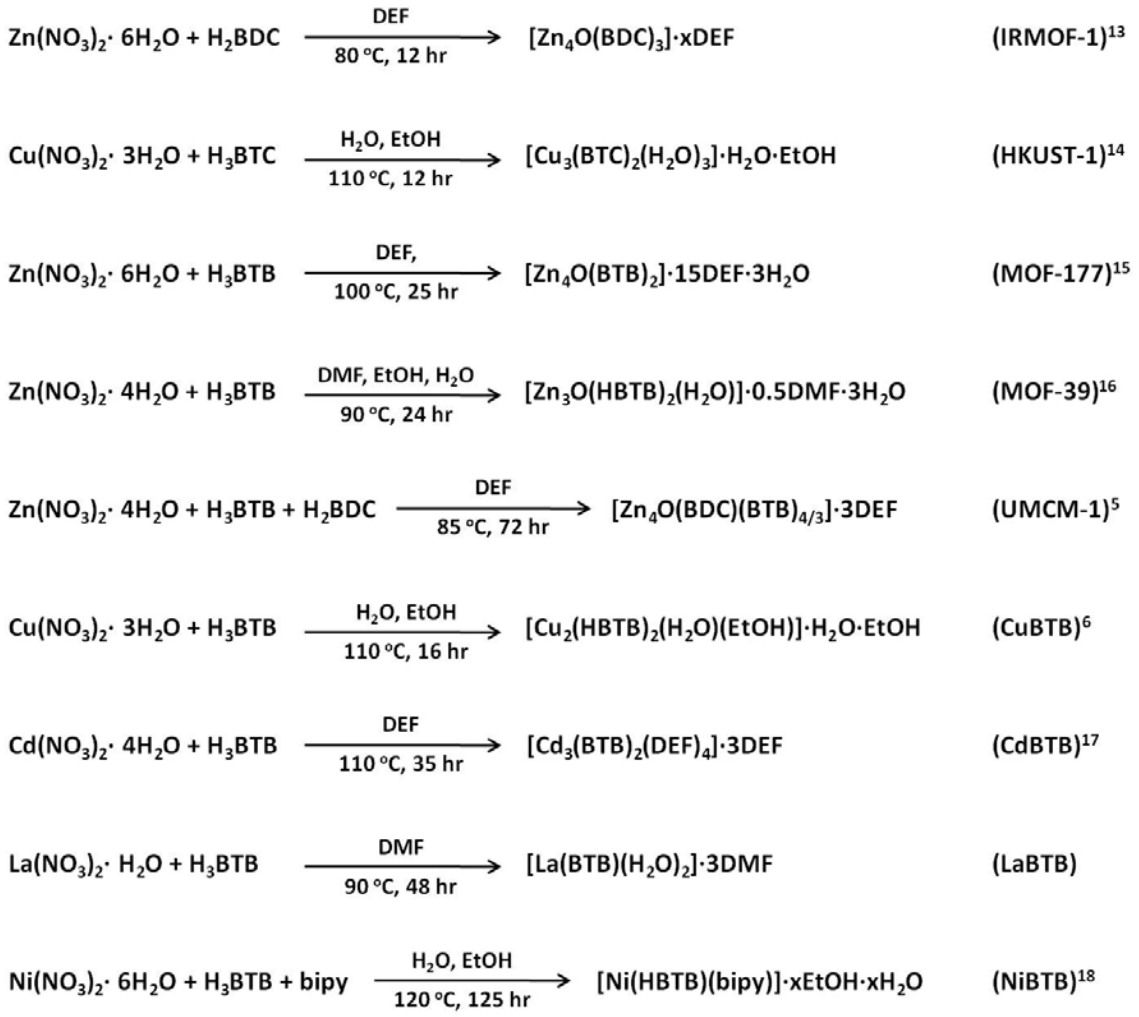

Scheme 9.1 Synthesis methods of MOFs

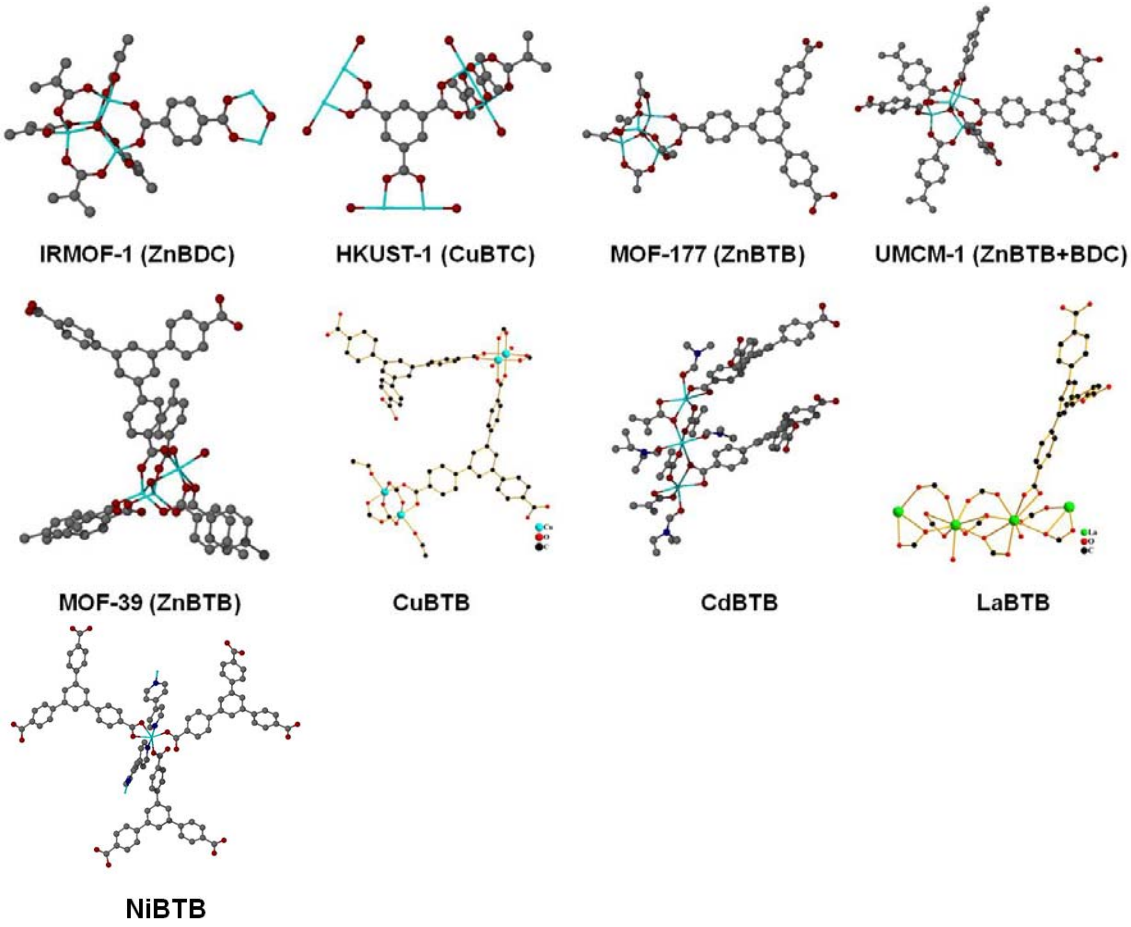

Figure 9.1 Crystal structure of examined MOFs

9.1.2 Thermal Analysis.

Thermogravimetric analysis (TGA) coupled with differential scanning calorimetry (DSC) was carried out with a NETZSCH STA 449 F1 Jupiter®. The examined sample was first put under isothermal condition of 30 ^{o}C and helium atmosphere with 20 mL/min flow rate for 10 min, and then heated at a rate of 20 ^{o}C/min. The examined temperature ranges from 30 ^{o}C to 750 ^{o}C.

9.1.3 Heat Capacity Measurement.

To measure heat capacity, differential scanning calorimetry was performed with a NETZSCH STA 449 F1 Jupiter® at a heating rate of 10 ^{o}C/min under helium atmosphere with 20 mL/min flow rate. The examined temperature range from 50 ^{o}C to 200 ^{o}C, and a continued 3-cycle scan were carried out for baseline correction, standard reference material, and the examined MOFs. Detailed calculation method of heat capacity will be given in the next section.

9.1.4 Heat Capacity Calculation

At constant pressure, the specific heat capacity (C_P) indicates the amount of energy required to heat one unit mass of a material by one Kelvin, which could be defined by the following equitation:

$$C_P(T) = \frac{dH(T)}{dT} \cdot \frac{1}{m} \tag{9.3}$$

Individual C_p values at different temperatures can be determined from recorded DSC data according to the following equation:

$$C_P(T) = \frac{DSC_{sample} - DSC_{baseline}}{DSC_{reference} - DSC_{baseline}} \cdot \frac{M_{reference}}{M_{sample}} \cdot C_{P,reference} \tag{9.4}$$

in which C_P is the specific heat of the sample at temperature T; $C_{P,\ reference}$ is the specific heat of the standard reference material, which is sapphire normally; ($DSC_{sample} - DSC_{baseline} = h(s)$) is the recorded DSC signal of the sample with baseline correction; ($DSC_{reference} - DSC_{baseline} = h(r)$) is the recorded DSC signal of sapphire with baseline correction; M is the mass of sample or sapphire. The illustrated calculation method is also presented in Scheme 9.2

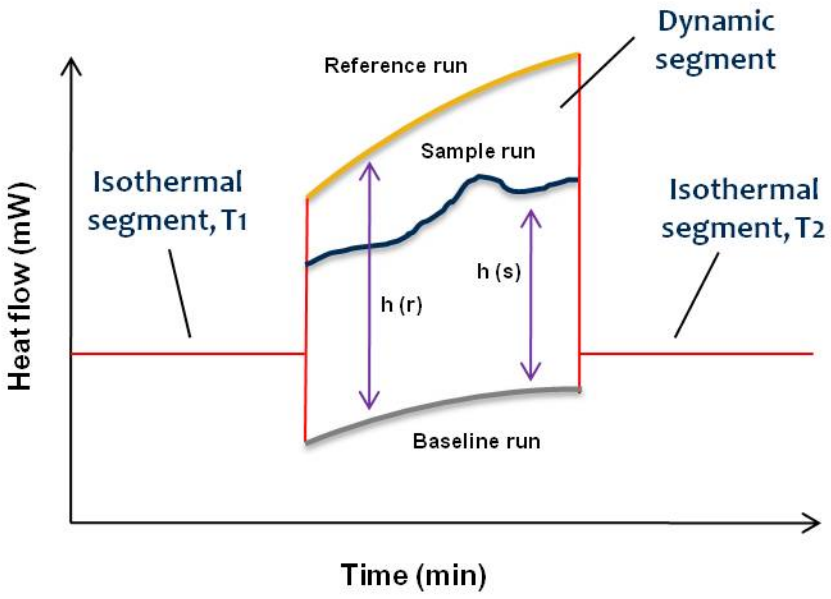

Scheme 9.2 Heat capacity calculation by DSC measurement

Figure 9.2 demonstrates the practical measurement curve for a solid ligand, H_2BDC. The top figure shows the continued 3-cycle scan for the standard reference material (sapphire), which is already corrected with a baseline run. The examined sample was held at 40 ^oC for 20 minutes, and then heated up to 200 ^oC at a heating rate of 10 ^oC/min. Another isothermal segment keeps the sample at 200 ^oC for 40 minutes before cooling down to 40 ^oC. After that, a new cycle will start. Three parameters including temperature, TG signal (mass loss) and DSC signal (heat flow) were recorded simultaneously. The bottom figure shows the measurement with the baseline correction for H_3BTB. For achieving better accuracy, the calculation of heat capacity is always based on the third scan. If TG signal shows mass loss more than 0.5% indicating that the remaining solvent was evaporated from the crystal, more scan is required. With this method, the experimental error of heat capacity is less than 2% between our measurement results and standard data of sapphire.

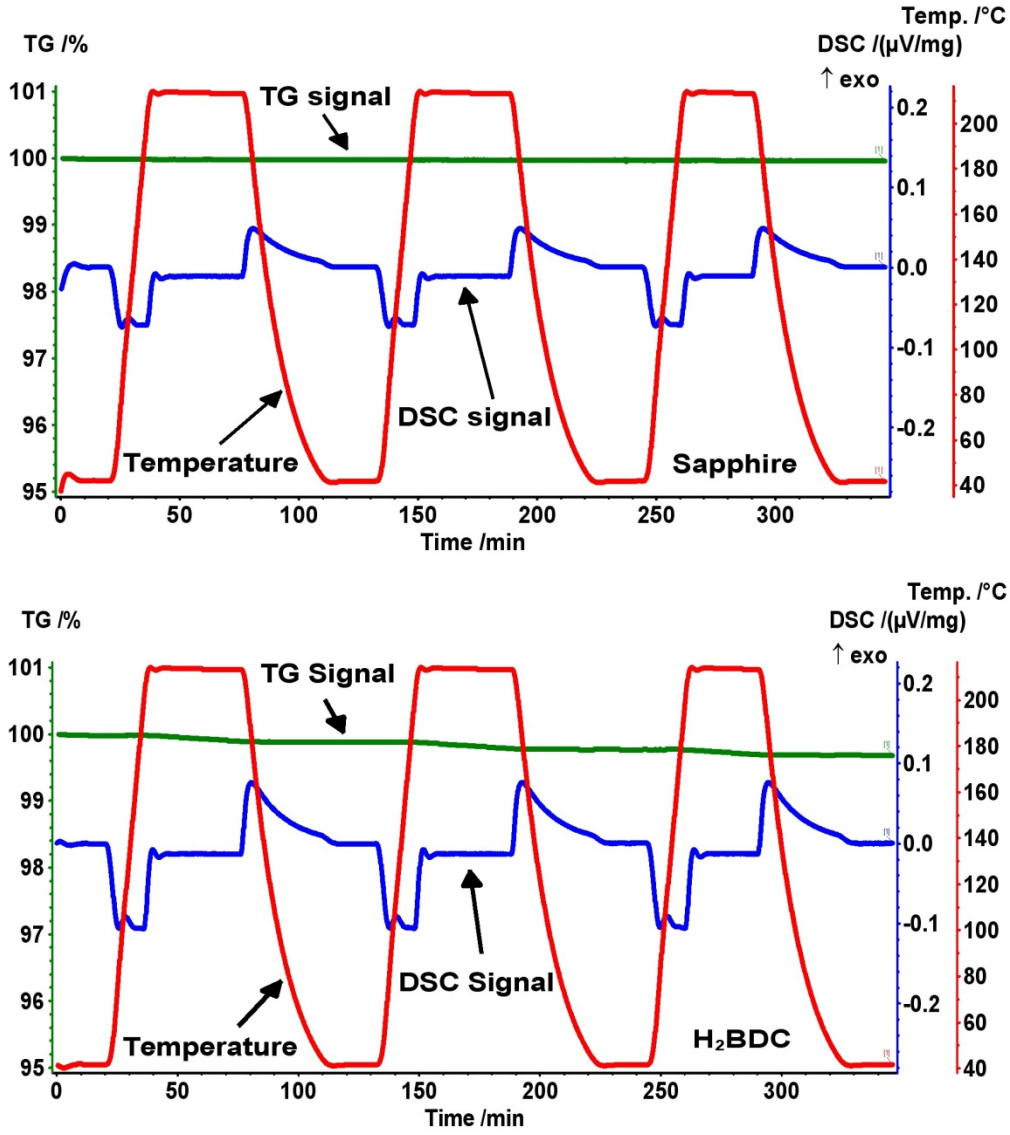

Figure 9.2 Heat capacity measurement of H_2BDC using DSC. (green line: TG signal; blue line: DSC signal; red line: temperature)

9.2 RESULTS AND DISCUSSION

9.2.1 THERMAL PROPERTIES OF ORGANIC LIGANDS

Thermal properties of three ligands (H_2BDC, H_3BTC, and H_3BTB) are investigated first and presented in Figure 9.3. The thermal stability of solid H_2BDC is up to 322 ^oC without any substantial mass loss, and then a large endothermic peak on DSC curve with a large mass loss indicates the sublimation of H_2BDC. The endothermic peak is at 408.9 ^oC, which is close to the reported sublimation point at 1 atm, 402 ^oC.[9] According to the report of Bailey and Brown, H_2BDC possess two polymorphic structures, form I and form II.[10] The phase transition from form II to form I occurs over the temperature range 75 – 100 ^oC, while form I shows no evidence of phase changes on heating.[11] There is no phase transition under sublimation point observed from our DSC results, which confirms the conclusion of Davey and Maginn that commercial material was found to be form I.[11] The thermal stability of solid H_3BTC is greater than 300 ^oC, while an endothermic peak on DSC curve at around 305 ^oC indicates the existence of a polycrystalline β-phase H_3BTC in bulk material.[12] With the increase of temperature, melting and evaporation processes of α-phase H_3BTC occur. The second endothermic peak is at around 380 ^oC, which is close to the reported melting point of α-phase, 375 ^oC.[12] The thermal analysis results of solid H_3BTB are more complex due to solvent in the product. Our TGA data show that the mass loss is up to 14.02% at 187 ^oC, which is in accordance with properties (total impurities $\leq$ 20 % solvent) provided by the manufacturer of H_3BTB. Two endothermic peaks at around 291 and 312 ^oC indicate the possible phase transition of solid H_3BTB. To investigate the impact of heating rate on the results of thermal analysis, two more measurements were performed for H_3BTC and

H_3BTB using a heating rate of 10 ^oC/min and 5 ^oC/min (Figure 9.4 and Figure 9.5). The comparison of the results demonstrates that fast heating rates decrease the temperature resolution due to the large temperature gradients within the sample, and make the observed phase transition point move towards the higher temperature.

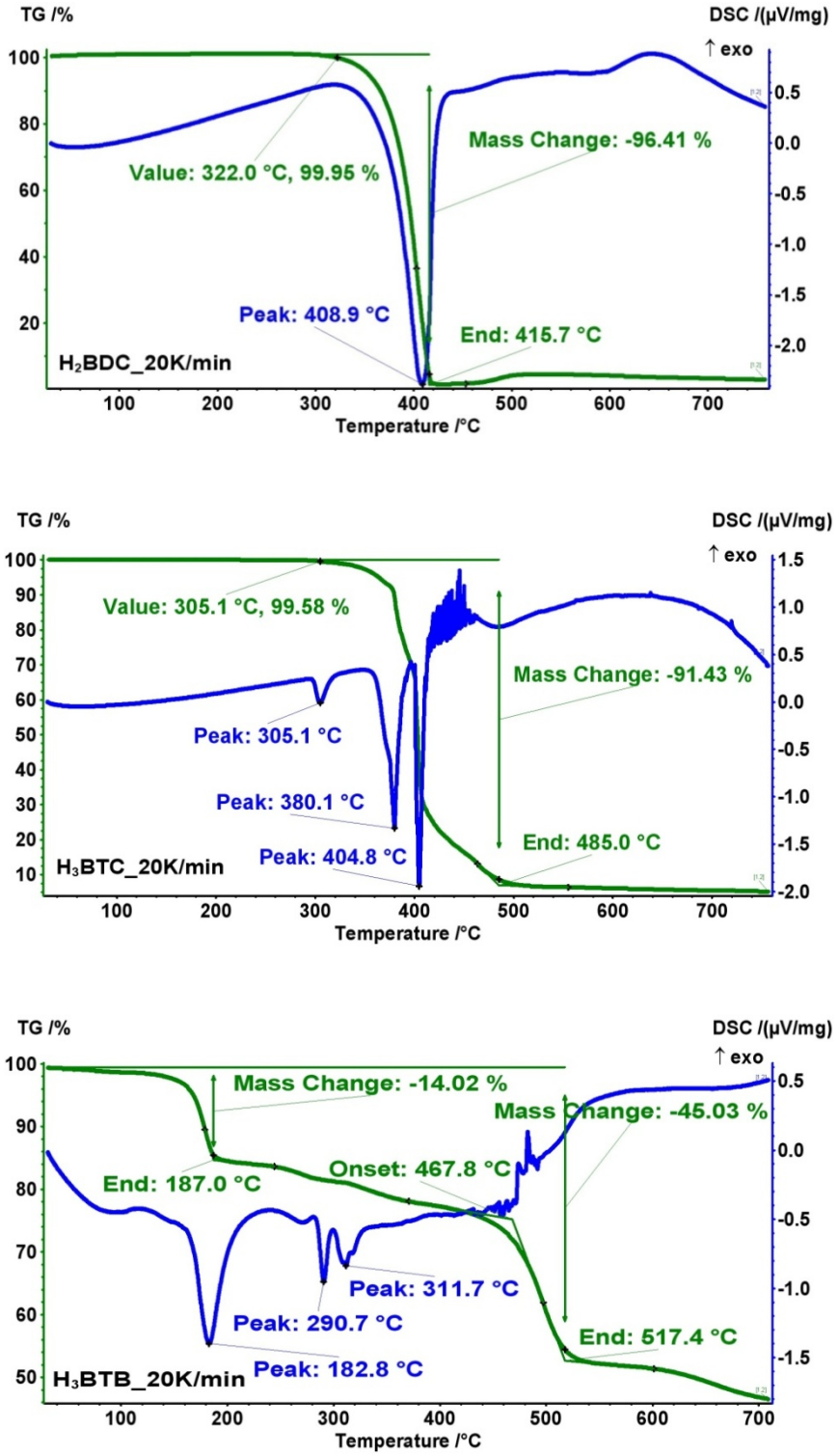

Figure 9.3 TGA-DSC results of H_2BDC, H_3BTC, and H_3BTB. (green line: TGA curve; blue line: DSC curve)

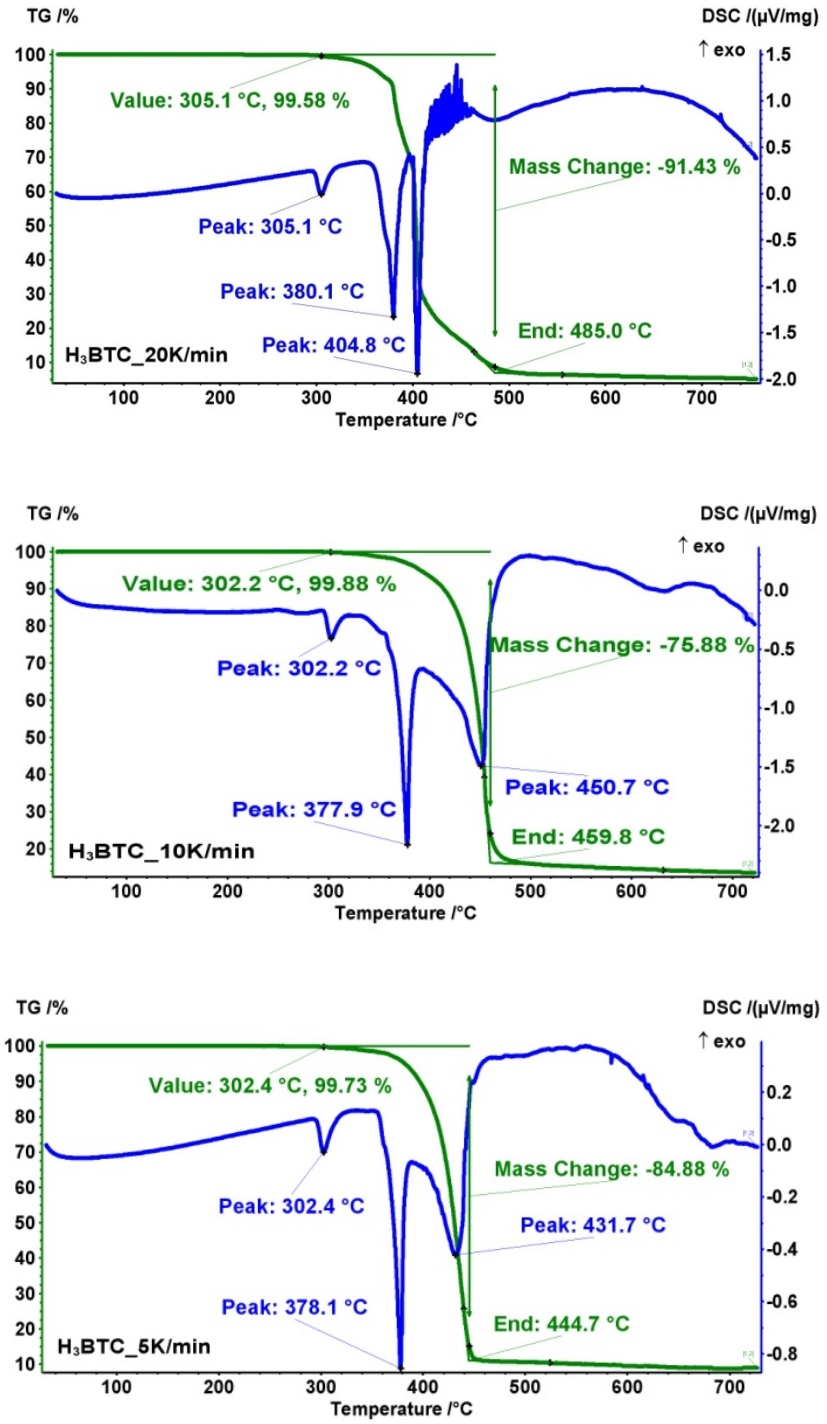

Figure 9.4 The impact of heating rates on TGA-DSC results of H_3BTC. (green line: TGA curve; blue line: DSC curve)

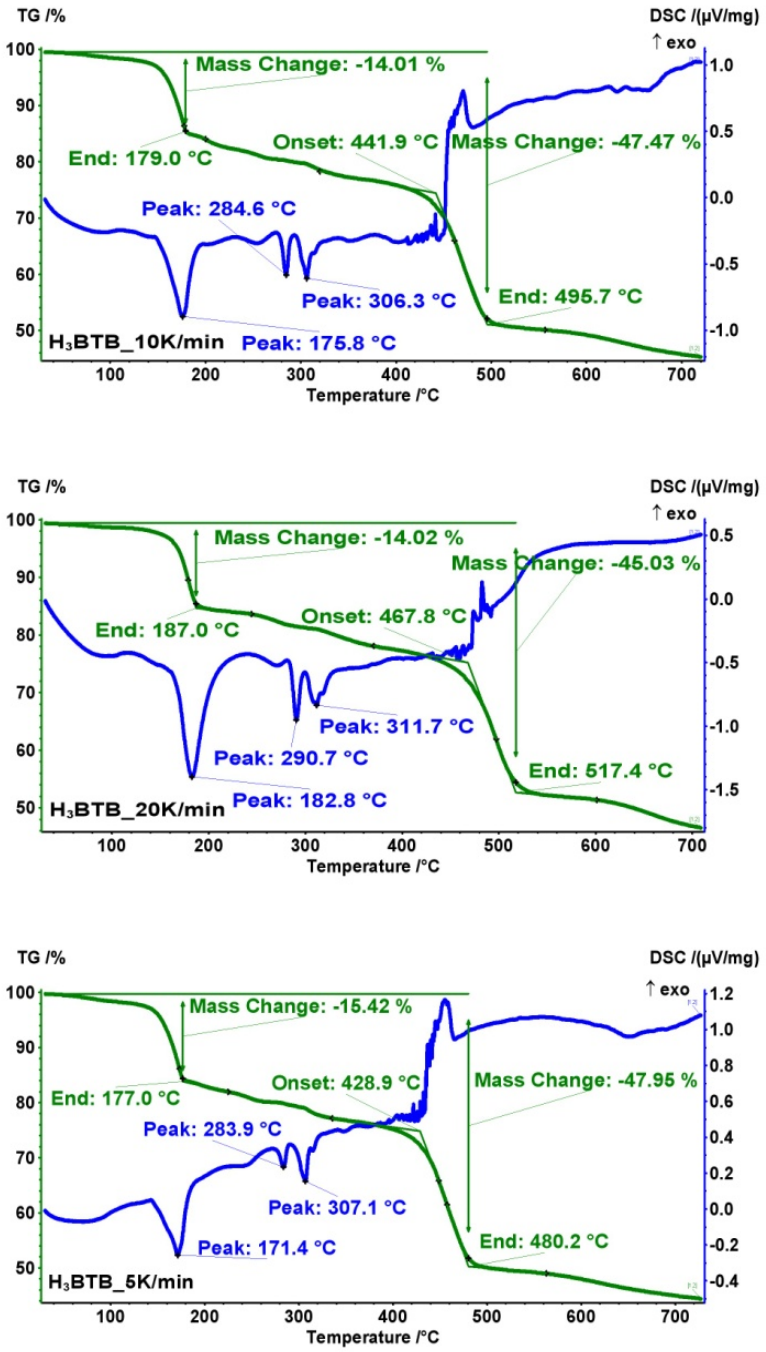

Figure 9.5 The impact of heating rates on TGA-DSC results of H_3BTB. (green line: TGA curve; blue line: DSC curve)

9.2.2 Thermal Properties of Examined MOFs.

Thermal properties of nine MOFs using as-synthesized samples including IRMOF-1,[13] HKUST-1,[14] MOF-177,[15] MOF-39,[16] UMCM-1,[5] CuBTB,[6] CdBTB,[17] LaBTB, and NiBTB[18] are investigated according to the above-mentioned method. The TG and DSC curves are presented from Figure 9.6 to Figure 9.14. The thermal properties of MOFs are summarized and listed in Table 9.1 for comparison. The distance of metal-oxygen bond is also provided from the single-crystal structural data. Among the examined MOFs, the length of metal-oxygen bonds follow the order of La > Cd > Ni > Cu ≈ Zn. To study the impact of the local coordination environment of MOFs on the thermal stability, we define a discrete metal-oxygen cluster as a Secondary Building Unit (SBU), and it would be easier for us to discuss this issue with a simplified symbol. For example of IRMOF-1, 4Zn(4) could be used to represent the coordination number of metals per SBU, in which each Zn-O SBU includes four Zn atoms, and they are all 4 coordinated. In the case of MOF-39, 2Zn(4)+Zn(5+1) indicates that there are two 4-coordinated Zn atoms and one 6-coordinated Zn atom per SBU, in which (5+1) means one of the coordination sites is occupied by one solvent molecule so that it may not have important effect on the thermal stability of the whole framework. In the case of LaBTB, the SBU is the continued La-O chain instead of a discrete cluster so that nLa(8+1) is used to represent its local coordination environment.

Among the examined MOFs, LaBTB possesses the highest thermal stability, which is up to 560 ^{o}C. HKUST-1 and CuBTB have the lowest thermal stability, which is less than 300 ^{o}C. Zn, Cd, Ni-based MOFs have the thermal stability of middle range, which is larger than 300 ^{o}C and less than 500 ^{o}C. The high thermal stability of LaBTB is

definitely due to the higher coordination number possessed by La atom, which is common in lanthanide elements. IRMOF-1, MOF-177, and UMCM-1 are composed of different ligands possessing distinct framework topology, however the same coordination environment within one SBU. TGA results present that all three MOFs possess the same thermal stability. The same situation occurs in the case of HKUST-1 and CuBTB. HKUST-1 is a three-periodic framework, while CuBTB is a two-dimensional layer structure. However, they possess the almost same thermal stability due to the same local coordination environment. Thus, our experimental results substantially demonstrate that the thermal stability of MOFs is mainly determined by the coordination number and local coordination environment instead of framework topology.

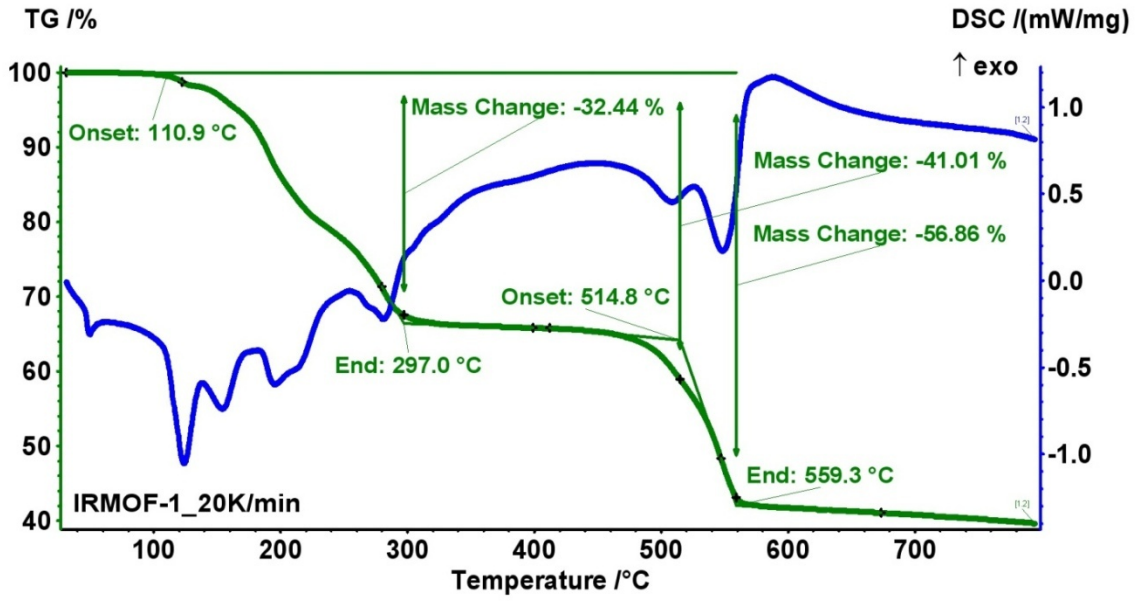

Figure 9.6 Thermal analysis result of IRMOF-1

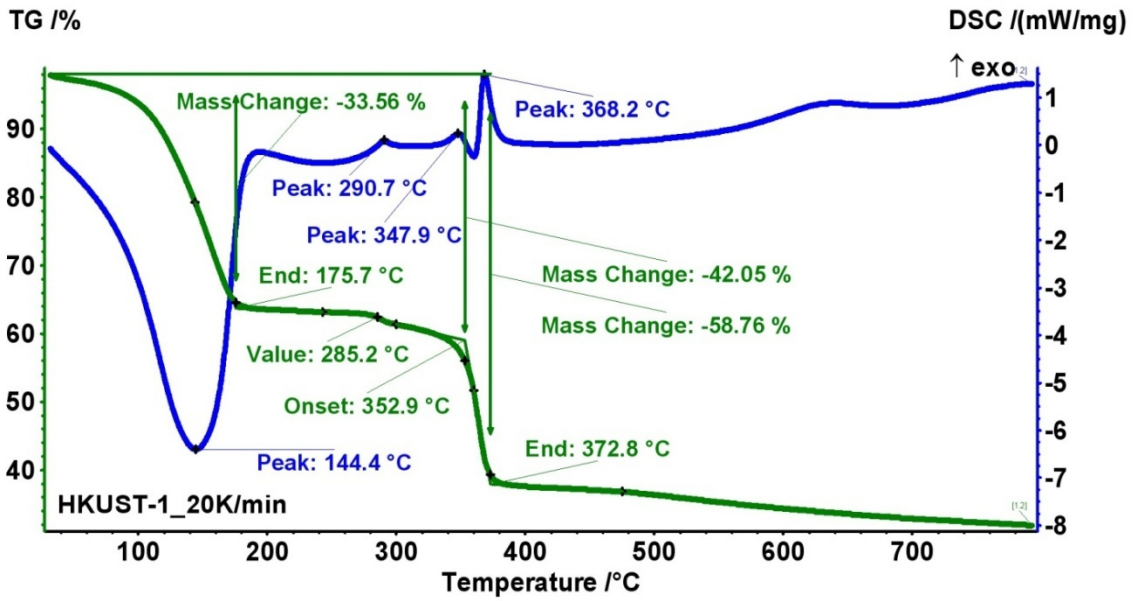

Figure 9.7 Thermal analysis result of HKUST-1

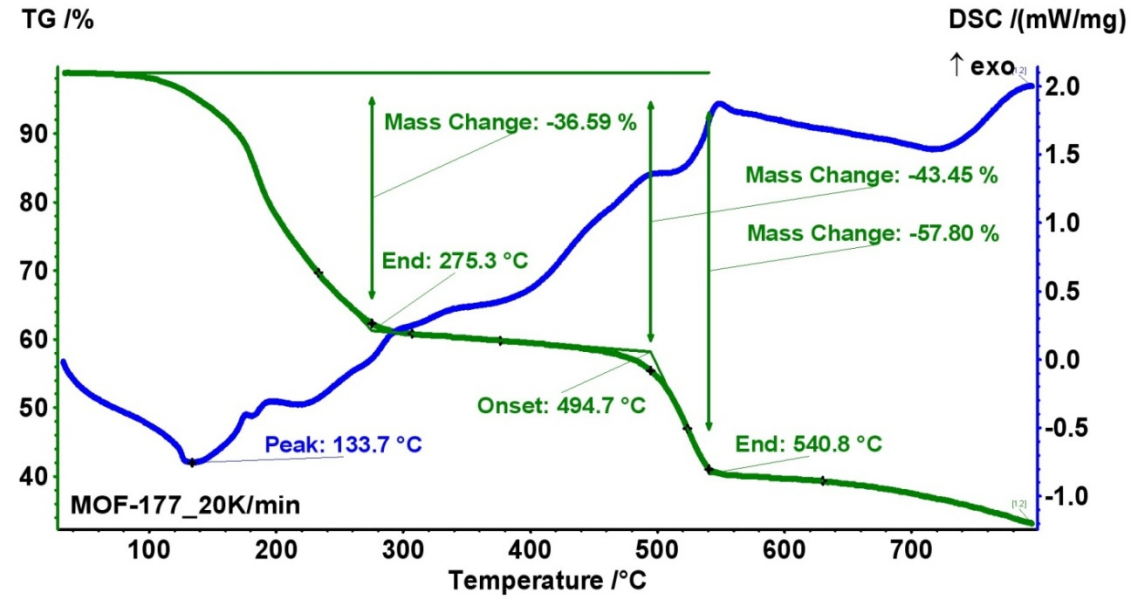

Figure 9.8 Thermal analysis result of MOF-177

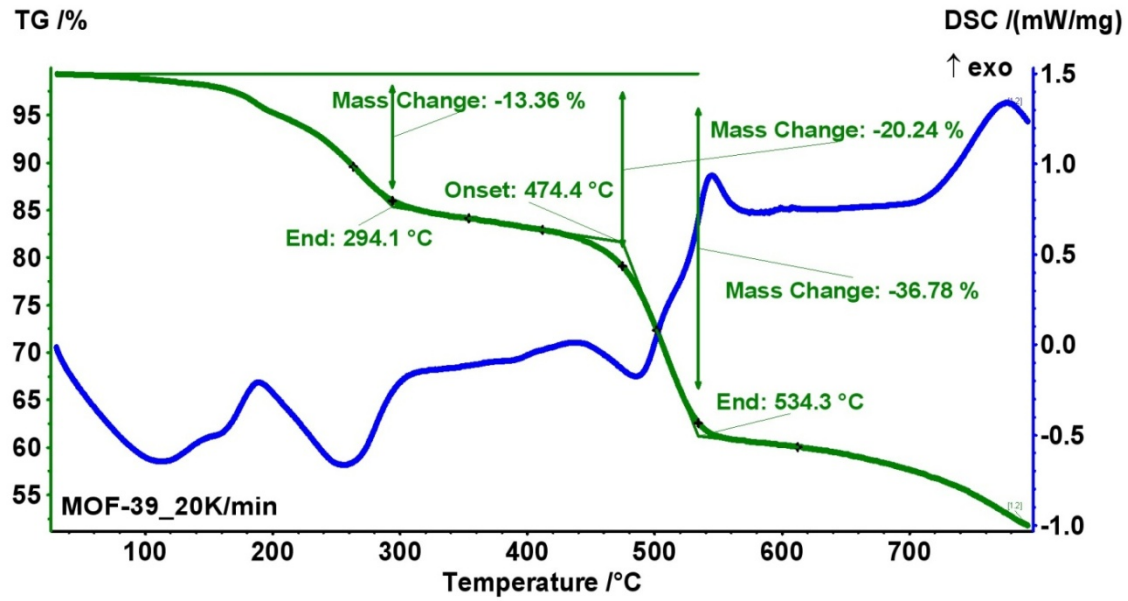

Figure 9.9 Thermal analysis result of MOF-39

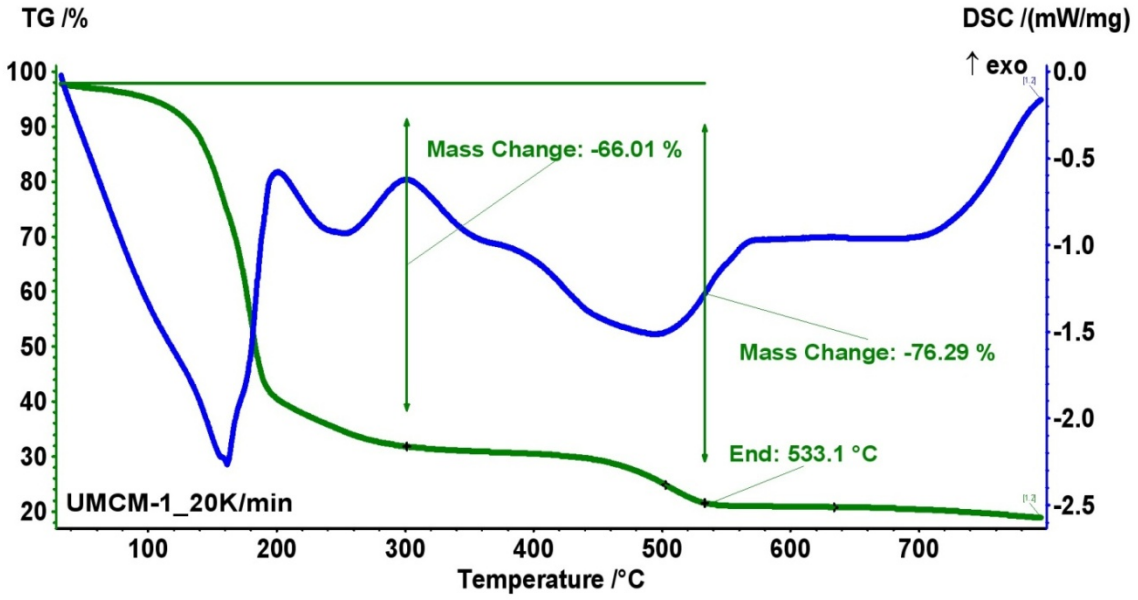

Figure 9.10 Thermal analysis result of UMCM-1

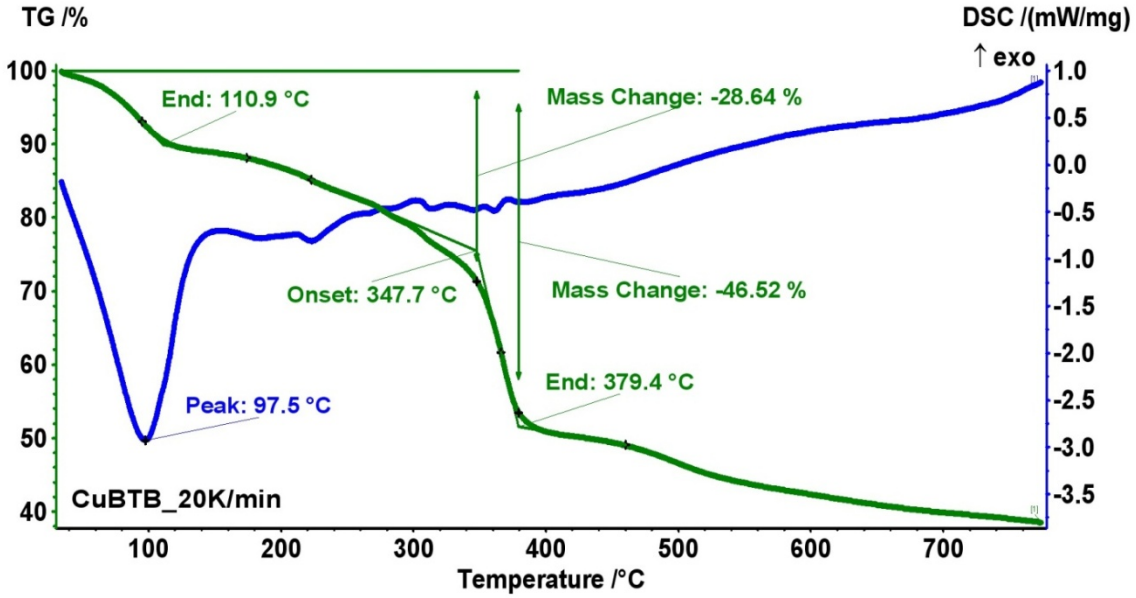

Figure 9.11 Thermal analysis result of CuBTB

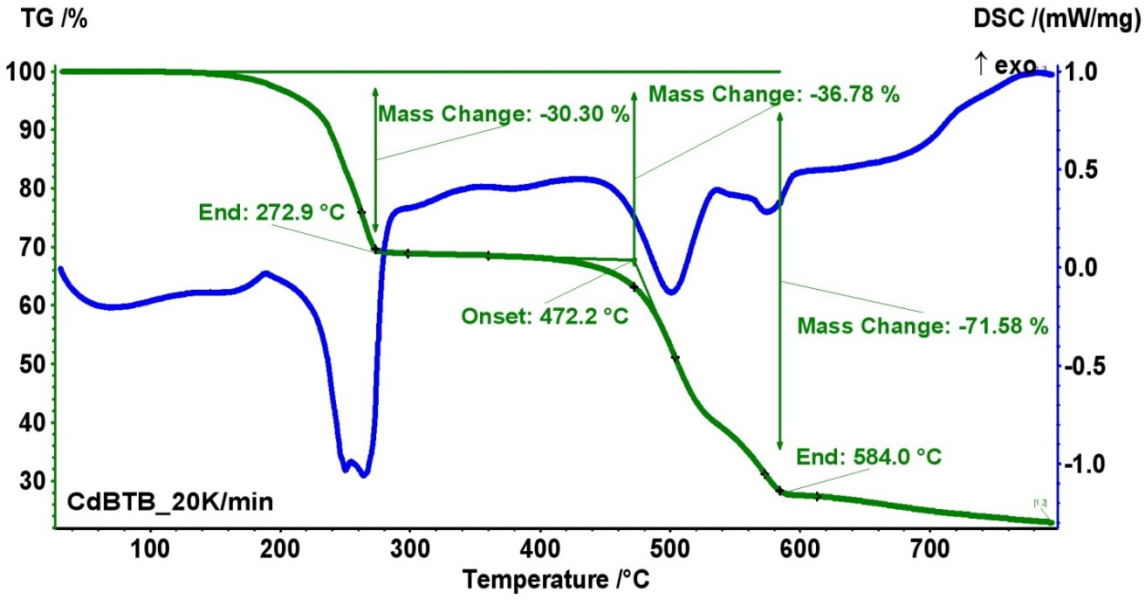

Figure 9.12 Thermal analysis result of CdBTB

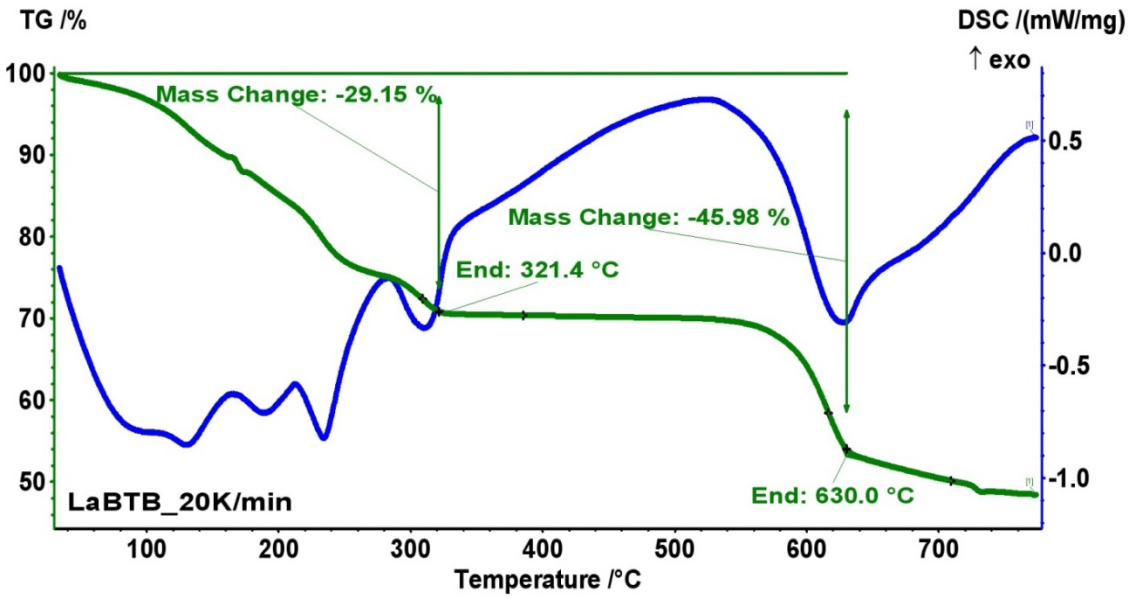

Figure 9.13 Thermal analysis result of LaBTB

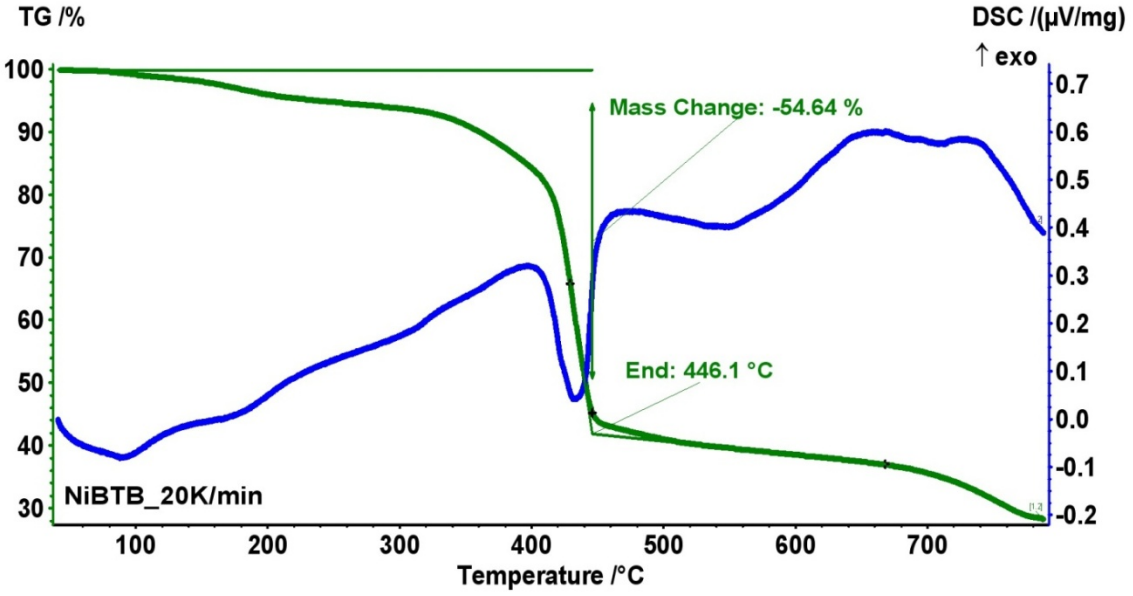

Figure 9.14 Thermal analysis result of NiBTB

Table 9.1 Thermal properties of the examined MOFs

MOFs	Distance of metal-oxygen bond (Å)	Coordination numbers of metal (per SBU)	T_{end} (^oC) Solvent removal	$T_{stability}$ (^oC)	Mass loss at T_{end} (%)
IRMOF-1 (ZnBDC)	1.922-1.941	4Zn(4)	297.0	460	32.4
HKUST-1 (CuBTC)	1.952	2Cu(5+1)	175.7	285	33.6
MOF-177 (ZnBTB)	1.889-1.978	4Zn(4)	273.5	460	36.6
MOF-39 (ZnBTB)	1.913-2.092	2Zn(4)+Zn(5+1)	294.1	440	13.4
UMCM-1 (ZnBTB+BDC)	1.907-1.949	4Zn(4)	300	460	66.0
CuBTB	1.955-1.962	2Cu(5+1)	-	290	-
CdBTB	2.173-2.348	2Cd(5+1)+Cd(4+2)	272.9	420	30.3
LaBTB	2.428-2.758	nLa(8+1)	321.4	560	29.2
NiBTB	2.02-2.151	Ni(6)	-	380	-

9.2.3 HEAT CAPACITIES OF ORGANIC LIGANDS

Molar heat capacity of H_2BDC, H_3BTC, and H_3BTB are presented in Figure 9.15. The magnitude of the values well followed the order of complexity of molecules because more complex molecules can have more internal degrees of freedom. The heat capacity of H_3BTB is almost 1.5 times larger than that of H_3BTC at about 320 K, which can be explained by the principle of Boltzmann distribution since more phenyl rings possess better resonance stabilization in H_3BTB than in H_3BTC so that they well increased the energy threshold required to cause bond rupture. The heat capacity of H_2BDC is a little lower than that of H_3BTC since H_2BDC has one less carboxylic group than H_3BTC. The group-contribution method for estimating the heat capacity of solid organic compounds developed by Goodman et al.[19] were applied to compare with our experimental results. In both cases of H_2BDC and H_3BTC, the modeling results are very close to our experimental results, which give an accuracy of less than 4% over the examined temperature range. In the case of H_3BTB, the modeling result overestimated the specific heat capacity of H_3BTB up to 11% compared with our experimental data, which is still in the range of the average deviation of approximately 13% estimated by the author of the modeling.[19]

Assuming that different functional groups contribute to the heat capacity of an organic compound, a simple method is proposed to calculate the heat capacity contribution of different organic functional groups, as shown in the following expressions.

$$\begin{matrix} x = C_{p,\ COOH} \\ y = C_{p,\ C6H4} \\ z = C_{p,\ C6H3} \end{matrix} \Rightarrow \begin{cases} 2x + y = C_{p,\ H2BDC} \\ 3x + z = C_{p,\ H3BTC} \\ 3x + 3y + z = C_{p,\ H3BTB} \end{cases} \qquad 9.5$$

For example, the heat capacity of H_2BDC, H_3BTC, and H_3BTB at 323 K is 0.195, 0.213, and 0.525 kJ/(mol·K), respectively. The above equation is solved as:

$$\begin{matrix} 2x + y = 0.195 \\ 3x + z = 0.213 \\ 3x + 3y + z = 0.525 \end{matrix} \Rightarrow \begin{cases} x = 0.046 \\ y = 0.104 \\ z = 0.076 \end{cases} \quad 9.6$$

So, the heat capacity contribution of one carboxylate (COOH), one di-deprotonated benzene ring (C_6H_4), and one tri-deprotonated benzene ring (C_6H_3) at 323 K is 0.046, 0.104, and 0.076 kJ/(mol·K) , respectively. By solving the linear equations under different temperatures, the heat capacity contribution of different organic functional groups could be plotted as a function of temperature. As shown in Figure 9.16, the heat capacity contribution of deprotonated benzene ring apparently increases with the increasing temperature, while the heat capacity contribution of carboxylate does not change much with the temperature.

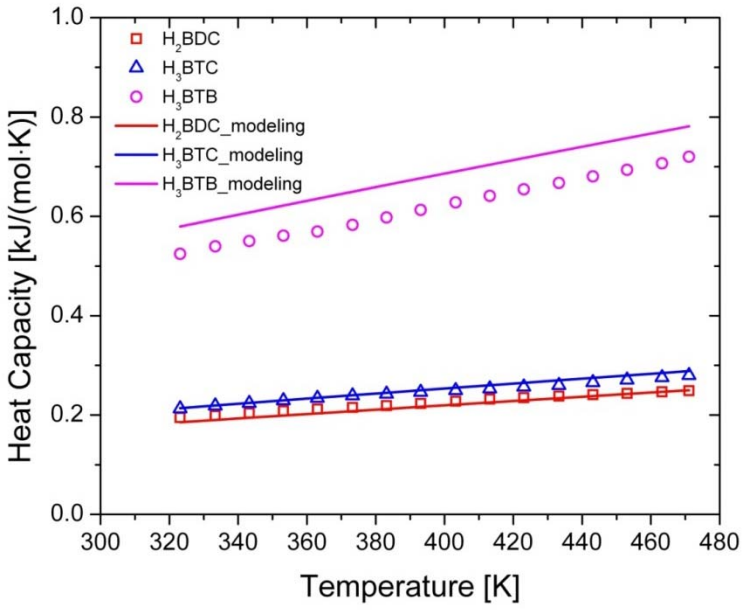

Figure 9.15 Molar heat capacity of H_2BDC, H_3BTC, and H_3BTB compared with the modeling results calculated from the group-contribution method.

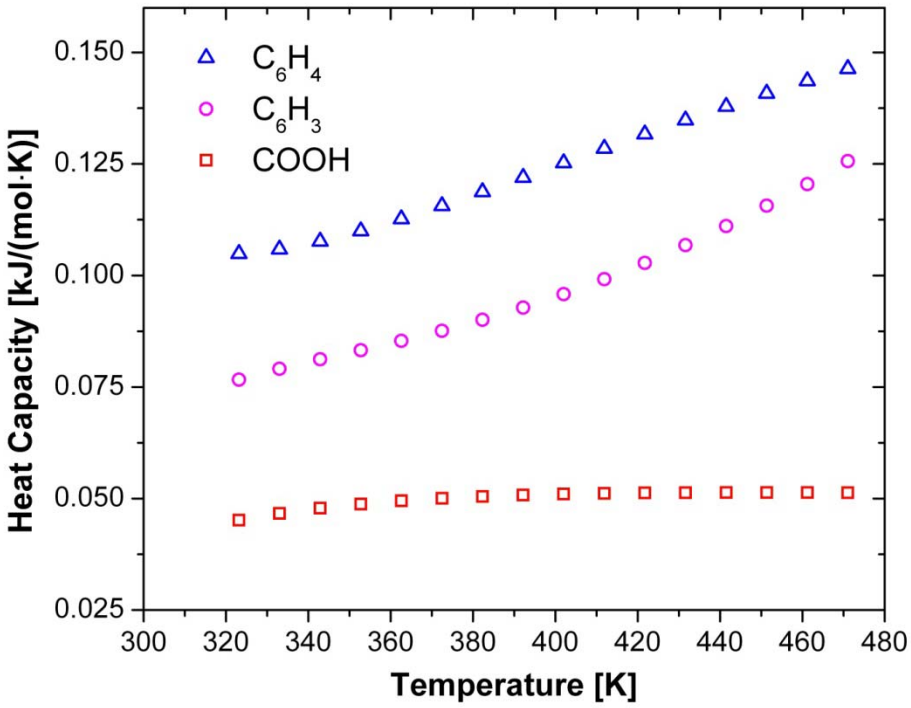

Figure 9.16 Molar heat capacity contribution of different organic functional groups.

9.2.4 HEAT CAPACITIES OF MOFS

Specific heat capacity (*Cp*) of all examined MOFs are compared with several other solids including coordination polymers,[20-23] carbon nanotubes,[24] zeolites,[25-26] and minerals[27] (Figure 9.17). Among all examined materials, MgBTC possesses the highest *Cp* over the examined temperature, while ferrosilite ($Fe_2Si_2O_6$) possesses the lowest *Cp*. Cabon nanotubes present the almost linear temperature-specific heat curve, while *Cp* of double-wall nanotubes is 1.3 times that of single-wall nanotubes. It is worth noting that the *Cp* curve of HKUST-1 indicates a thermal anomaly at around 130 ^{o}C, which is due to the change of coordinated H_2O in the framework.[20] IRMOF-1 possesses the lowest *Cp* among the examined nine MOFs in this work.

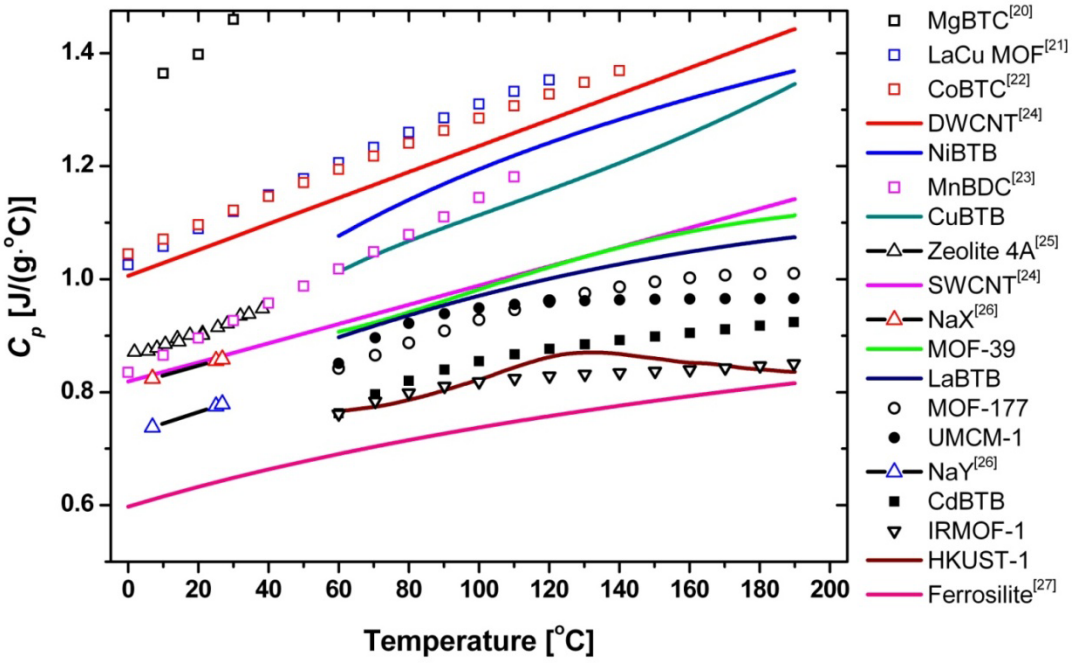

Figure 9.17 Comparison of specific heat capacity of MOFs, coordination polymers, carbon nanotubes, zeolites and minerals.

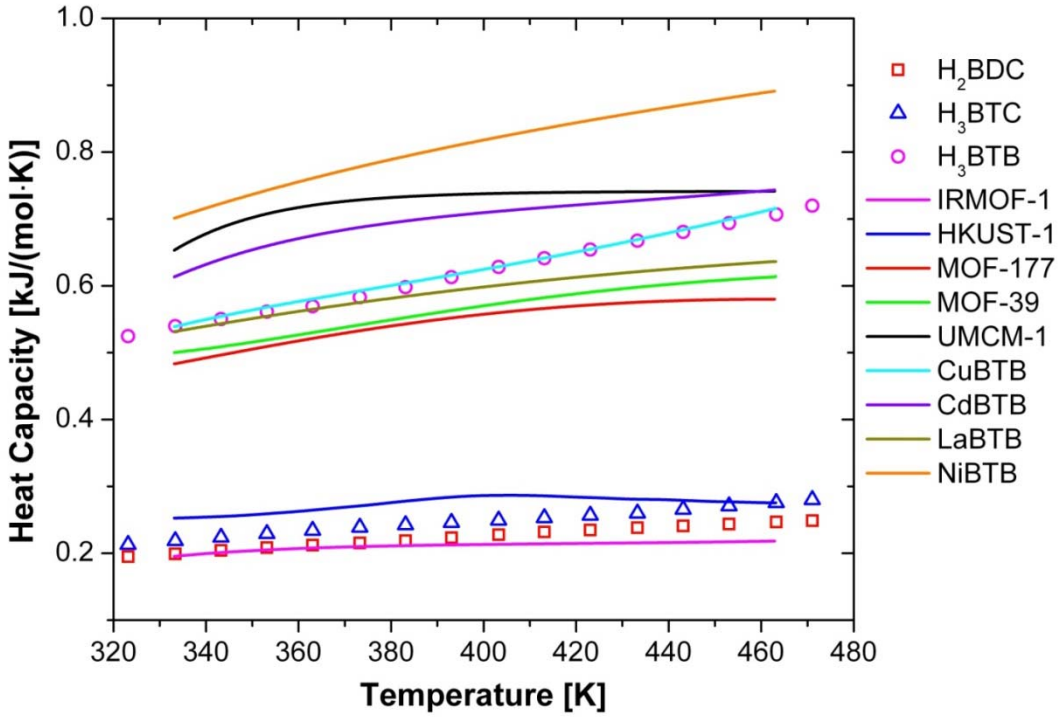

Figure 9.18 Comparison of molar heat capacity of MOFs and three organic ligands.

To investigate the impact of organic ligands on the heat capacity of MOFs, the molar heat capacities of all examined MOFs are compared with those of three ligands (H_2BDC, H_3BTC, and H_3BTB). The molar mass of MOFs is calculated based on one molar ligand or one molar major ligand in the case of mixed-ligand MOFs. For example of IRMOF-1, the molecular form is $[Zn_{\frac{4}{3}}O_{\frac{1}{3}}(BDC)]$ instead of $[Zn_4O(BDC)_3]$ without considering associated solvent molecules, so that the molar mass of IRMOF-1 is given by:

$$M_{IRMOF-1} = 1 \times M_{BDC} + \frac{3}{4} \times M_{Zn} + \frac{1}{4} \times M_O = 256.64 g/mol$$

According to the similar rule, the molar mass of all examined MOFs are $M_{IRMOF-1}$ = 256.64 g/mol, $M_{HKUST-1}$ = 329.46 g/mol, $M_{MOF-177}$ = 574.19 g/mol, M_{MOF-39} = 551.5 g/mol, M_{UMCM-1} = 767.67 g/mol, M_{CuBTB} = 532.01 g/mol, M_{CdBTB} = 804.35 g/mol, M_{LaBTB} = 592.34 g/mol, M_{NiBTB} = 651.31 g/mol. As shown in Figure 9.18, the molar heat capacities of IRMOF-1, HKUST-1, and CuBTB are very close to the molar heat capacities of H_2BDC, H_3BTC, and H_3BTB, respectively. Except for HKUST-1 demonstrating a thermal anomaly at around 403 K, the heat capacity of other MOFs show a slight linear increasing tendency with the temperature. NiBTB, UMCM-1, and CdBTB possess higher molar heat capacity due to larger molar mass, while LaBTB, MOF-177, and MOF-39 possess lower molar heat capacity than that of H_3BTB.

Furthermore, the molar heat capacity contribution of Secondary Building Unit (SBU) in MOFs are calculated based on the above mentioned group-contribution method. The SBU of each examined MOF are listed in Table 9.2. Figure 9.19 presents the molar heat capacity contribution of SBU in all examined MOFs. It is very interesting to notice

that almost all heat capacity curve of SBU go through a maximum with the temperature, which indicate a possible thermal structural transformation of SBUs.

Table 9.2 Secondary Building Unit (SBU) of the examined MOFs

MOFs	SBU	Molar Mass of SBU (g/mol)
IRMOF-1 (ZnBDC)	$Zn_4C_6O_{13}$	362.52
HKUST-1(CuBTC)	$Cu_2C_4O_{10}H_4$	315.09
MOF-177 (ZnBTB)	$Zn_4C_6O_{13}$	362.53
MOF-39 (ZnBTB)	$Zn_3C_6O_{14}H_4$	496.14
UMCM-1(ZnBTB+BDC)	$Zn_4C_6O_{13}$	362.53
CuBTB	$Cu_2C_6O_{10}H_8$	367.09
CdBTB	$Cd_3C_{20}O_4N_4H_{44}$	741.23
LaBTB	$LaC_3O_7H_2$	288.91
NiBTB	$NiC_{13}O_6N_2H_9$	347.69

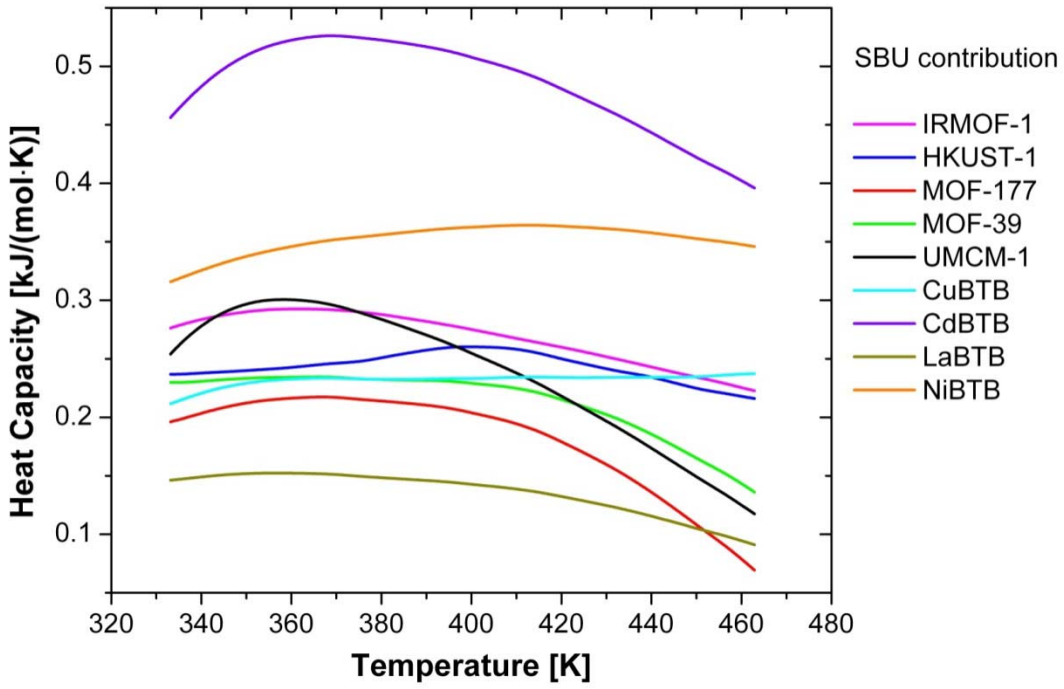

Figure 9.19 Molar heat capacity contribution of SBU in MOFs.

9.3 CONCLUSIONS

Nine MOFs and three organic ligands are examined by thermal analysis techniques. Thermal stability and heat capacity are reported. Among the examined MOFs, LaBTB possesses the highest thermal stability, which is up to 560 ^{o}C. HKUST-1 and CuBTB have the lowest thermal stability, which is less than 300 ^{o}C. Zn, Cd, Ni-based MOFs have the thermal stability of middle range, which is larger than 300 ^{o}C and less than 500 ^{o}C. The high thermal stability of LaBTB is definitely due to the higher coordination number possessed by La atom, which is common in lanthanide elements. Thermal stability of three organic ligands is higher than 300 ^{o}C, in which they could melt or sublime before decomposing. Heat capacity of organic ligands is increasing with

increasing temperature, giving a linear curve. Specific heat capacity (*Cp*) of all examined MOFs are compared with several other solids. Except for HKUST-1 demonstrating a thermal anomaly at around 403 K, the heat capacity of other MOFs show a slight linear increasing tendency with the temperature. NiBTB, UMCM-1, and CdBTB possess higher molar heat capacity due to larger molar mass, while LaBTB, MOF-177, and MOF-39 possess lower molar heat capacity than that of H_3BTB. Compared with other porous materials, the specific heat capacity of MOFs are comparable to that of zeolites, while the values change with varied MOFs. Thus, a fixed-bed adsorber filled with MOFs may have the similar thermal effect as with zeolites.

9.4 REFERENCES

(1) Ma, S. Q. *Pure Appl Chem* **2009**, *81*, 2235.

(2) Ma, S. Q.; Zhou, H. C. *Chem Commun* **2010**, *46*, 44.

(3) Snurr, R. Q.; Hupp, J. T.; Nguyen, S. T. *Aiche J* **2004**, *50*, 1090.

(4) Zou, R. Q.; Abdel-Fattah, A. I.; Xu, H. W.; Zhao, Y. S.; Hickmott, D. D. *Crystengcomm* **2010**, *12*, 1337.

(5) Mu, B.; Schoenecker, P. M.; Walton, K. S. *J Phys Chem C* **2010**, *114*, 6464.

(6) Mu, B.; Li, F.; Walton, K. S. *Chem Commun* **2009**, 2493.

(7) Farrusseng, D.; Daniel, C.; Gaudillere, C.; Ravon, U.; Schuurman, Y.; Mirodatos, C.; Dubbeldam, D.; Frost, H.; Snurr, R. Q. *Langmuir* **2009**, *25*, 7383.

(8) Walton, K. S.; LeVan, M. D. *Ind Eng Chem Res* **2005**, *44*, 7474.

(9) Lucchesi, C. A.; Lewis, W. T. *J Chem Eng Data* **1968**, *13*, 389.

(10) Bailey, M.; Brown, C. J. *Acta Crystallographica* **1967**, *22*, 387.

(11) Davey, R. J.; Maginn, S. J.; Andrews, S. J.; Black, S. N.; Buckley, A. M.; Cottier, D.; Dempsey, P.; Plowman, R.; Rout, J. E.; Stanley, D. R.; Taylor, A. *J Chem Soc Faraday T* **1994**, *90*, 1003.

(12) Herbstein, F. H.; Kapon, M.; Reisner, G. M. *Acta Crystallogr B* **1985**, *41*, 348.

(13) Kaye, S. S.; Dailly, A.; Yaghi, O. M.; Long, J. R. *J Am Chem Soc* **2007**, *129*, 14176.

(14) Chui, S. S. Y.; Lo, S. M. F.; Charmant, J. P. H.; Orpen, A. G.; Williams, I. D. *Science* **1999**, *283*, 1148.

(15) Chae, H. K.; Siberio-Perez, D. Y.; Kim, J.; Go, Y.; Eddaoudi, M.; Matzger, A. J.; O'Keeffe, M.; Yaghi, O. M. *Nature* **2004**, *427*, 523.

(16) Kim, J.; Chen, B. L.; Reineke, T. M.; Li, H. L.; Eddaoudi, M.; Moler, D. B.; O'Keeffe, M.; Yaghi, O. M. *J Am Chem Soc* **2001**, *123*, 8239.

(17) Mu, B.; Huang, Y. G.; Walton, K. S. *Crystengcomm* **2010**, *12*, 2347.

(18) Heck, R.; Bacsa, J.; Warren, J. E.; Rosseinsky, M. J.; Bradshaw, D. *Crystengcomm* **2008**, *10*, 1687.

(19) Goodman, B. T.; Wilding, W. V.; Oscarson, J. L.; Rowley, R. L. *J Chem Eng Data* **2004**, *49*, 24.

(20) Song, L. F.; Jiang, C. H.; Zhang, J. A.; Sun, L. X.; Xu, F.; Tian, Y. Q.; You, W. S.; Cao, Z.; Zhang, L.; Yang, D. W. *J Therm Anal Calorim* **2010**, *101*, 365.

(21) Lv, X. C.; Tan, Z. C.; Gao, X. H.; Zhang, Z. H.; Yang, L. N.; Zhao, J. N.; Sun, L. X.; Zhang, T. *Thermochim Acta* **2006**, *450*, 102.

(22) Jiang, C. H.; Song, L. F.; Zhang, J. A.; Sun, L. X.; Xu, F.; Li, F.; Jiao, Q. Z.; Sun, Z. G.; Xing, Y. H.; Du, Y.; Zeng, J. L.; Cao, Z. *J Therm Anal Calorim* **2010**, *102*, 1087.

(23) Song, L. F.; Jiang, C. H.; Jiao, C. L.; Zhang, J. A.; Sun, L. X.; Xu, F.; Jiao, Q. Z.; Xing, Y. H.; Du, Y.; Cao, Z.; Huang, F. L. *J Therm Anal Calorim* **2010**, *102*, 1161.

(24) Silva, G. G.; Musumeci, A. W.; Gomes, A. P.; Liu, J. W.; Waclawik, E. R.; George, G. A.; Frost, R. L.; Pimenta, M. A. *J Mater Sci* **2009**, *44*, 3498.

(25) Qiu, L. Y.; Murashov, V.; White, M. A. *Solid State Sci* **2000**, *2*, 841.

(26) Qiu, L. Y.; Laws, P. A.; Zhan, B. Z.; White, M. A. *Can J Chem* **2006**, *84*, 134.

(27) Cemic, L.; Dachs, E. *Physics and Chemistry of Minerals* **2006**, *33*, 457.

CHAPTER 10

AIR PURIFICATION APPLICATION OF MOFS

As mentioned in Chapter 1, ammonia (NH_3) and sulfur dioxide (SO_2) are regarded as the high-hazard gases according to a classification set in 1998, and both of them are high vapor pressure chemicals (7600 and 2994 mm Hg at 25 ^oC, respectively), which make them very difficult to remove using current NBC filters. A recent report about the adsorption removal of sulfur dioxide, ammonia, chlorine, dichloromethane, ethylene oxide, and carbon monoxide on MOFs indicates the great potential of these hybrid porous materials as novel air filters.[1] However, very few adsorption studies have been performed for TIC/MOF systems. Thus, in this chapter, we examine ammonia (NH_3) and sulfur dioxide (SO_2) sorption capacity of several representative MOFs to decrease knowledge gaps in this area.

10.1 MOF MATERIALS AND MICROPORE PROPERTIES

So far, 6 MOFs were selected and synthesized in our lab for air purification experiments. Three different metals (Zn, Cu, Zr) and five different ligands are employed to create the MOFs. Two different functional groups including base and acid are combined into the structure. Pore size and specific surface area were measured according single-crystal structure and N_2 adsorption experiments. The structural details are summarized in Table 10.1.

Table 10.1 Structural summary of MOFs for air purification experiments

Sample	Metal	Ligand	Functional Group	Pore size (Å)	Surface area (m^2/g)
DMOF[2]	Zn	BDC, DABCO	-	7.5, 3.2	2000
DMOF-NH_2[3]	Zn	NH_2-BDC, DABCO	Amino (-NH_2)	7.5, <3.2	1300
UIO-66-NH_2[4]	Zr	NH_2-BDC	Amino (-NH_2)	<6	1160
ZnMOF	Zn	3,5a-Htrz	Amino (-NH_2)	6, 4.3	700
CuMOF	Cu (UMCs)	3a,5c-Htrz	Amino (-NH_2)	12	500
CuBTB[5]	Cu (UMCs)	H_3BTB	Carboxylic (-COOH)	12.5, 8, 5.4	600

Table 10.1 Continued

Ligand	**Structure**
Terephthalic acid (BDC)	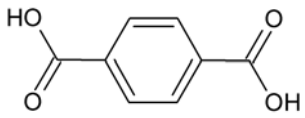
1,4-diazabicyclo[2.2.2]octane (DABCO)	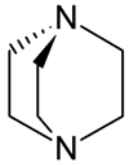
2-Aminoterephthalic acid (NH_2-BDC)	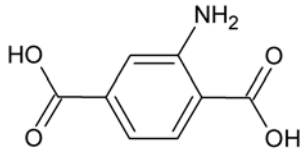
3,5-diamino-1,2,4-triazole (3,5a-Htrz)	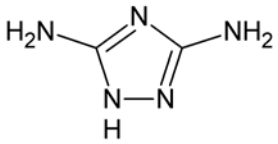
3-amino-1H-1,2,4-triazole-5-carboxylic acid (3a,5c-Htrz)	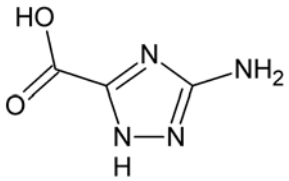
1,3,5-tris(4-carboxyphenyl) benzene (H_3BTB)	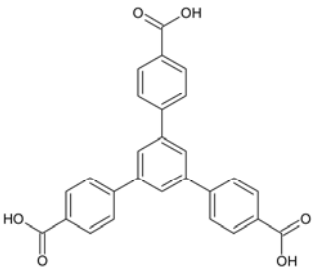

10.2 SORPTION BREAKTHROUGH EXPERIMENTS

The NH_3 and SO_2 sorption breakthrough measurements were performed by our sponsors at Edgewood Chemical Biological Center (ECBC). Experimental feed concentration is 1000 mg/m^3 (equal to 1438 ppm for ammonia, or 382 ppm for sulfur dioxide), while feed flow rate is 20 cc/min. Two humidity conditions were tested including dry air feed and with 80% relative humidity at ambient temperature.

Figure 10.1 and 10.2 presents NH_3 breakthrough curves of the examined MOFs, among which the new Cu-BTB MOF reported by our lab possesses the best ammonia adsorption capacity under both dry air and 80% relative humidity conditions. In addition, it is worthy of note that water is greatly favorable to the ammonia adsorption on Cu-BTB, which doubles the capacity of Cu-BTB. Compared with CuMOF, the outstanding performance of Cu-BTB also demonstrates the important role played by carboxylic functional group. Figure 10.3 and 10.4 presents SO_2 breakthrough curves of the MOFs. DMOF and ZnMOF which possess N atoms in their structures present potential SO_2 adsorption capacity. Although amino functional group does not perform as well as we expected for acid gas sorption, the water does facilitate SO_2 interaction with amino functional groups in humidity conditions. Saturation capacities of MOFs for NH_3 and SO_2 are listed in Table 6 for comparison.

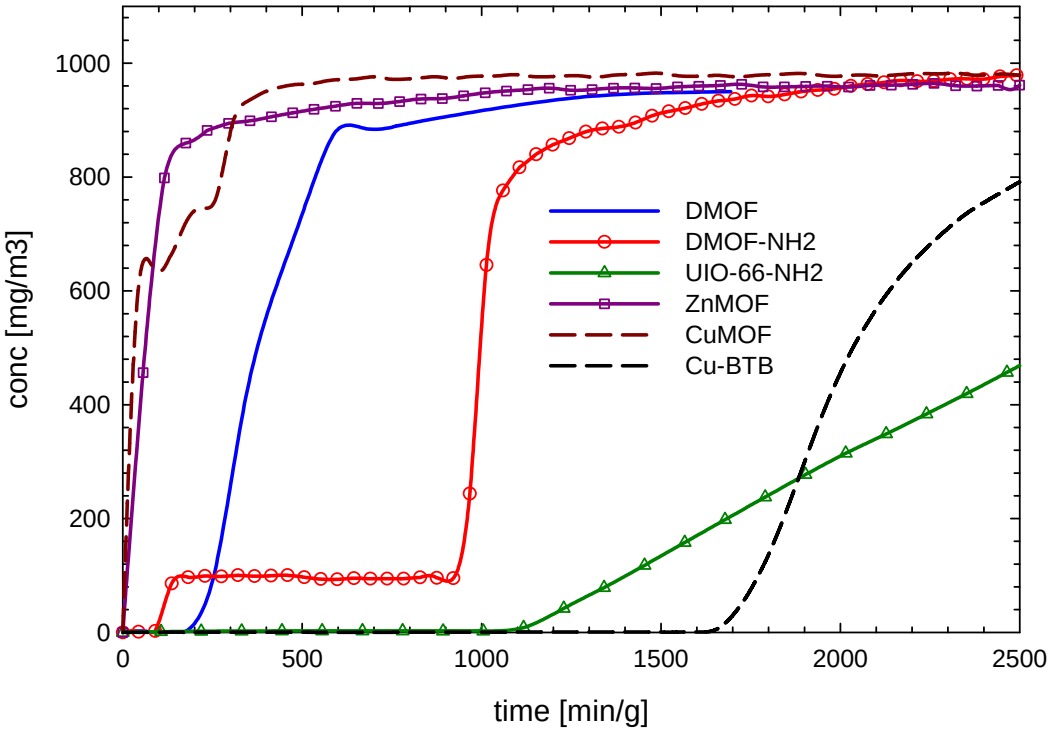

Figure 10.1 NH_3 breakthrough results under dry air conditions

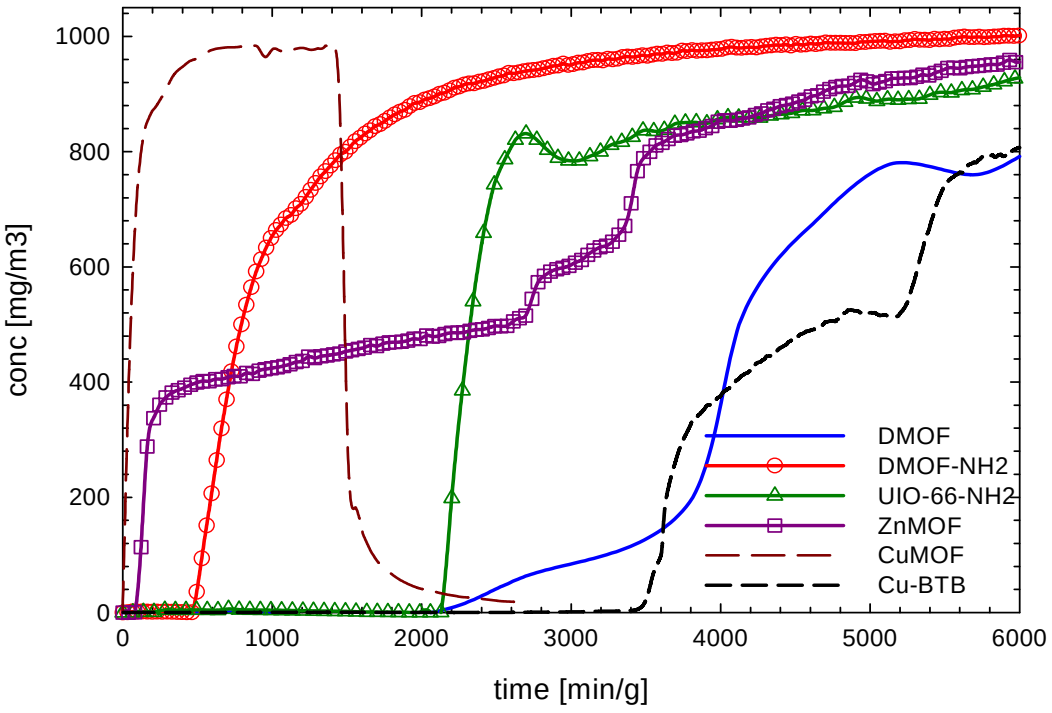

Figure 10.2 NH_3 breakthrough results under 80% RH conditions

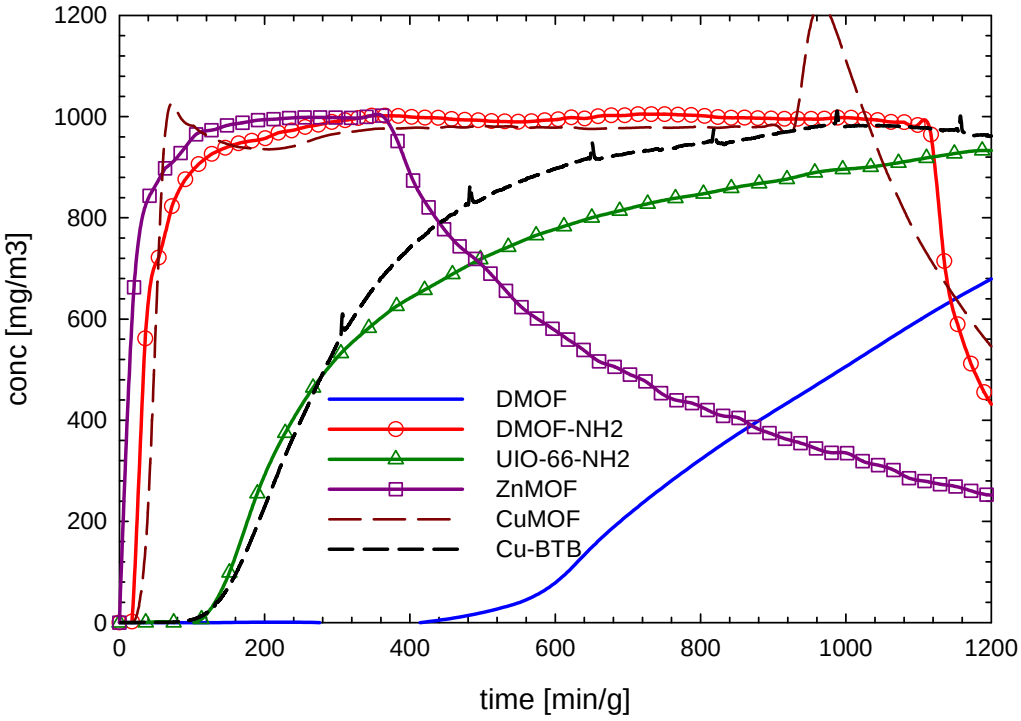

Figure 10.3 SO_2 breakthrough results under dry air conditions

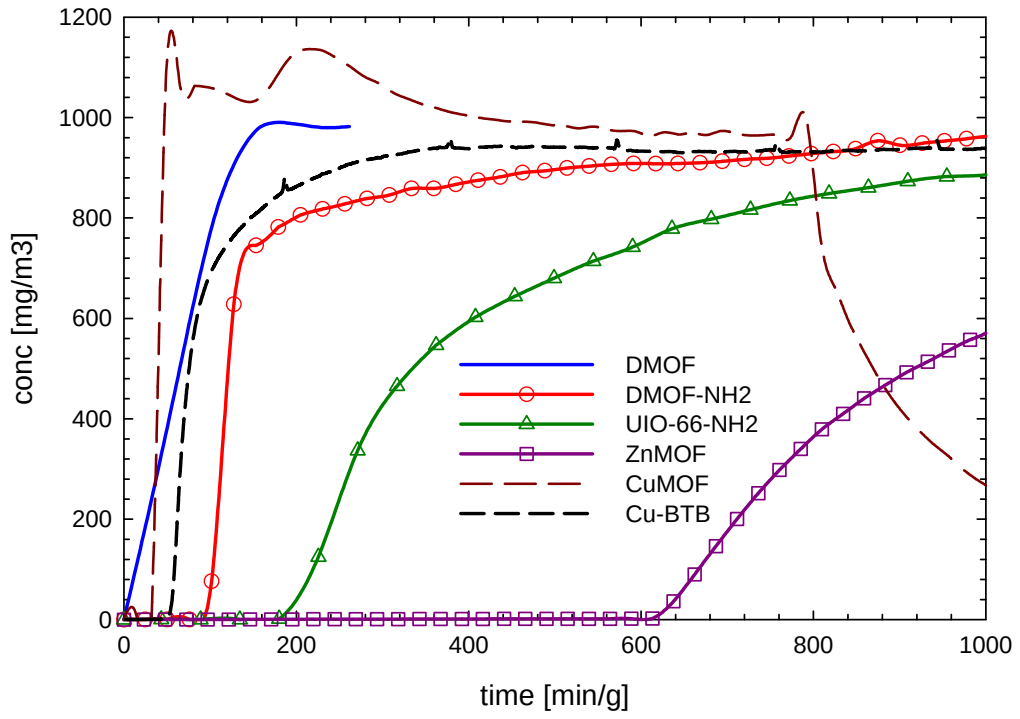

Figure 10.4 SO_2 breakthrough results under 80% RH conditions

Table 10.2 Saturation capacities of MOFs for NH_3 and SO_2

Sample	NH_3		SO_2		UMCs	Functional Group	Pore Size (Å)	Surface Area (m^2/g)
	Dry (mol/kg)	80% RH (mol/kg)	Dry (mol/kg)	80% RH (mol/kg)				
DMOF	0.27	5.56	0.32	0.02	-	-	7.5, 3.2	2000
DMOF-NH_2	1.23	1.29	0.0176	0.0797	-	Amino (-NH_2)	7.5, <3.2	1300
UIO-66-NH_2	4.04	3.43	0.151	0.159	-	Amino (-NH_2)	<6	1160
ZnMOF	0.25	2.59	0.0084	0.48	-	Amino (-NH_2)	6, 4.3	700
CuMOF	0.2	0.144	0.022	0.0066	Cu	Amino (-NH_2)	12	500
Cu-BTB	2.19	5.95	0.113	0.055	Cu	Carboxylic (-COOH)	12.5, 8, 5.4	650

10.3 CONCLUSIONS

In conclusion, breakthrough results demonstrated that (1) Lewis acid sites (unsaturated metals centers, UMCs) and carboxylic functional group (–COOH) are more effective than H-bonding groups (-NH2) for base gas adsorption (NH3); (2) water is helpful to NH3 adsorption on MOFs except for UIO-66-NH2 and CuMOF, and is helpful to SO2 adsorption on DMOF-NH2, UIO-66-NH2, and ZnMOF; (3) while base functional groups (-NH2) may improve the adsorption capacity of acid gas, they may block the pore and lead to the decrease of pore volume and surface area; (4) pore sizes play a certain

role for diffusion of molecules in pores, while surface area is not so important for our application; (5) while functional groups or active sites play an important role for specific molecule adsorption, increasing the density of active sites is the primary challenge for future material synthesis.

10.4 REFERENCES

(1) Britt, D.; Tranchemontagne, D.; Yaghi, O. M. *P Natl Acad Sci USA* **2008**, *105*, 11623.

(2) Lee, J. Y.; Olson, D. H.; Pan, L.; Emge, T. J.; Li, J. *Adv Funct Mater* **2007**, *17*, 1255.

(3) Wang, Z. Q.; Tanabe, K. K.; Cohen, S. M. *Inorg Chem* **2009**, *48*, 296.

(4) Cavka, J. H.; Jakobsen, S.; Olsbye, U.; Guillou, N.; Lamberti, C.; Bordiga, S.; Lillerud, K. P. *J Am Chem Soc* **2008**, *130*, 13850.

(5) Mu, B.; Li, F.; Walton, K. S. *Chem Commun* **2009**, 2493.

CHAPTER 11

CONCLUSIONS

There is no doubt that metal-organic frameworks (MOFs) are becoming one of the most exciting research areas in nanoporous materials. These organic-inorganic hybrids possess highly porous structure, chemical versatility, and structural tailorability, which are the main characteristics and merits of porous MOFs, and put them at the forefront of materials science. As mentioned in Chapter 1, besides the studies focused on gas adsorption application, an increasing number of MOFs are now being explored for their interesting properties. These emerging application-oriented studies include heterogeneous catalysis,[1] chiral separation,[2-3] drug delivery,[4-8] luminescence,[9] magnetism,[10-11] nonlinear optics,[12-14] semiconductivity,[15-16] and as nanoreactors.[17] Thus, the interdisciplinary application studies would be one of the major driving forces behind MOFs, which should have a very bright future. In this chapter, we first summarize the results and significant conclusions about synthesis and gas adsorption studies of MOFs, and then some personal thoughts are provided here as a perspective of future work.

11.1 CONCLUSIONS

As discussed in Chapter 1, the objective of our research is three-fold involving both fundamental and application studies. Progress towards meeting the project objectives is summarized below:

(1) Five novel MOFs were synthesized and characterized in our lab, which greatly enrich the variety of MOFs composed of H_3BTB ligand, and result in the number of

known BTB-MOF structures increases to 30 according to the results of literature and Cambridge Structural Database (CSD) investigation. By analyzing the synthesis procedures, structural topologies, and functional properties, such more synthesis-structure-property relation information will undoubtedly facilitate better understanding of the reaction mechanism in coordination chemistry. Some important conclusions could be drawn: water-ethanol systems can facilitate the formation of crystals of Cu-based MOFs easier than other solvents; DEF-DMF systems are the better choice for obtaining Zn or Co based MOFs; lanthanide-based MOFs usually possess higher thermal stability than transition-metal based MOFs; Cu-based MOFs have lower thermal stability than Zn or Co based MOFs; higher temperature and the presence of strong deprotonation agents facilitate the formation of 3-dimensional frameworks.

(2) Some representative MOF or newly synthesized MOF materials were produced successfully, and various characterization measurements and gas adsorption experiments were performed in this work. Pure-component high-pressure adsorption isotherms, heat of adsorption, adsorption selectivity, and heat capacity data were collected experimentally and further calculated theoretically. The examined gases involve CO_2, CH_4, N_2, O_2, and H_2. These data will be very useful to gain better understanding of the relationship between the crystal structure and gas adsorption ability, to evaluate the applicability of widely-used adsorption models on novel porous MOF materials, and to develop more practical adsorption models for potential industrial application of MOFs. Some important conclusions could be drawn: big pore volume and high surface area are required for gas storage application, while it is not the case for adsorptive separation; selective adsorption ability of MOFs can be improved by introducing unsaturated metals

centers and functional group into the framework as demonstrated by Cu-BTB; Dubinin's micropore-filling mechanism provides better theoretical explanation for gas adsorption on MOFs; opportunity exists for develop more accurate adsorption models for flexible MOFs.

(3) Six MOFs were tested with adsorption breakthrough experiments of air purification at Edgewood Chemical Biological Center (ECBC). Three different metals (Zn, Cu, Zr) and five different ligands are employed to create the MOFs. Two different functional groups including base and acid are combined into the structure. Pore size and specific surface area were measured according single-crystal structure and N_2 adsorption experiments. The experimental results show that MOF materials provide significant improvement over traditional NBC filter media, a special impregnated activated carbon (I-AC). In particular, Cu-BTB provides protection against NH_3 that is more than 1000 times better than I-AC. Some important conclusions could be drawn: lewis acid sites (unsaturated metals centers, UMCs) and carboxylic functional group (–COOH) are more effective than H-bonding groups ($-NH_2$) for base gas adsorption (NH_3) as demonstrated by Cu-BTB which presents the best ammonia adsorption capacity among the all examined porous materials; while base functional groups ($-NH_2$) may improve the adsorption capacity of acid gas, they may block the pore and lead to the decrease of pore volume and surface area; pore sizes play an important role for diffusion rates of molecules in pores, while surface area is not so important for our application. Thus, our work demonstrates that MOFs provide significant improvement over activated carbon, and are potential advanced materials for improved air purification system which have wide applications involving individual protective device and collective protective system.

11.2 PERSPECTIVE ON FUTURE DIRECTION

Some personal thoughts are provided here as a perspective of future work. With respect to synthesis efforts of MOFs using BTB ligand, attempts to decrease the density of whole material for increasing porosity per mass unit were carried out by using lighter metals such as Mg and Al. However, only some unknown powder crystals were obtained in several experiments, and attempts to get their crystal structure using single-crystal diffraction technology are not successful so far. However, it is not impossible to synthesize new MOFs with these metal centers under proper reaction conditions. Furthermore, it is worthwhile to attempt using lanthanide and Zr as metal centers to provide more stable and functional advanced porous material.

With respect of synthesis technology, solvothermal and hydrothermal reaction are still most widely used approaches. Scale-up of reaction is a bottleneck for industrial scaled, or sometimes even bench scaled production, just like any other scale-up issue of reactors confusing chemical engineers for many years. Thus, further crystallization and nucleation mechanism study involving thermodynamics and kinetics will help us to understand the growth process of MOFs, and facilitate the solving of scale-up issue, which should be an excellent fundamental research topic.

With respect of long-term stability of MOFs, it is well known that MOFs behave poorly according to the long-term stability compared with other porous materials such as activated carbon, zeolites, and carbon nanotubes. To date, there is no systematic method to measure the long-term stability of porous materials. Thus, to design such method and to develop it as a standard method just like we measure surface area using N_2 at 77 K will be a very meaningful work to do.

11.3 REFERENCES

(1) Lee, J.; Farha, O. K.; Roberts, J.; Scheidt, K. A.; Nguyen, S. T.; Hupp, J. T. *Chem Soc Rev* **2009**, *38*, 1450.

(2) Morris, R. E.; Bu, X. H. *Nat Chem* **2010**, *2*, 353.

(3) Crassous, J. *Chem Soc Rev* **2009**, *38*, 830.

(4) An, J. Y.; Geib, S. J.; Rosi, N. L. *J Am Chem Soc* **2009**, *131*, 8376.

(5) Horcajada, P.; Serre, C.; Maurin, G.; Ramsahye, N. A.; Balas, F.; Vallet-Regi, M.; Sebban, M.; Taulelle, F.; Ferey, G. *J Am Chem Soc* **2008**, *130*, 6774.

(6) Horcajada, P.; Chalati, T.; Serre, C.; Gillet, B.; Sebrie, C.; Baati, T.; Eubank, J. F.; Heurtaux, D.; Clayette, P.; Kreuz, C.; Chang, J. S.; Hwang, Y. K.; Marsaud, V.; Bories, P. N.; Cynober, L.; Gil, S.; Ferey, G.; Couvreur, P.; Gref, R. *Nat Mater* **2010**, *9*, 172.

(7) Taylor-Pashow, K. M. L.; Della Rocca, J.; Xie, Z. G.; Tran, S.; Lin, W. B. *J Am Chem Soc* **2009**, *131*, 14261.

(8) Huxford, R. C.; Della Rocca, J.; Lin, W. B. *Curr Opin Chem Biol* **2010**, *14*, 262.

(9) Allendorf, M. D.; Bauer, C. A.; Bhakta, R. K.; Houk, R. J. T. *Chem Soc Rev* **2009**, *38*, 1330.

(10) Huang, Y. G.; Jiang, F. L.; Hong, M. C. *Coordin Chem Rev* **2009**, *253*, 2814.

(11) Kurmoo, M. *Chem Soc Rev* **2009**, *38*, 1353.

(12) Janiak, C. *Dalton T* **2003**, 2781.

(13) Yu, Z. P.; Xie, Y.; Wang, S. J.; Yong, G. P.; Wang, Z. Y. *Inorg Chem Commun* **2008**, *11*, 372.

(14) Zhang, L. J.; Yu, J. H.; Xu, J. Q.; Lu, J.; Bie, H. Y.; Zhang, X. *Inorg Chem Commun* **2005**, *8*, 638.

(15) Alvaro, M.; Carbonell, E.; Ferrer, B.; Xamena, F.; Garcia, H. *Chem-Eur J* **2007**, *13*, 5106.

(16) Silva, C. G.; Corma, A.; Garcia, H. *J Mater Chem* **2010**, *20*, 3141.

(17) Ferey, G. *Chem Soc Rev* **2008**, *37*, 191.